

**HZDR-089**

**HIGH-YIELD OPTICAL UNDULATORS  
SCALABLE TO OPTICAL FREE-ELECTRON  
LASER OPERATION BY TRAVELING-WAVE  
THOMSON-SCATTERING**

Klaus Steiniger

Wissenschaftlich-Technische Berichte  
HZDR-089 · ISSN 2191-8708

**WISSENSCHAFTLICH-  
TECHNISCHE BERICHTE**

**hZDR**



**HELMHOLTZ  
ZENTRUM DRESDEN  
ROSSENDORF**



Wissenschaftlich-Technische Berichte  
HZDR-089

Klaus Steiniger

**HIGH-YIELD OPTICAL UNDULATORS  
SCALABLE TO OPTICAL FREE-ELECTRON  
LASER OPERATION BY TRAVELING-WAVE  
THOMSON-SCATTERING**

**HZDR**

 **HELMHOLTZ**  
| ZENTRUM DRESDEN  
| ROSSENDORF

Druckausgabe: ISSN 2191-8708

Elektronische Ausgabe: ISSN 2191-8716

Die elektronische Ausgabe erscheint unter Creative Commons License (CC BY 4.0):

<https://www.hzdr.de/publications/Publ-27169>

<urn:nbn:de:bsz:d120-qucosa-234292>

Die vorliegende Arbeit wurde sowohl als Dissertation an der Fakultät Mathematik und Naturwissenschaften der Technischen Universität Dresden sowie als Wissenschaftlich-Technischer Bericht des Helmholtz-Zentrum Dresden – Rossendorf mit der Berichtsnummer **HZDR-089** veröffentlicht.

2018

Herausgegeben vom

Helmholtz-Zentrum Dresden - Rossendorf

Bautzner Landstraße 400

01328 Dresden

Germany



# **HIGH-YIELD OPTICAL UNDULATORS SCALABLE TO OPTICAL FREE-ELECTRON LASER OPERATION BY TRAVELING-WAVE THOMSON-SCATTERING**

Dipl.-Phys. Klaus Steiniger

Geboren am: 24. Dezember 1986 in Karl-Marx-Stadt, jetzt Chemnitz

## **DISSERTATION**

zur Erlangung des akademischen Grades

## **DOCTOR RERUM NATURALIUM (DR. RER. NAT.)**

Erstgutachter

**Prof. Dr. Ulrich Schramm**

Zweitgutachter

**Priv.-Doz. Dr. Atoosa Meseck**

**Prof. Dr. Thomas Cowan**

Eingereicht am: 25. Juli 2017

Verteidigt am: 15. Dezember 2017

Die Dissertation wurde in der Zeit von Januar 2013 bis Juli 2017 am Helmholtz-Zentrum Dresden – Rossendorf im Institut für Strahlenphysik angefertigt.





## KURZFASSUNG

Inkohärente und kohärente Lichtquellen werden in allen Feldern der physikalischen Forschung intensiv eingesetzt. Im Besonderen ermöglichen hoch-brillianten Röntgenquellen, wie Synchrotrone der dritten Generation und Freie-Elektronen Laser, einzigartige Experimentiertechniken wodurch diese zu unverzichtbaren Werkzeugen wurden. Sie sind allerdings auch im Umfang zu Großforschungseinrichtungen herangewachsen. Um den hohen Bedarf an hoch-brillianten Lichtquellen zu decken, besteht daher die Notwendigkeit neuartige und kompakte Quellen zu entwickeln welche auf dem Maßstab eines Labors realisierbar sind.

Diese Dissertation widmet sich der Traveling-Wave Thomsonstreuung (TWTS) welche die Realisierung ultra-kompakter, intrinsisch synchronisierbarer und hoch-brillianten Röntgenquellen ermöglicht. TWTS ist eine Methode der Streuung von Laserpulsen an relativistischen Elektronen. Dabei durchquert ein Elektronenpuls mit nahezu Lichtgeschwindigkeit einen Laserpuls. Während der Durchquerung beginnen die Elektronen im Feld des Laserpulses zu oszillieren wobei sie Strahlung emittieren. Die ausgesandte Strahlung besitzt eine deutlich kürzere Wellenlänge als das Laserfeld aufgrund der hohen Elektronengeschwindigkeit und der damit verbundenen großen Dopplerverschiebung. Das besondere an TWTS ist, dass Elektronen- und Laserpropagationsrichtung einen Winkel einschließen sowie pulsfrentverkippte Hochleistungslaserpulse eingesetzt werden. Dadurch können um Größenordnungen längere Interaktionsdistanzen als in herkömmlichen frontalen Thomsonstreuungsanordnungen erreicht werden.

TWTS ermöglicht dadurch die Realisierung optischer Freie-Elektronen Laser (OFEL) und inkohärenter Strahlungsquellen mit einer um Größenordnungen erhöhten Photonenausbeute gegenüber Thomsonstreuungsquellen in frontalen Interaktionsanordnungen. Werden modernste Elektronenbeschleuniger und Lasersysteme genutzt, dann ist der Betrieb optischer Freie-Elektronen Laser bereits heute mit TWTS möglich.

Das wird in der Dissertation am Beispiel eines Vakuumultraviolettstrahlung emittierenden TWTS OFEL gezeigt. Dessen Anforderungen an die Qualität der Elektronen- und Laserpulse werden im Detail in der Arbeit besprochen sowie weitere Beispiele weicher und harter Röntgenstrahlung emittierender TWTS OFEL präsentiert. Diese Anforderungen werden anhand von Skalierungsvorschriften ermittelt welche aus einer selbstkonsistenten, 1.5 dimensional Theorie zur Wechselwirkung zwischen Elektronen und Laserfeld in TWTS abgeleitet sind. Sowohl die Theorie zur Wechselwirkung als auch die Ableitung der Skalierungsvorschriften sind Teile dieser Dissertation. Eine wichtige Erkenntnis der Theorie ist die qualitative Äquivalenz von Elektronen- und Strahlungsfeldbewegungsgleichungen in TWTS zu denen herkömmlicher Freie-Elektronen Laser. Das beweist analytisch die Möglichkeit zur Realisierung eines OFEL mit TWTS.

Einen weiteren wichtigen Teil dieser Dissertation bildet die Arbeit zur Generierung der Laserpulse mit verkippter Pulsfront. Optische Aufbauten zur Verkipfung der Laserpulsfront werden vorgestellt und für einige der präsentierten TWTS OFEL ausführlich dargelegt. Die Aufbauten verkippen nicht nur die Laserpulsfront sondern gewähren gleichzeitig Kontrolle über die Laserpulsdispersionen. Dadurch kann während der gesamten Interaktionen eine ausreichend hohe Qualität des Laserfeldes sichergestellt werden, was für TWTS OFEL und inkohärente TWTS Lichtquellen mit großem Interaktionswinkel unbedingt notwendig ist. Ein Beispiel einer inkohärenten TWTS Lichtquelle wird ebenfalls präsentiert. Diese emittiert Strahlung mit einer um Größenordnungen höheren spektrale Photonendichte als eine herkömmliche Thomsonquelle in einer frontalen Streuanordnung mit vergleichbaren Laser- und Elektronenpulsen.

## ABSTRACT

All across physics research, incoherent and coherent light sources are extensively utilized. Especially highly brilliant X-ray sources such as third generation synchrotrons or free-electron lasers have become an invaluable tool enabling experimental techniques that are unique to these kinds of light sources. But these sources have developed to large scale facilities and a demand in compact laboratory scale sources providing radiation of similar quality arises nowadays.

This thesis focuses on Traveling-Wave Thomson-Scattering (TWTS) which allows for the realization of ultra-compact, inherently synchronized and highly brilliant light sources. The TWTS geometry provides optical undulators, through which electrons pass and thereby emit radiation, with hundreds to thousands of undulator periods by utilizing pulse-front tilted laser pulses from high peak-power laser systems.

TWTS can realize incoherent radiation sources with orders of magnitude higher photon yield than established head-on Thomson sources. Moreover, optical free-electron lasers (OFELs) can be realized with TWTS if state-of-the-art technology in electron accelerators and laser systems is utilized.

This thesis will show that TWTS OFELs emitting ultraviolet radiation are realizable today with existing technology for electron accelerators and laser systems. The requirements on electron bunch and laser pulse quality of these ultraviolet TWTS OFELs are discussed in detail as well as the corresponding requirements of TWTS OFELs emitting in the soft and hard X-ray range. These requirements are derived from scaling laws which stem from a self-consistent analytic description of the electron bunch and radiation field dynamics in TWTS OFELs presented within this thesis. It is shown that these dynamics in TWTS OFELs are qualitatively equivalent to the electron bunch and radiation field dynamics of standard free-electron lasers which analytically proves the applicability of TWTS for the realization of an optical free-electron laser.

Furthermore, experimental setup strategies to generate the pulse-front tilted TWTS laser pulses are presented and designs of experimental setups for the above examples are discussed. The presented setup strategies provide dispersion compensation, required due to angular dispersion of the laser pulse, which is especially relevant when building compact, high-yield hard X-ray TWTS sources in large interaction angle setups. An example of such an *enhanced Thomson* source by TWTS, which provides orders of magnitude higher spectral photon density than a comparable head-on interaction geometry, is presented, too.

# CONTENTS

Kurzfassung	3
Abstract	4
1. Motivation	7
2. Principles of Free-Electron Lasers	11
2.1. What is a Free-Electron Laser?	11
2.2. Microbunching and Coherent Radiation Amplification in an FEL	15
2.2.1. Microbunching without Radiation Field Gain	15
2.2.2. Microbunching and Radiation Amplification with Radiation Field Gain	17
2.3. Requirements on Electron Bunch and Radiation Beam Parameters	19
2.4. Radiation Properties of Self-Amplified Spontaneous Emission FELs	22
3. Traveling-Wave Thomson-Scattering for Compact and Bright Light Sources	25
3.1. Limits of Standard Head-On Thomson Scattering	26
3.2. Scalable Optical Undulators with Traveling-Wave Thomson-Scattering	27
3.3. Why Compact Free-Electron Laser Schemes Have Higher Quality Requirements on Electron Bunches	29
3.4. Traveling-Wave Thomson-Scattering for Optical Free-Electron Lasers	30
4. Description and Generation of TWTS Laser Pulses	35
4.1. Dispersions of Pulse-Front Tilted Laser Pulses	35
4.2. Evaluating Frequency and Amplitude Variations of Optical Undulators in TWTS geometries without Dispersion Compensation During Interaction	39
4.2.1. Analytic Description of Pulse-Front Tilted Laser Pulses	39
4.2.2. Approximating Optical Undulator Amplitude Variation During Interaction	41
4.2.3. Approximating Optical Undulator Frequency Variation During Interaction	42
4.3. TWTS Setups without Focusing in the Interaction Plane and without Dispersion Compensation During Interaction	43
4.4. TWTS Setups with Full Dispersion Compensation During Interaction but without Focusing in the Interaction Plane	45
4.4.1. Dispersion Compensation During Interaction by Exploiting the Plane of Optimum Compression	45
4.4.2. Two Grating Setups to Control Orientation of Pulse-Front Tilt and Plane of Optimum Compression Independent of Each Other	47

4.4.3.	Obtaining Parameters for the Setup . . . . .	50
4.4.4.	Variations in Undulator Frequency and Amplitude from Misalignments in the Setup . . . . .	52
4.5.	TWTS Setups with Full Dispersion Compensation During Interaction and with Focusing in the Interaction Plane . . . . .	54
4.5.1.	Focusing and Pulse-Front Tilt Generation with an Off-Axis Cylindrical Mirror . . . . .	55
4.5.2.	Realization and Limits of the Out-Of-Focus Interaction geometry . . . . .	56
4.5.3.	Variations in Undulator Frequency and Amplitude from Misalignment and Out-Of-Focus Interaction . . . . .	65
<b>5.</b>	<b>Traveling-Wave Thomson-Scattering for Optical Free-Electron Lasers</b>	<b>67</b>
5.1.	Foundations of the TWTS OFEL Theory . . . . .	67
5.1.1.	Plane Wave Ansatz for the Laser Field . . . . .	67
5.1.2.	Off-Axis Radiation Emission . . . . .	69
5.2.	Derivation of the TWTS OFEL Equations of Motion . . . . .	72
5.2.1.	Pendulum Equations of TWTS OFELs . . . . .	73
5.2.2.	Self-Consistent Equations of Motion of TWTS OFELs . . . . .	76
5.2.3.	TWTS OFEL Equations of Motion in Universal Scaling . . . . .	77
5.3.	Scaling Laws of TWTS OFELs . . . . .	78
<b>6.</b>	<b>Examples of TWTS Light Sources</b>	<b>83</b>
6.1.	Hard X-Ray Enhanced Thomson Source . . . . .	87
6.1.1.	Determining Optical setup Parameters . . . . .	87
6.1.2.	Modeling the setup in ZEMAX . . . . .	91
6.2.	A Vacuum Ultraviolet TWTS OFEL Realizable Today . . . . .	93
6.2.1.	Determining Electron Bunch Parameters . . . . .	93
6.2.2.	Determining Optical Setup Parameters . . . . .	98
6.2.3.	Optical Components Alignment Tolerances . . . . .	99
6.3.	Scaling Towards Shorter Wavelengths and Compacter Setups . . . . .	100
6.3.1.	Employing Higher Power Laser Pulses . . . . .	101
6.3.2.	Reducing Electron Energy Spread . . . . .	102
6.3.3.	Employing Longer Wavelengths Laser Systems . . . . .	103
6.3.4.	Employing Laser Wakefield Accelerators . . . . .	105
6.4.	Å TWTS OFEL to Observe Plasma Dynamics During Laser Driven Ion Acceleration from Solid Foils at HZDR . . . . .	108
6.4.1.	Imaging Electron and Ion Distributions with Femtosecond and Nanometer Scale Resolution . . . . .	108
6.4.2.	Determining Parameters of the Å TWTS OFEL . . . . .	109
6.4.3.	Applying the Å TWTS OFEL to Plasma Dynamics Studies . . . . .	114
<b>7.</b>	<b>Conclusion &amp; Outlook</b>	<b>119</b>
<b>A.</b>	<b>Macro to Evaluate Laser Pulse Dispersions in ZEMAX</b>	<b>123</b>
<b>B.</b>	<b>Calculating Scattering Images from 2D Electron Number Density Data</b>	<b>129</b>
	<b>Publications by the Author</b>	<b>135</b>
	<b>References</b>	<b>137</b>
	<b>Ein herzliches Dankeschön</b>	<b>161</b>

# 1. MOTIVATION

Free-electron lasers (FEL) enabled numerous scientific discoveries throughout various fields of science ranging from e.g. chemistry [1–3] over atomic and molecular physics [4–6] as well as material physics [7–9] to structural biology [10–12]. They can provide intense, ultrashort and coherent radiation pulses with central wavelengths within a spectral region ranging from several hundred micrometers (Terahertz scale) down to a tenth of a nanometer (Ångström scale), depending on design [13]. Accordingly, the range in applications of FELs is large as illustrated by the selection of works above.

FELs providing infrared radiation are available for decades by now but the quest for understanding matter at atomic length and time scales and beyond has driven the development towards hard X-ray FELs providing radiation pulses of femtosecond durations and Ångström wavelengths. These enabled, for example, the study of transient nanoscale dynamics of matter or the determination of structure of small samples *before* these are destroyed by the intense FEL radiation pulse [14–19]. But the continuous progress towards shorter radiation wavelength came on the expense of increased machine size. While FELs providing far infrared radiation can be realized on a ten meter scale [20] modern hard X-ray FELs have several hundred meter space requirements [21, 22]. Naturally, these large scale facilities have higher costs in construction, operation and personnel. It is therefore desirable to find a feasible solution to reduce the size of these machines again. This requires to find alternate ways to drive the process underlying radiation generation in an FEL, since the size increase is inherent to the conventional method used to build these machines.

In a conventional FEL radiation is produced by relativistic electrons traveling through an undulator, a device consisting of an array of permanent magnets pairs facing each other with different polarities. From pair to pair the orientation of the magnets is flipped such that the resulting magnetic field in the undulator resembles a plane magnetic wave. Electrons traversing the undulator propagate between the poles of the magnet pairs and thus wiggle with the period of the undulator magnetic field. Thereby they emit radiation at a wavelength determined by their energy  $E_e$  and the undulator magnetic field period  $\lambda_u$

$$\lambda_{\text{FEL}} \propto \frac{\lambda_u}{E_e^2}.$$

The interaction distance required to drive radiation generation until saturation, where no more electron kinetic energy can be converted into radiation, also scales with electron energy and undulator period

$$L_{\text{sat}} \propto E_e \lambda_u^{1/3}.$$

In order to reduce the size of FELs alternative undulator concepts therefore aim at reducing the undulator period from the centimeter scale available with conventional undulators into the millimeter or micrometer scale. Reducing the undulator period by one to two orders of magnitude allows for a significant reduction of the light source size since the required electron energy to produce radiation in the X-ray range reduces by an order of magnitude, too, which allows for an order of magnitude reduction of the kilometer-scale spanning electron accelerators and thus a significant reduction of facility cost. Furthermore, reduced undulator periods also reduce the interaction distance required to achieve saturation in FEL radiation production which gives rise to another reduction of facility size, though it is not as tremendous as the reduction in electron accelerator length.

Alternative undulator concepts include dielectric structures [23, 24], circular corrugated microwave waveguides [25] and helical waveguides for microwave pulses copropagating with the electrons [26]. However, laser pulses [27, 28] are the only scalable alternative to conventional magnetic undulators since they avoid the generation of electron beam wakefields by surrounding structures as well as are able to provide undulators of several hundred periods lengths at field strengths necessary to drive radiation generation until saturation. When utilizing laser pulses as optical undulators the electron wiggling motion is induced by the electric field of the laser and the wiggling period is given by the laser wavelength. It is typically on the micrometer scale for high-power laser systems and thus three to four orders of magnitude smaller than the period of magnetic undulators. On a fundamental level the radiation generation in optical undulators is completely equivalent to magnetic undulators which becomes clear when comparing the electromagnetic fields and their induced motion in the electron rest frame [29].

In fact, the idea to utilize optical undulators to build an FEL is more than thirty years old and a couple of incoherent sources have been built already [30–38]. Nowadays a few of these are routinely operated [39–41] and these are the only existing sources of well defined high flux radiation at picometer scale wavelengths. Light sources employing optical undulators are commonly dubbed *Thomson scattering* or *inverse Compton scattering* sources [42–45].

A recent development is the realization of all-optical Thomson sources [46–54] by utilizing *laser wakefield acceleration* (LWFA) of electrons [55–60]. Laser wakefield accelerators are able to accelerate electron bunches to energies on the scale of gigaelectronvolts within a few centimeter acceleration distance and to produce electron bunch charges on the scale of hundred picocoulombs [61, 62]. Electron acceleration takes place by focusing a high-power laser pulse to micrometer scale transverse widths into an underdense plasma, i. e. a plasma of low enough density such that the laser pulse is not reflected at the vacuum-plasma transition region, in order to excite a charge density wave [63]. In LWFA driven Thomson sources the largest component is the laser system itself since acceleration and scattering take place on a centimeter scale. Therefore, these compact sources can be considered “table-top” in comparison to conventional accelerator driven sources employing radiofrequency cavities for electron acceleration and magnetic undulators for radiation generation.

Although there have been many realizations of incoherent Thomson sources, an optical FEL (OFEL) could not be demonstrated up to date. Reasons can be found in the extremely challenging requirements on the quality of electron bunches and laser pulses inherent to the head-on scattering geometry of proposed optical FEL schemes so far [64–66].

Traveling-Wave Thomson-Scattering (TWTS) geometries [67, 68] overcome this problem of head-on geometries allowing for the realization of optical free-electron lasers [KS1]. Within this thesis it is shown that OFELs [KS2, KS3] can be realized by TWTS today. With TWTS the electron bunch and laser pulse requirements for TWTS OFEL operation can be lowered to a level feasible with current state-of-the-art technology in electron accelerators and laser systems. The combination of TWTS and LWFA thereby allows for ultra compact setups with inherent synchronization of electrons and laser. Using conventional accelerated electrons is of course possible, too.

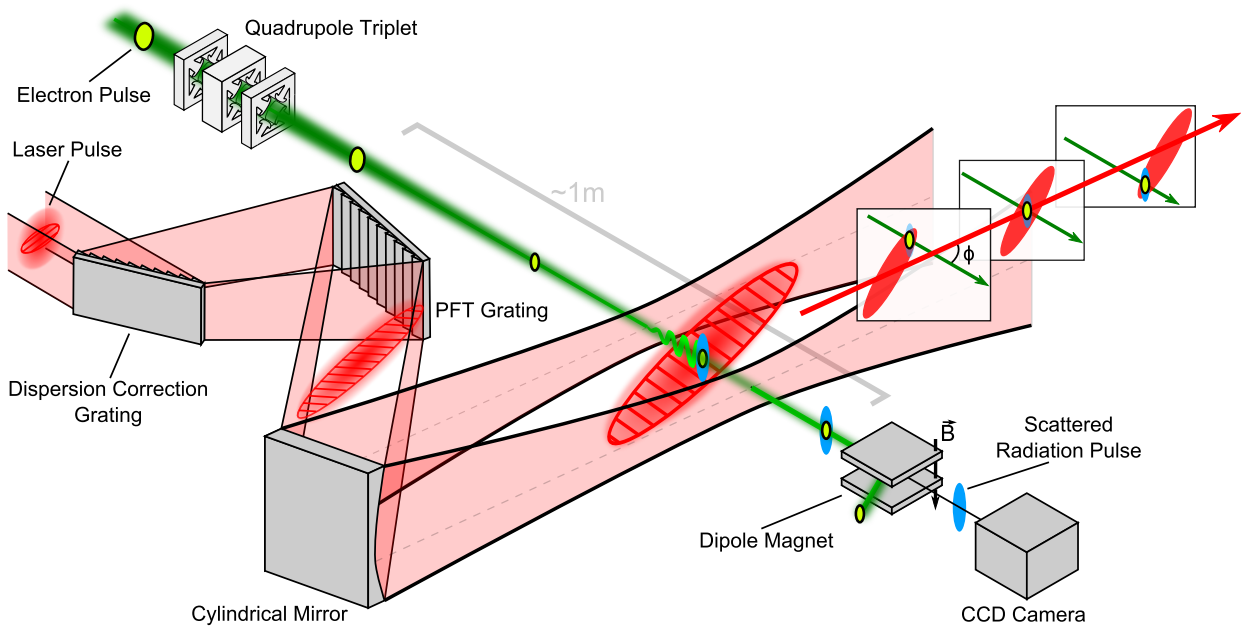


Figure 1.1.: The Traveling-Wave Thomson-Scattering geometry for incoherent high yield hard X-ray sources and TWTS OFELs. Radiation is produced by relativistic electrons flying through an optical undulator realized by a pulse-front tilted laser pulse. These are prepared by letting a laser pulse from a high peak-power laser system pass through a grating pair arrangement which first tilts the laser pulse-front and second controls laser dispersion along the electron trajectory. In order to achieve sufficient undulator strength for a high yield radiation source the laser pulse is focused by a cylindrical mirror. It is aligned parallel to the electron trajectory and its focal line coincides with the electron trajectory. The laser pulse front tilt ensures continuous overlap of electrons and laser pulse throughout the whole time the electrons need to cross the transverse laser pulse profile. With a pulse front tilt of half the interaction angle, which is enclosed by the electron and laser propagation direction, overlap can be maintained over hundreds to thousands of undulator periods. The actual interaction distance in TWTS geometries is only limited by available laser power or size of optics. (Originally in [KS2])

The TWTS geometry is depicted in fig. 1.1. It overcomes the limitations of head-on Thomson scattering by switching into a side scattering geometry where electron bunch and laser pulse propagation directions enclose the interaction angle  $\phi$ . In order to maintain overlap between electrons and laser pulse until saturation in radiation production is achieved, the laser pulse front is tilted with respect to its propagation direction by half the interaction angle. Tilting the laser pulse-front allows to realize interaction distances on the centimeter to meter scale which is much longer than the laser pulse length which otherwise limits the achievable interaction distance. In TWTS the interaction distance is instead determined by the laser pulse width rather than its length and thus only limited by the available laser power or the size of available optics. Therefore, interaction distances in TWTS geometries can become much longer than the pulse length of high-repetition-rate high-power laser systems which are used for high-yield TWTS as well as head-on Thomson sources.

The availability of several hundred period long optical undulators by TWTS is not only attractive for TWTS OFEL operation, but also for operating incoherent radiation sources in the hard X-ray and  $\gamma$ -ray region where TWTS geometries can lead to orders of magnitude higher photon fluxes

than can be achieved in head-on Thomson scattering geometries today.

Apart from the straight forward realization of a TWTS OFEL as depicted in fig. 1.1, a Raman FEL has been proposed, too, producing radiation from the interaction of a relativistic electron bunch flying through an optical lattice formed by two TWTS laser pulses [69, 70].

Since the first presentation of TWTS in ref. [67] in the year 2009, the idea of a TWTS OFEL has been proposed repeatedly by other groups [71, 72] in the following years. Although these tried to present methods for the generation of pulse-front tilted laser pulses for TWTS OFELs [71, 72], they did not consider that high power laser pulses are required for TWTS OFEL realization which renders their setups useless as these used optical components that do not withstand the energy fluence of a high-power laser pulse. This comes, however, at no surprise as there was no theoretical description of TWTS OFELs at this time from which electron bunch and laser pulse requirements for TWTS OFEL operation could be determined. This thesis remedies both of these issues. First, the TWTS OFEL electron equations of motion are derived within a 1.5D theory and proven to be formally equivalent to the equations of motion of a conventional FEL. Second, scaling laws for electron bunch as well as laser pulse requirements are deduced by making use of the results from the analytical theory. Third, optical setups for the generation of TWTS laser pulses [KS4] are provided which are suitable for high power laser pulses since only reflective optics are used.

In the following the thesis structure is outlined. The next chapter explains the basic physical principles of FELs. Chapter 3 explains in more detail the advantages of Traveling-Wave Thomson-Scattering over head-on Thomson scattering, especially in terms of photon conversion efficiency and the influence of quantum effects, and it gives reasons for the reduced electron and laser pulse requirements for OFEL operation in TWTS geometries compared to head-on Thomson scattering geometries. At the same time it explains why OFELs have higher requirements on electron bunch quality than conventional magnet undulator based FELs. Chapter 4 then goes into the details of generating pulse-front tilted laser pulses for TWTS taking compensation of perturbing laser pulse dispersion into account. The presented optical setup strategies allow to control and remove perturbing laser pulse dispersion along the electron trajectory. This is an important prerequisite for the realization of TWTS OFELs since dispersion is introduced with the pulse-front tilt and may hinder coherent radiation amplification. Chapter 5 derives the TWTS OFEL equations of motion in a fully dispersion compensated laser field as it can be produced by the setups presented in chapter 4. Within a 1.5D theory it is shown that the TWTS OFEL equations of motion are formally equivalent to the equations of motion of a conventional FEL which implies that the microbunching instability will develop and coherent amplification of radiation will take place in TWTS OFELs. Furthermore scaling laws for electron bunch and laser pulse requirements as well as requirements on the scattering geometry and produced radiation are derived. These build the basis for the examples presented in chapter 6. It explains the use of the scaling laws derived in the preceding chapters to design setups for incoherent TWTS sources as well as TWTS OFELs. Specifically it presents setups for an incoherent source producing 30 keV photons at an interaction angle of  $120^\circ$  and of a TWTS OFEL producing vacuum ultraviolet radiation which are both realizable today. It additionally highlights measures to be taken to achieve lasing at extreme ultraviolet as well as soft and hard X-ray wavelengths in conjunction with the requirements on electron bunches and laser pulses. For an Ångström TWTS OFEL the electron bunch and laser pulse quality requirements, the optical setup for its realization as well as its application to probe the femtosecond and nanoscale dynamics of laser driven plasmas by coherent diffraction imaging are thoroughly discussed. The final chapter 7 concludes the thesis and gives an outlook on possible types of applications for incoherent TWTS sources and TWTS OFELs, and lists further uses of TWTS besides being a light source.

## 2. PRINCIPLES OF FREE-ELECTRON LASERS

### 2.1. WHAT IS A FREE-ELECTRON LASER?

Free-electron lasers (FELs) are light sources emitting directed, coherent, small bandwidth and high intensity radiation with a broad variability in central wavelength. FELs emitting terahertz radiation with millimeter wavelengths have been built [73] as well as hard X-ray FELs emitting sub-nanometer radiation [74, 75]. Light is produced in an FEL by relativistic electrons traversing an undulator whose oscillating (electro-) magnetic field forces the electrons to follow an oscillatory trajectory causing the emission of dipole radiation. The relativistic velocity of the electrons thereby confines the radiation into a narrow cone in the forward direction [42]. Undulators are built to mimic an electromagnetic plane wave in the rest frame of the electrons and can either be realized by an array of magnets where north- and south pole face each other with alternating orientation along the array or by a laser field. If a laser provides the oscillating field, it is called an optical undulator. Figures 2.1a and 2.1b visualize a magnetic and an optical undulator, respectively, and the respective oscillating electron trajectories therein.

The FEL wavelength is determined by resonance of the radiation with the periodic electron motion in the undulator. Resonance exists when the phase position of an electron inside the radiation wave is the same at the beginning of each undulator period. Then the faster radiation wave slips one wavelength with respect to the electron while it moves one undulator period further. According to fig. 2.1c, the resonance condition for the wavelength being coherently amplified by a single electron in an undulator is

$$\lambda_{sc} = T_{und}(c - \tilde{v} \cos \theta) \stackrel{\theta \ll 1}{\approx} c T_{und}(1 - \tilde{v}/c + \theta^2/2), \quad (2.1)$$

where  $c$  is the speed of light,  $\tilde{v}$  the mean velocity of the electron and  $T_{und}$  is the time an electron needs to travel one undulator period. This time depends on the relative velocity between an electron and the undulator field. To good approximation  $T_{und} = \lambda_u/c$  for on axis injection into a magnetic undulator and  $T_{und} = \lambda_{Laser}/(c + \tilde{v}) \approx \lambda_{Laser}/2c$  for a counterpropagating laser undulator. While an electron traverses the undulator its mean velocity  $\tilde{v}$  is smaller than its incoming velocity  $v_0 \approx c [1 - 1/(2\gamma_0^2)]$ , with  $\gamma_0$  being the electrons relativistic Lorentz factor, due to the ponderomotive force of the undulator field. It is given by

$$\tilde{v} = c \left[ 1 - \frac{1 + a_0^2/2}{2\gamma_0^2} \right],$$

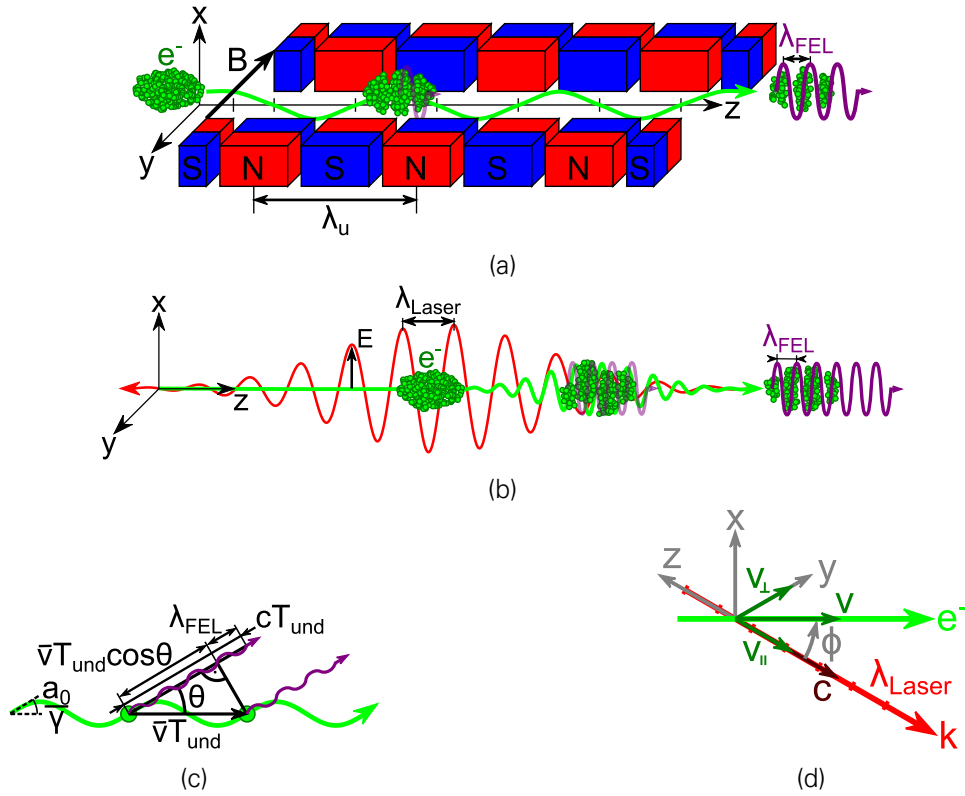


Figure 2.1.: (a) An electron bunch traversing a magnetic undulator wiggles and produces monochromatic radiation due to the magnetic field force. Radiation produced by the electrons acts back on the bunch and leads to microbunching. Microbunches are separated by a radiation wavelength  $\lambda_{FEL}$  allowing for coherent amplification of radiation. (b) The electric field of a laser forces the electrons to wiggle just as the magnetic field of a magnetic undulator in a conventional FEL does. Such an optical FEL (OFEL) develops microbunching and allows for coherent amplification of radiation but on a much shorter distance due to the micrometer-scale laser wavelength  $\lambda_{Laser}$  being orders of magnitude smaller than the typical centimeter-scale periods  $\lambda_u$  of magnetic undulators. (c) Visualizes the resonance condition for coherent amplification of a single wavelength  $\lambda_{FEL}$  by a single electron. An electron traveling at speed  $\bar{v}$  oscillates once in the undulator field during the time  $T_{und}$  and thereby covers the distance  $\bar{v}T_{und}$ . At the same time a radiation wave covers the distance  $cT_{und}$  which encloses the projected electron distance. Their difference must equal an integer multiple of the radiation wavelength to ensure equal phase relation between electron and radiation at the beginning of every electron oscillation. Then the waves radiated during each oscillation constructively interfere. (d) Derivation of the electron oscillation period  $T_{und}$  in a laser undulator. A period corresponds to the time an electron with speed  $v$  needs to advance one laser period  $\lambda_{Laser}$ . It depends on the relative velocity between electron and laser wave in the direction of motion of the laser wave  $T_{und} = \lambda_{Laser}/(c - v_{||}) = \lambda_{Laser}/(c - v \cos \phi)$ .

where the dimensionless undulator strength parameter is

$$\begin{aligned}
 a_0 &= 0.934 \cdot B[\text{T}] \cdot \lambda_u[\text{cm}] && \text{(magnetic undulator) or} \\
 a_0 &= 0.85 \times 10^{-9} \cdot \lambda_{Laser}[\mu\text{m}] \cdot I^{1/2}[\text{W cm}^{-2}] && \text{(laser undulator with irradiance } I\text{).}
 \end{aligned}$$

Thus, the wavelength radiated by an electron in an undulator is given by

$$\lambda_{\text{sc}} = \frac{\lambda_{\text{und}}}{2\gamma_0^2} (1 + a_0^2/2 + \gamma_0^2 \theta^2), \quad (2.2)$$

which is obtained by inserting the expression for the electrons mean velocity  $\bar{v}$  and  $\lambda_{\text{und}} = cT_{\text{und}}$  into eq. (2.1). In FELs based on magnetic undulators or optical undulators in head-on scattering geometries the radiation is typically observed along the electron bunch propagation direction, i. e.  $\theta = 0$ , and thus their emitted wavelength is calculated by

$$\lambda_{\text{FEL}} = \frac{\lambda_{\text{und}}}{2\gamma_0^2} (1 + a_0^2/2).^1 \quad (2.3)$$

For relativistic electrons, where  $\beta_0 = v_0/c \approx 1$ , and not too strong optical undulators, i. e.  $\gamma_0^2 \gg a_0^2$ , relation (2.2) for the radiated wavelength in an undulator is easily generalized to arbitrary interaction angles where the electron and laser propagation direction enclose the angle  $\phi$ . Non-collinear propagation of electrons and laser field prolongs the time until one undulator period is passed and thus increases the undulator period to

$$\lambda_{\text{und}} = cT_{\text{und}} = \frac{c\lambda_{\text{Laser}}}{c - \bar{v} \cos \phi} = \frac{\lambda_{\text{Laser}}}{(1 - \beta_0 \cos \phi)}$$

as it is depicted in fig. 2.1d.

The undulator strength parameter  $a_0$  can also be seen as the normalized deflection angle, as shown in fig. 2.1c, and mainly determines the composition of the radiation spectrum. With increasing undulator strength  $a_0 \gtrsim 1$  electrons are deflected beyond the  $1/\gamma$  cone along their mean direction of motion into which most of radiation is emitted leading to a pulsed radiation time structure, see fig. 2.2. A Fourier decomposition of a pulse train observed in the forward direction shows that its spectrum has significant contributions from harmonics of the fundamental radiation frequency for  $a_0 \gtrsim 1$ . Along the forward direction only odd harmonics are observed due to the alternating electric field polarization direction from pulse to pulse which originates from the change in acceleration direction during each undulator half period.

When using radiation in scattering experiments from small samples, e.g. to image nano objects [76], short and well collimated radiation pulses of high irradiance and small bandwidth are required to obtain a substantial scattering signal before the object is destroyed by the pulse itself. The quantity characterizing these pulses best is peak spectral brightness [77]

$$\mathcal{B} = \frac{N_{\text{phot}}}{\tau_{\text{pulse}} \Delta A \Delta \Omega \frac{\Delta \lambda}{\lambda}} \quad (2.4)$$

giving the number of photons  $N_{\text{phot}}$  within the spectral bandwidth  $\Delta \lambda/\lambda$  in a pulse of duration  $\tau_{\text{pulse}}$  radiated from the source area  $\Delta A$  into the solid angle  $\Delta \Omega$ . Generally, scattering signals become better the higher the peak brightness of a source is. But electron bunch quality limits the achievable peak brightness. The source area, radiation divergence and spectral width of the radiation can be at best as good as the respective parameters of the electron bunch where its energy spread limits the spectral width. In order to achieve high photon flux at high peak brightness accelerators providing electrons need to produce high charge electron bunches with low emittance, i.e. small energy spread and small angular divergence allowing for strong focusing.

<sup>1</sup> This definition of the FEL radiation wavelength is only appropriate in interaction geometries where radiation is primarily emitted along the electron propagation direction. That is, for magnetic and optical undulators where electrons propagate collinear to the undulator axis or the laser pulse propagation direction, respectively. In Traveling-Wave Thomson-Scattering geometries the primary radiation emission direction encloses an angle with the electron bunch propagation direction which results in a small modification for the TWTS OFEL radiation wavelength relation. See ch. 5, specifically eq. (5.11).

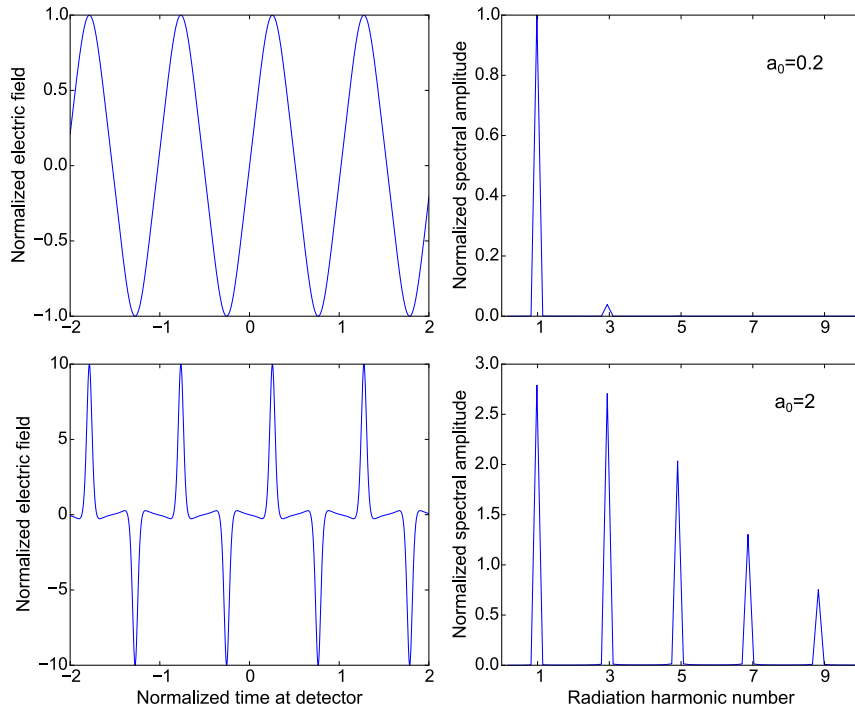


Figure 2.2.: Time structure and spectrum of radiation emitted by a relativistic electron ( $\gamma_0 = 40$ ) along its mean propagation direction which interacts with an intense laser pulse in a head-on scattering geometry. Time structure (left) and spectrum (right) are shown for two different optical undulator parameters  $a_0 = 0.2$  (top) and  $a_0 = 2$  (bottom). For  $a_0 = 2$  most radiation is emitted into harmonics owing to deflection of the electron by an angle larger than  $1/\gamma$  with respect to its mean direction of motion during each oscillation half cycle. The large deflection angle leads to radiation emission outside the  $1/\gamma$ -cone with respect to the mean direction of motion into which most of the radiation energy is emitted. This causes a pulsed radiation time structure as it is observed along the mean electron direction of motion. These short pulses have broad spectra due to the strong undulator field and their spectrum peaks at resonances of the coherent amplification process.

Increasing electron bunch quality also allows to transit from incoherent to coherent radiation generation further increasing brightness. Normally the power radiated by an electron bunch traversing an undulator is proportional to the number of electrons  $N_e$  in the bunch since these are distributed randomly along the longitudinal coordinate and therefore radiate independently. The power observed is proportional to the superposition of the complex electric fields  $E_j$  with phases  $\phi_j$  radiated by all  $N_e$  electrons

$$P_{\text{rad}} \propto \left| \sum_j^{N_e} E_j e^{i\phi_j} \right|^2 = \sum_j^{N_e} E_j^2 + \sum_{j \neq k}^{N_e} \sum_k^{N_e} E_j E_k e^{i(\phi_j - \phi_k)}. \quad (2.5)$$

It becomes proportional to  $N_e$  for randomly phase distributed electrons, since the phase factor  $\exp[i(\phi_j - \phi_k)]$  in the second term averages to zero. In an FEL however, undulators are build long enough for the radiation to act back on the electron bunch which then develops a substructure in the form of microbunches that are separated by a radiation wavelength. Then the phases of the electrons are not random anymore but become correlated, i.e. the phase difference  $\phi_j - \phi_k$  is fixed

to multiples of  $2\pi$ . Hence the phase factor in the second term approaches unity and radiated power scales as  $N_g^2$ . This is one of three reasons for the several orders of magnitude higher peak brightness of FELs compared to synchrotron radiation sources which employ undulators much shorter than the distance required for microbunching. The second reason for the higher peak brightness in FELs is their smaller relative radiation bandwidth  $\Delta\lambda_{\text{FEL}}/\lambda_{\text{FEL}} = 1/N_{\text{und}}$  which is inversely proportional to the number of undulator periods  $N_{\text{und}}$  [78].<sup>2</sup> The third reason is the higher collimation of FEL radiation. From the number of transverse radiation field modes present in FEL radiation, the least diffracting one is strongest amplified and eventually dominates which leads to spatial coherence [80]. This mode is diffraction limited in divergence owing to coherence and has the smallest possible product of  $\Delta A \Delta \Omega = \lambda_{\text{FEL}}^2/4$  [81]. Fig. 2.3 compares peak spectral brightness of a few synchrotron, Thomson, betatron and FEL based light sources.

## 2.2. MICROBUNCHING AND COHERENT RADIATION AMPLIFICATION IN AN FEL

### 2.2.1. MICROBUNCHING WITHOUT RADIATION FIELD GAIN

Microbunching of electrons in an FEL is driven by the combined fields of undulator  $\mathbf{E}$  and initial (spontaneous) radiation  $\mathbf{E}_{\text{rad}}$ . Their potentials,  $\mathbf{A}$  and  $\mathbf{A}_{\text{rad}}$  respectively, constitute together the 'ponderomotive' potential  $V$  which determines the electron motion in an FEL.

$$V = -q\mathbf{v} \cdot (\mathbf{A} + \mathbf{A}_{\text{rad}})$$

As in the simplest case  $\mathbf{E} = E_0 \sin(k_0(ct + z))\mathbf{e}_x$  and  $\mathbf{E}_{\text{rad}} = E_{\text{rad}} \cos(k_1(ct - z))\mathbf{e}_x$  are plane waves, their potentials are plane waves, too, and thus the ponderomotive potential takes the form of a traveling series of periodic potential wells. Electrons in an electron beam, being distributed over many ponderomotive potential wells, experience a modulation of their kinetic energy  $E_{\text{kin}} = (\gamma - 1)mc^2$  depending on their position within the ponderomotive potential

$$\frac{d\gamma}{dt} = -\frac{e}{mc^2} (\mathbf{E}_{\text{rad}} + \mathbf{E}) \cdot \mathbf{v} \propto a_0 E_{\text{rad}} [\cos((k_1 + k_0)ct - (k_1 - k_0)z) + \cos((k_1 - k_0)ct - (k_1 + k_0)z)], \quad (2.6)$$

which is written for head-on Thomson scattering where  $v_x = (a_0/\gamma_0) \cos[k_0(ct - z)]$  [42]. This equation shows that the combined fields of laser and radiation modulate the electrons kinetic energy as if it would interact with two waves of different frequency, period and phase velocity. While the first wave represented by the first term has a phase velocity

$$v_{\text{ph}} = c \frac{k_1 + k_0}{k_1 - k_0} > c$$

the second wave represented by the second term has a phase velocity

$$v_{\text{ph}} = c \frac{k_1 - k_0}{k_1 + k_0} < c.$$

The energy modulation induced by the first wave oscillates with twice the incident laser frequency and thus averages out over one undulator period. Since only long term kinetic energy loss or gain of electrons over many undulator periods are significant for microbunching, this first

<sup>2</sup>The relative electron bunch energy spread needs to be below this limit as well. Otherwise amplification is strongly mitigated [79, 80].

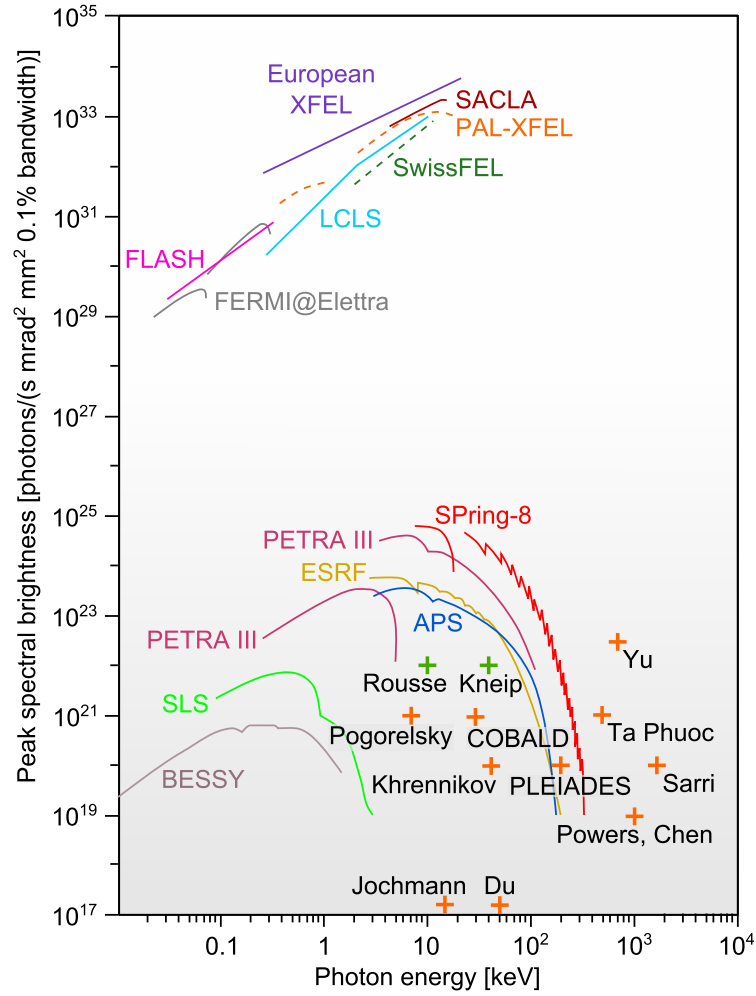


Figure 2.3.: Peak spectral brightness for various types of light sources. The grey shaded area comprises sources of incoherent radiation from magnetic undulators (continuous lines), optical undulators (orange crosses) and betatron oscillations during laser-wakefield acceleration (green crosses). About half of the sources using optical undulators are compact “table-top” setups making use of laser-wakefield accelerated electrons. Free-electron lasers producing coherent radiation reach highest peak spectral brightnesses. Dashed lines mark facilities currently under construction. (Adapted from ref. [82] and data from [31, 33, 37, 49, 54, 83, 84].)

wave does not need to be considered further. In contrast, the slower phase velocity of the second wave allows it to copropagate with the electron beam and induce a long term kinetic energy loss or gain over many undulator periods. This second wave is called the ‘ponderomotive wave’. The electrons phase in the ponderomotive wave

$$\theta = (k_1 - k_0)ct - (k_1 + k_0)z$$

is called the ‘ponderomotive phase’. The kinetic energy modulation in the ponderomotive wave is such that the resulting drift in phase  $\theta$  is towards phase positions of ponderomotive potential minima leading to bunching of electrons at the minima. Analyzing the potential energy of an electron in the combined electromagnetic potential of laser and radiation

$$V \propto -a_0 E_{\text{rad}} \sin(\theta),$$

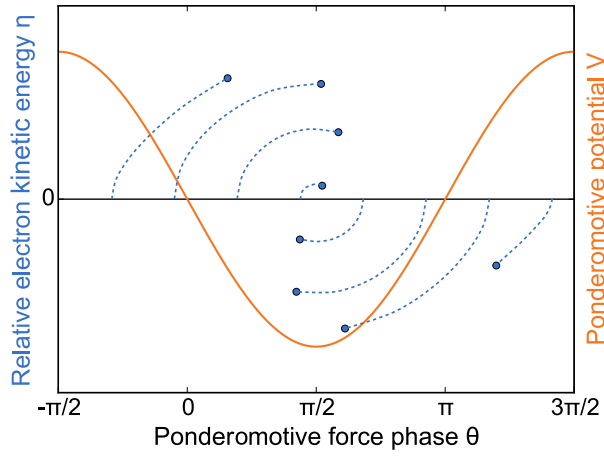


Figure 2.4.: Pendulum-like electron phase space motion in the ponderomotive potential of combined undulator and radiation field. Electrons are initially monoenergetic ( $\eta = (\gamma_0 - \gamma_j)/\gamma_0 = 0$ ) and uniformly distributed in ponderomotive phase  $\theta = (k_1 - k_0)ct - (k_1 + k_0)z$ . During interaction they gain kinetic energy while losing potential energy or vice versa depending on their phase. Then electrons are either faster or slower than the ponderomotive wave leading to spatial bunching of the electron beam at minima of the ponderomotive potential.

shows that these minima are spaced by one FEL radiation wavelength and thus radiation in an FEL is coherently amplified by each microbunch.

Figure 2.4 depicts the temporal evolution of an electrons normalized kinetic energy

$$\eta = (\gamma_0 - \gamma)/\gamma_0$$

and ponderomotive phase  $\theta$  neglecting the fast oscillation of the first wave. In this one-dimensional, plane-wave limit with  $a_0 \ll 1$  the equations of motion for the  $j$ th electron are

$$\dot{\gamma}_j = -\frac{a_0 e E_{\text{rad}}}{2\gamma_j m c} \cos \theta_j, \quad \dot{\theta}_j = 4k_0 c \frac{\gamma_0 - \gamma_j}{\gamma_0}, \quad (2.7)$$

which can be reduced to a pendulum equation for the phase

$$\ddot{\theta}_j - \Omega^2 \cos \theta_j = 0 \quad \text{with } \Omega^2 = 2ek_0 a_0 E_{\text{rad}}/\gamma_0^2 m$$

being the square of the oscillation angular eigenfrequency for electrons near potential minima. These minima are located at  $\theta = (4n + 1)\pi/2$ ,  $n \in \mathbb{N}$  and accordingly electrons oscillate in ponderomotive phase around these positions. Electrons starting in potential minima are neither accelerated nor decelerated but remain constant in ponderomotive phase  $\dot{\theta} = 0$ . This again expresses that radiation is produced at a wavelength being in resonance with the electron oscillation in the undulator. Consequently, the FEL radiation wavelength relation (2.3) is also obtained if  $\dot{\theta} = 0 = (k_1 - k_0)c - (k_1 + k_0)\dot{z}$  is solved for  $k_1$ .

## 2.2.2. MICROBUNCHING AND RADIATION AMPLIFICATION WITH RADIATION FIELD GAIN

The microbunch-wise coherent superposition of radiation increases its power by orders of magnitude over spontaneous emission during interaction. Thus, the implicitly made assumption of a

constant radiation field in the above description of electron dynamics does not hold. Rather a temporal evolution of amplitude  $E_{\text{rad}}(t)$  and phase  $\Upsilon(t)$  of the radiation field  $\mathbf{E}_{\text{rad}} = E_{\text{rad}}(t) \cos(k_1(ct - z) + \Upsilon(t))\mathbf{e}_x$  needs to be taken into account. Writing the field in this form focuses on the basic processes of the interaction modeled in an infinitely long electron beam and radiation field. The finite spatial extents of electron, laser and radiation pulse are neglected as well as transverse momentum components of electrons, the influence of space charge on electron dynamics, radiation diffraction and slippage of the FEL pulse with respect to the electron beam (see ref. [80] for a sophisticated treatment). By including the slowly varying phase  $\Upsilon(t)$  the variation of radiation phase velocity during interaction is taken into account. The radiation phase velocity variation stems from the evolution of the charge distribution in the electron beam, which represents a medium within the radiation wave propagates.

As a consequence of the radiation phase drift during amplification the phase velocity of the ponderomotive wave drifts as well. Accordingly the phase of an electron therein changes during radiation amplification leading to a reinterpretation of ponderomotive phase  $\theta \rightarrow \theta + \Upsilon$ . The temporal evolution of radiation field phase, radiation field amplitude and individual electron ponderomotive phases are connected via Maxwell's equations and the above pendulum equations. Both radiation field phase and amplitude are driven by the transverse electron beam current  $J_x = \sum_j -e\delta(\mathbf{r} - \mathbf{r}_j)v_{x,j}$  depending on electron positions and hence ponderomotive phases which in turn depend on radiation amplitude and phase. Thus in an FEL the radiation field couples electron dynamics allowing for coherent amplification of the radiation itself. The set of FEL equations of motion becomes self-consistent by adding to eq. 2.6 the temporal evolution of radiation field amplitude  $a_{\text{rad}} = eE_{\text{rad}}/mc^2k_1$  and phase  $\Upsilon$

$$\begin{aligned} \frac{d(\gamma_j/\gamma_0)}{dt'} &= -a_0 a_{\text{rad}} \cos(\theta_j + \Upsilon), & \frac{d\theta_j}{dt'} &= 2 \frac{\gamma_0 - \gamma_j}{\gamma_0}, \\ \frac{da_{\text{rad}}}{dt'} &= \gamma_0 \frac{\Omega_p^2}{(k_1 c)^2} a_0 \langle \cos(\theta + \Upsilon) \rangle, & \frac{d\Upsilon}{dt'} &= -\gamma_0 \frac{\Omega_p^2}{(k_1 c)^2} \frac{a_0}{a_{\text{rad}}} \langle \sin(\theta + \Upsilon) \rangle, \end{aligned} \quad (2.8)$$

which assumes  $\gamma_j \simeq \gamma_0$  and where  $\Omega_p^2 = e^2 n_e / \epsilon_0 m \propto n_e$  is the plasma frequency of the electron beam with number density  $n_e$ ,  $\epsilon_0$  is the vacuum permittivity,  $\langle \dots \rangle = (1/N_e) \sum_j^{N_e} (\dots)$  is an average over all electrons in the potential and the time derivative is with respect to the number of optical undulator periods passed  $t' = k_u ct$ .

Electron dynamics according to the self-consistent equations of motion are visualized in fig. 2.5, assuming electrons are initially uniformly distributed in phase  $\theta$  and are monoenergetic, i. e. their normalized kinetic energy  $p_j \propto (\gamma_0 - \gamma_j)/\gamma_0 = 0$  for all electrons. In addition, the radiation field phase and amplitude are assumed to vanish initially resulting in an initially vanishing ponderomotive potential  $V$ .

At the beginning radiation power increases quickly by a few orders of magnitude owing to a transfer of kinetic energy from the majority of electrons into radiation. Compared to the constant radiation field case of eqs. (2.7) and fig. 2.4, where the amount of electrons losing kinetic energy was the same as those gaining kinetic energy, this imbalanced transfer of electron kinetic energy is caused by a drift of the ponderomotive phase. Due to this drift most electrons initially in an accelerating phase reduce their acceleration while electrons initially in a decelerating phase are decelerated even stronger which at the same time increases emission of radiation. With increasing radiation the potential becomes stronger leading to stronger microbunching. This again increases radiation production and ponderomotive phase shift leading to continued radiation amplification owing to this self-amplifying feedback. Shortly before saturation well separated microbunches have developed and are spaced in phase by  $2\pi$  equaling one radiation wavelength. Thereafter electrons spread out in phase again and the ratio of electrons taking energy from the radiation field to electrons supplying energy to the radiation field slowly inverses which finally

leads to a decrease in radiation power.

During amplification radiation power increases exponentially  $P_{\text{rad}}(t) \propto e^{ct/L_G} = e^{4\pi\sqrt{3}\rho ct/\lambda_u}$ . Thereby the gain length  $L_G$

$$L_G = \frac{\lambda_u}{4\pi\sqrt{3}\rho} \quad (2.9)$$

is the distance an electron bunch travels within the undulator field during a relative radiation power increase of  $e$ . The dimensionless Pierce parameter  $\rho$  is a measure for the coupling of the radiation field to the electron bunch and solely determines (in this one dimensional theory) the speed at which radiation power increases

$$\rho = \left( \frac{\gamma_0^2 a_0^2 \Omega_{p,rel}^2}{8 (k_1 c)^2} \right)^{\frac{1}{3}} \quad (\text{for } a_0^2/2 \ll 1), \quad (2.10)$$

where  $\Omega_{p,rel} = \Omega_p/\sqrt{\gamma_0}$  is the true oscillation frequency of space charge waves propagating along the mean electron direction of motion.

The coupling depends on incident laser power  $a_0^2$  as well as electron energy  $\gamma_0$  and increases when these are increased due to the increase in radiated power from incoherent scattering  $P_{\text{inc}} \propto a_0^2 \gamma_0^2$ . The ratio of electron beam plasma frequency to radiation frequency quantifies the influence of the electron bunch as a medium for the radiation wave. If the radiation frequency is large compared to the plasma frequency, the electron beam will be almost transparent to the radiation. Then the radiation phase modulation  $\hat{\gamma}$ , which is the root of sustained microbunching and thus coherent amplification, is weaker and the development of microbunching takes longer, cf. eq. (2.8). This is why undulators of X-ray FELs starting from spontaneous radiation are one hundred meters long and FELs providing microwave radiation and starting from spontaneous radiation are a few meters long [85].

Typical values for Pierce parameters of free-electron lasers starting amplification from their own incoherent emitted radiation are  $10^{-3} < \rho < 10^{-4}$ . Its value is of importance not only when determining the length of an undulator required to achieve saturation, but it is also a measure of FEL efficiency and bandwidth. At saturation when the scaled radiation power  $a^2 = P_{\text{rad}}/\rho P_e \approx 1$ , where  $P_e = \gamma_0 mc^2 I_p/e$  is the power of an electron beam of peak current  $I_p$ , the transfer of electron beam power into radiation power is directly proportional to  $\rho$  which thus determines FEL efficiency. The FEL bandwidth can be calculated when deriving radiation field growth for a multi frequency radiation field and is found to be  $\Delta\lambda_{\text{FEL}}/\lambda_{\text{FEL}} \approx 2\rho$  [82]. This at the same time determines the electron energy spread at saturation  $\Delta\gamma/\gamma \leq \rho$  which sets an upper limit on the initial electron energy spread since larger energy spreads greatly reduce amplification [79, 80].

Besides electron energy spread, there are three dimensional properties of electron bunches and radiation which affect its amplification in a real setup. There are, for example, electron bunch emittance and radiation diffraction. The next section gives an overview on the most important parameters and their limits in order to drive the exponential amplification process.

## 2.3. REQUIREMENTS ON ELECTRON BUNCH AND RADIATION BEAM PARAMETERS

Large electron energy spreads increase the gain length, broaden the radiation spectrum and if the radiation produced at startup is too broadband, will inhibit microbunching and hence radiation amplification. An upper limit for acceptable electron energy spread can be derived from the radiation bandwidth at saturation [80] given by the Pierce parameter

$$\frac{\Delta\lambda_{\text{FEL}}}{\lambda_{\text{FEL}}} \approx 2\rho. \quad (2.11)$$

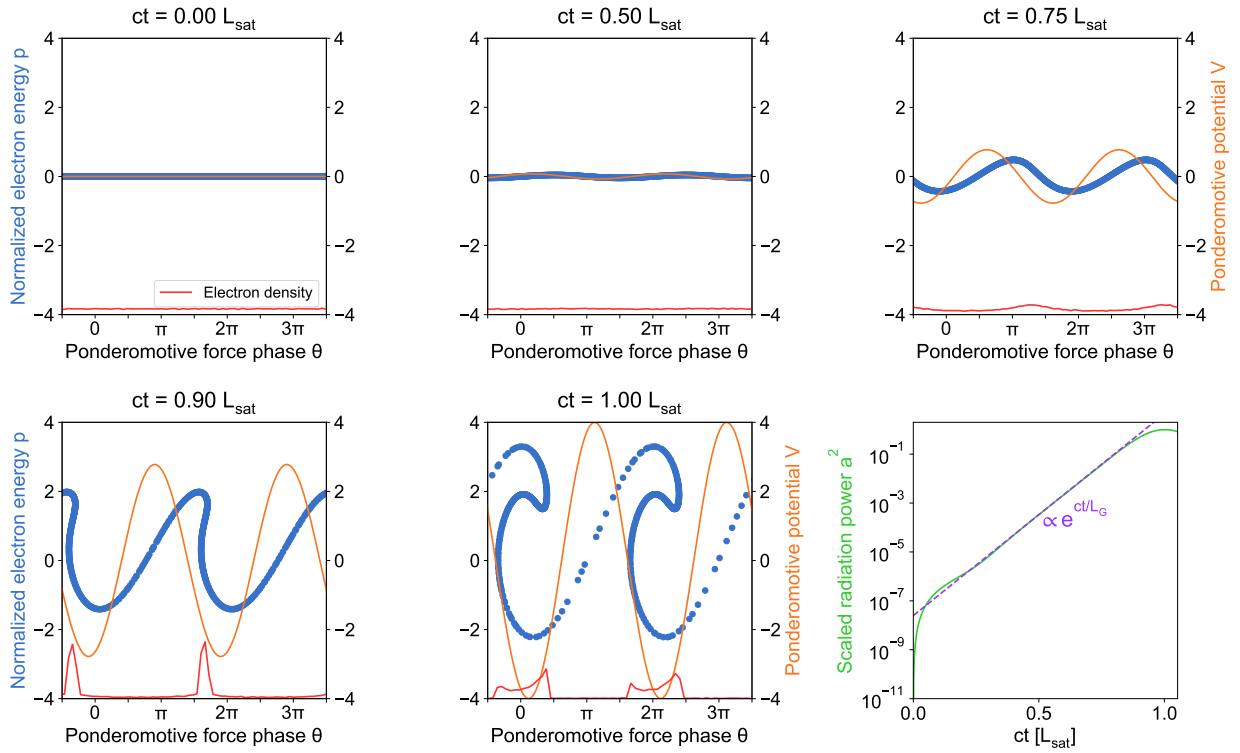


Figure 2.5.: Temporal evolution of electron phase space (blue), ponderomotive potential (orange) and electron density (red) in an FEL together with the increase in radiation power until saturation is reached.  $L_{\text{sat}}$  is the distance traveled by electrons until saturation. Initially electrons are monoenergetic and uniformly distributed in ponderomotive phase  $\theta$ . During interaction radiation is produced which increases the ponderomotive potential leading to confinement of electron phase space motion into intervals enclosing the potential minima. The bunching induced in this way drives the ponderomotive potential phase, the evolution of which forces the majority of electrons to transfer energy to the radiation field which in turn increases the ponderomotive potential and thus electron bunching. This positive feedback loop provides for exponential amplification of radiation  $P_{\text{rad}} \propto e^{ct/L_G}$  over many gain length  $L_G$  until maximum bunching and shortly after saturation is achieved.

The FEL radiation wavelength relation eq. (2.3) connects electron beam energy spread  $\Delta\gamma_0/\gamma_0$  to radiation bandwidth  $2\Delta\gamma_0/\gamma_0 = \Delta\lambda_{\text{FEL}}/\lambda_{\text{FEL}}$  yielding as a limit

$$\frac{\Delta\gamma_0}{\gamma_0} \leq \rho. \quad (2.12)$$

The longitudinal space-charge field can disturb microbunching, too. Space charge is not of importance as long as the reduced plasma oscillation wavelength  $k_p^{-1}$ , with  $k_p^2 = \Omega_p^2/\gamma_0^3 c^2$ , is larger than the gain length [86]

$$k_p^{-1} > L_G, \quad (2.13)$$

which is usually fulfilled in optical undulators where gain lengths are in the millimeter range.

Space charge already impacts the electron beam dynamics before acceleration by introducing a divergence to the beam which is linked to electron beam emittance. An electron beam doubles its cross section after propagation by a distance  $\beta^* = \sigma_b^2 \gamma_0 / \epsilon_N$ , where  $\sigma_b$  is the rms cross-sectional radius of the electron beam and  $\epsilon_N$  its normalized emittance. As depicted in fig. 2.6a, this

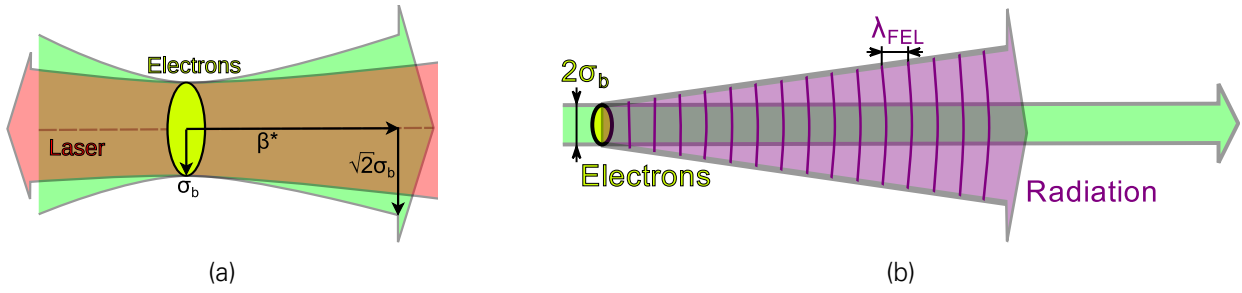


Figure 2.6.: (a) Loss of overlap between electrons and laser field due to electron beam divergence. (b) Parts of the divergent radiation beam decouple from amplification by leaving the area swept over by the electron beam of rms cross-sectional radius  $\sigma_b$ .

increase in size reduces overlap with the laser and further reduces the electron density on axis and hence the coupling as well as the effective number of electrons producing radiation. As both lead to a reduction of amplification there is a limit on electron beam emittance

$$\epsilon_N \leq \frac{2\sigma_b^2\gamma_0}{L_{sat}}, \quad (2.14)$$

which requires saturation of the amplification within two  $\beta^*$ . This limit is typically not of importance for FELs using magnetic undulators where the increasing strength of the undulator field towards the poles provides natural focusing and where strong focusing using quadrupoles is applied between undulator sections. But it is of importance for optical undulators where interaction distances are in the sub-meter range which does not allow for refocusing and where laser beam profiles are typically not tailored to provide natural focusing.

Overlap of the electron beam with the radiation beam is of importance, too. The radiation beam naturally diverges during interaction such that radiation leaks out of the electron bunch and is lost for amplification, see fig. 2.6b. Since new radiation is produced continuously during interaction, the loss can be offset by gain. The diffraction loss is small if the Rayleigh length  $z_R = 4\pi\sigma_b^2/\lambda_{FEL}$  of the radiation is larger than the gain length

$$z_R > L_G. \quad (2.15)$$

Equating the radiation and electron beam characteristic divergence lengths,  $z_R$  and  $\beta^*$  respectively, yields a condition for perfect matching of electron beam emittance  $\epsilon_N$  and radiation beam emittance

$$\epsilon_N = \frac{\gamma_0\lambda_{FEL}}{4\pi}, \quad (2.16)$$

which ensures good spatial (transverse) coherence. A more accurate estimate for the degree of transverse coherence can be made by calculating the transverse coherence parameter [87, 88]

$$\hat{\epsilon} = \frac{2\pi\epsilon_N}{\gamma_0\lambda_{FEL}}, \quad (2.17)$$

which is on the order of unity,  $\hat{\epsilon} \approx 1$ , for optimum transverse coherence. This requirement for optimum transverse coherence can be recast into a requirement on normalized transverse electron beam emittance

$$\epsilon_N = \frac{\gamma_0\lambda_{FEL}}{2\pi}. \quad (2.18)$$

Comparing this requirement for transverse coherence to the requirement for equal electron bunch and radiation divergence (2.16), it can be seen that the radiation divergence needs to

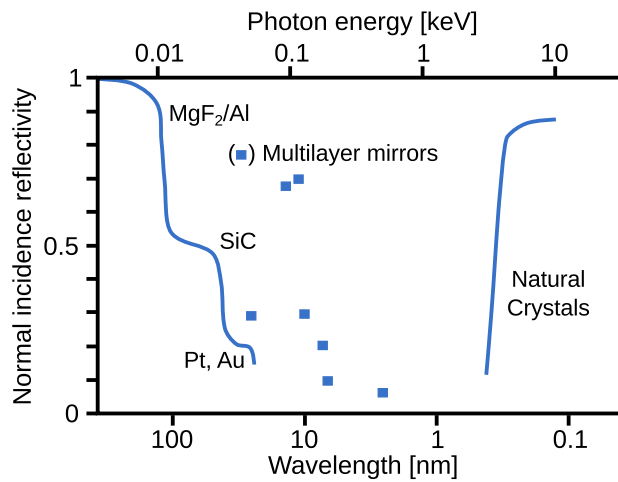


Figure 2.7.: Reflectivity of mirrors under normal incidence for typical metallic coatings as well as for multi-layer mirrors and atomic crystals at the Bragg angle. No high reflectivity materials are available for EUV, soft and hard X-ray wavelengths which could be used for resonator mirrors. (Adapted from ref. [77]).

be smaller than the electron bunch divergence for optimum transverse coherence. Since microbunching is initiated where the radiation irradiance is largest, a smaller radiation divergence facilitates the microbunching process. On the other hand, a microbunch develops only over the whole electron bunch width if the radiation diverges, since divergence propagates information about the radiation phase, along which microbunches develop, from the bunch center across the whole bunch. Therefore, radiation divergence is necessary but must not be too strong in order to ensure a uniform microbunch front which makes transverse coherence possible. Useful transverse coherence is typically available in the range  $\hat{\epsilon} = 0.5 \dots 10$ .

## 2.4. RADIATION PROPERTIES OF SELF-AMPLIFIED SPONTANEOUS EMISSION FELS

Free-electron lasers reaching high photon output in the extreme ultraviolet and X-ray range make use of self-amplification of emitted spontaneous radiation (SASE) described in section 2.2. This is necessary as mirrors for resonators are not available in this spectral region since the reflectivity of metals typically used as mirror coatings quickly drops to zero and reflection from multilayer mirrors or atomic crystals using the Bragg angle has too low reflectivity as shown in fig. 2.7.

The amplification from spontaneous radiation is a stochastic process varying in its starting conditions from shot-to-shot which leads to intrinsic shot-to-shot variations of FEL radiation spectra and pulse structure [89]. A typical FEL spectrum is not a smooth bell shaped curve but consists of a few peaks as shown in fig. 2.8. The same holds for the temporal pulse structure with similar intensity fluctuations over a pulse duration. These originate from the difference between electron bunch length and the length over which phase correlation in an FEL can develop. To achieve temporal phase correlation the electrons must synchronize their oscillation via the radiation field. But synchronization cannot take place over the whole electron bunch as the radiation originating at the end of the bunch does not sweep over the whole bunch until the end of the undulator. On the contrary, electron bunch lengths for existing X-ray FELs are several tens of micrometer while the advance of the radiation field with respect to the electron bunch is typically ten micrometer after passing one thousand undulator periods. The cooperation length  $l_c = \lambda_{\text{FEL}}/4\pi\rho$  over which

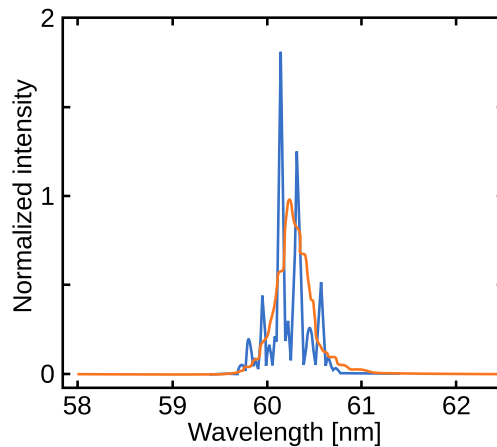


Figure 2.8.: Single shot and averaged spectra of the SCSS FEL. The single shot spectrum (blue) consists of a few peaks the position of which differs from shot-to-shot. The continuous spectrum (orange) is an average over 100 shots displaying an average spectrum bandwidth of 0.58% FWHM. (Adapted from ref. [91]).

temporal coherence in an FEL pulse develops is determined by the radiation slippage over a gain length. With it and the electron bunch length  $l_b$  the number of spikes in an FEL pulse can be estimated by  $l_b/2\pi l_c$  [90]. These can be several ten in existing X-ray FELs.

One method to improve temporal coherence is seeding of an FEL with radiation at a subharmonic wavelength of the undulator radiation [92]. Such a high-gain harmonic-generation (HGFG) FEL emitting extreme ultraviolet radiation has been built at FERMI [93, 94]. In HGFG a temporally coherent pulse at a sub-harmonic of the target X-ray wavelength provides an initial radiation field when overlapped with an electron bunch in a short undulator section (modulator) of the same period as the undulators later used for X-ray amplification (radiator). In the modulator electrons start their pendulum motion and obtain a small energy spread. In a following dispersive section this energy spread is converted into a regular density modulation representing a microbunching at a multiple of the radiation wavelength. This microbunching then is a coherent seed for X-ray amplification in the radiator producing temporally coherent FEL pulses [95]. This scheme can be repeated several times where the first stage is used to produce a coherent seeding field for the second stage modulator and so forth.

While the temporal coherence of FELs is limited, they become almost fully transverse coherent when interaction lasts until saturation. Spatial coherence is reached when the radiation consists only of a single transverse field mode. At the beginning of radiation amplification many modes are excited and compete in reshuffling the electrons to initiate the feedback loop. But only the fundamental gaussian mode has its highest intensity on the electron beam axis where electron density is largest and its divergence is smallest compared to all other modes. For both reasons it is in favor over other modes and has the largest growth rate which is referred to as 'gain guiding' [96, 97]. The exponential amplification of the fundamental gaussian mode is a strong process that can lead to transverse coherence even if the electron beam divergence is larger than the radiation field divergence as opposed to sources of spontaneous radiation offering only good coherence if this condition is met [98].



### 3. TRAVELING-WAVE THOMSON-SCATTERING FOR COMPACT AND BRIGHT LIGHT SOURCES

Today operating or planned X-ray free-electron lasers are based on conventional magnetic undulators for radiation generation. These have periods on the centimeter scale and thus require GeV electron energies to produce X-rays, according to the scattered wavelength relation (2.3). Therefore, X-ray FELs require kilometer scale conventional accelerators. Reducing the undulator period to millimeter or sub-millimeter scale would allow for a substantial decrease of the facilities through the reduced demand in electron energy, which would allow for a considerable decrease of accelerator size. Optical undulators from high power laser pulses are able to provide the desired decrease in undulator period. Optical undulators furthermore circumvent the technological challenges encountered when miniaturizing magnetic undulators. These partially arise from the required reduction of undulator gap that is needed to maintain a constant undulator field on axis when reducing the magnet size in order to reduce the period [99, 100]. Small gaps require for example low divergence electron beams and increase the back action of electron beam wakefields on the beam itself. On the other hand, handling as well as magnet-to-magnet magnetization stability during operation becomes increasingly difficult with higher magnetization but larger gaps.

With laser undulators the undulator period  $\lambda_{\text{und}}$  is determined by the central wavelength  $\lambda_{\text{Laser}}$  of the laser and the interaction angle  $\phi$  enclosed by the electron and laser direction of propagation, see fig. 2.1d,

$$\lambda_{\text{und}} = \frac{\lambda_{\text{Laser}}}{1 - \beta_0 \cos \phi},$$

where  $\beta_0 = v_0/c$  is the normalized initial electron velocity. With high-power-laser wavelengths typically at  $1 \mu\text{m}$  accessible undulator periods range from 500 nm to 3 mm at interaction angles between  $180^\circ$  and  $1.5^\circ$ , assuming relativistic electrons  $\beta_0 \approx 1$ . The corresponding radiated wavelength at arbitrary interaction angle  $\phi$  is

$$\lambda_{\text{sc}} = \frac{\lambda_{\text{Laser}}}{2\gamma_0^2(1 - \beta_0 \cos \phi)} (1 + a_0^2/2 + \gamma_0^2\theta^2) \quad (3.1)$$

where the observation direction and the electron beam axis together enclose the observation

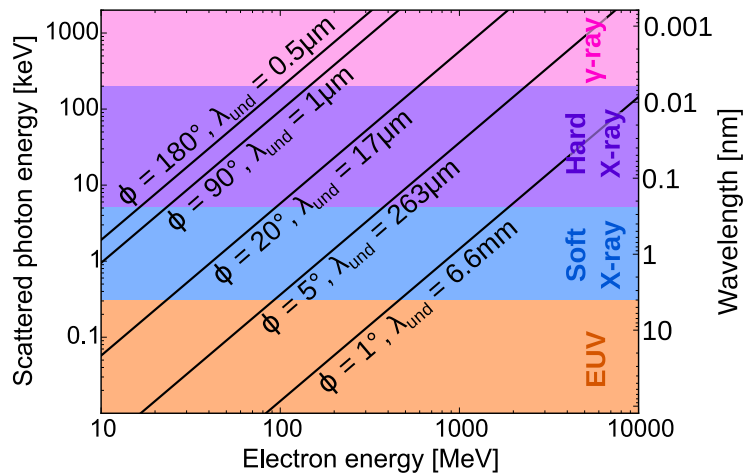


Figure 3.1.: Scaling of scattered photon energy for optical undulators with laser wavelength  $\lambda_{\text{Laser}} = 1 \mu\text{m}$  in dependence of electron energy and interaction angle  $\phi$ . The corresponding undulator period  $\lambda_{\text{und}} \approx \lambda_{\text{Laser}}/(1 - \cos \phi)$  is given for each interaction angle. With constant electron energy the scattered photon energy can be tuned from the extreme ultraviolet (EUV) to the hard X-ray range just by adjusting the interaction angle.

angle  $\theta$ . Figure 3.1 shows the scaling of emitted photon energy with electron energy and interaction angle for on axis ( $\theta = 0$ ) observation. Even for fixed energy electron sources the interaction angle grants control over scattered photon energy over orders of magnitude.

### 3.1. LIMITS OF STANDARD HEAD-ON THOMSON SCATTERING

As of today a couple of Thomson scattering sources have been realized, see fig. 2.3, most of them in a head-on scattering geometry. The yield of these sources has become comparable to third generation light sources and for photon energies of a few hundred keV and above they are the only high yield sources. But when aiming at higher photon yields limits of the standard Thomson scattering geometry are encountered which restrict the realization of a source with high yield and small bandwidth, i.e. a harmonic-free spectrum [67]. The photon yield of a Thomson source scales with the number of electrons  $N_e$  in the bunch, the number of undulator periods  $N_{\text{und}}$  and the scaled laser amplitude  $a_0 = 0.85 \times 10^{-9} \cdot \lambda_{\text{Laser}}[\mu\text{m}] \cdot I^{1/2}[\text{W cm}^{-2}]$ , for a laser with irradiance  $I$ ,

$$N_{\text{phot}} = \alpha N_e N_{\text{und}} a_0^2,$$

where  $\alpha \approx 1/137$  is the fine structure constant [43].

For a fixed electron source the yield can be increased by either increasing the laser irradiance or by increasing the number of undulator periods. Increasing the laser irradiance is limited by  $a_0 < 1$  from the requirement of a small bandwidth, harmonic-free source in order to avoid photon losses from monochromators. Increasing the number of undulator periods is limited by spatial overlap of electrons and laser pulse in two ways.

First, in a head-on scattering geometry laser pulse defocusing during interaction limits the interaction distance to approximately twice the Rayleigh length  $z_R = \pi w_0^2 / \lambda_{\text{Laser}}$  of the laser pulse, see fig. 3.2a. Increasing the laser width  $w_0 > 2\sigma_e$  to values larger than twice the electron beam rms cross-sectional radius  $\sigma_e$  increases the possible interaction distance but results in a waste of laser photons due to non-optimum overlap. The maximum number of undulator

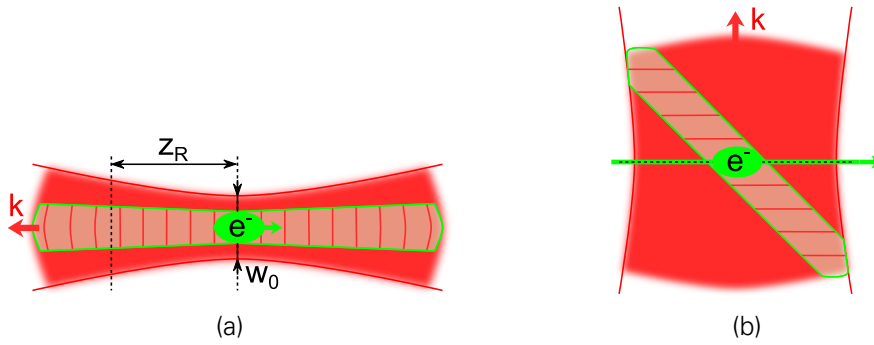


Figure 3.2.: (a) Non-optimum overlap between laser and electron pulse to ensure efficient interaction over two Rayleigh lengths  $z_R$ . The laser pulse focal width is chosen larger than the electron pulse width to mitigate field amplitude reduction from defocusing. Poor overlap results in a waste of laser energy. (b) In a standard side-scattering geometry laser energy is wasted, too. Wide laser pulses are needed to obtain the maximum number of optical undulator periods given by the number of laser oscillations. The actual region of overlap between electron and laser pulse is only a small fraction of the complete laser pulse but in side scattering the interaction length is not limited by laser defocusing since the laser focus is on the electron trajectory.

periods achievable in a head-on geometry equals the number of laser oscillations within the pulse duration  $\tau_0$ , provided the laser width is properly matched in order to include the interaction distance within two Rayleigh lengths  $2z_R = c\tau_0/2$ . Assuming for example a  $1\ \mu\text{m}$  wavelength laser pulse, a target scaled amplitude  $a_0 = 0.5$  and an optical undulator length of 5000 periods, i. e.  $c\tau_0/\lambda_{\text{Laser}} = 5000$ , the required laser width is  $w_0 = 20\ \mu\text{m}$  in order to match the laser focal region of  $2z_R$  to the possible interaction distance of  $2500\lambda_{\text{Laser}}$ . In an ultra-compact setup utilizing laser-wakefield acceleration these  $20\ \mu\text{m}$  can be already twice the size of the electron bunch after acceleration. The laser energy requirement is therefore four times higher than it would need to be if the laser width could be matched to the electron bunch diameter.

Second, in a side-scattering geometry, see fig. 3.2b, the laser width depends on the number of laser oscillation periods within the laser, too. The width must be chosen to allow the electron bunch to oscillate in all available laser periods within the laser pulse duration. If the laser width is too small, the electron bunch will only oscillate in a fraction of the available laser periods since the transverse laser profile ends before the whole longitudinal laser profile has swept over the electron bunch. The matched width of the laser pulse  $w_0 = c\tau_0 \sin \phi / (1 - \beta_0 \cos \phi)$  is given by its duration and the interaction angle. Carrying on the last example for an interaction angle of ninety degree, the required pulse width is  $w_0 = 5\ \text{mm}$ , the 250-fold of the above head-on scattering case since the overlap between laser pulse and electrons is even worse. However, ninety degree side scattering has on the one hand the advantage of being independent of the laser Rayleigh length since the electrons move within the laser focal plane. On the other hand it allows matching of the laser pulse focal width to the electron beam width in the direction transverse to laser and electron propagation direction, i.e. allows for optimum overlap in this direction.

### 3.2. SCALABLE OPTICAL UNDULATORS WITH TRAVELING-WAVE THOMSON-SCATTERING

The disadvantage of waisting laser energy in standard Thomson scattering sources can be overcome in Traveling-Wave Thomson-Scattering (TWTS). TWTS realizes optimum overlap of electron

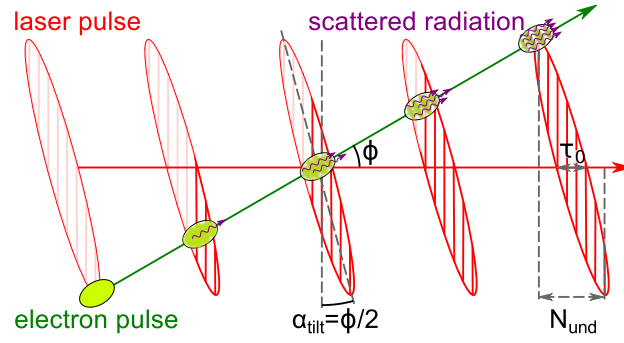


Figure 3.3.: Traveling-Wave Thomson-Scattering (TWTS) optimizes the electron and laser pulse overlap by employing a side-scattering geometry and pulse-front tilted laser pulses. Phase fronts are perpendicular to the laser propagation direction and the angle between phase fronts and pulse front defines the pulse-front tilt angle  $\alpha_{\text{tilt}}$ . The combination of side scattering at an angle  $\phi$  and pulse-front tilt of half the interaction angle  $\alpha_{\text{tilt}} = \phi/2$  ensures continuous overlap of electrons and laser over the whole laser pulse width while the electrons traverse it. In TWTS the number of undulator periods  $N_{\text{und}}$  becomes independent of laser pulse duration  $\tau_0$  but is determined by laser pulse width. (Originally in [KS4])

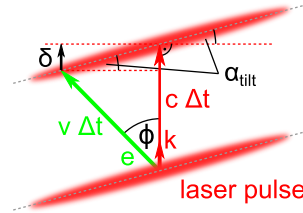


Figure 3.4.: Laser pulse-front tilt angle  $\alpha_{\text{tilt}}$  is determined by matching the delay  $\delta$  of the pulse-front along the horizontal direction to the electron pulse delay,  $\delta = v\Delta t \sin(\phi) \tan(\alpha_{\text{tilt}}) \stackrel{!}{=} c\Delta t - v\Delta t \cos \phi$ .

and laser pulse by making use of a side-scattering geometry and a tilt of the laser pulse-front.

With a tilt of the laser pulse-front there is a longitudinal offset between irradiance maxima across the transverse laser profile. The angle enclosed by the pulse-front and phase-fronts, which are aligned perpendicular to the laser pulse direction of propagation, is the pulse-front tilt angle  $\alpha_{\text{tilt}}$ . The pulse-front tilt in TWTS ensures continuous overlap of laser pulse and electrons during the interaction, even when these are far from the laser pulse center, see fig. 3.3. A tilt  $\alpha_{\text{tilt}} = \phi/2$  by half the interaction angle optimally compensates the lag of the electrons during their propagation obliquely to the laser pulse propagation direction. Following fig. 3.4 this matches the delay of the laser pulse front  $\delta = \beta_0 c \Delta t \sin(\phi) \tan(\alpha_{\text{tilt}})$  to the electron lag along the laser pulse propagation direction  $\delta = c \Delta t (1 - \beta_0 \cos \phi)$ , acquired within the time  $\Delta t$ ,

$$\alpha_{\text{tilt}} = \arctan \left( \frac{1 - \beta_0 \cos \phi}{\beta_0 \sin \phi} \right) \stackrel{\gamma_0 \gg 1}{\simeq} \phi/2, \quad (3.2)$$

assuming relativistic electron pulses.

With complete overlap of electrons and laser pulse provided by the combination of pulse-front tilt and side scattering the number of undulator periods becomes independent of laser pulse duration in TWTS. The interaction distance is instead controlled solely by the horizontal laser pulse width within the interaction plane spanned by laser and electron propagation direction.

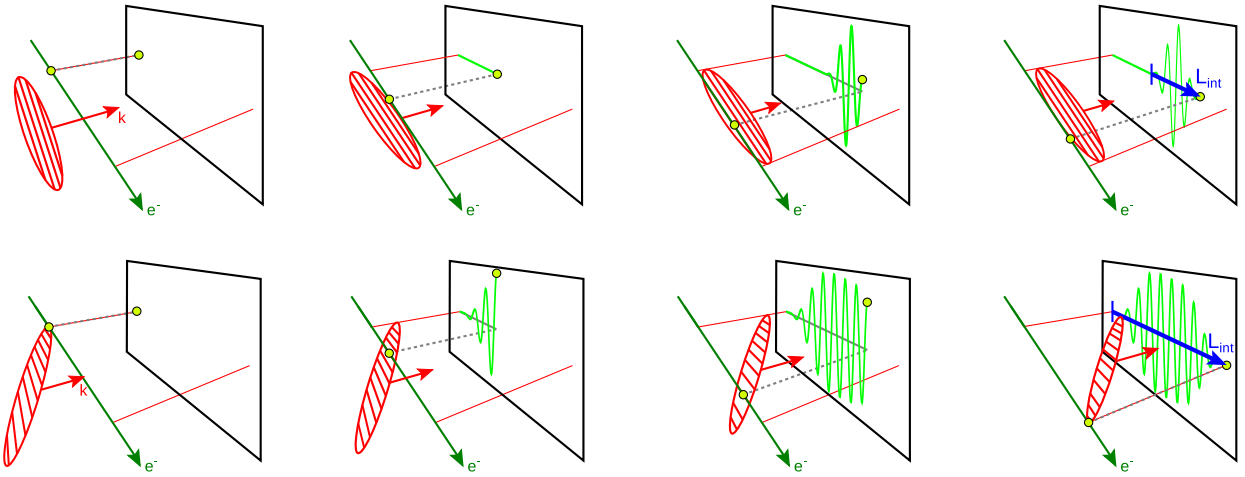


Figure 3.5.: Compared to standard Thomson scattering much longer interaction distances  $L_{\text{int}}$  can be provided with the same laser energy using TWTS which employs pulse-front tilted laser pulses and side scattering. (Originally in [KS2])

The number of undulator periods is thus only limited by available laser power and size of optics.

Defocusing of the laser pulse in the interaction plane imposes no problem. With centimeter wide laser pulses used for long optical undulators the Rayleigh length is several hundred meter and therefore much larger than the centimeter to meter distances covered by the laser pulse during interaction. In the plane perpendicular to the interaction plane the laser can be focused directly on the electron trajectory by a cylindrical mirror, the focal line of which is aligned with the electron beam axis. In the longitudinal direction the laser pulse needs to enclose the electron bunch if all electrons in the bunch shall produce radiation. All in all there is optimum overlap between electron and laser pulse and no waste of laser energy in TWTS. As depicted in fig. 3.5, this optimum overlap allows for the realization of longer optical undulators and thus a brighter light source in TWTS than in standard Thomson scattering geometries using the same laser system.

### 3.3. WHY COMPACT FREE-ELECTRON LASER SCHEMES HAVE HIGHER QUALITY REQUIREMENTS ON ELECTRON BUNCHES

Using optical undulators in head-on scattering geometries in order to realize compact optical free-electron lasers (OFEL) has been discussed for decades [27, 28, 65]. Yet they have not been experimentally demonstrated due to the extremely challenging requirements on the quality of laser and electron beams [66, 101] arising from their low MeV range electron energies in conjunction with the scaling of electron beam requirements presented in section 2.3.

The Pierce parameter [102, 103] is the fundamental scaling parameter for the electron beam requirements. In ch. 5 and ref. [KS2] it is derived for an OFEL at arbitrary interaction angle  $\phi$  and in terms of electron bunch peak current  $I_p$ , electron bunch rms cross-sectional radius  $\sigma_b$  and Lorentz factor  $\gamma_0$  as well as scaled laser amplitude  $a_0$  and optical undulator period  $\lambda_{\text{und}} \approx \lambda_{\text{Laser}}/(1 - \cos \phi)$  it is given by

$$\rho = \left[ \frac{1}{16\gamma_0^3} \frac{I_p}{I_A} \left( \frac{\lambda_{\text{und}} a_0 f_B}{2\pi\sigma_b} \right)^2 \right]^{1/3} \stackrel{a_0^2 \ll 2}{\approx} \left[ \frac{\gamma_0}{4} \frac{I_p}{I_A} \left( \frac{\lambda_{\text{FEL}} a_0}{2\pi\sigma_b} \right)^2 \right]^{1/3},$$

using the approximation  $\lambda_{\text{FEL}} \approx \lambda_{\text{und}}/2\gamma_0^2$  for the FEL radiation wavelength  $\lambda_{\text{FEL}}$ , and where

$I_A \approx 17$  kA is the Alfvén current,  $f_B = [J_0(\chi) - J_1(\chi)]$  is the Bessel function factor with  $J_n(\chi)$  being the  $n$ th Bessel function of the first kind and  $\chi = a_0^2/(4 + 2a_0^2)$ .

As can be seen from the right-hand side, the Pierce parameter and hence the electron radiation coupling reduces when realizing a target radiation wavelength  $\lambda_{\text{FEL}}$  with compact undulators requiring low electron energies. With decreasing coupling the gain bandwidth, being the region of the radiation spectrum that is coherently amplified, becomes smaller, too. According to the scaling laws for electron beam requirements from section 2.3 this directly translates into a smaller acceptable electron relative energy spread  $\Delta\gamma_0/\gamma_0 \leq \rho \propto \gamma_0^{1/3} \lambda_{\text{FEL}}^{2/3}$  and acceptable normalized transverse emittance  $\epsilon_N \leq \sigma_b \sqrt{2\rho} \propto \gamma_0^{1/6} \lambda_{\text{FEL}}^{1/3}$ . Although the dependence on electron energy seems to be weak, the reduction from GeV to MeV energies for X-ray wavelengths makes a huge difference in quality requirements.

Yet, the TWTS geometry is in favor over head-on geometries at this point. The variability of TWTS with respect to the interaction angle allows to prefer small interaction angle scenarios  $\phi \lesssim 20^\circ$  with undulator periods up to hundreds of micrometers and corresponding electron energies on a 100 MeV-scale for X-ray wavelengths. These are still two orders of magnitude smaller than the centimeter periods of conventional magnetic undulators, which enables a significant decrease in facility size, but these optical undulator periods are large enough to yield feasible requirements on electron beam quality.

The next section contrasts in a particular example a TWTS OFEL setup to two head-on OFEL scenarios, where the difference between the head-on setups is the central wavelength of the laser systems used to generate the optical undulator field. It is shown that for TWTS the aforementioned possibility of not using the smallest possible undulator period results in higher efficiency in laser to radiation photon conversion, higher brightness, weaker normalized transverse emittance requirement and better transverse coherence.

### 3.4. TRAVELING-WAVE THOMSON-SCATTERING FOR OPTICAL FREE-ELECTRON LASERS

The freedom to choose an interaction angle and thus the electron energy can be used to considerably soften the electron beam requirements in TWTS OFELs compared to head-on OFEL schemes [KS1]. In this section OFELs radiating at 13.5 nm using two different types of electron sources are compared. Electron sources are a standard radio-frequency accelerator and a laser-wakefield accelerator.

Both accelerators are assumed to provide electron pulses with equal peak current of 5 kA to ease comparison. The high current value is necessary to allow for head-on OFEL realization in general. Radio frequency accelerated (rf) electrons have higher emittance  $\epsilon_N = 1\pi$  mm mrad and bunch charge  $Q_{\text{el}} = 500$  pC but longer pulse duration  $\tau_{\text{el}} = 100$  fs. Due to the higher emittance a larger focal width  $\sigma_b = 15$   $\mu\text{m}$  is chosen to achieve a sufficient depth of focus. Laser wakefield accelerated (LWFA) electrons have emittance  $\epsilon_N = 0.2\pi$  mm mrad, bunch charge  $Q_{\text{el}} = 50$  pC, pulse duration  $\tau_{\text{el}} = 10$  fs and focal width  $\sigma_b = 5$   $\mu\text{m}$ .

The TWTS OFELs make use of different laser systems for each of the electron sources. For the rf electrons a 750 TW laser with 120 fs pulse duration and 1  $\mu\text{m}$  wavelength is chosen and for the LWFA electrons a 202 TW, 30 fs, 800 nm system. The former resembles the PEnELOPE system currently under construction at HZDR [104, 105] and the latter the DRACO system operating at HZDR [106, 107]. Two head-on OFEL schemes based on different laser systems are compared to TWTS for each of the electron sources. One scheme utilizes a 10.64  $\mu\text{m}$  wavelength CO<sub>2</sub> laser and the other an 800 nm Ti:sapphire system. All laser systems provide optical undulators of strength  $a_0 = 0.6$  to facilitate comparison.

Table 3.1.: Experimental parameters of head-on and TWTS OFELs radiating at 13.5 nm using either rf-accelerated or laser wakefield accelerated (LWFA) electrons. Parameter values are obtained by the scaling laws presented in ch. 5 and ref. [KS2].

Parameter	TWTS	TWTS	Ti:sa	Ti:sa	CO <sub>2</sub>	CO <sub>2</sub>
	RF acc.	LWFA	RF acc.	LWFA	RF acc.	LWFA
Resonant wavelength [nm]	13.5	13.5	13.5	13.5	13.5	13.5
Laser wavelength [μm]	1	0.8	0.8	0.8	10.64	10.64
Interaction angle [°]	6.75	4.6	180	180	180	180
Undulator wavelength [μm]	143	245	0.4	0.4	5.32	5.32
Electron energy [MeV]	40	52.6	1.6	1.6	7.3	7.3
Peak current [kA]	5	5	5	5	5	5
Norm. emittance [mm mrad]	1.0	0.2	0.8	0.4	1	0.5
Rel. energy spread	0.3%	0.69%	0.12%	0.24%	0.18%	0.38%
Undulator parameter $a_0$	0.6	0.6	0.6	0.6	0.6	0.6
Laser energy [J]	90.0	6.1	22.7	1.2	4.5	1.0
Intensity profile stability	3.9%	8.8%	1.5%	3.2%	2.4%	4.9%
Gain length [mm]	2.16	1.63	$16.0 \times 10^{-3}$	$8.0 \times 10^{-3}$	0.13	$65.0 \times 10^{-3}$
Interaction distance [mm]	34.54	26.13	0.25	0.12	0.22	0.10
EUV Photons	$2.9 \times 10^{12}$	$8.7 \times 10^{12}$	$8.5 \times 10^{10}$	$1.8 \times 10^{10}$	$48.0 \times 10^{10}$	$10.0 \times 10^{10}$

In order to reach the target radiation wavelength of 13.5 nm the electron energies for the CO<sub>2</sub> and Ti:sapphire system need to be 7.3 MeV and 1.6 MeV, respectively. In TWTS the electron energy is not solely determined by the radiation wavelength but also depends on the interaction angle. In TWTS the variability in interaction angle allows to tweak the electron and laser quality requirements in order to find the best trade-off. The best requirement on energy spread (eq. (2.12)) at the given emittance (which needs to be sufficient to fulfill the requirements (5.23) and (2.14)) are found at interaction angles of 6.75° and 4.6° for rf acceleration and LWFA setup, respectively. The corresponding electron energies are 40 MeV and 53 MeV, respectively. These are still small compared to conventional FELs using magnet undulators with centimeter scale undulator periods. For example, the FLASH FEL [108] produces 13.5 nm radiation with an undulator of 2.73 cm period requiring 681 MeV electron energy which is an order of magnitude larger than the requirement of the TWTS setups featuring undulator periods on the scale of 200 μm. Furthermore the 27 m interaction distance at FLASH is three orders of magnitude larger than the 35 mm of the TWTS OFEL using rf-accelerated electrons. The complete electron and laser parameters of the TWTS OFELs are summarized in tab. 3.1.

Comparing the electron energy spread requirements, TWTS already shows its advantage over head-on Thomson schemes. The TWTS setups have a twofold higher energy spread acceptance than the CO<sub>2</sub> laser setups and an almost threefold higher acceptance than the Ti:sapphire setups. Furthermore, the 1 mm mrad emittance of the rf-accelerated electrons is actually a bit too large for the Ti:sapphire laser setup (0.7 mm mrad) but is sufficient for CO<sub>2</sub> and TWTS OFELs.

As explained above, higher energy spread acceptance is due to a better coupling and hence higher efficiency of the TWTS setups. Extending the concept of FEL efficiency for optical FELs from conversion of electron beam into radiation power to the conversion of optical undulator photons into OFEL photons per electron gives a good measure for the impact of the optimized overlap in TWTS setups. Figure 3.6a compares efficiency in terms of radiated OFEL photons over incident optical undulator photons per electron for TWTS and head-on OFEL setups. Highest efficiency for each electron source is achieved in TWTS setups although the laser energy requirement is larger. Yet, the total number of radiated photons  $N_{\text{phot}}$

$$N_{\text{phot}} = \rho N_e \frac{E_e}{E_{\text{phot}}}, \quad (3.3)$$

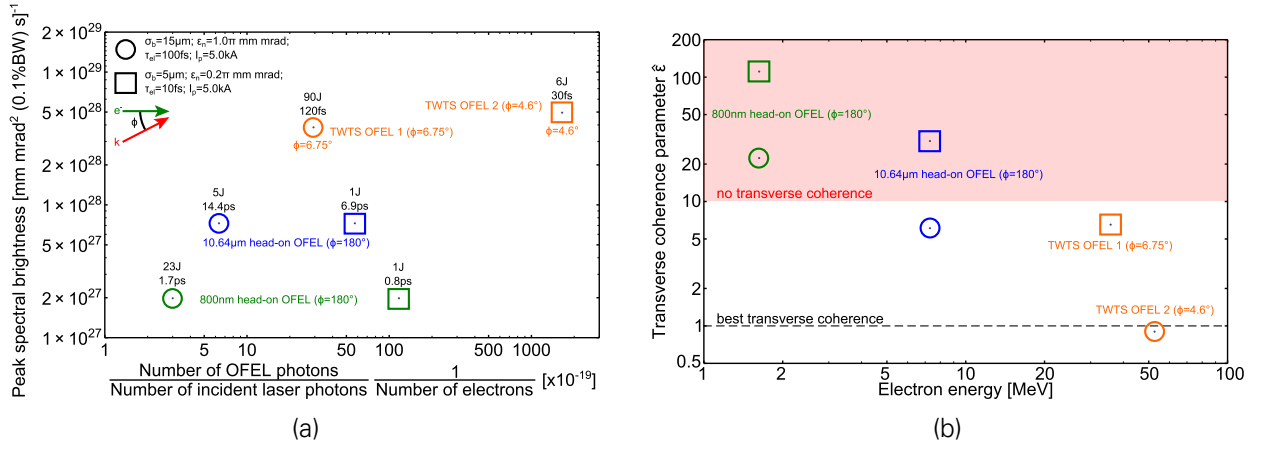


Figure 3.6.: (a) Photon conversion efficiency and peak spectral brightness compared for head-on and TWTS OFELs utilizing radio frequency accelerated (circles) or laser wakefield accelerated (squares) electron bunches. Two head-on OFEL setups based on different laser systems are compared to TWTS OFELs. One head-on setup is based on a Ti:sapphire laser system with 800 nm wavelength and the other based on a CO<sub>2</sub> laser system with 10.64 μm wavelength. Required laser energy and pulse duration are given for every configuration. (b) Required electron energy and degree of transverse coherence  $\hat{\epsilon}$  for each of the OFEL setups. The choice of small interaction angles in TWTS OFELs allows for higher electron energies resulting in better transverse coherence due to better matching of electron and radiation beam divergence. (Originally in [KS1])

is orders of magnitude larger in TWTS compared to the head-on setups because the photon yield scales with the product of Pierce parameter  $\rho$  and electron energy  $E_e = \gamma_0 mc^2$ , both of which are larger in TWTS. The photon yield furthermore scales with the number of electrons in the bunch  $N_e = Q_{el}/e$  and the photon energy  $E_{phot} = hc/\lambda_{FEL}$  both of which are equal for TWTS and head-on.

The scaling of photon output with electron energy also results in a higher peak spectral brightness of TWTS OFELs compared to head-on schemes. Assuming a diffraction limited gaussian radiation beam  $\Delta\lambda\Delta\Omega \approx \lambda_{FEL}^2$  [81, p. 672] with a pulse duration of approximately the electron pulse duration  $\tau_{pulse} \approx \tau_{el}$ , the peak spectral brightness  $\mathcal{B}_{FEL}$  of an FEL is calculated from the total radiated number of photons  $N_{phot}$  and its relative bandwidth measured in units of 0.1%  $\Delta\lambda_{FEL}/\lambda_{FEL}[0.1\%] = 1000 \cdot 2\rho$

$$\mathcal{B}_{FEL} = \frac{N_{phot}}{\tau_{el}\lambda_{FEL}^2 2\rho} 0.001 \propto E_e. \quad (3.4)$$

Peak brightnesses of head-on and TWTS OFELs are shown in fig. 3.6a, too. TWTS OFELs have an order of magnitude higher peak spectral brightness than the CO<sub>2</sub> setup and a factor of twenty higher peak spectral brightness than the Ti:sapphire head-on setup.

The advantage of higher electron energies in TWTS does not stop at higher brightnesses. TWTS OFEL radiation also has higher transverse coherence than head-on setups as shown in fig. 3.6b. It plots the transverse coherence parameter  $\hat{\epsilon} = 2\pi\epsilon_N/\gamma_0\lambda_{FEL}$ , cf. eq. 2.17, of all OFELs over electron energy. TWTS OFELs utilizing laser wakefield accelerated electron bunches achieve optimum transverse coherence and with rf-accelerated electrons the radiation becomes at least partially transverse coherent or better. The same is obtained with laser wakefield accelerated electrons in the head-on setup utilizing a CO<sub>2</sub> laser which at the same time marks the best

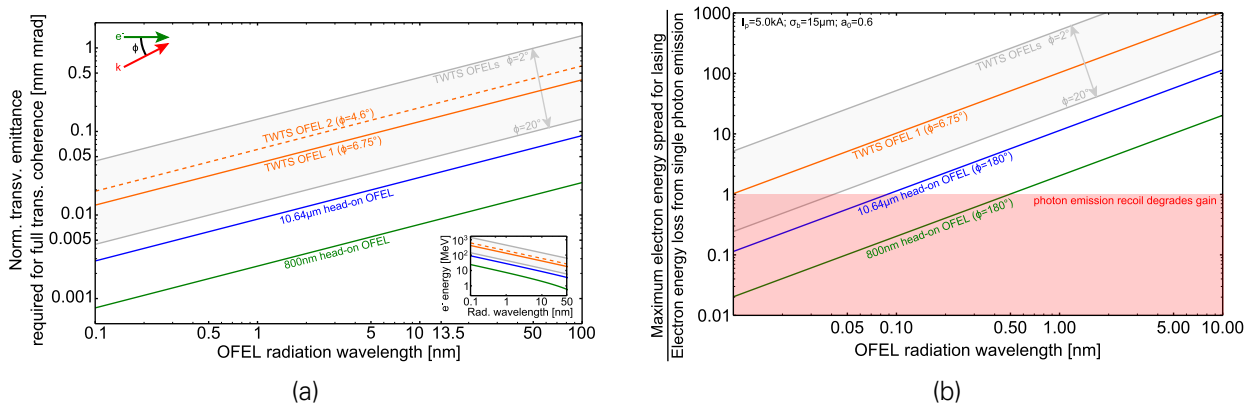


Figure 3.7.: (a) Required transverse normalized emittance to obtain fully transverse coherent radiation in head-on and TWTS OFELs in dependence of radiation wavelength. The inset shows the scaling of required electron energy to radiate at a target wavelength. (b) Scaling of the impact of photon emission recoil in dependence of the OFEL radiation wavelength. If the photon emission recoil becomes larger than the maximum acceptable electron energy spread for an OFEL setup, the photon output will reduce significantly. (Originally in [KS1])

result obtained with head-on setups. The remaining three head-on setups deliver only incoherent radiation.

A generalization of this example is obtained when recasting the condition  $\hat{\epsilon} \approx 1$  for optimum transverse coherence into a condition on normalized transverse electron beam emittance, cf. (2.18),

$$\epsilon_N \approx \frac{\gamma_0 \lambda_{\text{FEL}}}{2\pi}.$$

The scaling of required transverse emittance for optimum transverse coherence is shown in fig. 3.7a in dependence of OFEL radiation wavelength. TWTS OFELs operating at small interaction angles are able to deliver fully transverse coherent radiation for extreme ultraviolet and larger radiation wavelengths with existing electron accelerators delivering beams with normalized emittances well below 1 mm mrad [75, 109–112]. Head-on OFEL schemes have one to two orders of magnitude lower limits being far from realization especially at the low MeV level electron energies.

Furthermore, these low energy beams are problematic in terms of beam transport due to their space charge dominated dynamics. During electron beam transport from the rf-gun to the interaction region space charge increases emittance and during FEL interaction counteracts microbunching. While the latter is not a problem for head on OFEL setups due to their short gain lengths, see the limit on the reduced electron beam plasma oscillation period (2.13), controlling the emittance increase during transport is technically challenging.

Besides space charge, the quantum recoil experienced by an electron after a photon emission becomes problematic for the low energy beams at X-ray wavelengths, too. If the photon emission recoil  $\delta E_e = hc/\lambda_{\text{FEL}}$  is on the order of the acceptable electron energy spread  $\Delta E_e \leq \rho \gamma_0 m c^2$ , an electron does not contribute anymore to radiation amplification after a single photon emission which significantly reduces the total photon output [80, 113]. The scaling of the ratio of acceptable energy spread to photon emission recoil in dependence of the OFEL wavelength is shown in fig. 3.7b for TWTS and head-on OFELs using parameters of the rf-accelerated electron beams. The TWTS OFEL is in the classical regime even for sub- $\text{\AA}$  radiation wavelength in contrast to the head-on setups for which gain degradation is expected already at wavelengths of 1  $\text{\AA}$  and 5  $\text{\AA}$  for

the CO<sub>2</sub> and Ti:sapphire systems, respectively.

The presented results for photon conversion efficiency, brilliance, transverse coherence and gain degradation from quantum effects show that TWTS geometries are superior to standard head-on Thomson setups for optical free-electron laser realization. The increase of photon output and more important the reduction of electron beam quality requirements becomes possible by the free choice of interaction angle and hence electron energy which allows to balance all electron beam requirements. In later chapters of this thesis more scaling laws are derived that include requirements on laser systems providing the pulses for TWTS OFELs and required space and optics parameters to prepare these pulses. Then it is still the variability in interaction angle which gives the opportunity to balance all the requirements and allows to find setups realizable with laser and electron accelerator technology available today.

## 4. DESCRIPTION AND GENERATION OF TWTS LASER PULSES

The successful realization of an optical free-electron lasers (OFEL) in the TWTS geometry depends not only on the quality of electron beams which was already a topic in the last chapter. It is of equal importance to provide high quality laser pulses resembling as close as possible a plane wave along the electron trajectory. Yet, the introduction of a pulse-front tilt to a laser pulse is associated with the introduction of dispersion to the pulse. In brief, during interaction laser pulse dispersion can increase the laser pulse duration and spatially separate its frequencies contained in its spectrum. The latter causes a shift of radiated frequency during the interaction leading to a broadening of the radiation spectrum which necessarily must be smaller than the gain bandwidth when aiming for optical free-electron laser operation. The former reduces the laser amplitude and thereby the optical undulator strength. This reduction can be very rapid and cut the interaction significantly.

The chapter begins with an overview of the dispersions introduced with pulse-front tilts and quantifies their impact on the interaction. Then methods for dispersion compensation in TWTS geometries are discussed and it is shown that pulses being locally free of perturbing dispersion can be generated. A novel method for the generation of such laser pulses featuring dispersion compensation along the electron trajectory is presented. These pulses provide a plane wave optical undulator field and allow for TWTS OFELs at arbitrary interaction angles.

Since pulses for TWTS OFELs are usually required to have high field strength, focusing of these pulses may be necessary. Combining pulse-front tilt generation and focusing is a topic on its own which is treated in the last section of this chapter. It presents another novel method for the generation of laser pulses for TWTS OFELs providing focusing and allowing for compact setups by making use of an out-of-focus interaction geometry.

### 4.1. DISPERSIONS OF PULSE-FRONT TILTED LASER PULSES

Two methods are known to generate pulse-front tilted laser pulses. One is by the combination of spatial dispersion and group-delay dispersion [114] and the other by angular dispersion [115–117]. It follows a short introduction to these kind of dispersions assuming short, gaussian laser pulses [118, 119]. That is, the transverse amplitude profile of the pulse follows a gaussian distribution and the frequency spectrum follows a gaussian distribution with central frequency  $\Omega_0 = 2\pi c/\lambda_{\text{Laser}}$ . The pulse distortions described in the following are only a few of the distortions a laser pulse can exhibit but these are the ones to deal with in a laser pulse for TWTS. An

overview over all first order laser pulse distortions is given in ref. [118] and refs. [120, 121] give a general introduction to laser pulse dispersions.

**Angular Dispersion (AD)** All frequencies contained within the spectrum of the laser pulse propagate into different directions. Angular dispersion  $AD$  is defined as the first order coefficient in the expansion of the angle  $\theta \approx AD \cdot (\Omega - \Omega_0)$  enclosed by the propagation directions of frequency  $\Omega$  and central laser frequency  $\Omega_0$

$$AD = \left. \frac{d\theta}{d\Omega} \right|_{\Omega=\Omega_0}.$$

For example, angular dispersion is introduced to a laser pulse during diffraction at a grating since each of the frequencies within the laser pulse is diffracted into a different direction

$$\sin \psi_{\text{out}}(\Omega) = -n_1 \frac{2\pi c}{\Omega} + \sin \psi_{\text{in}}, \quad (4.1)$$

where diffraction is into  $-1$ st order and  $n_1$  is the line density of the grating. Thus  $\theta_{\text{grating},1} = \psi_{\text{out},1}(\Omega) - \psi_{\text{out},1}(\Omega_0)$  and

$$AD_{\text{grating},1} = \left. \frac{d\psi_{\text{out},1}}{d\Omega} \right|_{\Omega=\Omega_0} = \left. \frac{d \sin \psi_{\text{out},1}}{d\Omega} \frac{1}{\frac{d \sin \psi_{\text{out},1}}{d\psi_{\text{out},1}}} \right|_{\Omega=\Omega_0} = \frac{\sin \psi_{\text{in},1} - \sin \psi_{\text{out},1}}{\Omega_0 \cos \psi_{\text{out},1}}.$$

Figure 4.1 visualizes the consequences of angular dispersion in terms of laser pulse widening and elongation due to spatial frequency separation. Further a pulse-front tilt is introduced with an angle

$$\tan \alpha_{\text{tilt},1} = \Omega_0 AD_{\text{grating},1} = \frac{\sin \psi_{\text{in},1} - \sin \psi_{\text{out},1}}{\cos \psi_{\text{out},1}}. \quad (4.2)$$

The relation between pulse-front tilt and angular dispersion is found from an inverse Fourier transform of the electric field of a laser pulse with angular dispersion from frequency to time domain

$$E(y, z = 0, \Omega) = e^{\tau_0^2(\Omega - \Omega_0)^2/4} e^{i\frac{\Omega_0}{c}AD(\Omega - \Omega_0)y} \xrightarrow{FT} E(y, z = 0, t) \propto e^{-(t - \frac{y}{c}\Omega_0AD)^2/\tau_0^2},$$

where  $\Omega_0AD(\Omega - \Omega_0)/c \approx k_y(\Omega)$  is approximately the  $y$ -component of the wavevector of frequency  $\Omega$  and the  $z$ -axis points along the propagation direction of the pulse. The electric field in time-domain shows a temporal delay  $t_0 = (y/c)\Omega_0AD$  in maximum irradiance arrival along the transverse direction  $y$  which is just the definition of a pulse-front tilt about an angle

$$\tan \alpha_{\text{tilt}} = \frac{dc t_0}{dy} = \Omega_0 AD.$$

Introducing pulse-front tilts by diffraction of a laser pulse at a grating is the method chosen for TWTS. The compensation of pulse elongation and widening due to AD is presented later in this chapter.

**Spatial Dispersion (SD)** The separation of frequencies along the transverse direction, i.e.  $y$ -axis, is called spatial dispersion. In gaussian pulses, where the spatial distribution of each frequency follows its own gaussian, spatial dispersion  $SD$  is quantified by the offset of a frequencies distribution center  $y_0$  from the laser pulse center  $y_0(\Omega_0) = 0$ . Spatial dispersion  $SD$

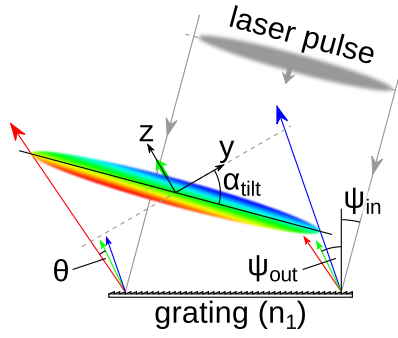


Figure 4.1.: Diffraction of a laser pulse at a grating of line density  $n_1$ . The initially dispersion free pulse is incident to the grating under the angle  $\psi_{in}$  and outgoing under the angle  $\psi_{out}$ . At the grating every frequency  $\Omega$  contained in the pulse is diffracted in a different direction which is called angular dispersion ( $AD$ ). The angle  $\psi_{out}$  refers to the outgoing angle of the central laser frequency  $\Omega_0$  (green). The angle enclosed by the propagation direction of a different frequency and the central laser frequency is  $\theta(\Omega) = \psi_{out}(\Omega) - \psi_{out}(\Omega_0)$ . Angular dispersion causes transverse and longitudinal separation of frequencies, called spatial dispersion ( $SD$ ) and group-delay dispersion ( $GDD$ ), respectively, and thus leads to an increase of pulse width and duration. Furthermore, a pulse-front tilt by an angle  $\alpha_{tilt}$  is introduced because the pulse envelope can not travel faster than the speed of light. In this picture diffraction is into the first order ( $\psi_{out} > \psi_{in}$ ) leading to a negative pulse-front tilt ( $\alpha_{tilt} < 0$ ).

is defined as the first order coefficient in the expansion of the frequency separation distance  $y_0(\Omega) \approx SD(\Omega - \Omega_0)$

$$SD = \left. \frac{dy_0}{d\Omega} \right|_{\Omega=\Omega_0}.$$

As seen from the picture, angular dispersion inherently introduces spatial dispersion after propagation by a distance  $z$ . With  $y_0(\Omega) = -z \tan \theta(\Omega) \approx -z\theta(\Omega)$  the connection between  $SD$  and  $AD$  is

$$SD(z) = -zAD = -\frac{z}{\Omega_0} \tan \alpha_{tilt}.$$

Spatial dispersion in a gaussian pulse causes widening and elongation of the pulse. Widening is caused by the frequencies which strongest diverge since the distance between the outer edges of their spatial distributions defines the pulse width

$$W = w \left[ 1 + \left( 2 \frac{SD}{w\tau_0} \right)^2 \right]^{1/2},$$

where the dispersion-free laser width  $w$  takes widening from defocusing into account. Elongation is due to local bandwidth reduction when spatial distributions of frequencies do not overlap anymore

$$\tau = \tau_0 \left[ 1 + \left( 2 \frac{SD}{w\tau_0} \right)^2 \right]^{1/2},$$

where  $\tau_0$  equals two times the rms duration of the laser irradiance and is thus related to the full width at half-maximum duration of the irradiance  $\tau_{FWHM,I} = \sqrt{2 \ln 2} \tau_0$ , which is typically meant when saying 'pulse duration'. Both pulse distortions from spatial dispersion only affect laser pulses in large interaction angle TWTS scenarios. For typical TWTS conditions, where

laser pulses span several ten laser wavelengths longitudinally and transversely,  $\Omega_0\tau_0 \gg 1$  and  $w_0 \gg \lambda_{\text{Laser}}$  respectively, pulse elongation and widening are negligible for interaction angles  $\phi \lesssim 130^\circ$ , since

$$2 \frac{SD}{w\tau_0} = -\frac{1}{2\Omega_0\tau_0} \frac{w_0 \cos \phi \tan(\phi/2)}{w \sin \phi} \approx -\frac{1}{2\Omega_0\tau_0} \frac{\cos \phi \tan(\phi/2)}{\left[\sin^2 \phi + \lambda_{\text{Laser}}^2/(2\pi w_0)^2\right]^{1/2}} \stackrel{\phi \lesssim 130^\circ}{\ll} 1,$$

assuming the interaction ends after a laser propagation distance of  $z = L_{\text{int}} \cos(\phi)/2$  from the focus, with  $L_{\text{int}} = w_0/\sin \phi$  being the interaction length which is itself determined by the laser pulse width  $w_0$ , and the pulse-front tilt angle  $\alpha_{\text{tilt}} = \phi/2$  equals half the interaction angle  $\phi$ .

**Group Delay Dispersion (GDD)** The longitudinal/temporal separation of frequencies in a laser pulse is called group delay dispersion. The temporal separation along the laser pulse axis can be seen as an additional slow phase shift on top of the regular phase progression of a plane wave  $\varphi(z, \Omega) = z\Omega/c + (GDD/2)(\Omega - \Omega_0)^2$ . Assuming the dependence of the phase  $\varphi$  from  $\Omega$  is known, group delay dispersion is defined as

$$GDD = \left. \frac{d^2 \varphi}{d\Omega^2} \right|_{\Omega=\Omega_0}.$$

With angular dispersion, each frequency travels at a different speed along the laser pulse direction of propagation which results in  $GDD$ . Considering only the phase variation in the longitudinal direction, the phase of a pulse with angular dispersion is  $\varphi(z, \Omega) = z(\Omega/c) \cos \theta(\Omega)$  and  $GDD$  can be connected to  $AD$

$$GDD = -\frac{\Omega_0}{c} zAD^2 = -\frac{z}{\Omega_0 c} \tan^2 \alpha_{\text{tilt}}.$$

Group delay dispersion in a gaussian pulse causes its elongation  $\tau_0 \rightarrow T$  and a continuous shift of central laser frequency  $\Omega_0 \rightarrow \omega$  during interaction. Both effects are due to the temporal separation of frequencies.

$$T = \tau_0 \left[ 1 + \left( 2 \frac{GDD}{\tau_0^2} \right)^2 \right]^{1/2}$$

$$\omega(t) = \Omega_0 \left[ 1 + \frac{2}{\Omega_0 \tau_0} \frac{t}{\tau_0} \frac{2GDD/\tau_0^2}{1 + (2GDD/\tau_0^2)^2} \right]$$

Although the frequency shift will be always small as long as  $\Omega_0\tau_0 \gg 1$ , the pulse elongation can become large even after a short interaction distance in the ten centimeter range and thus significantly diminish interaction due to the reduction in field amplitude.

As an example, for a laser of wavelength  $\lambda_{\text{Laser}} = 1 \mu\text{m}$ , pulse duration  $\tau_0 = 25 \text{ fs}$ , pulse-front tilt  $\alpha_{\text{tilt}} = 60^\circ$  and a target interaction length of  $L_{\text{int}} = 25 \text{ cm}$  the laser pulse elongates beyond  $1000\tau_0$  towards the end of the interaction if the laser is fully compensated in the middle of the interaction. In this case, interaction with significant photon output terminates long before the target interaction distance is reached. On the other hand, for a laser pulse with the same wavelength, but  $\tau_0 = 150 \text{ fs}$ ,  $\alpha_{\text{tilt}} = 5^\circ$  the pulse duration increases to merely  $1.001\tau_0$  after the same interaction distance. This illustrates that laser pulse dispersion needs to be controlled. In large interaction angle setups, such as the first example, it is necessary to compensate dispersion during the interaction. Small interaction angle setups, such as the second example, might be

realized without dispersion compensation during the interaction but require dispersion compensation for propagation from the pulse-front tilting grating to the interaction region.

As a final consequence, when aiming for TWTS OFEL operation it is important to evaluate frequency and irradiance variations along the electron trajectory taking all dispersions into account. Therefore a fully analytic, wave-optical description of the electric field of a pulse-front tilted laser pulse is developed in the next section to evaluate these variations. Limits on acceptable irradiance and frequency variations for OFEL operation are derived, too. These limits help to decide on the necessity of dispersion compensation during the interaction. How dispersion compensation during the interaction can be accomplished is shown in the section following the next one.

## 4.2. EVALUATING FREQUENCY AND AMPLITUDE VARIATIONS OF OPTICAL UNDULATORS IN TWTS GEOMETRIES WITHOUT DISPERSION COMPENSATION DURING INTERACTION

Optical undulator frequency and amplitude variations induce variations in radiated wavelength. A limit on radiation wavelength variations is set by the gain bandwidth given by twice the Pierce parameter  $\rho$ . Wavelength variations must be smaller than the gain bandwidth  $\Delta\lambda_{\text{FEL}}/\lambda_{\text{FEL}} \leq 2\rho$ , cf. eq. (2.11), since otherwise the scattering output is reduced. With the Thomson formula (2.2) the wavelength variation limit can be recast into limits on frequency variation  $\Delta\tilde{\Omega}/\tilde{\Omega}$  and irradiance variation  $\Delta I/I = 2\Delta a_0/a_0$  along the electron trajectory [KS2]

$$\boxed{\begin{aligned} \frac{\Delta\tilde{\Omega}}{\tilde{\Omega}} &\leq 2\rho, \\ \frac{\Delta I}{I} &\leq 4\rho \frac{1 + a_0^2/2}{a_0^2}. \end{aligned}} \quad (4.3)$$

Laser frequency and irradiance variations along the electron trajectory are found from an analytic description of the laser electric field. This description is developed in the following section.

### 4.2.1. ANALYTIC DESCRIPTION OF PULSE-FRONT TILTED LASER PULSES

An analytic description of the laser electric field is obtained by assuming a pulse-front tilted laser which is free of perturbing dispersion in the middle of the interaction and with a gaussian spectrum  $\epsilon(\Omega - \Omega_0) = \exp[-(\Omega - \Omega_0)^2 \tau_0^2/4]$

$$\hat{E}(z = 0, y, \Omega) = \epsilon(\Omega - \Omega_0) e^{-\frac{y^2}{w_0^2}} e^{i\frac{(\Omega - \Omega_0)}{c} y \tan \alpha_{\text{tilt}}},$$

which is written in frequency space. Note,  $\tau_0$  is related to the full-width at half-maximum duration of the irradiance via  $\tau_{\text{FWHM},I} = \sqrt{2 \ln 2} \tau_0$  which is typically meant when saying ‘pulse duration’. In accordance with ref. [KS4], the field at every other position is found by propagating  $\hat{E}(z = 0, y, \Omega)$  along the z-axis with the Rayleigh-Sommerfeld diffraction integral [81, p. 636] [KS5]

$$\begin{aligned} \hat{E}(z, y, \Omega) &= \epsilon(\Omega - \Omega_0) \sqrt{\frac{\Omega}{2\pi c}} \frac{e^{-i(\frac{\Omega}{c}z - \frac{\pi}{4})}}{\sqrt{z}} \int_{-\infty}^{\infty} \hat{E}(z = 0, y, \Omega) e^{-i\frac{\Omega}{2cz}(y-\xi)^2} d\xi \\ &= \epsilon(\Omega - \Omega_0) \sqrt{\frac{w_0}{w(z)}} e^{-\left[y + \frac{(\Omega - \Omega_0)}{\Omega_0} z \tan \alpha_{\text{tilt}}\right]^2 \left[\frac{1}{w(z)^2} + i\frac{\Omega}{2cR(z)}\right]} \mathbf{x} \\ &\quad \times e^{-i\frac{\Omega}{c}z + i\frac{(\Omega - \Omega_0)}{c} y \tan \alpha_{\text{tilt}} + i\frac{(\Omega - \Omega_0)^2}{2\Omega_0 c} z \tan^2 \alpha_{\text{tilt}} + \frac{1}{2} \arctan \frac{z}{2R}} \end{aligned} \quad (4.4)$$

where  $w(z)^2 = w_0^2[1 + (z/z_R)^2]$  is the width of the pulse increasing with distance from the focus,  $R(z) = z[1 + (z_R/z)^2]$  is the radius of phase-front curvature and  $z_R = \pi w_0^2/\lambda_{\text{Laser}}$  is the Rayleigh length. This field representation already shows that the propagating pulse exhibits spatial dispersion and group-delay dispersion. Spatial dispersion is manifest in the exponent of the first exponential function which describes the transverse profile. Group-delay dispersion is manifest in the term  $\propto (\Omega - \Omega_0)^2$  in the complex argument of the field. Both dispersions emerge from angular dispersion during propagation. The field contains a third-order dispersion [121, 122] term  $\propto \exp[i(\Omega - \Omega_0)^3 z^2 \tan^2 \alpha_{\text{tilt}}/2\Omega_0^2 cR]$ , too. For TWTS it will be small and is neglected since laser pulses for TWTS typically contain several ten laser periods and have almost no phase and pulse curvature in order to limit optical undulator frequency variations and to achieve good overlap.

Before the field can be evaluated along the electron trajectory, it needs to be inversely Fourier transformed to time domain

$$E(z, y, t) = \frac{1}{2\pi} \int \hat{E}(z, y, \Omega) e^{i\Omega t} d\Omega.$$

The analytical result for the laser electric field in time domain is

$$\boxed{E(z, y, t) = \sqrt{\frac{w_0}{w}} e^{-\frac{y^2}{w^2}} e^{i\frac{\Omega_0}{c}(ct-z)} e^{-i\frac{\Omega_0}{2cR} y^2} e^{i\frac{1}{2} \arctan \frac{z}{z_R} \times} \times \frac{1}{\sqrt{\pi}} \left[ \tau^2 T^2 \right]^{-\frac{1}{4}} e^{-i\frac{1}{2} \arctan \left( 4 \frac{g}{\tau^2} \right)} e^{-\frac{l^2}{\tau^2}} e^{i4 \frac{(l^2 g - s^2 g - l s \tau^2 / 2)}{\tau^2 T^2}}}$$
 (4.5)

where

$$\begin{aligned} W^2 &= w^2 + 4SD^2/\tau_0^2, \\ T^2 &= \tau^2 + 16\frac{g^2}{\tau^2}, \\ \tau^2 &= \tau_0^2 + 4\frac{SD^2}{w^2}, \\ \tilde{L} &= l + 4\frac{sg}{\tau^2}, \\ l &= t - \frac{z}{c} + \frac{y}{c} \tan \alpha_{\text{tilt}} - \frac{y^2}{2cR} + \frac{y \Omega_0 SD}{c R}, \\ s &= \frac{2ySD}{w^2}, \\ g &= \frac{\Omega_0 SD^2}{2cR} + \frac{y SD}{c R} + \frac{1}{2} GDD \\ SD &= -\frac{z}{\Omega_0} \tan \alpha_{\text{tilt}}, \\ GDD &= -\frac{z}{\Omega_0 c} \tan^2 \alpha_{\text{tilt}} \end{aligned}$$

and the pulse is located at  $z = 0$  at  $t = 0$  where  $t = 0$  marks the middle of the interaction. As can be seen from this analytic pulse description, pulse distortions emerge from angular dispersion during propagation. The pulse width increases  $w_0 \rightarrow W$ , the pulse duration increases  $\tau_0 \rightarrow \tau \rightarrow T$  and the pulse front bends and rotates  $t - z/c + (y/c) \tan \alpha_{\text{tilt}} \rightarrow \tilde{L}$  due to defocusing and increasing dispersion. In addition to these distortions regarding the amplitude of the pulse also complex phase distortions emerge from dispersion and bending of the phase fronts as can be seen from the complex phase structure of the field.

#### 4.2.2. APPROXIMATING OPTICAL UNDULATOR AMPLITUDE VARIATION DURING INTERACTION

First, the variation of laser amplitude during the interaction is analyzed. There are in principle two sources of amplitude distortions, dispersion and defocusing, as it can be seen from the evolution of laser pulse irradiance  $I \propto EE^*$

$$\frac{I(y, z, t)}{I(0, 0, 0)} = \frac{1}{[1 + (z/z_R)^2]^{1/2}} e^{-2\frac{y^2}{w_0^2}} \left[1 + \tilde{D}^2\right]^{-1/2} e^{-2\frac{(\tilde{L}' + 2\frac{SD}{w_0\tau_0} \frac{y}{w_0} \tilde{D})^2}{(1 + \tilde{D}^2)}}, \quad (4.6)$$

where

$$\tilde{L}' = \frac{ct - z + y \tan \alpha_{\text{tilt}}}{c\tau_0}$$

$$\tilde{D} = 2\frac{z \tan^2 \alpha_{\text{tilt}}}{\Omega_0 \tau_0 c\tau_0}.$$

The first factor represents amplitude reduction from defocusing and scales with the ratio of Rayleigh length to the distance of the position where interaction ends from the focus  $L_{\text{dist}} = L_{\text{int}} \cos(\phi)/2 = w_0 \cos(\phi)/2 \sin \phi$  during interaction

$$\frac{L_{\text{dist}}}{z_R} = \frac{\lambda_{\text{Laser}} \cos \phi}{2\pi L_{\text{int}} \sin^2 \phi} = \frac{1}{4\pi} \left(1 - \tan^2(\phi/2)\right) \frac{\lambda_{\text{und}}}{L_{\text{int}}}.$$

The interaction will take place well within a Rayleigh length, since the aim of TWTS is to provide long optical undulators with many undulator periods  $L_{\text{int}} \gg \lambda_{\text{und}}$ . Thus there are no distortions from defocusing allowing to take  $w \rightarrow w_0$  and  $R \rightarrow \infty$ .

The second factor represents irradiance variation from the gaussian transverse profile. But the real transverse profile depends on the experimental conditions and can be manipulated. Therefore it is not taken into account in the approximation of expected irradiance variation given below. For this only the variation originating from laser dispersion is taken into account.

The remaining factors represent amplitude distortions from dispersion and only taking group delay dispersion into account since the effect of spatial dispersion is usually negligible for TWTS OFELs utilizing wide laser pulses. The impact of spatial dispersion is characterized by

$$2\frac{SD}{w\tau_0} = -\frac{1}{2\Omega_0\tau_0} \left(1 - \tan^2(\phi/2)\right) \ll 1$$

and for TWTS OFELs utilizing not too short laser pulses,  $\Omega_0\tau_0 = \lambda_{\text{Laser}}/2\pi c\tau_0 \gg 1$ , spatial dispersion does not significantly distort the pulse for moderate interaction angles  $\phi \leq 130^\circ$  where  $1 - \tan^2(\phi/2) \sim 1$  allowing to take  $\tau \rightarrow \tau_0$  and  $W \rightarrow w_0$ . This limit on interaction angles is no significant restriction on TWTS OFEL realization since TWTS OFELs will be typically operated at smaller interaction angles due to the lower electron and laser requirements, as has been motivated in sec. 3.3.

With the influence of defocusing and spatial dispersion expected to be negligible, group-delay dispersion will be the most significant contribution to amplitude distortions during the interaction. Along the trajectory of an electron located at the bunch center

$$z_{\text{el}} = ct \cos \phi \qquad y_{\text{el}} = -ct \sin \phi \qquad (4.7)$$

the overlap between electron and laser pulse is optimum and thus  $\tilde{L}' = 0$  always. In the middle of the interaction at  $t = 0$  the electrons are in the center of the laser pulse which is exactly at the

focus position where dispersion vanishes  $\tilde{D} = 0$ . Until the end of interaction at  $t_{\text{end}} = L_{\text{int}}/2c$  the dispersion term takes on a finite value

$$\Delta\tilde{D} = \frac{L_{\text{int}} \cos \phi \tan^2(\phi/2)}{\Omega_0 \tau_0 c \tau_0} = \frac{L_{\text{int}} \lambda_{\text{Laser}} \cos \phi \tan^2(\phi/2)}{(c \tau_0)^2} \cdot \frac{1}{2\pi}.$$

Expanding the irradiance variation taken at the end of interaction

$$\frac{I(y = -ct_{\text{end}} \sin \phi, z = ct_{\text{end}} \cos \phi, t_{\text{end}})}{I(0, 0, 0)} - 1 = \frac{\Delta I}{I}$$

for  $\Delta\tilde{D} \ll 1$  yields the variation of irradiance until the end of interaction

$$\left| \frac{\Delta I}{I} \right| = \frac{\Delta\tilde{D}^2}{2} = \frac{1}{2} \left( \frac{L_{\text{int}} \lambda_{\text{Laser}} \cos \phi \tan^2(\phi/2)}{(c \tau_0)^2} \right)^2 \stackrel{!}{\leq} 4\rho \frac{1 + a_0^2/2}{a_0^2}. \quad (4.8)$$

This is the first relation used to decide in TWTS OFEL setups on the necessity of dispersion compensation during interaction. The limit on the right-hand side yields for typical values of TWTS OFELs of  $\rho \sim 10^{-3}$  and  $a_0 \sim 0.5$  an acceptable irradiance variation of a few percent. For comparison, in the example scenario at the end of the last section, utilizing a 1  $\mu\text{m}$  wavelength, 150 fs pulse-duration laser-system to provide a 25 cm long optical undulator at  $10^\circ$  interaction angle, an irradiance variation of 1.1% is induced by dispersion. This is typically an acceptable value for TWTS OFELs but evaluation for a specific experiment with its parameter set is always required.

#### 4.2.3. APPROXIMATING OPTICAL UNDULATOR FREQUENCY VARIATION DURING INTERACTION

The optical undulator frequency  $\tilde{\Omega}(t)$  corresponds to the instantaneous frequency of the laser evaluated along the electron trajectory (4.7). The instantaneous frequency of the laser is given by the time derivative of the phase  $\tilde{\varphi}(z, y, t) = \text{Arg } E(z, y, t)$  of the complex laser field (4.5)

$$\tilde{\Omega}(t) = \frac{d}{dt} \tilde{\varphi}(ct \cos \phi, -ct \sin \phi, t).$$

Applying the same approximations as in the calculation of irradiance variation yields for the optical undulator frequency evolution

$$\tilde{\Omega}(t) = \frac{d}{dt} \left[ \Omega_0(1 - \cos \phi)t - \frac{1}{2} \arctan \tilde{D}(z = ct \cos \phi) \right] = \Omega_0(1 - \cos \phi) - \frac{\dot{\tilde{D}}}{2(1 + \tilde{D}^2)}.$$

from which the total variation of undulator frequency until the end of interaction at  $t_{\text{end}} = L_{\text{int}}/2c$  is obtained

$$\Delta\tilde{\Omega} = \tilde{\Omega}(t_{\text{end}}) - \Omega_0(1 - \cos \phi) = -\frac{\dot{\tilde{D}}}{2(1 + \Delta\tilde{D}^2)}.$$

Since it is already clear from the limit on irradiance variation that  $\Delta\tilde{D}^2 \ll 1$ , the limit on relative variation of undulator frequency can be approximated by

$$\left| \frac{\Delta\tilde{\Omega}}{\tilde{\Omega}} \right| = \frac{\dot{\tilde{D}}}{2\Omega_0(1 - \cos \phi)} = \frac{\lambda_{\text{Laser}}^2 \cos \phi \tan^2(\phi/2)}{(2\pi c \tau_0)^2} \stackrel{!}{\leq} 2\rho. \quad (4.9)$$

This is the second relation used to decide in TWTS OFEL setups on the necessity of dispersion compensation during the interaction. Compared to the first limit it does not scale with interaction length  $L_{\text{int}}$  but rather  $\lambda_{\text{und}} = \lambda_{\text{Laser}}/(1 - \cos \phi) \ll L_{\text{int}}$  which makes it in most cases of TWTS OFEL setups the weaker of both limits. For the above long pulse example its value is  $\Delta\tilde{\Omega}/\tilde{\Omega} = 6 \cdot 10^{-6}$  being well below the typical TWTS OFEL Pierce parameter  $\rho = 10^{-3}$ .

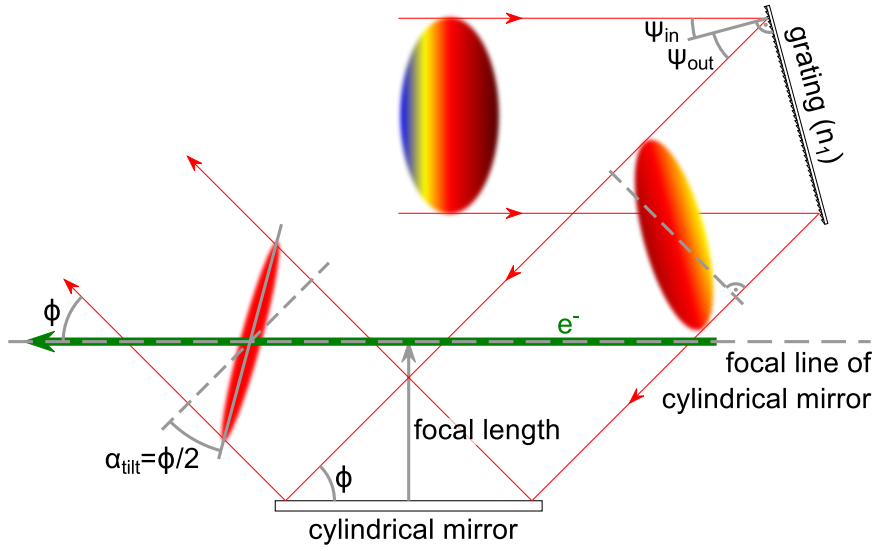


Figure 4.2.: Simplest case of a TWTS setup at an interaction angle  $\phi$ . An incoming laser pulse is diffracted at a grating of line density  $n_1$  which introduces a pulse-front tilt of half the interaction angle  $\alpha_{\text{tilt}} = \phi/2$ . Then the laser pulse is focused by a cylindrical mirror in the vertical direction which is perpendicular to the interaction plane spanned by laser and electron propagation directions. The focal line of the mirror coincides with the electron beam path such that the vertical laser diameter in the interaction region matches the electron beam diameter for optimum overlap. The incoming laser pulse has a positive group-delay dispersion to precompensate negative group-delay dispersion induced by angular dispersion from the grating together with propagation of the pulse from the grating to the interaction region. Full dispersion compensation exists only at one instant of time, in the middle of the electron-laser interaction.

### 4.3. TWTS SETUPS WITHOUT FOCUSING IN THE INTERACTION PLANE AND WITHOUT DISPERSION COMPENSATION DURING INTERACTION

This and the following sections present optical setups for the realization of TWTS. Their complexity increases step by step as every setup exhibits a new feature which satisfies a demand that might occur in TWTS OFEL realization. While the first setup just generates a pulse-front tilt, the second already allows for dispersion compensation during interaction and the third combines pulse-front tilt generation, dispersion compensation and focusing in the interaction plane which might be required to achieve the necessary optical undulator field strength.

The simplest case of a TWTS setup is depicted in fig. 4.2. An incoming laser pulse is diffracted at a grating which introduces a pulse-front tilt according to eq. (4.2)

$$\tan \alpha_{\text{tilt},1} = \frac{\sin \psi_{\text{in},1} - \sin \psi_{\text{out},1}}{\cos \psi_{\text{out},1}}.$$

The tilted pulse propagates to a cylindrical mirror which focuses it in the vertical direction being the direction perpendicular to the interaction plane spanned by laser and electron propagation directions. The focal line of the mirror is aligned with the electron trajectory such that the part of the pulse which is just crossing the electron beam axis has smallest vertical extent. During interaction the pulse-front tilt ensures continuous overlap of electrons and laser pulse and the interaction length is determined by the horizontal laser pulse width.

In the preceding sections the laser pulse was taken to be free of perturbing dispersion, i. e.  $SD$  and  $GDD$ , in the middle of the interaction corresponding here to the arrival of the laser pulse center at the mirror focal line. But laser dispersion starts with diffraction at the grating and continues all along the distance  $L_{\text{prop}}$  to the interaction point. This may be several meters over which frequencies separate increasing pulse width and duration.

The effect of spatial dispersion may still be small, provided that geometries with small interaction angles  $\phi \sim 10^\circ$ , corresponding to small pulse-front tilts, are chosen together with not too short laser pulses ( $\Omega_0\tau_0 = 2\pi c\tau_0/\lambda_{\text{Laser}} \gg 1$ ) of centimeter scale diameters. Then the factor

$$\left| 2 \frac{SD}{w_0\tau_0} \right| = \frac{L_{\text{prop}}\lambda_{\text{Laser}}}{\pi w_0 c\tau_0} \tan(\phi/2)$$

which determines pulse elongation and width increase due to spatial dispersion, see sec. 4.1, can be still a small quantity.

Group-delay dispersion will not be negligible on meter scale propagation distances

$$\left| 2 \frac{GDD}{\tau_0^2} \right| = \frac{L_{\text{prop}}\lambda_{\text{Laser}}}{\pi(c\tau_0)^2} \tan^2(\phi/2)$$

and thus will increase pulse duration many times over. Therefore, a precompensation of group-delay dispersion is necessary. That is, the incoming pulse already features a positive group-delay dispersion which is opposite in sign to negative group-delay dispersion developing after diffraction at the grating and subsequent propagation to the interaction point due to angular dispersion.

Group-delay dispersion of laser pulses is routinely modified in high power laser systems for chirped pulse amplification (CPA) [123, 124]. In CPA laser systems pulses are elongated in stretchers [125] by introducing positive group-delay dispersion in order to reduce the beam power below the threshold of nonlinear effects and self-focusing in the gain-medium during amplification [120, ch. 7]. After amplification the positive group-delay dispersion is removed in compressors [126] by multiple diffraction of the pulse at one or more gratings where the introduced dispersion temporally overlaps the frequencies again.

One option to provide precompensation for TWTS with high-power laser pulses could be the reduction of the compression ratio in the laser pulse compressor. Another could be an additional stretcher before the amplification chain in the laser system. Both methods aim to provide a residual positive group-delay dispersion of the laser pulse after the compressor. Full compression is then achieved during propagation of the laser from the pulse-front tilting grating to the interaction point. Assuming  $L_{\text{prop}}$  is the distance from the grating to the interaction point, the amount of  $GDD$  required for precompensation is

$$GDD_{\text{in}} = \frac{L_{\text{prop}}\lambda_{\text{Laser}}}{2\pi c^2} \tan^2 \alpha_{\text{tilt},1} . \quad (4.10)$$

As stated above, full compression is available only at one instant of time limiting this setup to small interaction angles.

With small interaction angles only small pulse-front tilts are needed and thus the difference between outgoing and incoming angle at the grating will be small. This has the drawback of using gratings of very low line density which permit diffraction into many orders. An outgoing laser pulse exists for every diffraction order resulting in low diffraction efficiency since the energy of the incoming pulse is distributed over all outgoing pulses. Thus only a fraction of the initial pulse energy will be available for OFEL realization. Additional propagation distance is also required to spatially separate these pulses and picking up the target order.

The next section presents a novel method to control and compensate  $SD$  and  $GDD$  in TWTS setups during interaction in order to overcome the limitations of this simple setup.

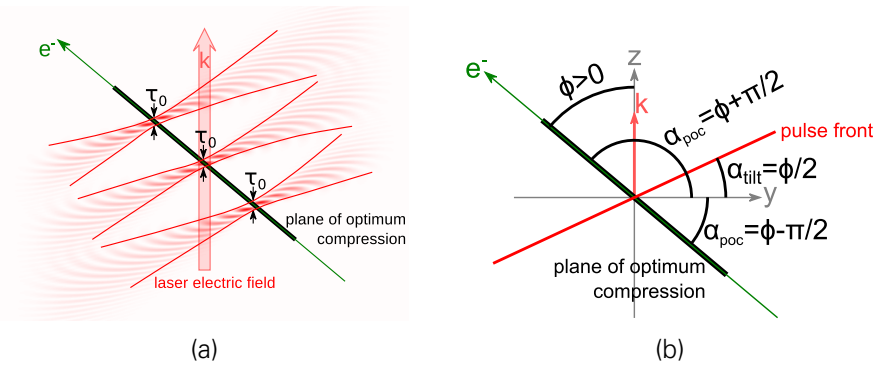


Figure 4.3.: (a) The electric field of a laser pulse plotted at different time steps during the interaction with an electron pulse in the TWTS geometry providing local laser dispersion compensation. That is, the laser pulse duration is shortest where the pulse overlaps with the electron trajectory. As a result, the electrons interact with a laser pulse free of undulator frequency and amplitude variations during interaction. (b) Required alignment of plane of optimum compression and pulse-front tilt in a TWTS geometry. For an interaction angle  $\phi$  the pulse front-tilt has to be  $\phi/2$ . For the plane of optimum compression there are two possible orientations,  $\phi + \pi/2$  and  $\phi - \pi/2$ . (Originally in [KS4])

#### 4.4. TWTS SETUPS WITH FULL DISPERSION COMPENSATION DURING INTERACTION BUT WITHOUT FOCUSING IN THE INTERACTION PLANE

The simple TWTS setup of the preceding section is limited in its usability. Missing dispersion compensation during the interaction limits it to small interaction angles with small pulse-front tilts. Generating small pulse-front tilts is only possible with low diffraction efficiency at the grating because most of the incoming pulse energy is lost by diffraction into higher orders. Both of these drawbacks are remedied with the novel setup strategy presented in the following. First the underlying principle for dispersion compensation during interaction is explained.

##### 4.4.1. DISPERSION COMPENSATION DURING INTERACTION BY EXPLOITING THE PLANE OF OPTIMUM COMPRESSION

In order to minimize intensity and optical undulator frequency variations during interaction, laser pulse dispersion needs to be removed. But there is no fully dispersion free pulse featuring a pulse-front tilt. Compensation of perturbing dispersion can be done only locally, i. e. the aim is to generate a pulse that is second order dispersion free only in the section which currently overlaps with the electron pulse. The vicinity of the electron beam path thus defines a volume in which the section of the laser pulse which is currently inside this volume is second order dispersion free while the rest of the pulse outside the volume is not, see fig. 4.3a. The plane containing the electron beam center trajectory and cutting this volume transverse to the interaction plane is called 'plane of optimum compression'.

A plane of optimum compression is nothing that needs be specifically generated. It exists always when a laser pulse is diffracted at a grating [127]. Exploiting it is a matter of controlling its orientation. Figure 4.3b visualizes the required orientations of pulse-front tilt and plane of

optimum compression in a TWTS setup. For a given interaction angle  $\phi$  these are

$$\boxed{\alpha_{\text{tilt}} = \phi/2 \qquad \alpha_{\text{poc}} = \phi \pm \pi/2} \quad (4.11)$$

in order to ensure optimum electron-laser overlap and vanishing second order dispersion along the electron trajectory, respectively. These conditions can be recast into a single condition which needs to be fulfilled for a proper TWTS setup

$$\alpha_{\text{poc}} - 2\alpha_{\text{tilt}} = \pm \frac{\pi}{2}. \quad (4.12)$$

The orientation of the plane of optimum compression for a pulse with angular dispersion can be derived by expanding the complex phase  $\varphi(\Omega)$  of its electric field up to second order in  $(\Omega - \Omega_0)$  [127]

$$\begin{aligned} \varphi(\Omega) &= \mathbf{k}(\Omega)\mathbf{r} = \frac{\Omega}{c}(z \cos \theta(\Omega) - y \sin \theta(\Omega)) \\ &\approx \frac{\Omega_0}{c}z + (z - y \tan \alpha_{\text{tilt}})\frac{(\Omega - \Omega_0)}{c} + \frac{1}{2}(y \tan \alpha_{\text{poc}} - z) \tan^2 \alpha_{\text{tilt}} \frac{(\Omega - \Omega_0)^2}{\Omega_0 c}, \end{aligned} \quad (4.13)$$

with

$$\boxed{\tan \alpha_{\text{tilt}} = \Omega_0 \theta' \qquad \tan \alpha_{\text{poc}} = -\frac{2\theta' + \Omega_0 \theta''}{\Omega_0 \theta'^2}}, \quad (4.14)$$

where  $\theta' = \left. \frac{d\theta}{d\Omega} \right|_{\Omega=\Omega_0}$  is the afore mentioned frequency derivative of the angle enclosed by the propagation directions of a frequency  $\Omega$  and the central frequency  $\Omega_0$  which is evaluated at the central frequency.

The pulse-front is defined by the plane along which first order dispersion vanishes  $z = y \tan \alpha_{\text{tilt}}$ . The orientation of the plane of optimum compression is along the plane where second order dispersion vanishes  $z = y \tan \alpha_{\text{poc}}$ . Note, by continuing the expansion to higher orders one can derive the orientation of more planes where a given order of dispersion vanishes. Unfortunately, these planes do not coincide in general. For example, the plane along which third order dispersion vanishes is given by  $\tan \alpha_{\text{tod}} = (\Omega_0 \theta'^3 - 3\theta'' - \Omega_0 \theta''')/(\theta'^2 + \Omega_0 \theta' \theta'')$ .

For diffraction at a grating the deviation angle is given by

$$\theta(\Omega) = \psi_{\text{out}}(\Omega) - \psi_{\text{out}}(\Omega_0), \quad (4.15)$$

where  $\psi_{\text{out}}$  is the diffraction angle of the pulse.

The plane of optimum compression orientation for diffraction at a single grating is obtained from eq. (4.14) using eq. (4.1),  $\psi_{\text{out},1} = \arcsin(-n_1 2\pi c/\Omega + \sin \psi_{\text{in},1})$ ,

$$\alpha_{\text{poc},1} = -\psi_{\text{out},1}. \quad (4.16)$$

For diffraction of an initially angular dispersion free pulse the plane of optimum compression is always aligned parallel to the grating surface independent of grating incidence angle or other laser parameters. This is a reasonable result since the grating plane is the last location where a diffracted pulse is dispersion free if it was before the diffraction.

However, the location of the plane of optimum compression is not fixed. Its position in the laser beam path can be controlled and relocated to the interaction point by positive group-delay dispersion. This is again a precompensation of negative group-delay dispersion introduced by angular dispersion from the grating and subsequent propagation equal to the precompensation introduced in the simple TWTS setup of the last section.

With the relations for orientation of plane of optimum compression and pulse-front tilt angle, (4.16) and (4.2) respectively, the grating incidence angle required to properly align plane of optimum compression and pulse-front tilt in a single grating TWTS setup can be determined. Recasting eq. (4.2) into

$$\sin \psi_{in,1} = \cos \psi_{out,1} \tan \alpha_{tilt,1} + \sin \psi_{out,1} .$$

and using relations (4.11) and (4.16) yields the result

$$|\psi_{in,1}| = 90^\circ , \quad (4.17)$$

which is independent of the scattering geometry. The conclusion is, a TWTS setup with second order dispersion compensation during interaction cannot be realized with a single grating setup. Rather a two grating setup is required.

#### 4.4.2. TWO GRATING SETUPS TO CONTROL ORIENTATION OF PULSE-FRONT TILT AND PLANE OF OPTIMUM COMPRESSION INDEPENDENT OF EACH OTHER

The amount of parameters in a setup of two gratings grants freedom in the choice of gratings and the corresponding incidence angles. The two grating setup thereby not only solves the above problem of unrealistic incidence angles, it also solves the problem of low diffraction efficiencies encountered in the simple setup.

In the following setup, (holographically recorded) gratings with high line densities can be used allowing for diffraction efficiencies well beyond 50%<sup>1</sup> [128]. High line densities permit diffraction only into the first order such that no energy is lost to other orders. Additionally, choosing incidence angles close to the Littrow angle, i.e. the incidence angle where the diffracted pulse is exactly counterpropagating to the incident pulse, yields optimum diffraction efficiencies.

Figure 4.4 shows the setup. Two gratings face each other, as in a laser compressor, such that the incoming pulse is first diffracted at one grating and then directly propagates to the second where it is diffracted again. In contrast to a laser compressor, the second grating will have a different line density  $n_2$  than the first one  $n_1$ , which mainly allows to control pulse-front tilt, and it will not be aligned in parallel to the first grating but instead have a small angle of rotation  $\epsilon$  out of parallel orientation which mainly allows to control the plane of optimum compression orientation. After diffraction at the second grating and redirection by a plane mirror the pulse is focused onto the electron trajectory with a cylindrical mirror as in the simple setup.

High line density gratings in this setup introduce large angular dispersion at every diffraction. Several possibilities exist for their interoperation and which one to choose depends largely on the target pulse-front tilt angle. When aiming for large pulse-front tilts close to 90° both gratings could in principle share the work and generate a fraction of the target tilt angle. When aiming for small tilt angles, the comparatively large tilt angle from the first grating could be either almost removed completely at the second grating or even overcompensated.

Figure 4.5 shows the scaling of pulse-front tilt angle, plane of optimum compression angle and condition (4.12) for a proper TWTS setup in dependence of second grating rotation angle  $\epsilon$  for several combinations of gratings. The left column corresponds to a setup with line density  $n_1 = 800$  lines per millimeter (l/mm) and incidence angle  $\psi_{in,1} = 18^\circ$  at the first grating, where  $\psi_{in,1}$  is close to its Littrow angle of 24.46° for a laser wavelength of 1035 nm. Three scalings are shown per variable of interest where each scaling corresponds to a different line density of the second grating with values of  $n_2[\text{l/mm}] \in [1000, 1200, 1400]$ . The parameters of the second

<sup>1</sup>The gratings bought from Plymouth Grating Laboratory, Inc. for the compressor of the Penelope laser system at HZDR actually have a diffraction efficiency > 95%.

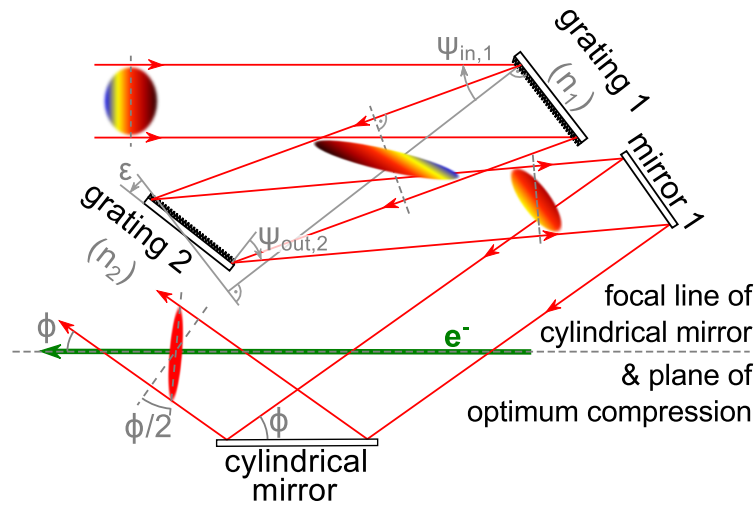


Figure 4.4.: Setup of optical components for TWTS utilizing pulses with local second order dispersion compensation. A laser pulse with positive group-delay dispersion enters the setup and is incident on the first diffraction grating under the angle  $\psi_{in,1}$ . Diffraction at the first grating introduces angular dispersion which tilts the laser pulse-front and ensures laser pulse compression until the interaction region. The second grating is used to align the plane of optimum compression with the electron trajectory for local dispersion compensation during interaction. Thereto the second grating is not aligned parallel to the first grating but rotated by an angle  $\epsilon$  with respect to the plane of the first grating. The pulse leaves the second grating under the angle  $\psi_{out,2}$  towards the first mirror which simply redirects the beam to the cylindrical mirror. This focuses the pulse in the plane perpendicular to the interaction plane, which is spanned by laser and electron propagation directions, on the electron trajectory for optimum overlap of electrons and laser pulse. (Originally in [KS4])

column differ from those of the first only by the choice of first grating parameters. The second column setups have  $n_1 = 1600$  l/mm and  $\psi_{in,1} = 61^\circ$  which is again close to its Littrow angle of  $55.89^\circ$ .

The scaling shows on one hand that the accessible range of pulse-front tilt angles is smaller with a large line density at the first grating. On the other hand, these kind of setups have a larger range in plane of optimum compression angles, although this means at the same time that these setups are more sensitive to misalignment. Due to the large range in plane of optimum compression orientation with  $n_2 > n_1$  more possible configurations for TWTS setups are found within the chosen ranges of parameters.

The choice of a grating pair for a target TWTS scenario is guided by the requirements of correct orientation of pulse-front tilt and plane of optimum compression as well as high diffraction efficiency. Within the range of possible grating pairs for one target scenario, gratings with small line densities reduce laser pulse distortions originating from spatial dispersion which is generated during propagation between the gratings. With higher line densities angular dispersion is larger after diffraction at the first grating and thus more spatial dispersion is generated during propagation to the second grating.

This can be used to precompensate the spatial dispersion which is generated during propagation from the second grating to the interaction point, since angular dispersion after first and second grating can be different in sign.

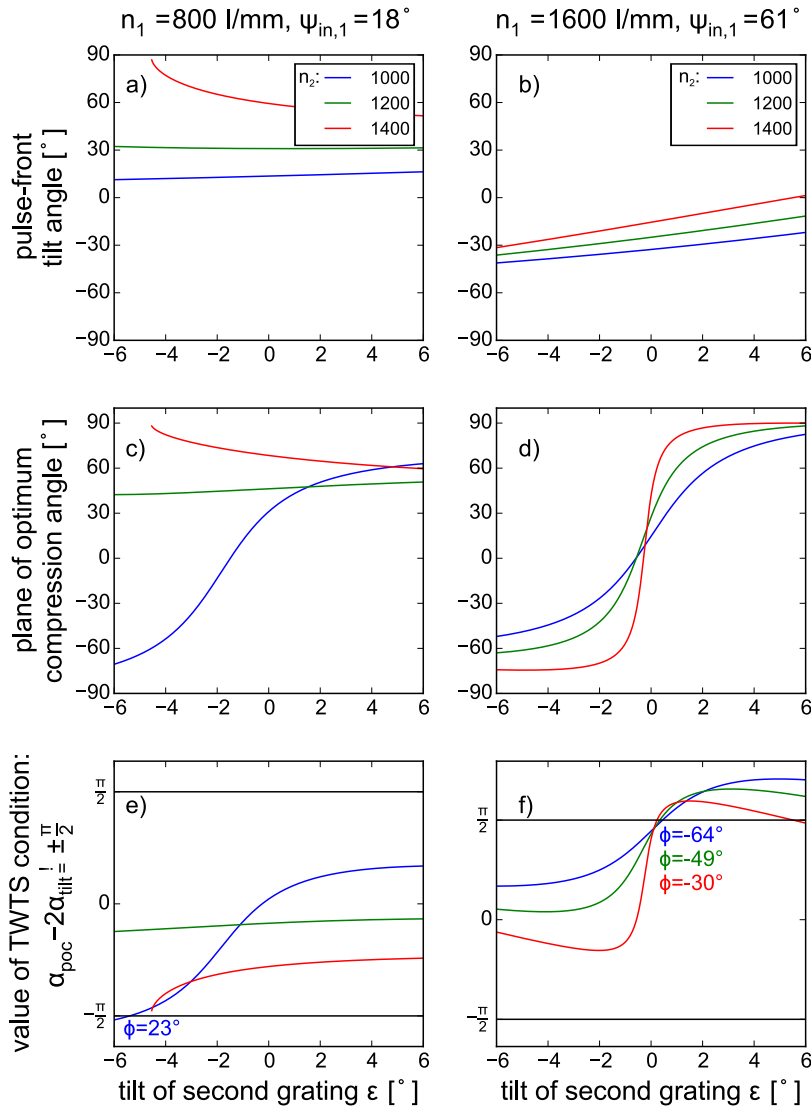


Figure 4.5.: Scaling of pulse-front tilt angle  $\alpha_{tilt}$ , plane of optimum compression  $\alpha_{poc}$  and condition (4.12) for their correct alignment in a TWTS geometry  $\alpha_{poc} - 2\alpha_{tilt} = \pm\pi/2$  in dependence of second grating rotation angle  $\epsilon$ . In the left column the first gratings line density is  $n_1 = 800$  l/mm and the incidence angle is  $\psi_{in,1} = 18^\circ$  while in the right column the first gratings line density is  $n_1 = 1600$  l/mm and the incidence angle is  $\psi_{in,1} = 61^\circ$ . Both incidence angles are chosen close to the Littrow angles for optimum diffraction efficiency. The scalings are shown for three different line densities of the second grating  $n_2 = 1000$  l/mm,  $1200$  l/mm and  $1400$  l/mm. For all  $\epsilon$  providing correct alignment of pulse-front tilt and plane of optimum compression the corresponding interaction angle  $\phi$  is printed. TWTS setups seem to be easier found with higher line density at the first grating but these have the drawback of generating more spatial dispersion and being more sensitive to misalignment. (Originally in [KS4])

### 4.4.3. OBTAINING PARAMETERS FOR THE SETUP

Four parameters determine the final orientation of pulse-front tilt and plane of optimum compression: Angle of incidence at the first grating  $\psi_{in,1}$ , second grating rotation angle  $\epsilon$  as well as first and second grating line densities,  $n_1$  and  $n_2$  respectively. These four parameters set the outgoing angle from the second grating  $\psi_{out,2}(\Omega)$  and thereby the angular difference in propagation direction between frequencies

$$\theta(\Omega) = \psi_{out,2}(\Omega) - \psi_{out,2}(\Omega_0),$$

which is related to the orientations by eq. (4.14). In order to obtain these, derivatives of  $\theta$  and thus the outgoing angle from the second grating must be known. These depend on second grating incidence angle  $\psi_{in,2}$  which depends on first grating outgoing angle  $\psi_{out,1}$  and second grating rotation angle  $\epsilon$

$$\psi_{in,2}(\Omega) = \epsilon - \psi_{out,1}(\Omega),$$

leading in total to the following system of equations defining pulse-front tilt and plane of optimum compression orientation

$$\begin{aligned} \tan \alpha_{\text{tilt}} &= \Omega_0 \theta', \\ \tan \alpha_{\text{poc}} &= -\frac{2\theta' + \Omega_0 \theta''}{\Omega_0 \theta'^2}, \\ \text{with } \theta' &= \left. \frac{d\theta}{d\Omega} \right|_{\Omega=\Omega_0} = \left. \frac{d}{d\Omega} \arcsin [\sin \psi_{out,2}(\Omega)] \right|_{\Omega=\Omega_0} \\ \text{where } \sin \psi_{out,2}(\Omega) &= -n_2 \frac{2\pi c}{\Omega} + \sin(\epsilon - \psi_{out,1}(\Omega)), \\ \sin \psi_{out,1}(\Omega) &= -n_1 \frac{2\pi c}{\Omega} + \sin \psi_{in,1} \end{aligned} \quad (4.18)$$

assuming diffraction into  $-1$ st order at first and second grating. The analytical solution to this system is

$$\begin{aligned} \tan \alpha_{\text{tilt},2} &= \frac{\sin(\epsilon - \psi_{out,1}) - \sin \psi_{out,2}}{\cos \psi_{out,2}} - \frac{\cos(\epsilon - \psi_{out,1})}{\cos \psi_{out,2}} \tan \alpha_{\text{tilt},1}, \\ \tan \alpha_{\text{poc},2} &= -\tan \psi_{out,2} + \frac{[\sin(\epsilon - \psi_{out,1}) + \cos(\epsilon - \psi_{out,1}) \tan \psi_{out,1}] \tan^2 \alpha_{\text{tilt},1}}{\cos \psi_{out,2} \tan^2 \alpha_{\text{tilt},2}}, \end{aligned} \quad (4.19)$$

where the first term of the relation for  $\tan \alpha_{\text{tilt},2}$  is the pulse-front tilt angle which would be generated by the second grating if the incoming pulse would not have a pulse-front tilt of  $\alpha_{\text{tilt},1}$  from the first grating. The second term in this relation thus characterizes the change in pulse-front tilt due to diffraction of an incident pulse carrying angular dispersion. The same holds for the change in plane of optimum compression orientation which is shifted from its undisturbed value by preexisting angular dispersion.

The following details the process of determining a parameter set for TWTS where a laser system with central frequency  $\Omega_0$  is assumed to be given. There are two common starting points. First, the interaction angle is not yet fixed and the gratings are supposed to be bought from stock of some company to minimize the cost of the setup. Second, a light source is designed to radiate at a specific wavelength with given electron energy such that the interaction angle is preset.

In the first case of given grating line densities ( $n_1, n_2$ ) the TWTS condition (4.12) for correct orientation of pulse-front and plane of optimum compression can be evaluated in dependence

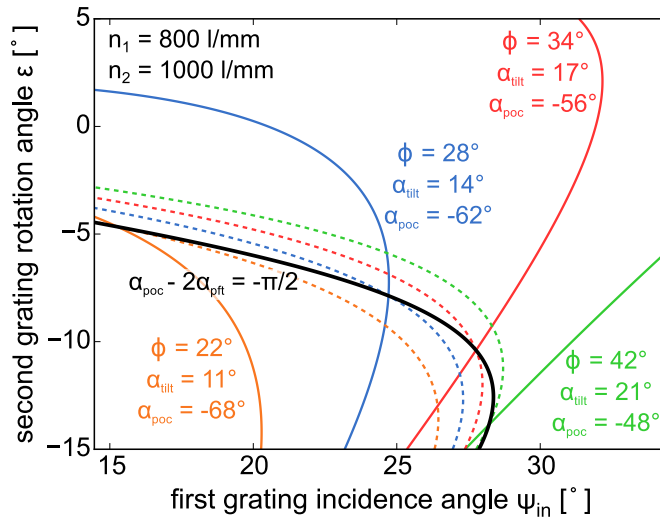


Figure 4.6.: Determining combinations of first grating incidence angle  $\psi_{in,1}$  and second grating rotation angle  $\epsilon$  yielding a TWTS setup with correct alignment of pulse-front tilt  $\alpha_{\text{tilt}}$  and plane of optimum compression  $\alpha_{\text{poc}}$  when the grating pair is preset. The laser wavelength is  $\lambda_{\text{Laser}} = 1035 \text{ nm}$ . Along solid colored lines  $\alpha_{\text{tilt}}$  is constant and along dashed colored lines  $\alpha_{\text{poc}}$  is constant. The coordinates of a crossing of dashed and solid lines of the same color yield a proper TWTS setup. All possible pairs  $(\psi_{in,1}, \epsilon)$  for proper TWTS setups are connected by the black line. (Originally in [KS4])

of first grating incidence angle  $\psi_{in,1}$  and second grating rotation angle  $\epsilon$ . This can be done graphically, as shown in fig. 4.6, by plotting contour lines of the function  $\alpha_{\text{poc}} - 2\alpha_{\text{pft}}$  at  $\pm\pi/2$  (black) which depends only on  $(\psi_{in,1}, \epsilon)$  for given  $(n_1, n_2)$ .

This example assumes a central laser wavelength of 1035 nm and the available gratings have line densities of 800 l/mm as well as 1000 l/mm. Setups using the 1000 l/mm grating as the first are not useful for TWTS since these do not allow to correctly align plane of optimum compression and pulse-front. Setups using the 800 l/mm grating as the first yield correct orientations over a wide range of first grating incidence angles and second grating rotation angles allowing for variability in the experimental setup despite the choice for a particular grating pair. This variability could be used to keep the grating incidence angles of both gratings close to the respective Littrow angles for high diffraction efficiencies, or to choose angles which permit diffraction solely into first order or to accommodate the setup in a lab with restrictions on the beam path. On the other hand, having a dedicated light source setup in mind, this variability can be used to tune its radiation wavelength by varying the interaction angle without the need of buying new gratings.

In the second case of given interaction angle  $\phi$  and thus given pulse-front tilt  $\phi/2$  as well as plane of optimum compression  $\phi \pm \pi/2$ , the analytical solutions (4.19) allow to calculate two of the four parameters  $(\psi_{in,1}, \epsilon, n_1, n_2)$  if the remaining two are given. For example, one can choose the first grating of the setup setting its line density  $n_1$  and incidence angle  $\psi_{in,1}$  and then calculate second grating incidence angle  $\psi_{in,2} = \epsilon - \psi_{out,1}$  and line density  $n_2$  to ensure correct  $\alpha_{\text{tilt}}$  and  $\alpha_{\text{poc}}$ . If, for example, the incidence angle on the second grating is far from its Littrow angle, one could tune the incidence angle at the first grating around its Littrow angle in order to optimize second grating parameters.

To follow this procedure, the above analytic solutions for pulse-front tilt and plane of optimum compression angle are transformed into a system of equations for the parameters  $s_i = s_i(s_o, \psi_{in,1}, n_1, \phi) = \sin(\epsilon - \psi_{out,1})$  and  $s_o = s_o(s_i, \psi_{in,1}, n_1, \phi) = \sin \psi_{out,2}$ . The first equation for  $s_i$  is obtained by rearranging (4.19) into equations for  $\sin \psi_{in,2} - \cos \psi_{in,2} \tan \alpha_{\text{tilt},1}$  and  $\sin \psi_{in,2} +$

$\cos \psi_{in,2} \tan \psi_{out,1}$ , respectively, then multiplying the first equation by  $\tan \psi_{out,1}$  as well as the second by  $\tan \alpha_{tilt,1}$  and afterwards adding the two equations. In a similar manner the equation for  $s_o$  is obtained.

$$s_i = \frac{\frac{\tan^2(\phi/2)}{\tan \alpha_{tilt,1}} \left( s_o - \sqrt{1 - s_o^2} \cot \phi \right) + \left( s_o + \sqrt{1 - s_o^2} \tan(\phi/2) \right) \tan \psi_{out,1}}{\tan \alpha_{tilt,1} + \tan \psi_{out,1}} \quad (4.20)$$

$$s_o = \frac{\frac{\tan^2 \alpha_{tilt,1}}{\tan(\phi/2)} \left( s_i + \sqrt{1 - s_i^2} \tan \psi_{out,1} \right) + \left( s_i - \sqrt{1 - s_i^2} \tan \alpha_{tilt,1} \right) \cot \phi}{\tan(\phi/2) + \cot \phi}$$

Outgoing angle  $\psi_{out,1}$  and pulse-front tilt angle  $\alpha_{tilt,1}$  after the first grating are given in terms of  $(\psi_{in,1}, n_1)$  by eqs. (4.1) and (4.2) respectively. The sought-for parameters of the second grating  $(\psi_{in,2}, n_2)$  are obtained from this set of equations by inserting, for example,  $s_o$  into the relation for  $s_i$  and solving the resulting implicit function. The obtained solution  $s_{i,sol}$  is related to second grating incidence angle by

$$\psi_{in,2} = \epsilon - \psi_{out,1} = \arcsin s_{i,sol}.$$

This solution is further used to calculate  $s_{o,sol} = s_o(s_{i,sol}, \psi_{in,1}, n_1, \phi)$  which is related to second grating line density by

$$n_2 = \frac{s_{o,sol} - s_{i,sol}}{\lambda_{Laser} m_2}, \quad (4.21)$$

where  $m_2$  is the order of diffraction at the second grating and is given by the sign of  $s_{o,sol} - s_{i,sol}$ , such that  $n_2 > 0$ .

This second procedure of determining optical setup parameters will be used when setups for TWTS OFELs are designed. In their realization the interaction angle as well as electron energy are determined from a trade-off between electron bunch and laser pulse quality requirements. Thus parameters of optical components and setup are chosen to accommodate the requirements of TWTS OFEL operation. However, there may be situations where TWTS OFEL parameter sets with fair electron and laser requirements require too much space which necessitates a redesign in order to achieve more compact optical setups at possibly increased electron and laser requirements.

#### 4.4.4. VARIATIONS IN UNDULATOR FREQUENCY AND AMPLITUDE FROM MISALIGNMENTS IN THE SETUP

Although the above presented setup utilizing the plane of optimum compression can provide perturbing dispersion free pulses during the interaction, variations in undulator frequency and amplitude can still occur when the plane of optimum compression or pulse-front tilt is not ideally aligned. A deviation from optimum alignment is caused by a misalignment of both the grating setup  $(\Delta\psi_{in,1}, \Delta\epsilon)$  as well as laser and electron beam pointing  $(\Delta\phi)$ . In the following undulator frequency and laser irradiance variation for misaligned setups are derived. Since these variations increase the bandwidth of scattered radiation, knowing their amplitude is important for building both incoherent sources with a target bandwidth and TWTS OFELs where radiation has to be emitted within the gain bandwidth.

Obtaining relations for undulator frequency and laser irradiance variation starts by deriving a description of the electric field of a TWTS pulse with local dispersion compensation in time domain and evaluating it along the electron trajectory. The phase of this pulse in Fourier space has already been derived in eq. (4.13). Its electric field in time domain is obtained from a Fourier

transform

$$\begin{aligned}
E(z, y, t) &= \frac{1}{2\pi} \int d\Omega e^{i\Omega t} \hat{E}_0 e^{-(\Omega-\Omega_0)^2 \tau_0^2/4} e^{-i\phi(\Omega)} \\
&= \frac{E_0}{[1+D^2]^{1/4}} e^{-L^2/(1+D^2)} e^{i\frac{\Omega_0}{c}(ct-z)} e^{-i\frac{1}{2} \arctan D} e^{iDL^2/(1+D^2)}, \quad (4.22)
\end{aligned}$$

where

$$D = \frac{2(y \tan \alpha_{\text{poc}} - z) \tan^2 \alpha_{\text{tilt}}}{\Omega_0 c \tau_0^2}, \quad L = \frac{ct - z + y \tan \alpha_{\text{tilt}}}{c \tau_0}. \quad (4.23)$$

In this representation,  $D$  is a measure for the impact of dispersion while  $L$  measures electron and laser pulse overlap.

With optimum alignment both  $D$  and  $L$  vanish during the entire interaction along the electron beam axis and the field becomes a plane wave during the entire interaction. For off-axis electrons  $D$  and  $L$  have nonzero values even for optimum alignment resulting in a varying undulator amplitude and frequency over the electron bunch.

Limits on electron beam and laser pulse parameters ensuring only negligibly small variation in undulator frequency and amplitude for optimum alignment are derived by inserting the electron trajectory

$$z_{\text{el}} = (ct + u) \cos \phi + v \sin \phi \quad y_{\text{el}} = -(ct + u) \sin \phi + v \cos \phi, \quad (4.24)$$

into  $D$  and  $L$ , where  $u$  and  $v$  are a longitudinal and horizontal offset of a single electron from the bunch center, respectively. From  $L$  a condition ensuring simply geometrical overlap of electrons and laser pulse is obtained by inserting the electron pulse duration  $\tau_b$  and rms cross-sectional radius  $\sigma_b$  as maximum values for  $|u|$  and  $|v|$ , respectively,

$$\frac{c\tau_b + \sigma_b \tan(\phi/2)}{c\tau_0} \ll 1. \quad (4.25)$$

From  $D$  a condition ensuring negligibly small dispersion is obtained

$$\frac{\lambda_{\text{Laser}} \tan^2(\phi/2)}{\pi c^2 \tau_0^2 \sin \phi} \sigma_b \ll 1 \quad (4.26)$$

If this condition is fulfilled, the phase of the optical undulator will be equal to a plane wave over the electron bunch during the entire interaction. This is an important condition for the realization of TWTS OFELs since phase variations are usually tolerable only in the per mille range whereas amplitude variations of a few percent are acceptable.

Assuming these requirements are fulfilled, variations in laser irradiance  $I$  and undulator frequency  $\tilde{\Omega}$  arising from misalignment can be attributed to nonzero values of the dispersion and overlap term at the electron position at the end of interaction,  $\Delta D$  and  $\Delta L$  respectively, as well as the time derivative of the dispersion term  $\Delta \dot{D}$ ,

$$\boxed{
\begin{aligned}
\left| \frac{\Delta I}{I} \right| &= \frac{1}{2} \Delta D^2 + 2 \Delta L^2, \\
\left| \frac{\Delta \tilde{\Omega}}{\tilde{\Omega}} \right| &= \frac{\lambda_{\text{Laser}}}{4\pi c(1 - \cos \phi)} \Delta \dot{D}.
\end{aligned}
} \quad (4.27)$$

These are related to misalignments in pulse-front tilt  $\Delta \tan \alpha_{\text{tilt}}$ , plane of optimum compression  $\Delta \tan \alpha_{\text{poc}}$  and interaction angle  $\Delta \phi$  by

$$\begin{aligned} \Delta D &= \frac{\lambda_{\text{Laser}}}{\pi c^2 \tau_0^2} \left\{ \left[ -\frac{L_{\text{int}}}{2} \sin \phi + \sigma_b \cos \phi \right] \tan^2(\phi/2) \Delta \tan \alpha_{\text{poc}} - \right. \\ &\quad \left. - 2\sigma_b \frac{\tan(\phi/2)}{\sin \phi} \Delta \tan \alpha_{\text{tilt}} + \tan^2(\phi/2) \frac{L_{\text{int}}}{2 \sin \phi} \Delta \phi \right\} \\ \Delta L &= \frac{1}{c\tau_0} \left[ \left( \frac{L_{\text{int}}}{2} \sin \phi - \sigma_b \cos \phi \right) \Delta \tan \alpha_{\text{tilt}} - \left( \frac{L_{\text{int}}}{2} \tan(\phi/2) - \sigma_b \right) \Delta \phi \right], \\ \Delta \dot{D} &= \frac{\lambda_{\text{Laser}} \tan^2(\phi/2)}{\pi c \tau_0^2} \left( \frac{\Delta \phi}{\sin \phi} - \sin \phi \Delta \tan \alpha_{\text{poc}} \right). \end{aligned} \quad (4.28)$$

All of these relations are obtained by error propagation.

Alignment errors of pulse-front tilt and plane of optimum compression due to misaligned gratings ( $\Delta \psi_{\text{in},1}$ ,  $\Delta \epsilon$ ) are found by numerically evaluating the system of eqs. (4.18). Then a variation of laser irradiance and undulator frequency until the end of interaction can be calculated with (4.27) by first varying e.g.  $\psi_{\text{in},1}$  from its working point, then calculating the corresponding change in  $\tan \alpha_{\text{tilt}}$ ,  $\tan \alpha_{\text{poc}}$  and  $\phi$  (given by the change in outgoing angle at the second grating) with (4.18) and third inserting these in (4.28). When the maximum acceptable variation in  $I$  and  $\tilde{\Omega}$  is reached, the maximum allowed variation  $\Delta \psi_{\text{in},1}$  is known. This procedure is repeated for  $\epsilon$  in order to find  $\Delta \epsilon$  and can be repeated for other setup parameters as well to determine their acceptable variation.

The values ( $\Delta \psi_{\text{in},1}$ ,  $\Delta \epsilon$ ) obtained by this procedure give an estimate for the required grating alignment tolerance when building incoherent sources and TWTS OFELs with this method. These estimates are very important since they allow to evaluate the realizability of a TWTS setup before actually building it and furthermore already point out which parts of a realization are more delicate than others.

## 4.5. TWTS SETUPS WITH FULL DISPERSION COMPENSATION DURING INTERACTION AND WITH FOCUSING IN THE INTERACTION PLANE

So far two methods for the generation of laser pulses for TWTS have been presented. One without dispersion compensation and one with full dispersion compensation during interaction but without focusing in the interaction plane spanned by laser and electron bunch propagation directions.

Yet focusing in the interaction plane can be vital for TWTS OFELs utilizing petawatt class lasers. In order to avoid damage on optics the energy in a petawatt pulse needs to be spread out over a large area. Typical petawatt pulses have diameters on the order of 20 cm to 25 cm during transport from the laser system to the experimental area to ensure an areal energy-density on the order of or lower than  $0.5 \text{ J cm}^{-2}$  which is a typical damage threshold of optical elements [129, ch. 5.6]. Without focusing reachable undulator amplitudes  $a_0$  are comparatively low to what can be reached with focusing. Taking for example the Penelope laser system planned at HZDR with design values of  $1.035 \mu\text{m}$  wavelength, 150 J energy, 25 cm beam diameter and 120 fs pulse duration [104], the undulator parameter reaches  $a_0 = 0.14$  when focusing the pulse in the vertical direction to 25  $\mu\text{m}$  diameter and leaving it unfocused in the interaction plane. The undulator strength in this example can be sufficient for TWTS OFEL operation but depending on the scenario a four- to fivefold increase can be required as well.

In situations requiring only a small increase in undulator strength focusing may not be necessary when the beams transverse profile is transformed before the grating setup. Forming with

a telescope to an unequal ratio of horizontal to vertical width while at the same time keeping the beam cross sectional area constant reduces the beam width in the interaction plane but also requires larger optics in the vertical plane. Available size of optics is the limiting factor of this approach. Aiming at an increase of undulator strength by a factor of two already requires a factor of four decrease in horizontal width, due to scaling of the undulator parameter with the square root of laser irradiance, and is attended by a factor of four increase in vertical width. For an originally round beam of 25 cm diameter this results in 1 m vertical diameter.

Focusing in the interaction plane can be implemented in the setup providing full dispersion compensation, which was presented in the last section. But focusing of a laser pulse with defined angular dispersion changes its angular dispersion since the deflection angle of a ray incident on a focusing mirror depends on its incidence location and incidence angle. Thus, neither pulse-front tilt nor plane of optimum compression keep their orientation after a focusing mirror.

Therefore, a novel method for the generation of laser pulses for TWTS OFELs including focusing in the interaction plane is presented in the following. It directly incorporates and makes use of the focusing mirror for pulse-front tilt generation. It further makes use of an out-of-focus interaction geometry, where the interaction point is not in the focus of the focusing mirror, in order to reduce the focusing distance of beams with centimeter scale diameters as used for TWTS OFELs. This technique is very important to keep TWTS OFELs compact since the focusing distances of these centimeter beams can be on the kilometer scale due to their 100 m scale Rayleigh length.

#### **4.5.1. FOCUSING AND PULSE-FRONT TILT GENERATION WITH AN OFF-AXIS CYLINDRICAL MIRROR**

A cylindrical mirror with a parabolic surface provides focusing in the interaction plane. It can also be used to introduce the required pulse-front tilt for TWTS [130, 131], if the cylindrical mirror is an off-axis focusing mirror and the laser pulse is spatially dispersed prior to focusing. Then  $SD$  transforms to angular dispersion, i. e. pulse-front tilt, during deflection at the mirror surface, since a frequencies deflection angle depends on its incidence position on the parabolically shaped mirror surface, see fig. 4.7a. During propagation from the mirror to the focus spatial dispersion reduces and in the focus spatial dispersion is fully removed while pulse-front tilt is present.

Figure 4.8 depicts a setup which makes use of this technique to generate laser pulses for TWTS OFELs. The setup consists of a grating pair to generate spatial dispersion which is transformed to angular dispersion and hence pulse-front tilt at the off-axis cylindrical mirror.

Furthermore, the setup makes use of an out-of focus interaction geometry where the interaction point is a distance  $\Delta f$  before the actual focus of the off-axis cylinder. This allows to reduce the laser propagation distance resulting in more compact setups compared to in-focus interaction geometries. With the interaction point lying between the focusing mirror and its focal line in the out-of-focus geometry the laser pulse can be focused stronger, i.e. it can be focused to a smaller focal width compared to an in-focus interaction geometry, which results in a shorter Rayleigh length, thus in a shorter focal distance and shorter laser propagation distance compared to an in-focus interaction geometry.

An interaction before the focus requires to compensate spatial dispersion before the focus, too. This is achieved by focusing a pulse that already features angular dispersion. Angular dispersion of the incident pulse changes the deflection angle at the off-axis cylinder for every frequency individually allowing to control the propagation distance after which the frequencies spatially overlap independent of the focusing distance, see fig. 4.7b. The incident pulse-front tilt is again introduced by rotation of the second grating away from parallel orientation to the first grating by an angle  $\epsilon$ .

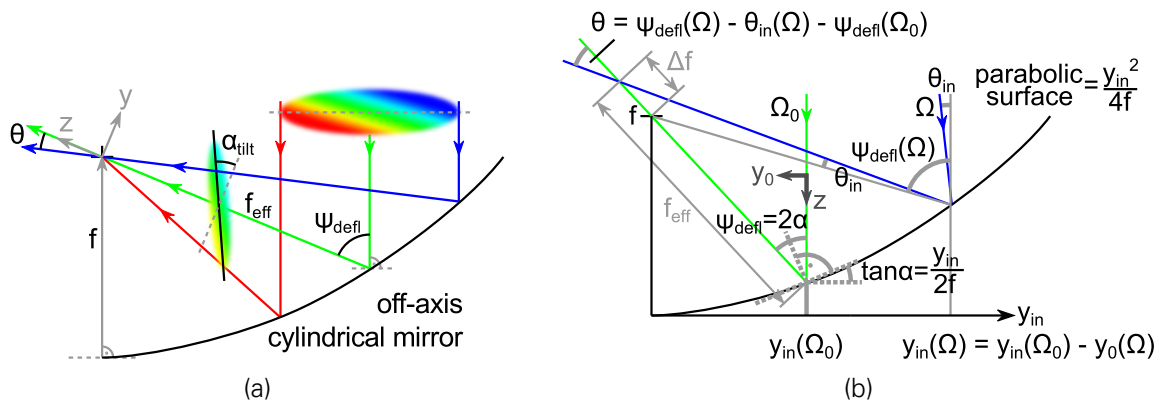


Figure 4.7.: (a) Transforming spatial dispersion to angular dispersion at an off-axis focusing mirror. Depending on the incidence position of a ray of frequency  $\Omega$  at the mirror surface, it is deflected by the unique angle  $\psi_{defl}(\Omega)$ . Angular dispersion is given by the difference in deflection angles  $\theta(\Omega) = \psi_{defl}(\Omega) - \psi_{defl}(\Omega_0)$  and introduces a pulse-front tilt  $\alpha_{tilt}$ . Spatial dispersion vanishes in the focus of the mirror. Depending on the deflection angle, a frequency has to travel the effective focal distance  $f_{eff} = f / \cos^2(\psi_{defl}(\Omega)/2)$  (b) Shifting the position where spatial dispersion vanishes by focusing laser pulses with angular dispersion. Then a frequencies deflection angle does not only depend on incidence position but further on  $\theta_{in}(\Omega)$  such that pulse-front tilt is determined by incident angular dispersion and deflection angle  $\theta(\Omega) = \psi_{defl}(\Omega) - \psi_{defl}(\Omega_0) - \theta_{in}(\Omega)$ . The deflection angle  $\psi_{defl}(\Omega)$  is twice the angle  $\alpha(\Omega)$  enclosed by a frequencies incident propagation direction and the mirror surface normal. The incidence position  $y_{in}(\Omega)$  of a frequency depends on its horizontal offset  $y_0(\Omega)$  from the central laser frequency  $y_{in}(\Omega) = y_{in}(\Omega_0) - y_0(\Omega)$ . (Originally in [KS4])

Although this setup looks very similar to the setup without focusing in the interaction plane, its working principle greatly differs. While the other setup used the second grating to ensure correct alignment of plane of optimum compression and pulse-front tilt directly, this setup uses the second grating to remove almost all of angular dispersion from the first grating but leaving only a small residual pulse-front tilt to ensure vanishing spatial dispersion as well as correct orientation of pulse-front tilt and plane of optimum compression after deflection at the cylindrical mirror at the interaction point. The use of two spatially separated cylindrical focusing mirrors in this setup provides an easy solution to fulfill the differing requirements on laser pulse width in horizontal and vertical direction. Focusing to different transverse widths requires different mirror curvature for each direction as well as different propagation distances after deflection.

#### 4.5.2. REALIZATION AND LIMITS OF THE OUT-OF-FOCUS INTERACTION GEOMETRY

The following explains the details of the out of focusing geometry and answers questions regarding choice of the focal distance, compensation of spatial dispersion outside the focus as well as orientation of pulse-front tilt and plane of optimum compression.

##### LIMITS ON THE OUT-OF-FOCUS DISTANCE

The out-of-focus distance of this setup cannot be chosen arbitrarily. Far from the focus, the phase-fronts of the laser pulse bend which effectively causes a drift of undulator frequency during the interaction since the distance between two phase fronts varies along the electron trajectory. The larger the phase front curvature is, the larger the drift of undulator frequency is

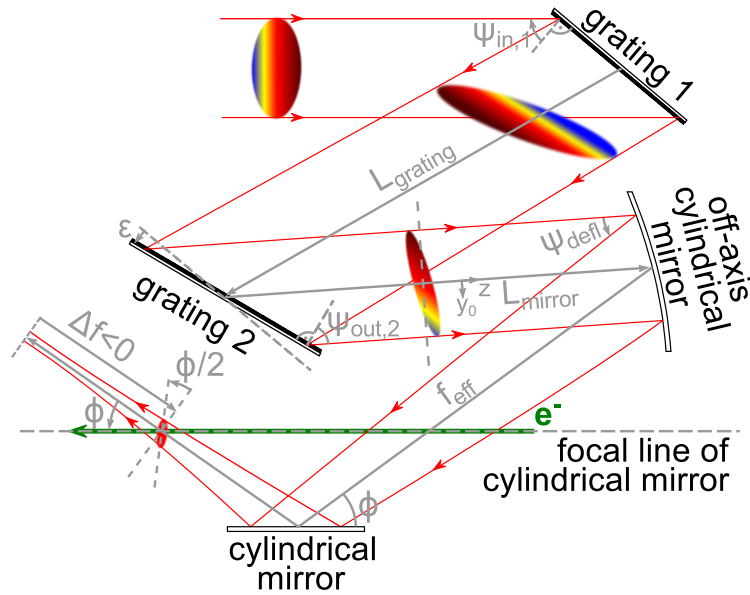


Figure 4.8.: Setup to generate laser pulses for TWTS OFELs in the out-of-focus interaction geometry providing focusing and local dispersion compensation. A laser pulse with positive group-delay dispersion enters a grating pair at an incidence angle  $\psi_{in,1}$  on the first grating. Line densities of first and second grating,  $n_1$  and  $n_2$  respectively, are chosen to produce large angular dispersion at the first grating and almost remove it completely at the second grating. The second grating is rotated by an angle  $\epsilon$  out of parallel orientation to the first grating. During propagation of the pulse about the distance  $L_{grating}$  to the second grating angular dispersion produces spatial dispersion. The horizontal offset of a frequency  $\Omega$  with respect to the central laser frequency  $\Omega_0$  is  $y_0(\Omega)$ . After diffraction at the second grating the pulse leaves the grating pair under the angle  $\psi_{out,2}$  and propagates the distance  $L_{mirror}$  to an off-axis cylindrical mirror at which the laser pulse is focused in the horizontal direction and deflected by the angle  $\psi_{defl}$ . Focusing a spatially dispersed laser pulse at an off-axis cylindrical mirror generates pulse-front tilt. The remaining small angular dispersion after the second grating thereby ensures vanishing spatial dispersion at the interaction point of electrons and laser pulse. The interaction point is a distance  $\Delta f$  before the focus of the off-axis cylindrical mirror with effective focal distance  $f_{eff}$ . During propagation to the interaction point the laser is also focused in the vertical direction by a second cylindrical mirror. Its focal line coincides with the electron trajectory. Electron and laser direction of propagation enclose the interaction angle  $\phi$ . At the interaction point group-delay dispersion of the input pulse is removed due to propagation with angular dispersion starting at the first grating. (Originally in [KS4])

during the interaction. While phase front curvature is largest at a distance of one Rayleigh length from the focus, phase fronts become flatter again farther away from the focus. The radius of phase-front curvature scales as

$$R(\Delta f) = \Delta f \left( 1 + \frac{z_R^2}{\Delta f^2} \right) \sim \Delta f.$$

which suggests that there is a minimum distance  $\Delta f \gg z_R$  from the focus at which the radius of phase front curvature is large enough that the undulator frequency drift is acceptable.

This limit is derived from the electric field (4.5) of the tilted propagating laser pulse by calculat-

ing the difference in instantaneous undulator frequency including phase-front curvature between middle and end of interaction,  $t = 0$  and  $t = t_{\text{end}} = L_{\text{int}}/2\beta c$  respectively,

$$\begin{aligned}\Delta\tilde{\Omega} &= \tilde{\Omega}(t_{\text{end}}) - \tilde{\Omega}(0) = \frac{d}{dt} [\text{Arg } E(\Delta f + c\beta t_{\text{end}} \cos \phi, -c\beta t_{\text{end}} \sin \phi, t_{\text{end}}) - \text{Arg } E(\Delta f, 0, 0)] \\ &\approx -\frac{\Omega_0}{c} \frac{y_{\text{el}}}{R} \dot{y} + \frac{c\dot{z}}{\Omega_0 w^2} - \dot{D} \left( \frac{1}{2} - \frac{l^2}{\tau_0^2} \right) + \Delta\tilde{D} \frac{2li}{\tau_0^2},\end{aligned}$$

where  $\beta \approx 1$  is the mean electron velocity normalized to  $c$  and only group-delay dispersion is taken into account since it has a larger impact on phase distortions than spatial dispersion. Note, as the laser is supposed to arrive at  $z = \Delta f$  at  $t = 0$  its time coordinate in  $l$  needs to be shifted  $t \rightarrow t + \Delta f/c$ . The first of these terms contributing to undulator frequency variation is related to phase-front curvature, the second to the Gouy phase and the third and fourth to group-delay dispersion.

The undulator frequency variation due the additional phase shift from the Gouy phase will be only of interest when laser and electrons are almost copropagating and the laser width is close to the electron beam diameter. Since this will not be the typical TWTS OFEL case where long interaction length and wide laser pulse are used, the laser width is assumed to be larger than the electron beam diameter  $w = L_{\text{int}} \sin \phi > 2\sigma_b$ .

On the basis of the above expression an estimate for total undulator frequency variation relative to  $\tilde{\Omega} = \Omega_0(1 - \beta \cos \phi)$  due to out-of-focus interaction from  $-t_{\text{end}}$  to  $+t_{\text{end}}$  can be obtained by assuming negligibly small dispersion, realized by either using small interaction angles or utilizing the plane of optimum compression, and assuming wide laser pulses with widths larger than the electron bunch diameter  $w = L_{\text{int}} \sin \phi > 2\sigma_b$  in order to achieve long interaction lengths,

$$\frac{\Delta\tilde{\Omega}}{\tilde{\Omega}} = -\frac{L_{\text{int}}}{R(\Delta f)} \frac{\sin^2 \phi}{(1 - \beta \cos \phi)} + \frac{\cos \phi}{4\pi^2 \sin^2 \phi (1 - \beta \cos \phi)} \frac{\lambda_{\text{Laser}}^2}{L_{\text{int}}^2}.$$

With typical interaction distances in the centimeter to meter range the second term corresponding to an undulator frequency shift by the Gouy phase will be small compared to undulator frequency variation from phase-front curvature represented in the first term. Thus, undulator frequency variation can be estimated by

$$\left| \frac{\Delta\tilde{\Omega}}{\tilde{\Omega}} \right| = \frac{L_{\text{int}}}{R(\Delta f)} \frac{\sin^2 \phi}{(1 - \beta \cos \phi)} \lesssim 2\rho, \quad (4.29)$$

where the limit for TWTS OFEL operation given by the Pierce parameter was already introduced in eq. (4.3). From this limit for undulator frequency variation a limit for the out-of-focus distance  $\Delta f$  is obtained by rearranging for a condition on the radius of phase front curvature  $R$  and inserting its definition from above

$$\left| \Delta f \left( 1 + \frac{z_R^2}{\Delta f^2} \right) \right| \gtrsim \frac{L_{\text{int}}}{2\rho} \frac{\sin^2 \phi}{(1 - \beta \cos \phi)}.$$

Since  $(1 + z_R^2/\Delta f^2)$  is always larger than one, a simpler but more stringent requirement can be given

$$\boxed{|\Delta f| \gtrsim \frac{L_{\text{int}}}{2\rho} \frac{\sin^2 \phi}{(1 - \beta \cos \phi)} \approx \frac{\lambda_{\text{Laser}} \sin^2 \phi}{2\rho^2 (1 - \beta \cos \phi)^2} = \frac{L_{\text{int}}^2 \sin^2 \phi}{2\lambda_{\text{Laser}}},} \quad (4.30)$$

which is used when determining the parameters of an out-of-focus geometry. The last two relations use the approximation of around twenty gain length as the required interaction length until saturation is reached in an FEL  $L_{\text{int}} \approx \lambda_{\text{Laser}}/(1 - \beta \cos \phi)\rho$ .

This is only a requirement on the minimum value of  $\Delta f$ , of course larger values than this minimum can be chosen. But these do not necessarily yield more compact setups. Large  $\Delta f$  may require large focal beam widths since these pulses converge slower which may be necessary to reach the target pulse width at  $\Delta f$  away from the focus. Generally, the most compact setups use the minimum value of  $\Delta f$  since reaching the target beam width as close as possible to the actual focus requires a large beam divergence and thus small focal width corresponding to small focal distances. A condition on  $\Delta f$  for compact TWTS OFEL setups is obtained by comparing the ratio of laser focal width  $w_0$  to target beam width  $w$  and using the relation  $w \approx w_0 z/z_R$  for laser beam width increase during propagation

$$\begin{aligned} \frac{w_0}{w} &= \frac{\lambda_{\text{laser}} \Delta f}{\pi w^2} \ll 1 \\ \Rightarrow |\Delta f| &\ll \frac{\pi L_{\text{int}}^2 \sin^2 \phi}{\lambda_{\text{Laser}}}. \end{aligned} \quad (4.31)$$

Using the above relation for the smallest out-of-focus distance the best achievable ratio of focal to target beam width due to the limit on acceptable undulator frequency variation from phase front curvature is  $w_0/w = 1/2\pi$ . Since the same factor is saved in focal distance of the laser pulse, a TWTS OFEL setup becomes more than six times smaller by utilizing the out-of-focus interaction. Actually, out-of-focus interaction geometries can become even more compact when laser systems providing more laser power than required for a specific TWTS OFEL are available. If more laser power is available, the laser pulse width at the interaction point can be larger than the minimum pulse width required to provide the interaction distance which would allow to use stronger focusing pulses. Thus, an excess of laser pulse power allows to use a focusing mirror with shorter focal distance.

## FOCUSING DISTANCE OF THE OFF-AXIS CYLINDRICAL MIRROR

There are two focusing distances related to off-axis focusing elements, namely parent focal distance  $f$  and effective focal distance  $f_{\text{eff}}$ . The latter is the true propagation distance of a beam from a focusing element to its focus. The parent focal distance  $f$  corresponds to the focal distance of an on-axis focusing element where the propagation directions of incident and outgoing ray of the central laser frequency are collinear. Effective and parent focal distance are related by

$$f_{\text{eff}} = \frac{f}{\cos^2(\psi_{\text{defl}}(\Omega_0)/2)},$$

where  $\psi_{\text{defl}}(\Omega_0)$  is the deflection angle of a ray of the central laser frequency which is incident parallel to the mirror axis, cf. fig. 4.7a.

A relation for the required focusing distance  $f_{\text{eff}}$  of the off-axis cylindrical mirror in a TWTS OFEL setup is obtained by rearranging the above relation for  $w_0/w$  for  $w_0$  and inserting it into the scaling of pulse width of a focusing laser

$$D_{\text{in}} w_0 = \lambda_{\text{Laser}} f_{\text{eff}}, \quad (4.32)$$

where  $D_{\text{in}}$  is the laser pulse clear aperture before focusing which encloses 99% percent of the laser pulse power if its transverse envelope is gaussian,

$$f_{\text{eff}} = \frac{D_{\text{in}} |\Delta f|}{\pi n_w L_{\text{int}} \sin \phi} = \frac{D_{\text{in}} \sin \phi}{2\pi n_w (1 - \beta \cos \phi) \rho}. \quad (4.33)$$

The second step uses relation (4.30) for  $|\Delta f|$ . The number  $n_w \geq 1$  thereby allows for larger laser pulse widths at the interaction point than the minimum required to provide the interaction distance

$$w = n_w L_{\text{int}} \sin \phi. \quad (4.34)$$

Thus, shorter focal distances are possible if more laser power than the minimum required for TWTS OFEL operation is available.

With the focal distance of the cylindrical mirror and the out-of-focus distance known, the total laser propagation distance from the mirror to the interaction point is given by

$$\begin{aligned} z_{\text{prop}} &= f_{\text{eff}} + \Delta f \\ &= \left( \frac{D_{\text{in}}}{\pi n_w L_{\text{int}} \sin \phi} - 1 \right) \frac{L_{\text{int}} \sin^2 \phi}{2\rho(1 - \beta \cos \phi)} \end{aligned}$$

where  $\Delta f < 0$  for an interaction before the focus.

### ORIENTATION OF PULSE-FRONT TILT AND PLANE OF OPTIMUM COMPRESSION

Combining spatial and angular dispersion in the pulse incident to the off-axis cylindrical mirror allows to control the deflection angle of every frequency individually. This is used to move the position where spatial dispersion is compensated and all frequencies overlap out of the mirrors focus to the interaction point. The resulting pulse-front tilt and plane of optimum compression orientations also depend on the incident pulse dispersion properties. Analytic expressions for these orientations are derived in the following.

Figure 4.7b shows ray traces for different frequencies contained in an angularly and spatially dispersed laser pulse which is incident to an off-axis focusing mirror with parent focal distance  $f$ . The incidence position  $y_{\text{in}}(\Omega)$  of a frequency  $\Omega$  on the mirror measured on a plane transverse to the laser pulse direction of propagation depends on the offset  $y_0(\Omega)$  of this frequency from the laser pulse axis due to spatial dispersion

$$y_{\text{in}}(\Omega) = y_{\text{in}}(\Omega_0) - y_0(\Omega).$$

Angular dispersion results in an incidence angle difference between frequencies. The deviation from mirror axis parallel incidence is given by  $\theta_{\text{in}}$ . Due to non-parallel incidence the deflection angle of a frequency changes from the parallel incidence deflection angle  $\psi_{\text{defl}}$  by its deviation angle  $\theta_{\text{in}}$

$$\psi_{\text{defl}}(\Omega) \rightarrow \psi_{\text{defl}}(\Omega) - \theta_{\text{in}}(\Omega),$$

where the parallel incidence deflection angle is given by

$$\psi_{\text{defl}}(\Omega) = 2 \arctan \frac{y_{\text{in}}(\Omega)}{2f}.$$

Therefore, frequencies do not overlap in the focus but elsewhere and their propagation direction deviates from the central laser frequencies propagation direction by

$$\theta(\Omega) = \psi_{\text{defl}}(\Omega) - \theta_{\text{in}}(\Omega) - \psi_{\text{defl}}(\Omega_0), \quad (4.35)$$

which determines pulse-front tilt and plane of optimum compression orientations via (4.14). For the setup shown in fig. 4.8 pulse-front tilt and plane of optimum compression orientations at the interaction point depend on the orientations of pulse-front tilt and plane of optimum compression after first and second grating, the laser propagation distances from first to second grating and second grating to off-axis cylindrical mirror, as well as deflection angle and effective focal

distance of the off-axis cylindrical mirror,  $\tan \alpha_{\text{tilt},1}$ ,  $-\tan \psi_{\text{out},1}$ ,  $\tan \alpha_{\text{tilt},2}$ ,  $\tan \alpha_{\text{poc},2}$ ,  $L_{\text{grating}}$ ,  $L_{\text{mirror}}$ ,  $\tan \psi_{\text{defl}}(\Omega_0)$  and  $f_{\text{eff}}$  respectively, and are given by

$$\begin{aligned} \tan \alpha_{\text{tilt}} &= \frac{\cos \psi_{\text{out},2}}{\cos \psi_{\text{in},2}} \frac{L_{\text{grating}}}{f_{\text{eff}}} \tan \alpha_{\text{tilt},1} - \left( \frac{L_{\text{mirror}}}{f_{\text{eff}}} - 1 \right) \tan \alpha_{\text{tilt},2} \\ \tan \alpha_{\text{poc}} &= \frac{\cos \psi_{\text{out},2}}{\cos \psi_{\text{in},2}} \frac{L_{\text{grating}}}{f_{\text{eff}}} \left[ 2 \left( \tan \psi_{\text{out},2} \frac{\tan \alpha_{\text{tilt},2}}{\tan \alpha_{\text{tilt},1}} + \tan \psi_{\text{in},2} \right) - \tan \psi_{\text{out},1} \right] \frac{\tan^2 \alpha_{\text{tilt},1}}{\tan^2 \alpha_{\text{tilt}}} - \\ &\quad - \left( \frac{L_{\text{mirror}}}{f_{\text{eff}}} - 1 \right) \frac{\tan^2 \alpha_{\text{tilt},2}}{\tan^2 \alpha_{\text{tilt}}} \tan \alpha_{\text{poc},2} - \\ &\quad - \tan \left( \frac{\psi_{\text{defl}}(\Omega_0)}{2} \right) \frac{1}{f_{\text{eff}}^2} \left[ \frac{\cos \psi_{\text{out},2}}{\cos \psi_{\text{in},2}} L_{\text{grating}} \frac{\tan \alpha_{\text{tilt},1}}{\tan \alpha_{\text{tilt}}} - L_{\text{mirror}} \frac{\tan \alpha_{\text{tilt},2}}{\tan \alpha_{\text{tilt}}} \right]^2. \end{aligned} \quad (4.36)$$

This already takes flips of pulse-front tilt and plane of optimum compression orientations at the second cylindrical mirror into account. In the derivation the incident horizontal offset  $y_0(\Omega)$  of a frequency from the central laser frequencies propagation axis is evaluated by

$$y_0(\Omega) = \frac{\cos [\psi_{\text{out},2}(\Omega_0) + \theta_2(\Omega)]}{\cos \theta_2(\Omega)} \frac{\cos \theta_1(\Omega)}{\cos [\psi_{\text{in},2}(\Omega_0) - \theta_1(\Omega)]} L_{\text{grating}} \tan \theta_1(\Omega) - L_{\text{mirror}} \tan \theta_2(\Omega). \quad (4.37)$$

Thereby,  $\theta_1(\Omega)$  and  $\theta_2(\Omega)$  are the angular deviation of a frequency  $\Omega$  from the propagation direction of the central frequency  $\Omega_0$  after first and second grating, respectively, just as for the previous setup without focusing. This form takes the laser pulse width change after diffraction at the second grating into account but gives only an approximate value for the incidence position  $y_{\text{in}}(\Omega)$  on the off-axis cylindrical mirror surface for cases where the incident pulse has a pulse-front tilt. With the help of fig. 4.9 the small necessary correction  $\Delta'$  to the actual given incidence position  $y_0'$ , measured from the central frequency incidence position, can be shown to be negligible. An estimate of the correction is given by

$$\frac{\Delta}{y_0} = \left[ \frac{y_0}{4f} - \tan \frac{\psi_{\text{defl}}(\Omega_0)}{2} \right] \tan \theta_{\text{in}}.$$

Following the discussion at the end of 4.5.2 and 4.5.3, only small incident angular propagation angle differences  $\theta_{\text{in}}$  are required between frequencies as well as off-axis cylindrical mirrors with large  $f/D_{\text{in}}$  are used making the correction  $\Delta$  a negligible quantity for TWTS OFELs.

## USING ANGULAR DISPERSION TO COMPENSATE SPATIAL DISPERSION BEFORE THE FOCUS

Up to now only the distance of the interaction point from the focus  $\Delta f$  and the effective focal distance  $f_{\text{eff}}$  of the off-axis cylindrical mirror are fixed by the limit on undulator frequency variation due to phase-front curvature and correct laser pulse width at the interaction point, respectively. As it is shown in the following, values of  $\tan \alpha_{\text{tilt},2}$  and spatial dispersion of the pulse before deflection at the off-axis cylindrical mirror are set by the requirement of vanishing spatial dispersion and correct pulse-front tilt by half the interaction angle at the interaction point.

First, required spatial dispersion prior to deflection at the off-axis cylindrical mirror is quantified. At the beginning it is thus verified that spatial dispersion of the pulse directly before and after deflection at the off-axis cylindrical mirror is to first order identical even for pulse-front tilted incident laser pulses. The position of a frequencies transverse distribution center  $y_{0,\text{defl}}(\Omega)$  after deflection at the mirror is related to its position before deflection  $y_0(\Omega)$  by

$$y_{0,\text{defl}}(\Omega) = -y_0(\Omega) \left\{ 1 + \frac{[2y_{\text{in}}(\Omega) - y_0(\Omega)] \sin [\psi_{\text{defl}}(\Omega) - 2\theta_{\text{in}}(\Omega)]}{4f \cos \theta_{\text{in}}(\Omega) \cos [\psi_{\text{defl}}(\Omega) - \theta_{\text{in}}(\Omega)]} \right\} \frac{\cos [\psi_{\text{defl}}(\Omega) - \theta_{\text{in}}(\Omega)]}{\cos \theta(\Omega)}.$$

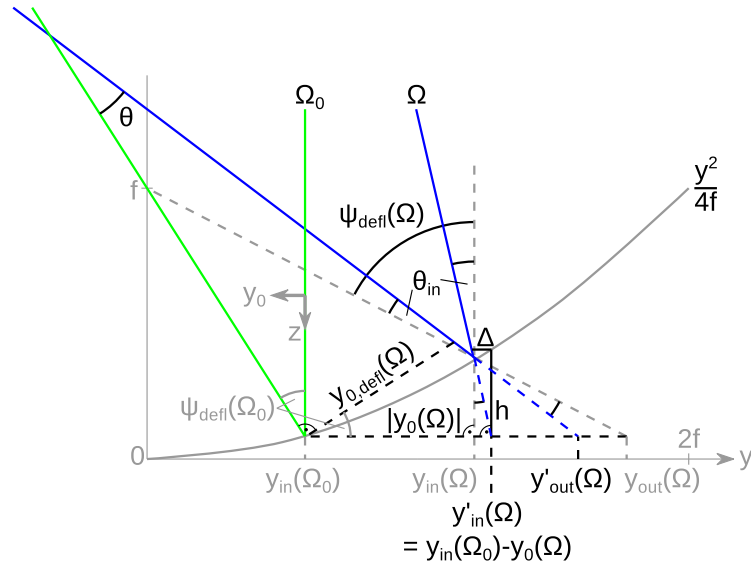


Figure 4.9.: Transformation of light ray coordinates during reflection at an off-axis cylindrical mirror. Primed quantities describe a ray whose propagation direction encloses the angle  $\theta_{in}$  with the mirror axis. A rays incidence coordinate on the mirror surface  $y_{in}$  deviates from its incidence coordinate on the  $y$ -axis  $y'_{in}$ . The deviation  $\Delta$  can be estimated by  $\Delta = h \tan \theta_{in}$ , where  $h = \left( y'_{in}(\Omega)^2 - y_{in}(\Omega_0)^2 \right) / 4f$ . Furthermore, the spatial offset  $y_{0,defl}(\Omega)$  of a frequency in the deflected pulse can be related to the spatial offset of the frequency before deflection  $y_0(\Omega)$ .

After deflection at the mirror spatial dispersion is given by a linear approximation of this expression, cf. section (4.1),

$$SD_{defl} = \left. \frac{dy_{0,defl}}{d\Omega} \right|_{\Omega=\Omega_0} = - \left. \frac{dy_0}{d\Omega} \right|_{\Omega=\Omega_0} =: -SD_{in} .$$

That is, spatial dispersion after deflection is opposite in sign to spatial dispersion before deflection but equal in absolute value. As expressed in this relation the value of spatial dispersion before deflection  $SD_{in}$  can be obtained from the relation for the offset of a frequencies transverse distribution center (4.37) by linear approximation

$$SD_{in} = \left. \frac{dy_0}{d\Omega} \right|_{\Omega=\Omega_0} = \frac{\cos \psi_{out,2}}{\cos \psi_{in,2}} \frac{L_{grating}}{\Omega_0} \tan \alpha_{tilt,1} - \frac{L_{mirror}}{\Omega_0} \tan \alpha_{tilt,2} \quad (4.38)$$

After deflection and while the pulse propagates to the interaction point spatial dispersion evolves as

$$SD(z) = -\frac{z + f_{eff}}{\Omega_0} \tan \alpha_{tilt} + SD_{in} ,$$

where  $\tan \alpha_{tilt}$  is given by (4.36),  $z = 0$  coincides with the off-axis cylindrical mirror focus and this expression takes a flip of spatial dispersion and pulse-front tilt at the second cylindrical mirror already into account. This relation is used to determine the required spatial dispersion of the pulse before deflection at the off-axis cylindrical mirror for vanishing spatial dispersion at the interaction point. Demanding  $SD(\Delta f) \stackrel{!}{=} 0$  yields

$$SD_{in,target} = \frac{\Delta f + f_{eff}}{\Omega_0} \tan(\phi/2) . \quad (4.39)$$

Second, the pulse front-tilt of the incident pulse is quantified by recasting the relation for final pulse-front tilt in (4.36) into a condition on  $\tan \alpha_{\text{tilt},2}$  and inserting (4.39)

$$\tan \alpha_{\text{tilt}} = \Omega_0 \frac{SD_{\text{in}}}{f_{\text{eff}}} + \tan \alpha_{\text{tilt},2} .$$

Correct pulse-front tilt at the interaction point is ensured by

$$\tan \alpha_{\text{tilt},2,\text{target}} = -\tan(\phi/2) \frac{\Delta f}{f_{\text{eff}}} , \quad (4.40)$$

where again  $\Delta f < 0$  for an interaction before the focus. This pulse-front tilt is always small since  $\Delta f/f_{\text{eff}} = \pi w/D_{\text{in}} \ll 1$ . Otherwise, if the input pulse width  $D_{\text{in}}$  would be on the order of the pulse width at the interaction point  $w$ , there would be no need for focusing at all.

At last, by combining requirements on incident spatial dispersion and residual pulse-front tilt after the second grating, a requirement on pulse-front tilt after the first grating can be obtained

$$\tan \alpha_{\text{tilt},1,\text{target}} = \frac{\Delta f (1 - L_{\text{mirror}}/f_{\text{eff}}) + f_{\text{eff}}}{\frac{\cos \psi_{\text{out},2}}{\cos \psi_{\text{in},2}} L_{\text{grating}}} \tan(\phi/2) \quad (4.41)$$

## OBTAINING PARAMETERS FOR THE SETUP

The setup providing focusing grants more freedom in the choice of parameters than the setup without focusing since more parameters influence the quantities of interest  $\alpha_{\text{tilt}}$  and  $\alpha_{\text{poc}}$ . The only parameters preset in this setup are  $(f_{\text{eff}}, \Delta f, SD_{\text{in}}, \tan \alpha_{\text{tilt},2}, \tan \alpha_{\text{tilt}}, \tan \alpha_{\text{poc}})$  and the distance of the second cylindrical mirror, which provides focusing in the vertical direction, from the interaction point. The latter is given by the projection of its focal distance along the propagation direction of the laser which is given by the interaction angle. The remaining parameters to be determined are first grating incidence angle  $\psi_{\text{in},1}$  and line density  $n_1$ , grating separation distance  $L_{\text{grating}}$ , second grating rotation angle  $\epsilon$  and line density  $n_2$ , the distance between second grating and off-axis cylindrical mirror  $L_{\text{mirror}}$  as well as the deflection angle at the off-axis cylindrical mirror  $\psi_{\text{defl}}$ . One possible procedure to determine the parameters of the grating setup is explained in the following.

The analytical solution for plane of optimum compression orientation at the interaction point can be recast into a condition on first grating diffraction angle  $\psi_{\text{out},1}$  by using the analytical solution for plane of optimum compression orientation after the second grating (4.19). Further, making use of the conditions on pulse-front tilt after first and second grating, (4.41) and (4.40) respectively, as well as setting  $L_{\text{grating,eff}} = L_{\text{grating}} \cos \psi_{\text{out},2} / \cos \psi_{\text{in},2}$ , the following system of

conditions on first grating parameters is obtained

$$0 = \frac{\sin \psi_{in,2} - \sin \psi_{out,2}}{\cos \psi_{out,2}} - \frac{\cos \psi_{in,2}}{\cos \psi_{out,2}} \tan \alpha_{tilt,1,target} - \tan \alpha_{tilt,2,target} , \quad (4.42)$$

$$\tan \psi_{out,1} = \left\{ 2 \frac{L_{grating,eff}}{f_{eff}} \left( \tan \psi_{out,2} \frac{\tan \alpha_{tilt,2,target}}{\tan(\phi/2)} + \tan \psi_{in,2} \frac{\tan^2 \alpha_{tilt,1,target}}{\tan^2(\phi/2)} \right) - \tan \left( \frac{\psi_{defl}(\Omega_0)}{2} \right) \frac{1}{f_{eff}^2} \left[ L_{grating,eff} \frac{\tan \alpha_{tilt,1,target}}{\tan(\phi/2)} - L_{mirror} \frac{\tan \alpha_{tilt,2,target}}{\tan(\phi/2)} \right]^2 + \cotan \phi - \left( \frac{L_{mirror}}{f_{eff}} - 1 \right) \left( \frac{\sin \psi_{in,2}}{\cos \psi_{out,2}} \frac{\tan^2 \alpha_{tilt,1,target}}{\tan^2(\phi/2)} - \tan \psi_{out,2} \frac{\tan^2 \alpha_{tilt,2,target}}{\tan^2(\phi/2)} \right) \right\} \quad (4.43)$$

$$\left/ \left[ \frac{L_{grating,eff}}{f_{eff}} \frac{\tan^2 \alpha_{tilt,1,target}}{\tan^2(\phi/2)} + \left( \frac{L_{mirror}}{f_{eff}} - 1 \right) \frac{\tan^2 \alpha_{tilt,1,target}}{\tan^2(\phi/2)} \frac{\cos \psi_{in,2}}{\cos \psi_{out,2}} \right] \right. \quad (4.44)$$

$$\sin \psi_{in,1} = \cos \psi_{out,1} \tan \alpha_{tilt,1,target} + \sin \psi_{out,1} ,$$

which depends on second grating incidence and deflection angle,  $\psi_{in,2}$  and  $\psi_{out,2}$  respectively, as well as  $L_{grating,eff}$ ,  $L_{mirror}$  and  $\psi_{defl}$ . The first of these equations restricts the choice of combinations  $(\psi_{in,2}, \psi_{out,2})$  to pairs ensuring correct pulse-front tilt  $\alpha_{tilt,2}$ .

By assuming values for all of these parameters the first grating incidence and diffraction angle can be determined. Thereby, the first grating line density is expected to be equal or similar to the second grating line density since the required pulse front tilt after the second grating  $\alpha_{tilt,2}$  is a small quantity.

The initial choice of second grating parameters will be driven by the requirement of high diffraction efficiency. However, this choice is not entirely free. There are secondary requirements, e.g. a large enough distance between the gratings, grating incidence angles not too far from the Littrow angle or availability of the corresponding first grating, that may require a refinement of the initial choice.

The parameters  $L_{mirror}$  and  $\psi_{defl}$  can be chosen to accommodate the space requirements in the lab and availability from manufacturers, respectively. Since the requirement on pulse-front tilt after the first grating scales only weakly with  $L_{mirror}$ , as long as it is small compared to  $f_{eff}$ , a later refinement of its value after the grating parameters have been evaluated from some initial guess will only result in a small change of grating parameters after a second iteration.

This setup also offers the possibility of using an uncompressed laser pulse as an input just as all the setups before. In this case laser pulse compression is accomplished during propagation from the first grating to the interaction point. This actually allows to use the compressor gratings for spatial dispersion and pulse-front tilt generation which means that there would be no additional set of gratings required in the experimental area. Group-delay dispersion that can be removed by the setup is given by

$$GDD_0 = \frac{1}{\Omega_0 c} \left( L_{grating} \tan^2_{tilt,1} + L_{mirror} \tan^2_{tilt,2} + (f_{eff} + \Delta f) \tan^2(\phi/2) \right) . \quad (4.45)$$

In the case of using an uncompressed pulse as an input, the  $GDD_0$  must match the absolute value of group-delay dispersion generated by the stretcher. This gives another condition which can be used to fix one of the free parameters in this setup, e.g.  $L_{grating}$  or  $L_{mirror}$ . It is obtained by solving (4.45) for the respective parameter.

### 4.5.3. VARIATIONS IN UNDULATOR FREQUENCY AND AMPLITUDE FROM MISALIGNMENT AND OUT-OF-FOCUS INTERACTION

As for the two grating setup without focusing, misaligned gratings and mirrors reduce the overlap of electrons and laser pulse leading to intensity and undulator frequency variations during interaction. Relations (4.27) and (4.28) used to estimate these variations are still applicable in this setup providing focusing, but variations in orientations of plane of optimum compression  $\tan \alpha_{\text{poc}}$  and pulse-front tilt  $\tan \alpha_{\text{tilt}}$  have to be calculated from possible misalignments of all sources in (4.36).

An additional source of undulator frequency and amplitude variations in this setup can be curvature of phase-fronts and pulse-front. While the former already has been estimated and used to derive the minimum out-of-focus distance, the latter is estimated now. The analytical formula for the laser field (4.5) is used. Since the plane of optimum compression is utilized in this setup, all dispersion terms are neglected for this estimate. Further the variation from the transverse envelope is neglected since its exact form depends on the laser system and can be manipulated. For the normalized irradiance remains

$$\frac{I(y, z, t)}{I(0, 0, 0)} = e^{-2\tilde{L}'^2},$$

where

$$\tilde{L}' = \frac{ct + \Delta f - z + y \tan \alpha_{\text{tilt}} - y^2/(2R)}{c\tau_0}.$$

Then total laser irradiance variation until the end of interaction can be estimated to be

$$\left| \frac{\Delta I}{I} \right| = \Delta \tilde{L}'^2 = \left( \frac{L_{\text{int}}^2 \sin^2 \phi}{8\Delta f c\tau_0} \right)^2.$$

Comparing this limit to the limit arising from undulator frequency variation due to phase front curvature the latter is stricter than the former due to typically acceptable percent level variations of laser irradiance.

Apart from curvature, aberrations may become a source of undulator frequency variation during interaction, too. Off-axis cylindrical mirrors with large  $f/\# = f/D_{\text{in}}$  must be used for TWTS OFELs in order to avoid coma from the mirror. With too small  $f/\#$  individual frequencies contained in the laser pulse do not share a common focus anymore but their individual foci are offset from each other which introduces again a kind of spatial dispersion. However, for TWTS OFELs the required effective focal distance scales as  $f/D_{\text{in}} \propto L_{\text{int}}/\lambda_{\text{und}} \sin \phi$  and thus  $f/\# \gg 1$  for all TWTS OFEL setups. Coma of the laser pulse can just become an issue in setups including focusing which are not meant for TWTS OFEL operation.



# 5. TRAVELING-WAVE THOMSON-SCATTERING FOR OPTICAL FREE-ELECTRON LASERS

Throughout the thesis it has been spoken about the Traveling-Wave Thomson-Scattering Optical Free-Electron Laser (TWTS OFEL) but no proof has been presented to justify this wording. During the thesis work it was shown for the first time by an analytic derivation of the TWTS OFEL equations of motion that OFELs can be realized with TWTS. The derivation presented in this chapter shows that the equations of motion for an interaction of electrons with a laser pulse in the TWTS geometry can be written in a form equivalent to standard FEL equations of motion which were presented in chapter 2.2.2. As a result, scaling laws can be derived for the requirements on electron and laser pulse quality for TWTS OFEL operation which can be used to determine electron and laser parameters for TWTS OFELs. A couple of examples are presented in the next chapter.

## 5.1. FOUNDATIONS OF THE TWTS OFEL THEORY

Before the TWTS OFEL equations of motion are derived the specialties of the TWTS interaction geometry with regard to OFEL realization are discussed. The analytical derivation of the electron and radiation field dynamics in TWTS OFELs is a self-consistent 1.5D theory. It takes into account differences in propagation directions between laser field, electrons and radiation field. It further assumes a plane wave laser and radiation field.

In this section the assumption of a plane wave laser field is justified, the off-axis radiation emission is explained, which is caused by non-collinear propagation of electron bunch and laser pulse, together with the resulting development of a tilted microbunching structure.

### 5.1.1. PLANE WAVE ANSATZ FOR THE LASER FIELD

The derivation of electron and radiation field dynamics in TWTS OFELs assumes a plane-wave laser field. The previous chapter presented methods for the generation of laser pulses for TWTS with the aim to achieve a plane wave field along the electron trajectory. By utilizing the plane of optimum compression it was shown that dispersion up to second order can be compensated along the electron trajectory. For the same setup the laser field along the electron trajectory was

already derived (eq. (4.22)) and it was shown that the field resembles a plane wave

$$E(z_{el}, y_{el}, t) = E_0 e^{i \frac{\Omega_0}{c} (ct - z_{el})} \quad (5.1)$$

along the electron trajectory  $(z_{el}, y_{el})$  provided laser pulse dispersion is negligibly small as well as electrons and laser pulse spatially overlap, eqs. (4.26) and (4.25) respectively, viz.

$$\frac{\lambda_{\text{Laser}}}{\pi c^2 \tau_0^2} \frac{\tan^2(\phi/2)}{\sin \phi} \sigma_b \ll 1 \quad \frac{c\tau_b + \sigma_b \tan(\phi/2)}{c\tau_0} \ll 1,$$

where  $\tau_b$  and  $\sigma_b$  are the electron pulse duration and rms cross-sectional radius, respectively. For the self-consistent TWTS OFEL theory it is assumed that these conditions are fulfilled as well as the change in laser field amplitude due to the transverse laser field envelope is negligibly small during the interaction, too. These assumptions are consistent with the slowly varying envelope approximation commonly used in FEL physics [132, 133].

The derivation of the electric field along the electron trajectory that leads to above conditions was based on an expansion of the laser phase up to second order in  $(\Omega - \Omega_0)$ . The validity of this approach can be verified by calculating the field along the electron trajectory from a field representation including all orders of dispersion. For this a representation of a laser pulse featuring the plane of optimum compression and including dispersion to all orders is needed which is found from the electric field of a pulse with angular dispersion in frequency space

$$\hat{E}(y, z, \Omega) = \hat{E}_0 e^{-(\Omega - \Omega_0)^2 \tau_0^2 / 4} e^{-i \frac{\Omega}{c} (z \cos \theta(\Omega) - y \sin \theta(\Omega))},$$

where  $\theta$  again represents angular dispersion and is the angle enclosed by the propagation direction of a frequency  $\Omega$  and the central frequency  $\Omega_0$ . A representation of the field of a pulse featuring the plane of optimum compression is found from this representation by using the results for correct orientation of plane of optimum compression after diffraction at a single grating which were obtained in the last chapter. That is,  $\theta$  is evaluated using (4.15), (4.16), (4.17) and  $\alpha_{\text{poc}} = \phi - \pi/2$ , where  $\phi$  is the interaction angle, which leads to

$$\begin{aligned} \theta(\Omega) &= \psi_{\text{out}}(\Omega) - \psi_{\text{out}}(\Omega_0) \\ &= \phi + \arcsin \left[ 1 - \frac{\Omega_0}{\Omega} (1 - \cos \phi) \right] - \frac{\pi}{2} \\ &=: \nu(\Omega) - \frac{\pi}{2}, \end{aligned}$$

with

$$\nu(\Omega) = \phi + \arcsin \left[ 1 - \frac{\Omega_0}{\Omega} (1 - \cos \phi) \right].$$

Then the field of the ideal TWTS pulse featuring the plane of optimum compression and including dispersion to all orders is given in frequency space by

$$\hat{E}(y, z, \Omega) = \hat{E}_0 e^{-(\Omega - \Omega_0)^2 \tau_0^2 / 4} e^{-i \frac{\Omega}{c} (z \sin \nu(\Omega) + y \cos \nu(\Omega))}.$$

The field in time domain is obtained by a Fourier transformation

$$E(y, z, t) = \frac{1}{2\pi} \int d\Omega e^{i\Omega t} \hat{E}(y, z, \Omega),$$

which can be calculated numerically along the electron trajectory and decomposed into its frequency components to evaluate undulator frequency and its variation given by its bandwidth.

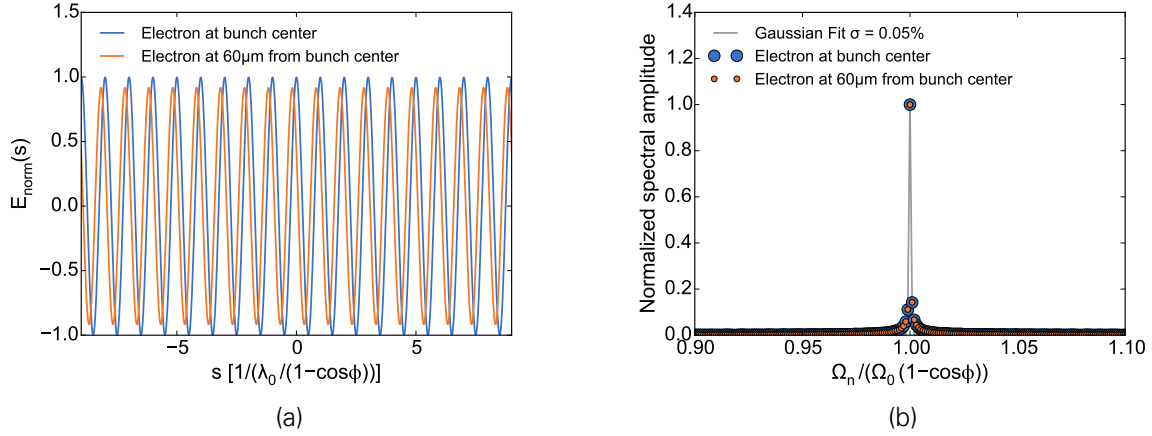


Figure 5.1.: (a) The electric field of a TWTS laser pulse featuring the plane of optimum compression sampled along the electron trajectory for an interaction angle  $\phi = 20^\circ$ . The field resembles a plane wave for both electrons in the center of the bunch and with  $60 \mu\text{m}$  horizontal offset from center. (b) The complete spectrum of the field along the electron trajectory for both electrons. Due to dispersion compensation the spectra are identical. Their relative full width at half maximum is obtained by a gaussian fit which yields  $\Delta\tilde{\Omega}/\tilde{\Omega} = 0.12\%$ . The calculation was performed for an interaction lasting over 1000 undulator periods and the field was sampled eight times per period.

Results of a field evaluation along the electron trajectory are shown in fig. 5.1 for an example setup using a laser system with wavelength  $\lambda_{\text{Laser}} = 1.035 \mu\text{m}$  and pulse duration  $\tau_0 = 120 \text{ fs}$  for interaction at an angle  $\phi = 20^\circ$  and an electron pulse rms cross-sectional radius of  $\sigma_b = 60 \mu\text{m}$ . They confirm the plane wave behavior of the laser field along the electron trajectory for setups making use of the plane of optimum compression.

Therefore it is assumed for the TWTS OFEL theory that above conditions for plane wave behavior of the laser field are fulfilled and thus the field of the laser pulse can be approximated locally, at the position of the electrons, by a plane wave (5.1).

### 5.1.2. OFF-AXIS RADIATION EMISSION

Compared to standard magnetic undulators or head-on Thomson scattering, coherent radiation amplification in TWTS optical undulators does not take place along the propagation direction of the electron beam. In a TWTS geometry the propagation directions of emitted radiation and electrons enclose an angle  $\phi_{\text{sc}}$ .

Coherent amplification of radiation under the angle  $\phi_{\text{sc}}$  is a result of oblique laser incidence. In contrast to standard magnetic undulators or head-on Thomson scattering, due to oblique incidence the planes of equal laser phase are not oriented perpendicular to the electron propagation direction but run across the electron bunch as it is depicted in fig. 5.2a. Thus there is a phase difference  $\Delta\varphi_{\text{in}}$  in observed laser field between electrons being aligned perpendicular to the direction of motion of the bunch. Accordingly the laser field induced oscillatory motion of these electrons is shifted by the same phase difference which results in a phase shift in emitted radiation  $\Delta\varphi_{\text{out}}$  between these electrons. Since the process of radiation emission from the oscillatory motion is the same for all electrons, the phase difference in emitted radiation and incident laser field is equal across the electron bunch

$$\Delta\varphi_{\text{out}} = \Delta\varphi_{\text{in}}.$$

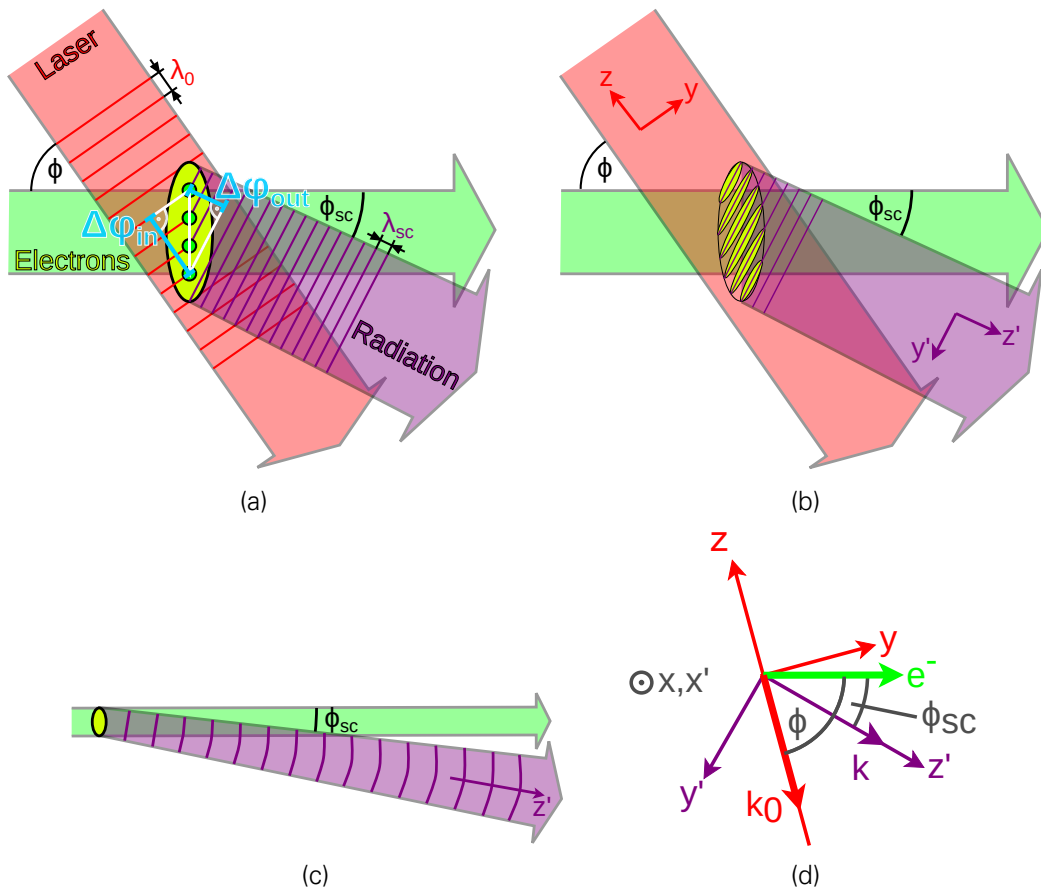


Figure 5.2.: (a) Sketch to determine the emission angle  $\phi_{sc}$  of radiation in TWTS OFELs with interaction angle  $\phi$ . Electrons (green) have different phases in the obliquely incident laser field where the phase difference is  $\Delta\phi_{in}$ . Since the scattering process is similar to diffraction into the zeroth order at a grating, the phase difference  $\Delta\phi_{out}$  between electrons in the outgoing radiation is equal to  $\Delta\phi_{in}$ . But the wavelength of emitted radiation  $\lambda_{sc}$  is much shorter than the laser wavelength  $\lambda_{Laser}$  ensuring  $\phi_{sc} \ll \phi$ . (b) Microbunching in an FEL develops along planes of equal radiation phase leading to a tilted microbunching structure with respect to the electron propagation direction in TWTS OFELs. (c) Radiation emission under the angle  $\phi_{sc}$  leads to a radiation 'walk-off' out of the electron bunch. (d) Coordinate systems used in the derivation of electron and radiation field equations of motion for TWTS OFELs. Red is the laser coordinate system and purple the primed radiation coordinate system. The  $x$ -axes of both systems coincide. Following the conventions often used in Thomson scattering literature, the incident laser pulse propagates in  $-z$  direction. The emitted radiation propagates along  $+z'$ . (Originally in [KS2])

This relation can be used to determine the radiation emission angle which gives the direction along which outgoing waves from electrons positively interfere. Drawing a comparison to diffraction at a grating, the radiation emission angle corresponds to the outgoing angle of the zeroth diffraction order. Assuming the distance between two electrons is  $a$  and using the relation for

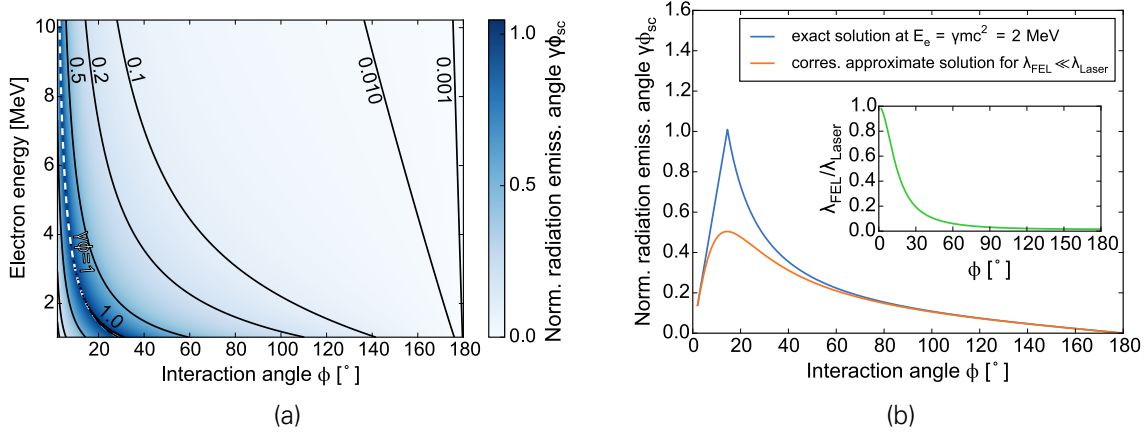


Figure 5.3.: (a) Contour plot of the normalized radiation emission angle  $\gamma\phi_{sc}$ , cf. fig. 5.2a, in dependence of interaction angle  $\phi$  and electron energy  $\gamma mc^2$  using the exact solution (5.2) and assuming  $a_0^2/2 \ll 1$ . Except for the region where  $\gamma\phi$  is on the order of unity, the emission angle is much smaller than the  $\sim 1/\gamma$  opening angle of the cone into which spontaneous radiation of the individual electrons is emitted,  $\phi_{sc} \ll 1/\gamma$ . This ensures coherent radiation amplification and keeps radiation walk-off small. (b) Line out of the normalized radiation emission angle  $\gamma\phi_{sc}$  scaling with interaction angle  $\phi$  for a constant electron energy of 2 MeV (blue). For a large portion of interaction angles  $\gamma\phi_{sc} \ll 1$  holds. Interaction angles below the interaction angle  $\phi = 1/\gamma$ , where  $\gamma\phi_{sc} = 1$ , result in forward scattering of radiation which is not of interest for light source applications since  $\lambda_{FEL} = \lambda_{Laser}$  for these interaction angles. The remaining interaction angles result in backward scattering allowing for short wavelengths production by large Doppler shifts, i. e.  $\lambda_{FEL} \ll \lambda_{Laser}$ . For these cases the approximate solution for the emission angle of coherent radiation (5.3) is plotted (orange). The scaling of its condition of validity  $\lambda_{FEL}/\lambda_{Laser} = [2\gamma^2(1 - \beta_0 \cos \phi)]^{-1} \ll 1$  is depicted, too, verifying good agreement between the exact and the approximate solution where it is applicable.

the scattered wavelength (2.1), with the observation angle  $\theta = \phi_{sc}$ ,

$$\begin{aligned}
 & \Delta\varphi_{out} = \Delta\varphi_{in} \\
 \Leftrightarrow & \quad a \frac{2\pi}{\lambda_{FEL}} \sin \phi_{sc} = \frac{2\pi}{\lambda_{Laser}} a \sin \phi \\
 \Leftrightarrow & \quad \sin \phi_{sc} = \frac{\lambda_{FEL}}{\lambda_{Laser}} \sin \phi \\
 \Leftrightarrow & \quad \phi_{sc} = \arcsin \left[ \frac{b}{\bar{\beta} \sqrt{1 + b^2}} \right] - \arctan b \quad (5.2)
 \end{aligned}$$

where  $b = \bar{\beta} \sin \phi / (1 - \beta_0 \cos \phi)$  and  $\bar{\beta} = 1 - (1 + a_0^2/2) / 2\gamma_0^2 \approx \beta_0$  is the average normalized electron velocity in the laser field.

Since typical TWTS OFEL scenarios will feature radiation wavelengths much smaller than the laser wavelength, the emission angle will be much smaller than the laser incidence angle  $\phi_{sc} \ll \phi$  and much smaller than unity  $\phi_{sc} \ll 1$  as can be seen from the third relation. An approximate solution for the emission angle of the coherent radiation can be obtained in this case by solving

the third relation with an iteration method

$$\phi_{sc} = \frac{\sin \phi}{2\gamma^2(1 - \beta_0 \cos \phi)} (1 + a_0^2/2) \quad \phi_{sc} \stackrel{\phi \ll 1}{\approx} \frac{(1 + a_0^2/2)}{\gamma^2 \phi} \quad (5.3)$$

using  $2\gamma^2(1 - \beta_0 \cos \phi) \gg 1$  implied by  $\lambda_{FEL} \ll \lambda_{Laser}$ . A scaling of the normalized emission angle  $\gamma\phi_{sc}$  with interaction angle  $\phi$  and electron energy  $\gamma mc^2$  using the exact solution (5.2) is depicted in fig. 5.3 for scenarios with small undulator amplitude  $a_0^2/2 \ll 1$ . The scaling shows that the emission angle of coherent radiation  $\phi_{sc}$  is always smaller or equal to the opening angle  $1/\gamma$  of the cone into which spontaneous radiation of individual electrons is emitted during Thomson scattering. The condition  $\gamma\phi_{sc} \lesssim 1$  is an important prerequisite for OFEL operation as otherwise coherent amplification of radiation is not possible.

The region of interaction angles corresponding to  $\phi_{sc} = 1/\gamma$  marks a threshold in the scattering process discriminating between forward and backward scattering. For interaction angles smaller than this threshold the scattering process observed in the electron rest frame is forward scattering corresponding to transmission of radiation. Forward scattering is undesirable for an OFEL since the radiation wavelength corresponds to the laser wavelength in this case. However, forward scattering can only occur for very low electron energies which are not of interest for OFELs as has been discussed in ch. 3.4. Interaction angles above the threshold correspond to backward scattering where large Doppler shifts of the incident laser light are possible allowing to produce X-rays.

As a consequence of off-axis radiation emission the microbunching structure of the electron beam will be tilted with respect to the propagation direction of the bunch as depicted in fig. 5.2b. Additionally, there are three more important consequences. Off-axis radiation emission leads to radiation 'walk-off' out of the electron bunch as depicted in fig. 5.2c. Second, due to walk-off radiation leaves the electron bunch and decouples from the amplification process earlier as if it would propagate along the electron bunch axis which reduces the scattering output. Third, lost radiation does not contribute anymore to microbunching which slows down the development of the FEL instability. It is therefore necessary to minimize the walk-off. A limit on acceptable walk-off is provided later in this chapter when scaling laws for TWTS OFELs are derived.

## 5.2. DERIVATION OF THE TWTS OFEL EQUATIONS OF MOTION

In the following equations of motion of an electron interacting with the electric field of an incident laser as well as the electric radiation field emitted by all other electrons in a bunch are derived for a TWTS geometry. This derivation has been done for the first time during the thesis work and takes into account the difference in propagation directions between laser pulse and electron bunch, measured by the interaction angle  $\phi$ , as well as radiation and electron bunch, measured by the emission angle  $\phi_{sc}$ . It was shown for the first time that the electron dynamics in a TWTS optical undulator is equally described to the dynamics in standard magnet undulator based free-electron lasers. Therefore, during the interaction in TWTS an FEL instability can develop leading to coherent radiation amplification by a microbunched electron pulse, just as in standard FELs, allowing for TWTS OFELs with orders of magnitude higher photon output than incoherent Thomson scattering sources.

The derivation of the electron equations of motion in a TWTS OFEL begins with the temporal evolution of the normalized electron energy  $\gamma = E_{el}/mc^2$ , where  $E_{el}$  and  $m$  is the electron energy and mass, respectively. The electron energy changes while it interacts with the electric laser field  $E$  and radiation field  $E_{rad}$

$$\dot{\gamma} = -\frac{e}{mc} (\mathbf{E}_{rad} + \mathbf{E}) \cdot \boldsymbol{\beta}, \quad (5.4)$$

where  $\boldsymbol{\beta}$  is the vector of the electron velocity normalized to the speed of light  $c$  and  $e$  the absolute value of the electron charge. According to the sketch of the interaction geometry shown in fig. 5.2d and in agreement with the conventions often used in Thomson scattering literature the laser propagation direction in the laser coordinate system is  $-z$  whereas the radiation propagation direction in the primed radiation coordinate system is  $+z'$ . The vertical axis of both systems,  $x$  and  $x'$  respectively, coincide. Following the discussion at the beginning of this chapter, a plane wave laser field  $E$  is assumed, c.f. eq. (5.1), and a variation of the laser amplitude is omitted as justified by the slowly varying envelope approximation,

$$\mathbf{E} = E_0 \sin(k_0 \eta) \mathbf{e}_x \quad (5.5)$$

$$\mathbf{E}_{\text{rad}} = E_{\text{rad}}(t) \cos[k\zeta + \Upsilon(t)] \mathbf{e}_x, \quad (5.6)$$

where  $k_0 = \Omega_0/c = 2\pi/\lambda_{\text{Laser}}$  is the laser field wave number,  $k$  an arbitrary radiation field number which is unknown at the moment,  $\eta = ct + z$  and  $\zeta = ct - z'$  are coordinates co-moving with the fields of laser and radiation respectively,  $E_{\text{rad}}(t)$  is the slowly varying radiation field amplitude increasing during the interaction due to coherent amplification and  $\Upsilon(t)$  is a slowly varying radiation phase characterizing the microbunching induced change of the electron bunch as a medium in which the radiation propagates. Assuming the electron bunch is much longer and wider than the slippage distance of the radiation with respect to the electron bunch center, there is no spatial dependency of the radiation field amplitude and phase  $\Upsilon$ .

The aim of the following is to derive the self consistent set of electron and radiation field equations of motion and rewrite these formally equal to the equations of motion of a standard magnet undulator based FEL presented for example in ref. [134].

Similar to the case of head-on OFELs introduced in ch. 2.2 the pendulum equations of motion for an electron in the combined fields of laser and radiation without gain are derived first. Then the temporal evolution of the radiation field amplitude  $E_{\text{rad}}(t)$  and phase  $\Upsilon(t)$  are calculated using the pendulum equations.

### 5.2.1. PENDULUM EQUATIONS OF TWTS OFELS

At first the temporal evolution of electron energy is analyzed starting by inserting into (5.4) expressions for the electric fields and the  $x$ -component of the time-dependent electron velocity in the laser field, which is calculated in ref. [43] in terms of the laser co-moving coordinate  $\eta$

$$\beta_x = \frac{a_0}{\gamma} \cos(k_0 \eta),$$

where  $a_0 = eE_0/mc\Omega_0$  is the normalized optical undulator amplitude. The normalized electron energy change becomes

$$\dot{\gamma} = -\frac{e}{mc} \frac{a_0}{\gamma} \left[ E_0 \sin(k_0 \eta) \cos(k_0 \eta) + E_{\text{rad}} \cos(k\zeta + \Upsilon(t)) \cos(k_0 \eta) \right].$$

Of these two terms, only the second is of importance for long-term energy transfer of electron kinetic energy to radiation field energy since the first term oscillates with twice the optical undulator frequency and has no net contribution over many undulator periods.

$$\dot{\gamma} = -\frac{e}{mc} \frac{a_0}{\gamma} E_{\text{rad}}(t) \frac{1}{2} \left[ \cos(k\zeta + \Upsilon(t) + k_0 \eta) + \cos(k\zeta + \Upsilon(t) - k_0 \eta) \right]$$

The electron energy evolution is obtained from this by first rewriting the radiation field phase  $k\zeta$  in the laser coordinate system

$$\begin{aligned} k\zeta &= k(ct - z') \\ &= k(ct - (y \sin(\phi - \phi_{\text{sc}}) - z \cos(\phi - \phi_{\text{sc}}))) \\ &= k\eta - k(y \sin(\phi - \phi_{\text{sc}}) + z [1 - \cos(\phi - \phi_{\text{sc}})]), \end{aligned}$$

and second inserting for  $(x, y, z)$  the electron trajectory calculated in ref. [43] for Thomson scattering at arbitrary laser energies and interaction angles

$$\begin{aligned}x(\eta) &= x_0 + \beta_{1x}\eta + r_1 \sin k_0\eta \\y(\eta) &= y_0 + \beta_{1y}\eta \\z(\eta) &= z_0 + \beta_{1z}\eta - z_2 \sin(2k_0\eta)\end{aligned}$$

with

$$\begin{aligned}\beta_{1x} &= 0 & r_1 &= \frac{a_0}{\gamma_0 k_0 (1 - \beta_0 \cos \phi)} \\ \beta_{1y} &= \frac{\beta_0 \sin \phi}{1 - \beta_0 \cos \phi} \\ \beta_{1z} &= \frac{1}{2} - \frac{1 + a_0^2/2 + \gamma^2 \beta_0^2 \sin^2 \phi}{2\gamma^2 (1 - \beta_0 \cos \phi)^2} & z_2 &= \frac{a_0^2}{8\gamma^2 (1 - \beta_0 \cos \phi)^2 k_0}.\end{aligned}$$

which yields for the radiation field phase

$$\begin{aligned}k\zeta + \Upsilon(t) &= k\eta \left\{ 1 - \sin(\phi - \phi_{sc})\beta_{1y} - \beta_{1z} [1 - \cos(\phi - \phi_{sc})] \right\} \\ &\quad + kz_2 \sin(2k_0\eta) [1 - \cos(\phi - \phi_{sc})] + \Upsilon(t).\end{aligned}$$

Accordingly, the phase of the oscillatory term in the electron energy change becomes

$$\begin{aligned}k\zeta + \Upsilon(t) \pm k_0\eta &= k_0\eta \left( \frac{k}{k_0} \left\{ 1 - \sin(\phi - \phi_{sc})\beta_{1y} - \beta_{1z} [1 - \cos(\phi - \phi_{sc})] \right\} \pm 1 \right) \\ &\quad + kz_2 \sin(2k_0\eta) [1 - \cos(\phi - \phi_{sc})] + \Upsilon(t).\end{aligned}\tag{5.7}$$

This expression can be further simplified for a TWTS OFEL by approximating the phase of an electron in the laser field  $\eta = ct + z$  by assuming a constant electron velocity

$$\eta \approx ct(1 + \bar{\beta}_z),$$

where  $\bar{\beta}_z$  is its average velocity in the laser field

$$\bar{\beta}_z = -\frac{\beta_0 \cos \phi + a_0^2/(4\gamma_0^2(1 - \beta_0 \cos \phi))}{1 + a_0^2/(4\gamma_0^2(1 - \beta_0 \cos \phi))},$$

which is reduced from its original velocity prior to interaction  $\beta_0$  due to the ponderomotive force of the laser field.

With the calculations shown so far, the change in electron energy can be written

$$\begin{aligned}\dot{\gamma} &= -\frac{e}{mc} \frac{a_0}{\gamma} E_{\text{rad}}(t) \frac{1}{2} \left\{ \cos[\theta_+(t) + \Upsilon(t) + kz_2[1 - \cos(\phi - \phi_{sc})] \sin(2k_0ct[1 + \bar{\beta}_z])] \right. \\ &\quad \left. + \cos[\theta_-(t) + \Upsilon(t) + kz_2[1 - \cos(\phi - \phi_{sc})] \sin(2k_0ct[1 + \bar{\beta}_z])] \right\},\end{aligned}$$

where

$$\theta_{\pm}(t) = k_0ct(1 + \bar{\beta}_z) \left( \frac{k}{k_0} \left\{ 1 - \sin(\phi - \phi_{sc})\beta_{1y} - \beta_{1z} [1 - \cos(\phi - \phi_{sc})] \right\} \pm 1 \right)\tag{5.8}$$

is the slow component of the phase by which the electron energy changes in the combined fields of optical undulator and radiation. The complete phase further consists of a fast varying component proportional to  $kz_2$  due to longitudinal oscillations in the optical undulator field. These

longitudinal oscillations allow coupling to higher harmonics of the radiation field, which are produced at optical undulator parameters  $a_0 \gtrsim 1$ , and reduce the energy transfer from electrons to the fundamental radiation field wave.

It is not necessary to include these fast repeating dynamics on the timescale of an undulator period into the calculation of the electron and radiation field dynamics to be able to study their long-term evolution. In order to obtain an expression for the slow long-term evolution of the electron energy, while properly taking into account the coupling to higher harmonics, the oscillatory terms in the electron energy evolution are expanded using the Bessel function relation  $\cos(a + b \sin c) = \sum_{m=-\infty}^{\infty} \cos(a + mc) J_m(b)$ , where  $J_m$  is the  $m$ th Bessel function of the first kind. Defining the ponderomotive phase, i.e. the phase of an electron in the combined optical undulator and radiation field, as

$$\theta(t) := \theta_-(t) = \theta_+(t) + 2k_0 ct(1 + \bar{\beta}_z),$$

the electron energy change becomes

$$\dot{\gamma} = -\frac{e}{mc} \frac{a_0}{\gamma} E_{\text{rad}}(t) \frac{1}{2} \sum_{m=-\infty}^{\infty} \cos[\theta(t) + \Upsilon(t) + m2k_0 ct(1 + \bar{\beta}_z)] \times \\ \times [J_m(kz_2[1 - \cos(\phi - \phi_{\text{sc}})]) + J_{m-1}(kz_2[1 - \cos(\phi - \phi_{\text{sc}})])]. \quad (5.9)$$

This expression shows that the electron energy evolution is actually driven by many ponderomotive waves. Every of these waves causes an oscillation of an electrons kinetic energy at the unique frequency  $\theta(t) + \Upsilon(t) + m2k_0 ct(1 + \bar{\beta}_z)$ . Thus the electron dynamics in the combined fields of undulator and radiation resembles the dynamics of a pendulum. Each waves contribution to the total energy change is determined by the value of the Bessel function factor  $J_m(kz_2[1 - \cos(\phi - \phi_{\text{sc}})]) + J_{m-1}(kz_2[1 - \cos(\phi - \phi_{\text{sc}})])$ .

In order to provide for continuous transfer of electron energy to the radiation field a ponderomotive waves phase needs to be nearly constant during the interaction, i. e.  $\theta(t) + m2k_0 ct(1 + \bar{\beta}_z) = 0$  for continuous radiation amplification. This condition can be used to determine the amplified radiation wavelengths in a TWTS OFEL. Note, each ponderomotive wave ensures energy transfer to a single associated radiation wave of wavelength  $\lambda_{\text{FEL},m}$ . Using the afore mentioned condition as well as eq. (5.8) and the approximation  $\bar{\beta}_z = -\beta_0 \cos \phi$  for relativistic electron bunches these wavelengths are obtained

$$\lambda_{\text{FEL},m} = -(2m - 1)\lambda_{\text{Laser}} g, \\ g = 1 - \sin(\phi - \phi_{\text{sc}}) \frac{\beta_0 \sin \phi}{1 - \beta_0 \cos \phi} \\ - \left[ \frac{1}{2} - \frac{1 + a_0^2/2 + \gamma_0^2 \beta_0^2 \sin^2 \phi}{2\gamma_0^2(1 - \beta_0 \cos \phi)^2} \right] [1 - \cos(\phi - \phi_{\text{sc}})], \quad (5.10)$$

with  $\gamma_0$  denoting the initial normalized electron energy. Not all of these possible wavelengths, which ensure constant ponderomotive phase during interaction, occur in a TWTS OFEL. Every  $m$  yielding a negative wavelength is not realized since the corresponding wave propagates opposite to the direction into which spontaneous radiation is emitted. Therefore these waves are neither radiated nor amplified. Amplified waves have  $m \in [-\infty, 0]$ .

A very good approximation of (5.10) is obtained for high electron energies  $\gamma_0^2 \gg a_0^2$ ,  $\beta_0 \sim 1$  and  $\phi_{\text{sc}}^2 \ll 1$  [43]

$$\lambda_{\text{FEL},n} = n\lambda_{\text{Laser}} \frac{(1 + a_0^2/2 + \gamma_0^2 \phi_{\text{sc}}^2)}{2\gamma_0^2(1 - \beta_0 \cos \phi)}, \quad (5.11)$$

where the number of an amplified harmonic is identified with  $n = -(2m - 1)$ . This relation is in agreement with eq. (2.2) confirming that the amplified radiation wavelengths of a TWTS OFEL are within the spectrum of spontaneously emitted radiation.

As pointed out before, producing harmonic rich radiation in a TWTS OFEL results in low electron-radiation coupling, which requires comparatively long interaction lengths, and a broad spectral bandwidth of the TWTS OFEL. With the aim of compact and narrow bandwidth TWTS OFELs, these will typically operate at non-relativistic irradiances ( $a_0 < 1$ ) producing radiation only at the fundamental wavelength ( $n = 1$ ). In this case, there is only one significant contribution to the energy change in (5.9) from the fundamental radiation wavelength corresponding to  $m = 0$ . The electron energy change expression therefore simplifies to

$$\dot{\gamma} = -\frac{k_1 c a_0 a_{\text{rad}}(t)}{\gamma} \frac{1}{2} [J_0(\chi) - J_1(\chi)] \cos[\theta(t) + \Upsilon(t)], \quad (5.12)$$

where  $\chi = a_0^2/(4 + 2a_0^2)$ ,  $k \approx k_1 = 2\pi/\lambda_{\text{FEL},1}$  and  $\phi_{\text{sc}} \ll \phi$  has been used in the argument of the Bessel functions.

The corresponding evolution of the ponderomotive phase  $\theta_j$  for the  $j$ th electron is obtained by inserting the radiation wave number  $k_1$  into (5.8) which yields for  $a_0 \ll 1$

$$\dot{\theta}_j = ck_0(1 - \beta_0 \cos \phi) \left( \frac{\gamma_0^2}{\gamma_j^2} - 1 \right) \stackrel{\gamma_0 \gg 1}{\approx} 2ck_0(1 - \beta_0 \cos \phi) \frac{\gamma_0 - \gamma_j}{\gamma_0}, \quad (5.13)$$

where  $\gamma_j$  are the individual normalized electron energies.

The first goal is achieved now. The electron equations of motion in a TWTS OFEL without radiation field gain are derived, eqs. (5.12) and (5.13), and they are similar to the pendulum equations known from standard FELs [132]. Therefore an optical undulator in a TWTS geometry yields the same electron dynamics as a magnetic undulator and produces the same radiation. In the following it is shown that radiation amplification in a TWTS OFEL is equal to a magnet based FEL, too.

### 5.2.2. SELF-CONSISTENT EQUATIONS OF MOTION OF TWTS OFELS

The temporal evolution of the radiation field is given by Maxwell's equations. In Coulomb gauge the temporal evolution of its potential  $\mathbf{A}_{\text{rad}}$  is given by

$$\left[ \frac{\partial^2}{\partial z'^2} - \frac{1}{c^2} \frac{\partial^2}{\partial t'^2} \right] \mathbf{A}_{\text{rad}} = -\mu_0 \mathbf{J},$$

where  $\mu_0$  is the permeability of free space and  $\mathbf{J}$  is the electron current density. With the radiation field envelope  $E_{\text{rad}}(t)$  and phase  $\Upsilon(t)$  being slowly varying functions, they can be assumed to be constant over an optical undulator cycle allowing to drop all second derivatives and squares of derivatives of these quantities. This corresponds to the slowly varying envelope approximation commonly used throughout FEL physics and results in first order equations for their temporal evolution.

Normalizing the radiation field envelope to  $a_{\text{rad}} = eE_{\text{rad}}(t)/(mc^2k)$ , these read

$$\frac{mc}{e} 2k \left\{ \cos[k(ct - z') + \Upsilon(t)] \frac{1}{c} \frac{\partial}{\partial t} a_{\text{rad}}(t) - a_{\text{rad}}(t) \sin[k(ct - z') + \Upsilon(t)] \frac{1}{c} \frac{\partial}{\partial t} \Upsilon(t) \right\} = -\mu_0 J_x. \quad (5.14)$$

The electron beam current on the right hand side can be formulated using the individual electron positions and velocities

$$J_x = \sum_{j=1}^N -e\delta(\mathbf{r} - \mathbf{r}_j(t))c\beta_{x,j}(t)$$

$$= \sum_{j=1}^N -e\delta(\mathbf{r} - \mathbf{r}_j(t))c\frac{a_0}{\gamma_j} \cos(k_0\eta),$$

with  $N$  corresponding to the number of electrons in the bunch. The above relation (5.14) containing the temporal evolution of radiation field envelope and phase can be split into two separate equations by first inserting the current and then multiplying by either  $\sin[k(ct-z')]$  or  $\cos[k(ct-z')]$  and afterwards averaging over a small volume  $V$  containing several radiation wavelengths in order to obtain an equation for the envelope or phase, respectively. The volume  $V$  must be small to allow for the approximation of constant envelope and phase therein. Thereby the products of laser and radiation field phase  $\sin[k(ct-z')]\cos(k_0\eta)$  and  $\cos[k(ct-z')]\cos(k_0\eta)$  are treated equal to the derivation of the pendulum equations where the Bessel function relation has been used to discriminate between slowly and fast varying terms. The resulting equations for the radiation field envelope  $a_{\text{rad}}$  and phase  $\Upsilon$  are

$$\frac{\partial}{\partial t} a_{\text{rad}}(t) = \frac{\mu_0 e^2 c n_e}{2mk_1} a_0 [J_0(\chi) - J_1(\chi)] \left\langle \frac{\cos[\theta_j(t) + \Upsilon(t)]}{\gamma_j} \right\rangle, \quad (5.15)$$

$$a_{\text{rad}}(t) \frac{\partial}{\partial t} \Upsilon(t) = -\frac{\mu_0 e^2 c n_e}{2mk_1} a_0 [J_0(\chi) - J_1(\chi)] \left\langle \frac{\sin[\theta_j(t) + \Upsilon(t)]}{\gamma_j} \right\rangle. \quad (5.16)$$

with the electron number density of the electron bunch  $n_e$  and the average  $\langle \cdot \rangle = \frac{1}{N_V} \sum_j^{N_V}$  over all electrons  $N_V$  in the volume  $V$ .

The above equations for the evolution of radiation field envelope and phase, (5.15) and (5.16) respectively, together with the electron equations of motion for energy change and ponderomotive phase, (5.12) and (5.13) respectively, form the self-consistent set of equations describing radiation and electron dynamics in a TWTS OFEL. These are already formally equivalent to the self-consistent set of equations for standard FELs, presented for example in refs. [132, 135]. By rewriting the above equations in 'universal scaling' the equivalence is better visible and at the same time the Pierce parameter for TWTS OFELs is obtained.

### 5.2.3. TWTS OFEL EQUATIONS OF MOTION IN UNIVERSAL SCALING

The Pierce parameter of the TWTS OFEL obtained from universal scaling is

$$\rho = \left[ \frac{a_0^2 f_B^2 \Omega_p^2}{32\gamma_0^3 c^2 k_0^2 (1 - \beta_0 \cos \phi)^2} \right]^{1/3} = \left[ \frac{1}{16\gamma_0^3} \frac{l_p}{l_A} \left( \frac{\lambda_{\text{Laser}} a_0 f_B}{2\pi\sigma_b (1 - \beta_0 \cos \phi)} \right)^2 \right]^{1/3}, \quad (5.17)$$

where  $\Omega_p = e^2 n_e / \epsilon_0 m$  is the plasma frequency of the electron bunch,  $f_B = [J_0(\chi) - J_1(\chi)]$  the Bessel function factor taking into account a reduced coupling due to radiation emission into higher harmonics,  $l_p$  the electron beam peak current,  $\sigma_b$  the electron beam rms cross-sectional radius, and  $l_A = 4\pi\epsilon_0 mc^3 / e \approx 17 \text{ kA}$  the Alfvén current. This Pierce parameter of TWTS OFELs is equivalent to the Pierce parameter of standard magnetic FELs. The only addition being the dependence on the interaction angle  $\phi$  taking into account the projection of the laser wavelength into the electron bunch direction of motion yielding the undulator period  $\lambda_{\text{und}} = \lambda_{\text{Laser}} / (1 - \beta_0 \cos \phi)$ .

The same projection is the only addition to the power gain-length of a TWTS OFEL

$$L_G = \frac{\lambda_{\text{Laser}}}{4\pi\sqrt{3}(1 - \beta_0 \cos \phi)\rho} \quad (5.18)$$

which is otherwise equivalent to the power gain-length of standard FELs, too.

Finally the self-consistent set of electron and radiation field equations of motion can be written in universal scaling, where time is scaled to gain-periods  $\bar{t} = ct/L_G\sqrt{3}$ , relative electron energy to  $p_j = (\gamma_0 - \gamma_j)/\rho\gamma_0$ , and the radiation field amplitude to  $\alpha$  measuring the power transferred from electron beam power  $P_e = \gamma_0 mc^2 I_p/e$  to radiation power  $P \approx \alpha^2 \rho P_e$  during the interaction, reaching approximately unity at saturation  $\alpha^2 \approx 1$ .

$$\frac{d\theta_j}{d\bar{t}} = p_j \quad \frac{dp_j}{d\bar{t}} = 2\alpha \cos(\theta_j + \Upsilon) \quad (5.19)$$

$$\frac{d\alpha}{d\bar{t}} = \langle \cos(\theta + \Upsilon) \rangle \quad \frac{d\Upsilon}{d\bar{t}} = -\frac{1}{\alpha} \langle \sin(\theta + \Upsilon) \rangle \quad (5.20)$$

these are formally equivalent to the equations of motion of standard FELs presented for example in ref. [134]. Therefore TWTS scattering geometries can exhibit the same electron and radiation field dynamics known from standard magnet undulator based FELs introduced in ch. 2.2. That is, microbunching of the electron pulse and coherent radiation amplification can be achieved in TWTS geometries.

In order to perform simulations of TWTS OFELs the system of equations of motion (5.20) is recast into a form that more facilitates their numerical integration. The form given above with the radiation field amplitude in the numerator of the radiation field phase equation does not allow for proper integration of this equation with initially vanishing radiation field. Therefore the scaled radiation field is redefined to  $\varepsilon = \alpha \exp[i\Upsilon] = \varepsilon_R + i\varepsilon_I$  which combines radiation field amplitude  $\alpha$  and phase  $\Upsilon$  into a single variable  $\varepsilon$ . Then the TWTS OFEL equations become

$$\frac{d\theta_j}{d\bar{t}} = p_j \quad \frac{dp_j}{d\bar{t}} = 2(\varepsilon_R \cos \theta_j - \varepsilon_I \sin \theta_j) \quad \frac{d\varepsilon_R}{d\bar{t}} = \langle \cos \theta \rangle \quad \frac{d\varepsilon_I}{d\bar{t}} = -\langle \sin \theta \rangle.$$

The 1.5D theory presented in this section proved for the first time the possibility of realizing optical free-electron lasers with Traveling-Wave Thomson-Scattering. It shows that neither the difference in propagation directions between laser and electron pulse, nor the difference between electron and radiation pulse directions of motion inhibits microbunching and exponential radiation amplification.

With the above proof of applicability of TWTS for OFEL realization, going further to a proof of principal experiment requires knowledge on electron, laser and radiation beam requirements for OFEL operation. As has been already qualitatively discussed in ch. 3.3, the differences in length and energy scales between TWTS OFELs and standard FELs lead to differences in free-electron laser requirements and performance. The following section provides scaling laws to evaluate electron, laser and radiation beam requirements as well as expected performance of TWTS OFELs.

### 5.3. SCALING LAWS OF TWTS OFELS

The fundamental parameters in TWTS OFEL scalings are the interaction angle  $\phi$ , the Pierce parameter  $\rho$  and the power gain length  $L_G$ , eqs. (5.17) and (5.18) respectively, as well as the interaction distance  $L_{\text{int}}$  required to achieve saturation.  $L_{\text{int}}$  is assumed to be  $16 \cdot L_G$  long according to numerical integration of the TWTS OFEL equations of motion (5.19) and (5.20). A result of a numerical integration is shown in fig. 5.4.

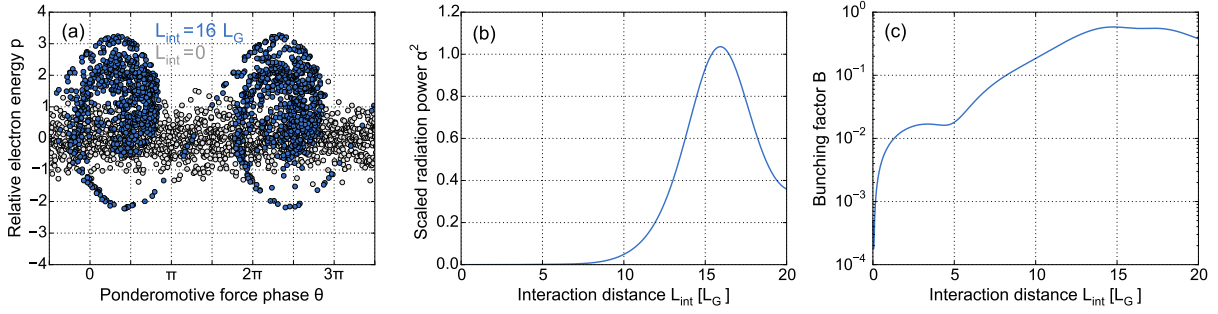


Figure 5.4.: Results of a numerical integration of the TWTS OFEL equations of motion (5.19) and (5.20) for 2000 electrons within an electron bunch slice of three radiation wavelengths along the propagation direction. Until saturation an interaction length of  $L_{\text{int}} = 16 \cdot L_G$  is required. (a) Electron phase space in universally scaled ponderomotive phase  $\theta$  and energy  $p$ . At  $t=0$  the initial electron distribution follows a normal distribution in  $p$  with standard deviation  $\sigma_p = 1/1.960$  which translates into a standard deviation in normalized energy of  $\sigma_\gamma/\gamma = \rho\sigma_p$ . The initial distribution in  $\theta$  follows from a two step initialization process which aims at keeping the initial bunching small. First, electrons are distributed on a regular grid, i.e. with equal spacing between each other. Second, the single electrons are displaced from their initial position within the interval enclosed by the initial positions of their closest neighbors according to a uniform distribution. After interaction over sixteen gain length the electron pulse is microbunched and the distance between two microbunches is  $2\pi$  corresponding to a radiation wavelength. (b) Radiation field growth during the interaction. Saturation is reached after  $L_{\text{int}} = 16 \cdot L_G$  where the scaled radiation field amplitude  $\alpha$  is on the order of unity. (c) Increase of electron microbunching during the interaction measured by the bunching factor  $B = |\langle \exp[i\theta] \rangle|$ , which vanishes for an unbunched pulse and approaches unity for maximum bunching. The initial value of the bunching factor in this simulation is  $B(0) = 4.9 \times 10^{-4}$ .

The proof of equivalence of electron and radiation field dynamics in TWTS OFELs to standard FELs allows for a simple approach directly using the results of standard FEL theory to assess the radiation bandwidth and 3D effects, such as electron beam emittance and radiation diffraction, in TWTS OFELs which are not accounted for in the 1.5D theory. Accordingly the scaling laws for electron beam requirements in terms of energy spread, space charge parameter and normalized emittance as well as the requirement on the Rayleigh length of the radiation being discussed in ch. 2.3 are applicable for TWTS OFELs, too. These and all other scaling laws presented in this section and in other sections are summarized for completeness in tab. 6.1.

Many of the conditions given are limits on quantities describing the quality of laser or electron pulses. Since virtually every quality reduction leads to an increase in radiation bandwidth, quality requirements can be derived from their impact on radiation bandwidth increase in the same way the limits in ch. 2.3 have been derived. That is, the relative radiation bandwidth increase  $\Delta\lambda_{\text{FEL}}/\lambda_{\text{FEL}}$  is calculated from the TWTS OFEL radiation wavelength relation (5.11) for the first harmonic ( $n = 1$ ) and the limit is set by the intrinsic FEL bandwidth

$$\frac{\Delta\lambda_{\text{FEL}}}{\lambda_{\text{FEL}}} \approx 2\rho.$$

Parameter variations larger than this limit reduce the efficiency in driving the FEL instability which at least increases the gain length and reduces the photon output.

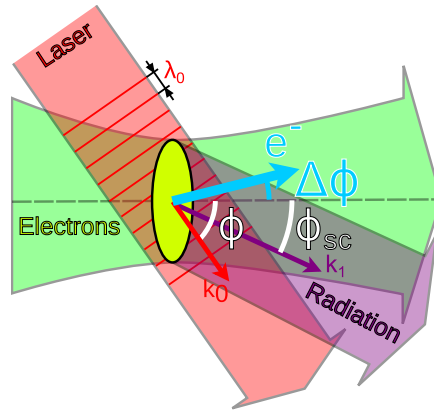


Figure 5.5.: Depicts the deviation in propagation angle  $\Delta\phi$  of an electron in a divergent beam. This electron produces radiation different from the nominal radiation wavelength due to the deviation in undulator period and radiation observation angle  $\Delta\phi$ .

Beyond the standard FEL scaling laws for electron beam and radiation requirements derived in this way in the first chapter there are scaling laws special to TWTS OFELs regarding the interaction geometry and the geometrical overlap of electrons and laser pulse as well as laser pulse quality and radiation walk-off.

Besides the electron beam emittance condition limiting electron beam divergence and ensuring good overlap, emittance is also a source of radiation bandwidth increase. For beams with non-zero normalized transverse emittance  $\epsilon_N$ , the propagation direction of a single electron can deviate from the mean propagation direction of the beam by

$$\Delta\phi = \epsilon_N / \gamma_0 \sigma_b, \quad (5.21)$$

where  $\sigma_b$  is again the electron beam rms cross-sectional radius. This individual deviation in propagation angle results in an individual deviation of interaction angle and radiation observation angle as visualized in fig. 5.5. The radiation wavelength of this electron is shifted from the minimum radiation wavelength emitted by straight propagating electrons due to the difference in undulator period  $\lambda_{\text{und}} = \lambda_{\text{Laser}} / (1 - \cos(\phi + \Delta\phi))$ . Although the wavelength shift is partly offset by the same angular difference in observation direction  $\phi_{\text{sc}} + \Delta\phi$  it contributes to bandwidth broadening and sets a limit on electron beam divergence

$$\frac{\gamma_0^2 \Delta\phi^2}{1 + a_0^2/2} \leq 2\rho, \quad (5.22)$$

assuming  $\Delta\phi/\phi \ll 1$ . This translates into a limit on normalized transverse emittance

$$\epsilon_N \leq \sigma_b \sqrt{2\rho(1 + a_0^2/2)}. \quad (5.23)$$

The laser pulse spot size at the interaction point and its duration must be large enough to provide the required interaction distance and full geometrical overlap of electrons and laser pulse. Assuming a flat-top transverse laser profile, the width  $w_y$  of the pulse in the horizontal direction, i.e. within the interaction plane spanned by laser and electron propagation direction, is in accordance with eq. (4.34) determined by the interaction distance

$$w_y = n_w L_{\text{int}} \sin \phi,$$

where  $n_w \gtrsim 1$  is a number measuring an increased pulse width from the minimum  $L_{\text{int}} \sin \phi$  needed for TWTS OFEL operation in order to save laser propagation distance in the setup providing focusing in the interaction plane which is depicted in fig. 4.8. The width in the vertical

direction  $w_x$ , i.e. the width to which the pulse is focused by the second cylindrical mirror in this setup, is given through the electron bunch rms cross-sectional radius  $\sigma_b$

$$w_x = \sqrt{2\pi}\sigma_b. \quad (5.24)$$

Using these two relations the required laser power  $P_{\text{Laser}}$  can be estimated from the optical undulator parameter  $a_0$  being related to laser irradiance  $I$ ,

$$P_{\text{Laser}} = I w_x w_y = \frac{\sqrt{8\pi}\pi^2 c^5 m^2 \epsilon_0}{e^2} \cdot \sigma_b \frac{a_0^2}{\lambda_{\text{Laser}}^2} n_w L_{\text{int}} \sin \phi$$

$$P_{\text{Laser}} [\text{TW}] = 34.29 \times 10^{-3} \cdot \sigma_b \frac{a_0^2}{\lambda_{\text{Laser}}^2} n_w L_{\text{int}} \sin \phi. \quad (5.25)$$

The corresponding laser pulse energy  $E_{\text{Laser}} = P_{\text{Laser}}\tau_0$  is estimated with the laser pulse duration  $\tau_0$  required to enclose the electron bunch of duration  $\tau_b$  and radius  $\sigma_b$ . One possible approximation for the required laser pulse duration has already been given where variations in optical undulator amplitude due to bad overlap were evaluated, cf. eq. (4.25),

$$\tau_0 \gtrsim \tau_b + \frac{\sigma_b}{c} \tan(\phi/2). \quad (5.26)$$

Another estimate obtained by approximating the electron bunch outline by an ellipsoid is given in ref. [68].

The chapter discussing the generation of laser pulses for TWTS OFELs has extensively dealt with laser irradiance variation  $\Delta I$  during the interaction already. These are important to control since they induce variations of optical undulator amplitude  $\Delta a_0/a_0 = (1/2)\Delta I/I$ , leading to radiation bandwidth broadening via  $\lambda_{\text{FEL}} \propto (1 + a_0^2/2)$ . An upper limit on laser irradiance variation is again obtained by error propagation

$$\frac{\Delta I}{I} \leq 4\rho \frac{1 + a_0^2/2}{a_0^2}. \quad (5.27)$$

This limit becomes in practice very demanding when aiming for undulator parameters of unity and beyond where undulator amplitude fluctuations may be required to stay within the sub-percent range. Providing laser pulses with such a high degree of uniformity may become challenging in an experiment due to surface imperfections of the many optical elements in a laser system which translate to phase and irradiance variation in the focus of the laser. Yet, this requirement regards essentially the experimentally easier to control transverse envelope of the pulse since electrons remain stationary within the longitudinal (i.e. temporal) envelope of the laser during interaction. Additionally, variations in laser envelope could in principle be remedied by a well controlled frequency chirp of the undulator [136, 137] which counterbalances the variation in undulator amplitude by a variation in undulator frequency. However, introducing a frequency chirp may considerably reduce the available laser intensity which can make this technique unpractical for TWTS OFELs.

Spatial variation of the undulator amplitude also causes a deflection of electrons by an angle  $\Delta\phi$  away from their original direction of propagation towards lower undulator amplitude regions due to the ponderomotive force  $\mathbf{F} = -mc^2 \nabla a_0^2 / 4\gamma_0$  [138], assuming  $a_0 \ll \gamma_0$ , associated with a gradient of undulator amplitude. A limit on laser irradiance variation is obtained by assuming a constant ponderomotive force during the entire interaction and linearly approximating the gradient  $\nabla a_0^2 \approx \sqrt{2/\pi} \Delta a_0^2 / \sigma_b$ . The resulting deflection angle  $\Delta\phi = \Delta a_0^2 L_{\text{int}} / \sqrt{8\pi} \gamma_0^2 \sigma_b$  is inserted into the limit for angular deviation (5.22). Then the second limit on acceptable laser irradiance variation is

$$\frac{\Delta I}{I} \leq \frac{4}{a_0} \left( \frac{\pi\rho(1 + a_0^2/2)\sigma_b^2\gamma_0^2}{L_{\text{int}}^2} \right)^{1/4}. \quad (5.28)$$

Finally, there is a limit on the maximum allowed radiation emission angle  $\phi_{sc}$  due to walk-off. Similar to diffraction of radiation, walk-off causes a part of the radiation to leave the electron bunch. A limit on  $\phi_{sc}$  is obtained by interpreting the distance after which the radiation has an offset of  $2\sqrt{2}\sigma_b$  from the electron beam axis as a Rayleigh length. Then the limit on radiation diffraction (2.15) can be reused to obtain

$$L_G < \frac{2\sqrt{2}\sigma_b}{\tan \phi_{sc}} \stackrel{1/\gamma_0 \leq \phi \ll 1}{\approx} 2\sqrt{2}\gamma_0^2 \phi \sigma_b, \quad (5.29)$$

where the approximation  $\tan \phi_{sc} \approx 1/\gamma_0^2 \phi$  valid for  $\gamma_0^{-1} \ll \phi \ll 1$  has been made. As can be seen from this relation, the walk-off becomes only relevant at very low electron energies and comparatively large interaction angles  $\phi = 1/\gamma_0$ .

## 6. EXAMPLES OF TWTS LIGHT SOURCES

Short-pulse high-yield ultraviolet to X-ray sources have found many applications nowadays. These range for example from studying laser ablation [139] and ionization dynamics with vacuum ultraviolet pulses during laser-matter interaction [140] to imaging single nano objects [76] and nanoscale dynamics [15] with extreme ultraviolet pulses. With hard X-ray pulses the structure of biological specimen can be determined or the impact of fast electron dynamics on laser ion acceleration studied [141]. Sources at  $\gamma$ -ray wavelengths can nondestructively assay spent fuel [142] or transmute long-living radioactive nuclear waste to short-lived isotopes [143]. Figure 6.1 provides an overview and gives references for experiments. These examples represent only a few of the possible applications making use of high-yield light sources within the wavelength range from 100 nm to 0.1 pm. By now the demand for beamtime at these kind of light sources exceeds the available beamtime by far [144].

TWTS OFELs and enhanced Thomson scattering sources can be used to realize high-yield and short-pulsed light sources at these wavelengths on a compact scale. The footprint of a TWTS light source can be one to two orders of magnitude smaller than existing large scale facilities. The possible femtosecond scale pulse durations and high photon numbers in the range of  $10^9$  to  $10^{12}$  per pulse for TWTS OFELs suit well for these kind of experiments.

The following sections present examples of TWTS OFELs emitting vacuum ultraviolet, extreme ultraviolet or X-ray radiation as well as an hard X-ray incoherent enhanced Thomson source. It is shown that TWTS OFELs can be realized today with existing technology for laser systems and electron accelerators.

Emphasis is put on the possibility to probe ion and electron distributions with femtosecond X-ray pulses from an Ångström TWTS OFEL in experiments performed at HZDR which explosively drive materials by irradiating these with short pulses from the petawatt laser system DRACO [KSc1]. These experiments may be conducted in the context of laser-ion-acceleration or warm-dense-matter [145–147] research. The short duration of the X-ray pulses thereby allows to obtain a sharp scattering image of picosecond fast process in the target while the high intensity allows to obtain a measurable scattering signal and the X-ray wavelength to penetrate the solid density target. By repeating these experiments under identical initial conditions one could for example observe the formation of shocks or the seeding and development of instabilities in the target [141] with multiple, temporally delayed Å pulses. For laser-ion-acceleration the plasma dynamics may then be linked to beam properties of the accelerated ions.

Figure 6.2 visualizes the setup within the Center for High-Power Radiation Sources at HZDR where the DRACO petawatt laser is utilized to irradiate the target. Thereby fast electron dynamics are induced which are probed by the Å TWTS OFEL driven by the PEnELOPE laser system. In this case of laser ion acceleration the target is ionized by the infrared laser pulse and electrons

Table 6.1.: Summary of the scaling laws used to estimate and tune the parameters of a TWTS OFEL setup. The three columns from left to right name the parameter of interest, its scaling law and a reference to the context where it appears and is explained in more detail. The table is subdivided into four parts corresponding from top to bottom to TWTS OFEL parameters, radiation parameters and requirements, electron bunch requirements, laser requirements and requirements on the optical setup depicted in fig. 4.8.

Description	Relation	Ref.
Optical undulator period	$\lambda_{\text{und}} = \lambda_{\text{Laser}} / (1 - \beta_0 \cos \phi)$	(2.1)
Radiated wavelength	$\lambda_{\text{FEL}} = \frac{\lambda_{\text{Laser}}(1 + a_0^2/2 + \gamma_0^2 \phi_{\text{sc}}^2)}{2\gamma_0^2(1 - \beta_0 \cos \phi)}$	(5.11)
Emission angle of coherent radiation for $\lambda_{\text{FEL}} \ll \lambda_{\text{Laser}}$	$\phi_{\text{sc}} \approx \frac{\sin \phi}{2\gamma_0^2(1 - \beta_0 \cos \phi)} (1 + a_0^2/2)$	(5.3)
Pierce parameter	$\rho = \left[ \frac{1}{16\gamma_0^3} \frac{I_b}{I_A} \left( \frac{\lambda_{\text{Laser}} a_0 f_b}{2\pi\sigma_b(1 - \beta_0 \cos \phi)} \right)^2 \right]^{1/3}$	(5.17)
Gain length	$L_G = \frac{\lambda_{\text{Laser}}}{4\pi\sqrt{3}(1 - \beta_0 \cos \phi)\rho}$	(5.18)
Interaction distance	$L_{\text{int}} \approx 16 \cdot L_G$	fig. 5.4
Radiated peak power	$P \approx \rho \gamma_0 m c^2 I_b / e$	(5.20)
Radiation defocusing	$\frac{L_G \lambda_{\text{FEL}}}{4\pi\sigma_b^2} < 1$	(2.15)
Walk-off	$\frac{L_G \tan \phi_{\text{sc}}}{2\sqrt{2}\sigma_b} < 1$	(5.29)
Relative electron energy spread	$\frac{\Delta\gamma_0}{\gamma_0} \leq \rho$	(2.12)
Emittance limit from $\lambda_{\text{FEL}}$ shift	$\epsilon_N \leq \sigma_b \sqrt{2\rho(1 + a_0^2/2)}$	(5.23)
Emittance limit for overlap	$\epsilon_N \leq 2\sigma_b^2 \gamma_0 / L_{\text{int}}$	(2.14)
Emittance limit for transverse coherence	$\frac{2\pi\epsilon_N}{\gamma_0 \lambda_{\text{FEL}}} = 0.5 \dots 10$	(2.17)
Space charge parameter	$\sqrt{\frac{I_b}{I_A} \frac{2}{\sigma_b^2 \gamma_0^3}} L_G < 1$	(2.13)
Laser width in interaction plane	$w_y = n_w L_{\text{int}} \sin \phi$	(4.34)
Laser focal width for overlap	$w_x = \sqrt{2\pi}\sigma_b$	(5.24)
Laser pulse duration for overlap	$\tau_0 \gtrsim \tau_b + \frac{\sigma_b}{c} \tan(\phi/2)$	(5.26)
Laser power	$P_{\text{Laser}} [\text{TW}] = 34.29 \times 10^{-3} \cdot \sigma_b \frac{a_0^2}{\lambda_{\text{Laser}}^2} n_w L_{\text{int}} \sin \phi$	(5.25)
Irradiance variation limit from wavelength shift	$\frac{\Delta I}{I} \leq 4\rho \frac{1 + a_0^2/2}{a_0^2}$	(5.27)
Irradiance limit from ponderomotive deflection	$\frac{\Delta I}{I} \leq \frac{4}{a_0} \left( \frac{\pi\rho(1 + a_0^2/2)\sigma_b^2 \gamma_0^2}{L_{\text{int}}^2} \right)^{1/4}$	(5.28)
Focal distance of second cylindrical mirror	$f_x = D_{\text{in},x} \sqrt{2\pi}\sigma_b / \lambda_{\text{Laser}}$	(4.32)
Effective focal distance of off-axis cylindrical mirror	$f_{\text{eff}} = \frac{D_{\text{in}} \sin \phi}{2\pi n_w (1 - \beta \cos \phi) \rho}$	(4.33)
Out-of-focus distance	$ \Delta f  \gtrsim \frac{L_{\text{int}} \sin^2 \phi}{2\rho(1 - \beta \cos \phi)}$	(4.30)

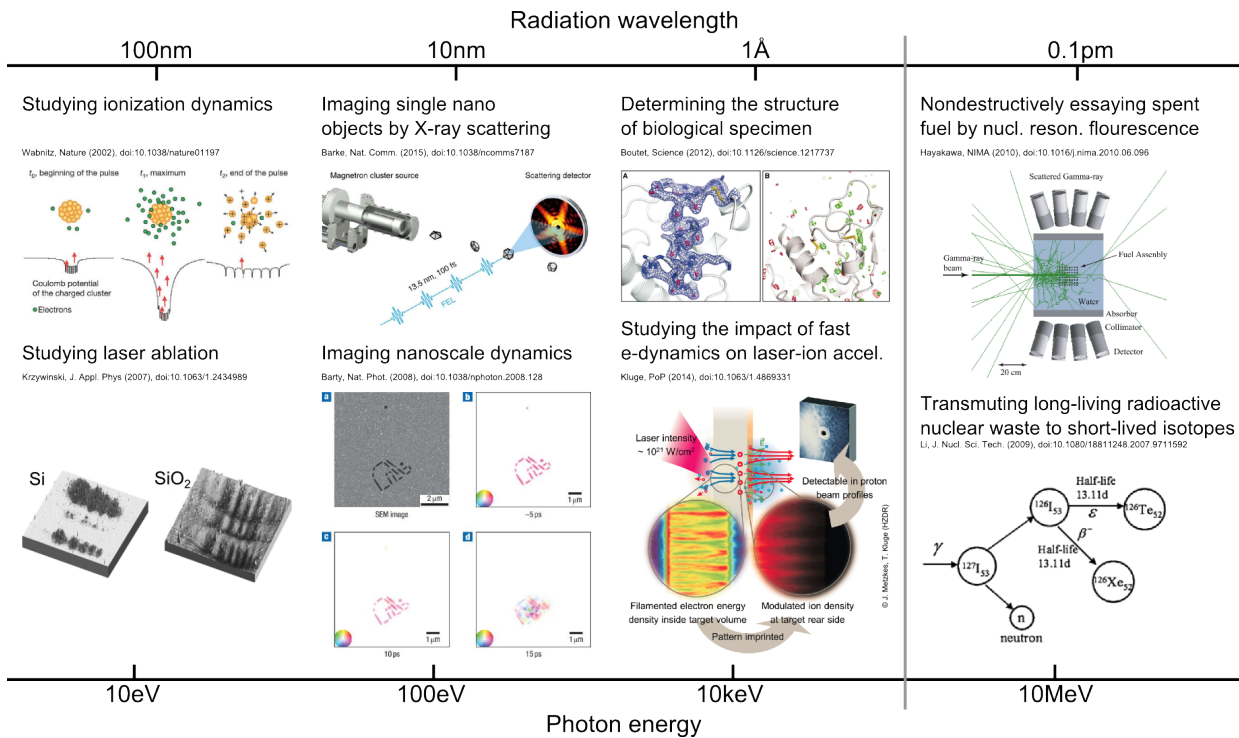


Figure 6.1.: Examples of applications of intense short-pulse light sources at vacuum ultraviolet (100 nm), soft X-ray (10 nm), hard X-ray (1 Å) or  $\gamma$ -ray wavelengths (0.1 pm). Today, free-electron lasers are high brightness sources at ultraviolet to hard X-ray wavelengths while  $\gamma$ -ray sources are realized by Thomson scattering. Thus the gray line divides between the spectral regions where high-yield sources with (left) or only limited (right) spatial coherence are available.

are accelerated out of the target by the laser ponderomotive force. The electric field building up between both ions in the target and electrons far from the target accelerate protons from the target surface but their beam properties depend on the properties of the accelerated electrons which are defined during the laser-target interaction. Linking plasma dynamics to ion beam properties becomes possible by repeatedly scattering pulses of the Å TWTS OFEL off the target in order to probe the rapidly changing electron distribution therein during and after laser irradiation. From the small-angle X-ray scattering (SAXS) images the electron distribution in the target can be reconstructed and modulations in electron density and their temporal evolution may be linked to properties of the accelerated proton beam. The design, requirements and performance of the Å TWTS OFEL is treated in detail in the last section of this chapter.

The presented examples of TWTS OFELs are driven by conventional or laser wakefield accelerated electrons. Laser wakefield acceleration allows for ultra-compact all-optical TWTS OFELs with the advantage of incoherent synchronization between laser and electrons. The optical design of the setups is detailed in the text as well as electron bunch and laser pulse requirements are discussed for the different TWTS OFELs. In the process of designing these sources the scaling laws of the last chapter are utilized and at the same time general design guidelines are deduced from these. The scaling laws are summarized in tab. 6.1.

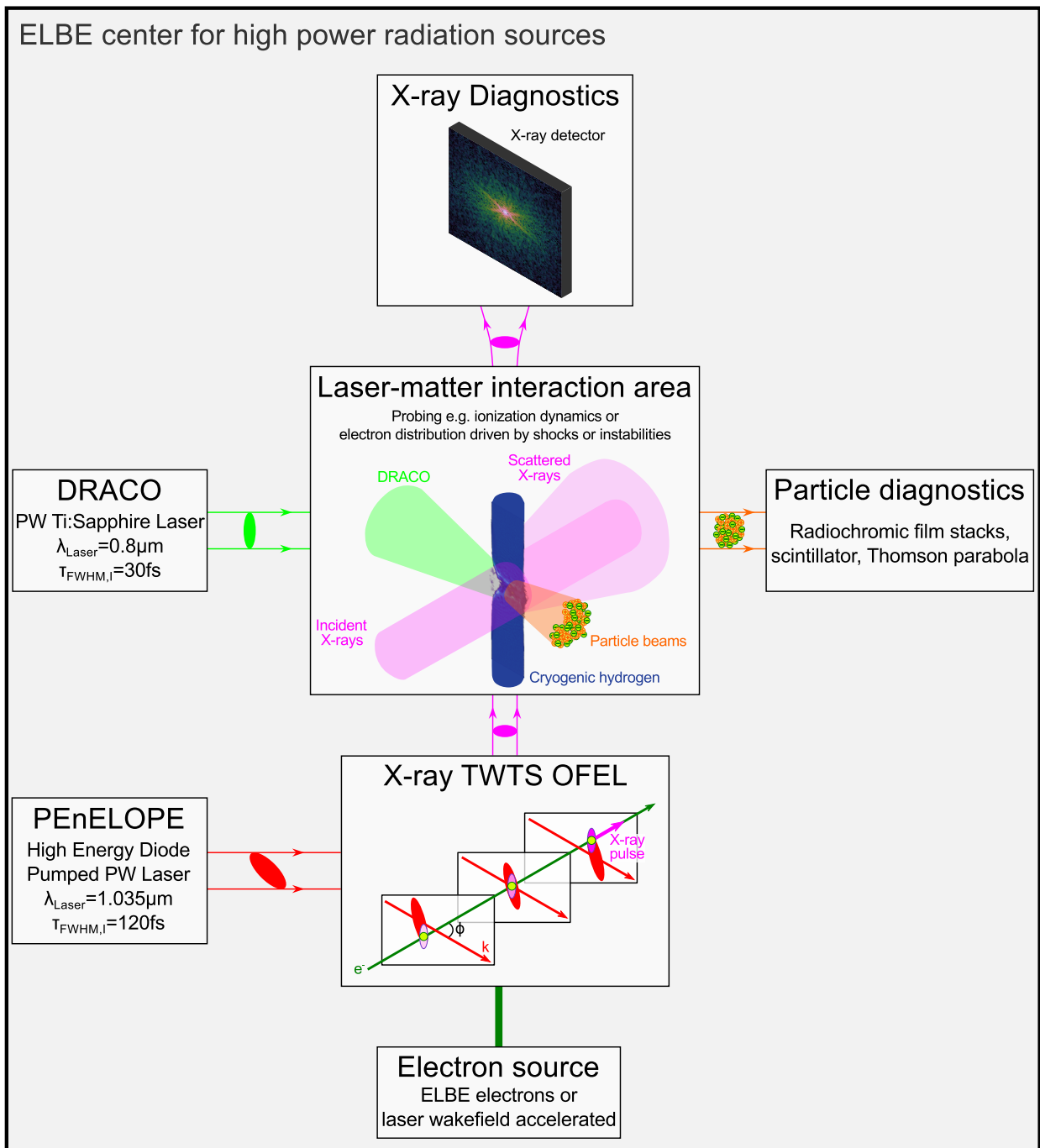


Figure 6.2.: Probing laser-driven solid-density matter with X-ray laser pulses at HZDR. While the solid density target can be pumped by the petawatt infrared laser DRACO, X-ray laser pulses can be provided by a TWTS OFEL utilizing infrared laser pulses from the petawatt laser system PEnELOPE as optical undulators. Sources for electron bunches driving the TWTS OFEL can be either the conventional radio-frequency accelerator ELBE or a compact laser wakefield accelerator. In this example protons are accelerated by irradiating a cryogenic hydrogen strand with DRACO laser pulses. The complex electron dynamics in the strand are probed by X-ray pulses from an Ångström TWTS OFEL in order to gain greater insight into the environment where protons are accelerated. This may allow to link initial laser and target conditions to proton pulse properties via their influence on electron acceleration.

## 6.1. HARD X-RAY ENHANCED THOMSON SOURCE

The first example of this chapter presents a setup of a yield-enhanced Thomson scattering source where Traveling-Wave Thomson-Scattering in a large interaction angle geometry is used to produce incoherent radiation with orders of magnitude higher spectral photon density than a head-on Thomson scattering source using the same laser system and electron source. These enhanced Thomson sources from TWTS could achieve spectral brightnesses in the hard X-ray range well above currently existing sources.

Today's hard X-ray sources are realized by head-on Thomson scattering due to available sub-micron optical undulator periods, cf. figs. 2.3 and 3.1 respectively, but are limited in interaction distance by the laser Rayleigh length. With TWTS geometries this limit does not exist anymore allowing for a significant brightness increase. In TWTS longer interaction distances are achievable and at the same time optical undulator amplitudes can be reduced to sub-relativistic levels which allows for higher photon yields at smaller bandwidth compared to head-on Thomson sources. High quality radiation from yield-enhanced Thomson sources by TWTS could be used for e. g. X-ray phase contrast or absorption imaging of dense and thick materials in order to non destructively detect cracks and other material defects [148–150], to obtain higher quality images in (medical) computer tomography [151–153], to assay spent nuclear fuel by nuclear resonance fluorescence [142], or for ultrafast nuclear science [154, 155].

Especially attractive is to combine laser wakefield acceleration of electrons and TWTS to build ultra-compact, high-yield radiation sources. Numerous possible applications of laser wakefield accelerator-based light sources are reviewed in ref. [156].

This specific example of an enhanced Thomson source utilizes electron bunches as they are supposed to be provided by the ELBE accelerator at HZDR using the superconducting radio-frequency electron gun [157], featuring an energy of 40 MeV, and a normalized transverse emittance of 2 mm mrad. The laser pulse scattered off these electrons has a wavelength of 800 nm, 25 fs pulse duration, 1 J energy and is focused to a diameter of 50  $\mu\text{m}$  which is large enough to contain the divergent electron bunch over the entire interaction distance.

The distribution of scattered photons in solid angle and energy is compared in fig. 6.3 for a head-on geometry and a TWTS geometry at 120° interaction angle. The photon distributions were calculated by Alexander Debus with the 3D radiation code CLARA [67, 158]. The scattered radiation in the case of head-on Thomson scattering is broader in bandwidth and distributed over a larger solid angle. The former results from the shorter interaction duration of the head-on geometry which is given in number of undulator periods  $N_{\text{und}}$  by approximately half the laser longitudinal full width at half maximum  $\sqrt{\ln 2} c \tau_0$  divided by the optical undulator period  $\lambda_{\text{Laser}}/2$ . In the TWTS geometry the number of undulator periods can be much larger since the requirement of an equal radiation wavelength at a smaller interaction angle requires to reduce the undulator parameter which can be achieved by increasing the laser width in the interaction plane resulting in longer interaction distances. Therefore the scattered photons are gathered within a smaller bandwidth leading to a higher photon density. The smaller undulator parameter also results in a better collimation of the radiation since the deflection angle of oscillating electrons scales with the undulator parameter which even further increases the photon density in TWTS setups. Together this leads to an almost two orders of magnitude higher photon density of the 120° TWTS setup compared to the head-on setup.

### 6.1.1. DETERMINING OPTICAL SETUP PARAMETERS

The large interaction angle of  $\phi = 120^\circ$  of this TWTS source requires a large pulse-front tilt of  $\phi/2 = 60^\circ$  to ensure optimum overlap of electrons and laser. As explained in ch. 4.1, with large pulse-front tilts dispersion needs to be compensated along the electron trajectory. If dispersion

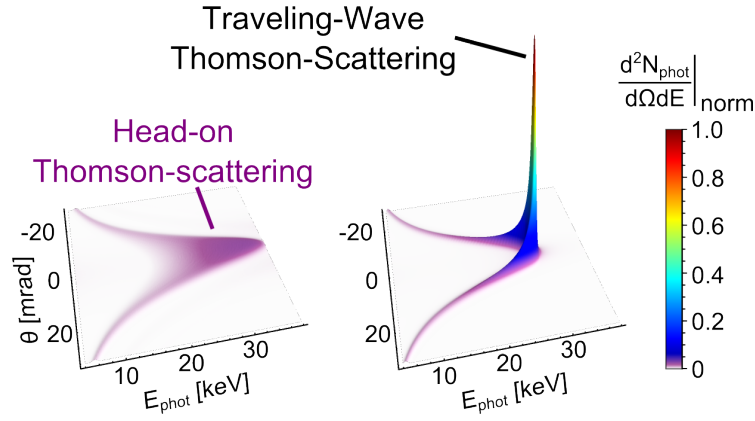


Figure 6.3.: Comparison of simulated spectral photon density from head-on Thomson scattering and a  $120^\circ$  interaction angle TWTS geometry. Both scenarios utilize a 25 fs, 1 J,  $\lambda_{\text{Laser}} = 800$  nm laser pulse focused to a diameter of  $50 \mu\text{m}$  full width at half maximum and a 40 MeV, 2 mm mrad norm. transv. emittance electron beam. The photon distribution for head-on scattering is broad in bandwidth and emission angle due to nonlinear Thomson scattering. In the TWTS setup the optical undulator amplitude can be reduced into the sub-relativistic regime by utilizing wider laser pulses. This allows for an increase of interaction distance to 42 mm instead of only half the longitudinal laser pulse length and at the same time reduces the bandwidth and angular spread of the beam leading to a significant increase of spectral photon density. (Originally in [KS2])

is not compensated, the laser pulse duration will increase to  $71\tau_0$  towards the end of the interaction when starting fully compensated. This requires a setup utilizing the plane of optimum compression. Fig. 4.4 sketches such a setup making use of two gratings to control the orientation of plane of optimum compression and pulse-front tilt independently of each other. According to fig. 4.3b their orientation needs to be  $\alpha_{\text{poc}} = 30^\circ$  and  $\alpha_{\text{tilt}} = 60^\circ$ , respectively.

Optical setup parameters, in terms of first and second grating incidence angles as well as line densities, are found from the coupled analytical relations 4.20 for second grating incidence and diffraction angle,  $\psi_{\text{in},2}$  and  $\psi_{\text{out},2}$  respectively, at given interaction angle. The procedure is outlined in the following. At first, the first grating line density  $n_1$  and corresponding range of incidence angles  $\psi_{\text{in},1}$  ensuring correct orientation of pulse-front tilt and plane of optimum compression are determined by scanning for the existence of a solution to the first equation of eq. (4.20),  $\sin \psi_{\text{in},2} = s_1(\sin \psi_{\text{out},2}, \psi_{\text{in},1}, n_1, \phi)$ , at different  $n_1$  and  $\psi_{\text{in},1}$ . The existence of a solution to this first equation at preset  $n_1$  and  $\psi_{\text{in},1}$  is determined from the existence of a root of the implicit function

$$0 = \sin \psi_{\text{in},2} - s_1(s_0(\sin \psi_{\text{in},2}, \psi_{\text{in},1}, n_1, \phi), \psi_{\text{in},1}, n_1, \phi), \quad (6.1)$$

where the root of this function  $\psi_{\text{in},2,\text{sol}}$  is actually the second grating incidence angle yielding a proper TWTS setup at the corresponding  $n_1$  and  $\psi_{\text{in},1}$ . This implicit function is obtained by inserting the second relation of the equation system (4.20)  $\sin \psi_{\text{out},2} = s_0(\sin \psi_{\text{in},2}, \psi_{\text{in},1}, n_1, \phi)$  into the first equation. By a parameter scan, the implicit function (6.1) is evaluated for  $\psi_{\text{in},2} \in [-90^\circ, 90^\circ]$  at many  $\psi_{\text{in},1}$  and fixed  $n_1$  as it is depicted in fig. 6.4. The range in  $\psi_{\text{in},1}$  for which the function is drawn is determined by demanding diffraction only into  $-1$ st order at the first grating in order to achieve high diffraction efficiency. By repeating these scalings for different  $n_1$  the range of usable first grating line densities is found to be between 1200 l/mm to 1500 l/mm for this  $\phi = 120^\circ$  TWTS setup. The largest range of usable first grating incidence angles is available with  $n_1 = 1250$  l/mm gratings where  $n_1 \lambda_{\text{Laser}} = 1$  and diffraction into higher orders does not

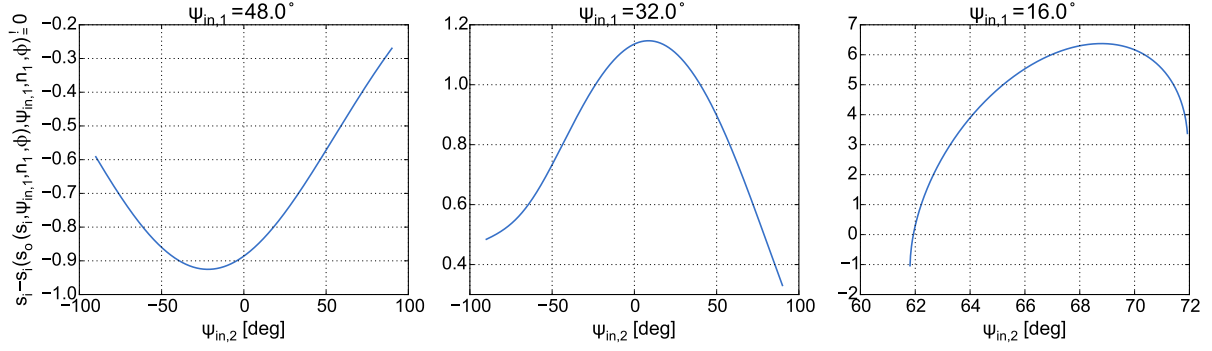


Figure 6.4.: Scaling of the implicit function  $\sin \psi_{in,2} = s_1(s_0(\sin \psi_{in,2}, \psi_{in,1}, n_1, \phi), \psi_{in,1}, n_1, \phi)$  with second grating incidence angle  $\psi_{in,2}$  for three different first grating incidence angles  $\psi_{in,1} \in (48^\circ, 32^\circ, 16^\circ)$  and fixed first grating line density  $n_1 = 1500$  l/mm. The range of  $\psi_{in,1}$  is determined by demanding diffraction only into  $-1$ st order. Roots of the implicit function correspond to proper TWTS setups with correct orientation of pulse-front tilt and plane of optimum compression. These are only existent for small first grating incidence angles  $\psi_{in,1} \sim 10^\circ$  and line densities  $n_1 \sim 1200$  l/mm to  $1500$  l/mm for this example of  $120^\circ$  interaction angle and  $800$  nm laser wavelength.

takes place.

These line densities where  $n_1 \lambda_{\text{Laser}} = 1$  generally mark an optimum with respect to variability of a setup for realizing also other interaction angles. Further, these line densities are the only ones usable for very large interaction angle setups close to  $180^\circ$  since only these allow for the realization of the required large pulse-front tilts due to their attainable large deviation between angle of incidence and angle of diffraction. Other possibilities to achieve correct orientation of pulse-front tilt and plane of optimum compression do not seem to be feasible.

Out of the range of possible first grating line densities the largest possible,  $n_1 = 1500$  l/mm, is chosen. It produces pulses with larger angular dispersion than the lower line density gratings which allows to produce a large amount of spatial dispersion on a shorter propagation distance from first to second grating. Spatial dispersion generated during propagation in the grating pair precompensates spatial dispersion generated after diffraction at the second grating. This is necessary since the laser pulse-front orientation has different sign during propagation from first to second grating than during propagation from second grating to the interaction point.

Apart from dispersion issues, whether a specific  $n_1$  is suitable may also depend on the values of the remaining parameters ( $\psi_{in,1}, \psi_{in,2}, n_2$ ) and (on-stock) availability of this grating pair. For fixed  $n_1$  the usable range in second grating incidence angles  $\psi_{in,2}$  and line densities  $n_2$  can be determined by plotting all the solutions  $\psi_{in,2,sol}$  of the equation system (4.20) and their corresponding  $n_{2,sol}$ , obtained from eq. (4.21) using  $\sin \psi_{out,2,sol} = s_0(\sin \psi_{in,2,sol}, \psi_{in,1}, n_1, \phi)$ , in dependence of the usable first grating incident angles which yield a proper TWTS setup for this  $n_1$ . The usable ranges in  $n_2$  and  $\psi_{in,2}$  for this TWTS source are shown in figs. 6.5a and 6.5b, respectively, at a chosen first grating line density of  $1500$  l/mm. The choice of a specific  $n_2$  can be facilitated by comparing the corresponding  $\psi_{in,2}$  to the Littrow angle of this grating as it is done in the figure. Since the combination  $n_1 = 1500$  l/mm,  $n_2 = 2300$  l/mm allows for a small deviation of second grating incidence angle from its Littrow angle this grating pair is the final choice for the  $120^\circ$  TWTS setup.

Now that the grating pair is chosen only the first grating incidence angle and second grating rotation angle  $\epsilon$  are left to be determined. This is easily done by plotting in dependence of these two parameters contours of constant pulse-front tilt and plane of optimum compression

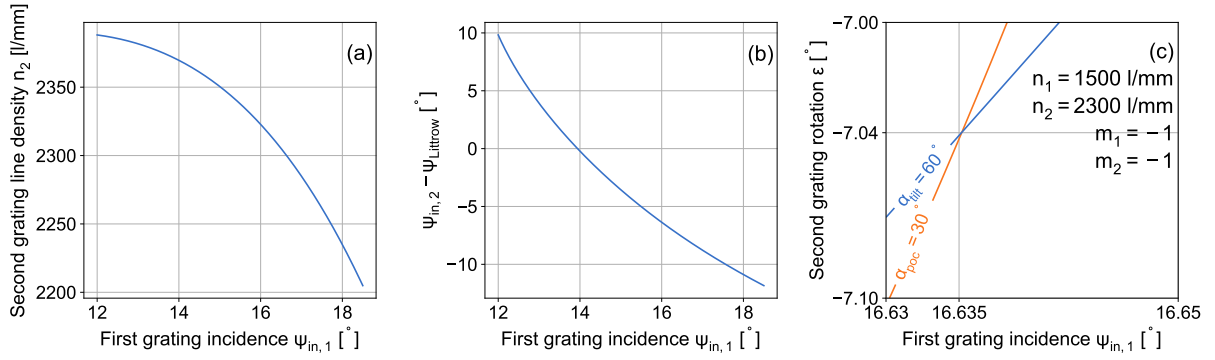


Figure 6.5.: For the  $\phi = 120^\circ$  TWTS scenario the scaling of (a) second grating line density  $n_2$  and (b) deviation of second grating incidence angle  $\psi_{in,2}$  from the gratings Littrow angle  $\psi_{Littrow}(n_2)$  is plotted in dependence of first grating incidence angle  $\psi_{in,1}$  at  $n_1 = 1500$  1/mm. (c) Dependence of second grating rotation angle  $\epsilon$  on  $\psi_{in,1}$  to maintain constant orientation of pulse-front tilt and plane of optimum compression at fixed line densities  $n_1 = 1500$  1/mm,  $n_2 = 2300$  1/mm. (a) and (b) are used to choose second grating line density by taking second grating diffraction efficiency into consideration which is high for second grating incidence angles close to their Littrow angle. (c) is used to determine  $\psi_{in,1} = 16.635^\circ$  and  $\epsilon = -7.043^\circ$  which yield correct orientation of pulse-front tilt  $\alpha_{tilt} = 60^\circ$  and plane of optimum compression  $\alpha_{poc} = 30^\circ$  for  $n_1 = 1500$  1/mm and  $n_2 = 2300$  1/mm. (Originally in [KS4])

as depicted in fig. 6.5c. The pair ( $\psi_{in,1} = 16.635^\circ$ ,  $\epsilon = -7.043^\circ$ ) corresponding to the crossing point of the contours  $\alpha_{tilt} = 60^\circ$  and  $\alpha_{poc} = 30^\circ$  mark the working point of the setup with the chosen grating pair ( $n_1 = 1500$  1/mm,  $n_2 = 2300$  1/mm).

A sketch of the setup is shown in fig. 6.6. The laser pulse input diameter is  $D_{in} = 50$  mm. After diffraction at the first grating the pulse propagates 15 cm to the second grating which adjusts pulse-front tilt and plane of optimum compression orientation. The propagation distances between first and second grating as well as second grating to cylindrical mirror are kept as short as possible in order to keep the setup compact. The overall setup size is essentially determined by the focusing distance of the cylindrical mirror providing focusing in the vertical direction. Its focal length  $f = 2.5$  m is determined by the target laser focal width of  $50 \mu\text{m}$  full-width at half-maximum of the intensity profile. The focusing distance covered by the laser pulse is increased to almost 2.9 m due to its non-normal incidence. While the laser pulse covers this distance its width increases significantly due to spatial dispersion arising from the large pulse-front tilt of  $60^\circ$ .

Two simple possibilities to precompensate spatial dispersion developing during propagation exist. First, another upstream grating pair could be used to generate opposite spatial dispersion. This grating pair could have much higher line density than the gratings used to adjust pulse-front tilt and plane of optimum compression which would allow to keep the setup compact.

Second, the grating pair already implemented in this setup could be used to generate the necessary precompensation by increasing the grating separation distance  $L_{grating}$ , though the pulse-front tilt after diffraction at the first grating would require 10 m grating separation in order to generate enough spatial dispersion. The necessary grating separation distance can be estimated

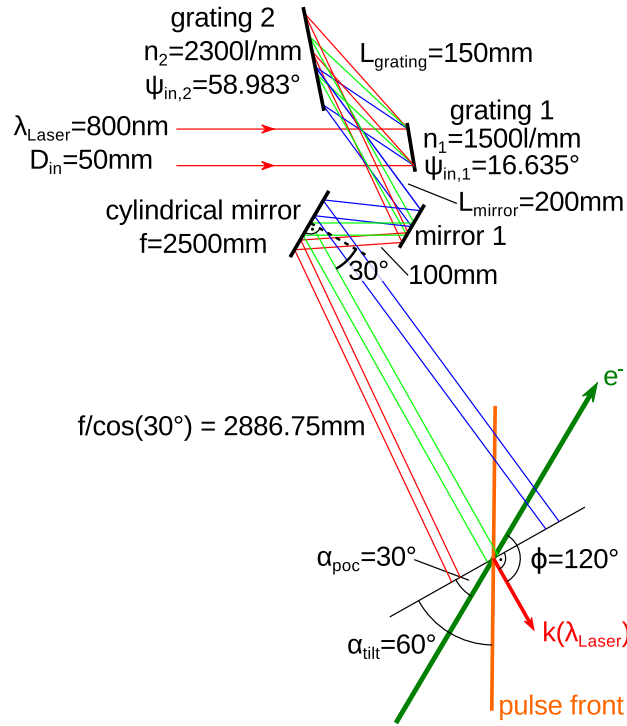


Figure 6.6.: Sketch of the hard X-ray enhanced Thomson source by TWTS at an interaction angle  $\phi = 120^\circ$  (not to scale). After diffraction at the first grating ray paths of different frequencies contained within the pulse spectrum are drawn. Blue and red rays correspond to edges of the 80 nm wide pulse spectrum, i.e. 760 nm and 840 nm, respectively. Spatial dispersion significantly increases the horizontal pulse width during vertical focusing. (Originally in [KS4])

from spatial dispersion evolution after diffraction at the second grating, cf. (4.38),

$$SD(z) = \frac{\cos \psi_{out,2}}{\cos \psi_{in,2}} \frac{L_{grating}}{\Omega_0} \tan \alpha_{tilt,1} - \frac{z}{\Omega_0} \tan \alpha_{tilt,2}$$

$$\Leftrightarrow L_{grating} = L_{prop} \frac{\cos \psi_{in,2} \tan \alpha_{tilt,2}}{\cos \psi_{out,2} \tan \alpha_{tilt,1}},$$

where  $L_{prop}$  is the laser propagation distance from the second grating to the interaction point. However, this estimate is not straightforward since generating more spatial dispersion within the grating pair also causes an increase in pulse width. This in turn requires larger distances between second grating and first mirror as well as first mirror and cylindrical mirror which in turn makes a larger grating separation distance necessary. Therefore, spatial dispersion precompensation by another grating pair of high line density might be the compacter variant in cases where spatial dispersion precompensation is really necessary.

### 6.1.2. MODELING THE SETUP IN ZEMAX

In order to complement the analytical approach used in this thesis to calculate orientations of pulse-front tilt and plane of optimum compression this enhanced Thomson scattering setup was also modeled in ZEMAX [159]. ZEMAX is an optical design software using ray tracing to simulate propagation of rays through optical setups. It allows to determine the orientations of pulse-front tilt and plane of optimum compression from raytracing without approximation which is used to validate the analytical formulas providing their orientation.

Table 6.2.: Results of sampling time delay  $TD$  and group-delay dispersion  $GDD$  along planes coinciding with expected pulse-front and plane of optimum, respectively, for the  $\phi = 120^\circ$  incoherent TWTS hard X-ray source. Nearly constant time delay and group-delay dispersion along expected pulse front and plane of optimum compression, respectively, demonstrate good agreement between independent simulation and analytic relations (4.14) for pulse-front tilt and plane of optimum compression orientation.

meas. along pulse-front	left edge	center	right edge
<b>Time delay <math>TD</math> [ps]</b>	17801.4909	17801.4894	17801.4879

meas. during interaction	begin	middle	end
<b>Group delay dispersion <math>GDD</math> [ps<sup>2</sup>]</b>	-15.401934	-15.401926	-15.401918

Within ZEMAX orientations of pulse-front tilt and plane of optimum compression are determined from the optical path lengths differences between rays of different wavelengths. More specifically, optical path lengths  $OPTH_i$  associated with different laser wavelengths  $\lambda_i$  are first converted to optical phases  $\varphi_i = \frac{2\pi}{\lambda_i}OPTH_i$ , where three wavelength  $\lambda_2 < \lambda_1 = \lambda_{\text{Laser}} < \lambda_3$  are traced through the setup, and second these wavelength specific phases are used to numerically calculate a derivative of the optical phase  $\varphi$  with respect to laser frequency. The first and second derivative of the optical phase represent time-delay  $TD$  and group-delay dispersion  $GDD$ , respectively,

$$TD = \left. \frac{d\varphi}{d\Omega} \right|_{\Omega=\Omega_0} \quad GDD = \left. \frac{d^2\varphi}{d\Omega^2} \right|_{\Omega=\Omega_0}.$$

According to eq. (4.13) time-delay is constant along the pulse-front and can thus be used to evaluate pulse-front tilt whereas group-delay dispersion is constant within the plane of optimum compression and can thus be used to evaluate its orientation. Time-delay and group-delay dispersion are calculated from the wavelength specific optical phases  $\varphi_i$  by

$$TD = \frac{\varphi_3 - \varphi_2}{2(\lambda_1 - \lambda_2)} \left( -\frac{2\pi c}{\Omega_0^2} \right) \quad GDD = \frac{\varphi_3 - 2\varphi_1 + \varphi_2}{(\lambda_1 - \lambda_2)^2} \left( \frac{2\pi c}{\Omega_0^2} \right)^2 - \frac{2}{\Omega_0} TD. \quad (6.2)$$

In ZEMAX the whole calculation is implemented in a macro which is written in the ZEMAX Programming Language ZPL and printed in appendix A. Table 6.2 list results of a  $TD$  and  $GDD$  sampling in ZEMAX of this enhanced Thomson scattering setup. Both  $TD$  and  $GDD$  are sampled at three different positions within planes that are oriented along pulse-front and plane of optimum compression as expected by the analytical expressions (4.19).  $TD$  is sampled at the center as well as left and right edge of the transverse pulse extent.  $GDD$  at begin, middle and end of the electron bunch path in the interaction region.

From both samplings it can be concluded that the analytical formulas derived within this thesis are consistent with raytracing in ZEMAX. The difference in time delay along the pulse front amounts to a 30  $\mu\text{rad}$  deviation in pulse-front tilt angle which results in 1% irradiance fluctuation during the interaction as evaluated from eq. (4.22). The difference in group-delay dispersion along the plane of optimum compression amounts to an increase of pulse duration to  $1.00004\tau_0$  during interaction. Both approximations assume full spatial and group delay dispersion in the middle of the interaction.

All things considered, this example clearly shows that incoherent TWTS light sources can be realized today. This enhanced Thomson setup produces high brightness hard X-ray radiation utilizing commercially available optics and a commercially available 800 nm, 1 J, 25 fs laser system

[160]. A yield-enhanced Thomson scattering setup using TWTS can be a first step towards a TWTS OFEL realization but at lower electron and laser quality requirements making it an ideal testbed. Two substantial challenges for the realization of TWTS OFELs are already faced in the realization of an enhanced Thomson source. First, diagnostic tools detecting and characterizing large pulse-front tilts and the plane of optimum compression orientation of TWTS pulses are required. Second, synchronization between electron bunch and laser pulse arrival time at the interaction point is required on the pulse duration level when aiming for high-duty TWTS light source operation. This could be achieved with an all-optical synchronization scheme similar to the system implemented at DESY [161] which demonstrated better than 30 fs rms facility-wide timing. Such a system is currently commissioned at HZDR, too [162].

The next example explains the details of a TWTS OFEL realization and prospects the possibilities of TWTS when high quality electrons bunches and laser pulses are available.

## 6.2. A VACUUM ULTRAVIOLET TWTS OFEL REALIZABLE TODAY

Vacuum ultraviolet (VUV) radiation from this TWTS OFEL could be used to study e. g. nonlinear light-matter interactions in terms of ionization dynamics in many-particle systems [140], reaction kinetics at surfaces with temporal resolution which is of relevance to engineering catalysts for the chemical or pharmaceutical industry [163–165], or to study ablation from material surfaces by intense ultraviolet irradiation being relevant, for example, to micromachining and -structuring as well as damage studies [139, 166].

Moreover, this VUV TWTS OFEL is realizable today with existing technology for laser systems and electron accelerators. A setup similar to the one presented in the following can serve as a proof-of-principle experiment for the demonstration of TWTS OFELs.

A VUV TWTS OFEL provides radiation at a wavelength being long compared to wavelengths available at existing extreme ultraviolet and X-ray free-electron lasers but making a start on a TWTS OFEL realization at a longer radiation wavelength has the advantage of lower laser pulse and electron bunch quality requirements.

The VUV TWTS OFEL design utilizes an out-of-focus interaction geometry as it is sketched in fig. 4.8. The laser system of this setup is of PEnELOPE [104] type, providing petawatt laser pulses with a final energy of 120 J at a pulse duration of 120 fs, a corresponding bandwidth of 50 nm and a wavelength of  $\lambda_{\text{Laser}} = 1.035 \mu\text{m}$ . An overview on the complete set of electron and optical undulator parameters gives tab. 6.3. Laser and optical components parameters as well as alignment tolerances are given in tab. 6.4 and 6.5, respectively.

The remainder of this example illustrates how to use all of the relevant scaling laws derived in this thesis, and summarized in tab. 6.1, in order to determine these parameters.

### 6.2.1. DETERMINING ELECTRON BUNCH PARAMETERS

Electrons are provided by a high brightness electron gun as they are commonly used across all extreme ultraviolet (EUV) to X-ray FEL facilities nowadays. These typically deliver 3 MeV to 8 MeV electron bunches of 100 pC to 500 pC charge, 2 ps to 9 ps rms duration, 0.1% relative rms energy spread and 0.5 mm mrad to 1 mm mrad normalized transverse emittance. Currently ongoing development projects based on photo cathodes exist at e.g. Cornell, FERMI@Elletra, HZB, HZDR, KIT, LCLS, PITZ and PSI where both normal as well as superconducting acceleration cavities are under investigation, and SACLA uses a thermionic cathode in their injector [109, 167–175].

Electron bunch parameters in this example are taken from the FERMI electron gun providing  $E_b = 4.7 \text{ MeV}$ ,  $Q = 350 \text{ pC}$ ,  $\sigma_{t,b} = 2.4 \text{ ps}$ ,  $\epsilon_n = 0.5 \text{ mm mrad}$  and  $\sigma_E = 9 \text{ keV}$  rms energy spread

Table 6.3.: Parameters and requirements on electrons and optical undulator for the VUV TWTS OFEL radiating at 100 nm and being realizable today.

Electron, laser and undulator parameters	VUV TWTS OFEL
Resonant wavelength [nm]	100
Interaction angle [°]	10.1
Undulator wavelength [ $\mu\text{m}$ ]	65
Electron energy [MeV]	15
Bunch charge [pC]	350
Peak current [kA]	0.8
Bunch duration (rms) [fs]	175
Bunch cross-sectional radius (rms) [ $\mu\text{m}$ ]	7
Norm. transv. emitt. [mm mrad]	0.5
Rel. energy spread	0.8%
Undulator parameter $a_0$	2
Transv. intensity profile stability	2.5%
Gain length [mm]	0.35
Interaction distance [mm]	5.66
Peak VUV power [MW]	104
Number of photons	$23 \times 10^{12}$
Peak spectral brightness [photons/(s mm <sup>2</sup> mrad <sup>2</sup> 0.1% bandwidth)]	$3 \times 10^{26}$

bunches [167].

Since delivered peak currents of  $I_p = Q/\sqrt{2\pi}\sigma_{t,b} = 58 \text{ A}$  are too low for OFEL operation, longitudinal bunch compression is necessary to achieve electron densities suitable for OFEL operation. This compression is accomplished by an accelerator radio-frequency cavity which decelerates the head and accelerates the tail of an electron bunch compared to its center. Subsequent propagation through a magnetic chicane consisting of four dipole magnets leads to longitudinal compression due to path length differences between electrons of different energies, where higher energy corresponds to shorter path length [176].

Producing an energy chirp in the bunch in order to compress it increases its total energy spread. Assuming the product  $\epsilon_{\text{long}} = \sigma_{t,b}\sigma_E$ , being proportional to the longitudinal emittance of the bunch, is constant during compression [78, sec. 13.4], the total rms energy spread of a bunch after compression to a desired peak current  $I_p$  is given by

$$\sigma_E = \frac{\sqrt{2\pi}I_p\epsilon_{\text{long}}}{Q}. \quad (6.3)$$

The relative energy spread of the bunch  $\sigma_E/E_b$ , being a significant quantity for OFEL operation, c.f. tab. 6.1, can be reduced again by further accelerating the bunch in order to increase its energy  $E_b$ . The corresponding relative energy spread then sets the required acceptance of the OFEL.

The rest of the OFEL parameters is obtained from the scaling laws in tab. 6.1 as it is shown in the following.

### CHOSING ELECTRON BUNCH ENERGY

The choice of electron bunch energy is intrinsically connected to a choice of interaction angle  $\phi$  since both determine the radiation wavelength  $\lambda_{\text{FEL}}$  via the Thomson formula (3.1). In order to get an impression on whether high or low interaction angles are preferable for TWTS OFELs in the

Table 6.4.: Parameters of optical setup components to form laser pulse for the VUV TWTS OFEL radiating at 100 nm and being realizable today.

Optical setup parameters	VUV TWTS OFEL
Laser wavelength $\lambda_{\text{Laser}}$ [ $\mu\text{m}$ ]	1.035
Laser cut-off bandwidth [nm]	50
Laser pulse duration as FWHM of irradiance [fs]	120 ( $\tau_0 = 102$ )
Laser peak power $P_{\text{Laser}}$ [TW]	997
Laser oversize at interaction point $n_w$	1.12
Laser input diameter $D_{\text{in}}$ [cm]	17.5
1st grating incidence angle $\psi_{\text{in},1}$ [ $^\circ$ ]	40.56
1st grating line density $n_1$ [1/mm]	1000
1st grating diffraction angle $\psi_{\text{out},1}$ [ $^\circ$ ]	-22.629
Grating separation $L_{\text{grating}}$ [m]	3.603
2nd grating rotation angle $\epsilon$ [ $^\circ$ ]	-4.343
2nd grating incidence angle $\psi_{\text{in},2}$ [ $^\circ$ ]	18.286
2nd grating line density $n_2$ [1/mm]	1030
2nd grating diffraction angle $\psi_{\text{out},2}$ [ $^\circ$ ]	-48.789
Distance between 2nd grating and off-axis cylindrical mirror $L_{\text{mirror}}$ [m]	2.0
Deflection angle at off-axis cylinder $\psi_{\text{defl}}$ [ $^\circ$ ]	15
Off-axis cylinder effective focal distance $f_{\text{eff}}$ [m]	32.429
Out-of-focus distance $\Delta f$ [m]	-0.647
Distance between off-axis cylinder and interaction point $z_{\text{prop}}$ [m]	31.783
Final pulse-front tilt angle $\alpha_{\text{tilt}}$ [ $^\circ$ ]	5.05
Final orientation of plane of optimum compression $\alpha_{\text{poc}}$ [ $^\circ$ ]	-79.896
Group-delay dispersion pre-compensation $GDD_0$ [ps $^2$ ]	8.758

Table 6.5.: Tolerances of optical component parameters for the VUV TWTS OFEL radiating at 100 nm and being realizable today.

Optical setup parameter tolerances	VUV TWTS OFEL
Interaction angle $\Delta\phi$ [mrad]	14
1st grating incidence angle $\Delta\psi_{\text{in},1}$ [mrad]	14
2nd grating rotation angle $\Delta\epsilon$ [mrad]	14
Grating separation $\Delta L_{\text{grating}}$ [mm]	290
Distance between 2nd grating and off-axis cylindrical mirror $\Delta L_{\text{mirror}}$ [m]	many
Effective focal distance $\Delta f_{\text{eff}}$ [mm]	2400

out-of-focus geometry, the scaling of effective focal distance  $f_{\text{eff}}$  of the off-axis cylindrical mirror with interaction angle is examined. This scaling largely determines the required propagation distance  $z_{\text{prop}}$  of the laser pulse from the off-axis cylindrical mirror to the interaction point

$$z_{\text{prop}} = f_{\text{eff}} - |\Delta f| = \left(1 - \frac{|\Delta f|}{f_{\text{eff}}}\right) f_{\text{eff}} \approx f_{\text{eff}},$$

where  $\Delta f$  is the out-of-focus distance and  $\Delta f/f_{\text{eff}} = \pi w/D_{\text{in}} \ll 1$  is assumed since otherwise focusing would not be required. The scaling of effective focal distance with interaction angle  $\phi$  and radiation wavelength  $\lambda_{\text{FEL}}$  is

$$f_{\text{eff}} = \frac{D_{\text{in}} \sin \phi}{2\pi n_w (1 - \beta \cos \phi) \rho} \propto \frac{\sin \phi}{(1 - \beta \cos \phi)^{5/6}} \lambda_{\text{FEL}}^{-1/2}$$

which shows that a TWTS OFEL will be more compact if a larger interaction angle is chosen to radiate at a target wavelength. On the other hand, a larger interaction angle increases electron bunch quality requirements since the Pierce parameter becomes smaller with a larger interaction angle

$$\rho \propto (1 - \beta \cos \phi)^{-1/6} \lambda_{\text{FEL}}^{1/2}.$$

Therefore, whenever a TWTS OFEL setup is designed, a trade-off between compactness and electron bunch quality requirements needs to be found. Further, these scalings suggest that a proof-of-principle experiment of a TWTS OFEL would not aim at X-ray radiation wavelengths but rather at vacuum ultraviolet or extreme ultraviolet wavelengths because longer radiation wavelengths reduce both the effective focal distance and the electron bunch quality requirements.

In essence, taking the above considerations into account, an electron energy of 15 MeV is chosen for this VUV TWTS OFEL.

### CHOOSING ELECTRON BUNCH PEAK CURRENT, RADIUS AND OPTICAL UNDULATOR STRENGTH

The above mentioned trade-off is in essence a trade-off between laser propagation distance  $z_{\text{prop}}$  and OFEL electron energy spread acceptance  $\rho \gtrsim \sigma_E/E_b$  which needs to be made when choosing electron bunch peak current  $I_p$ , its rms cross-sectional radius  $\sigma_b$  as well as optical undulator strength  $a_0$ .

All of the latter three parameters enter the Pierce parameter and thus influence the strength of radiation back reaction. As a consequence the choice of values of these parameters finally sets the gain bandwidth and saturation distance of this TWTS OFEL and therefore also sets requirements on electron bunch and laser parameters. That is to say  $I_p$ ,  $\sigma_b$  and  $a_0$  must be chosen to fit the requirements on electron bunch and laser parameters to the experimentally feasible values of effective focal distance  $f_{\text{eff}}$ , laser power  $P_{\text{Laser}}$ , electron bunch energy spread  $\sigma_E/E_b$  and its norm. transv. emittance  $\epsilon_n$ .

Scalings of the requirements on these parameters are shown in fig. 6.7. Scalings within one column are for fixed electron bunch peak current which varies from left to right column between  $I_p \in (0.4 \text{ kA}, 0.8 \text{ kA}, 1.2 \text{ kA})$ . Within one column every scaling is a contour plot of one requirement in dependence of optical undulator strength  $a_0$  and rms cross-sectional bunch radius  $\sigma_b$  where curves connect pairs  $(a_0, \sigma_b)$  along which a requirement stays constant. From top to bottom scalings are shown for requirements on effective focal distance measured in units of input laser diameter  $n_w f_{\text{eff}}/D_{\text{in}} = \sin \phi / [2\pi\rho(1 - \beta \cos \phi)]$  (orange, eq. (4.33)), laser power  $P_{\text{Laser}}$  (gray, eq. (5.25)), energy spread  $\rho$  (magenta, eq. (5.17)), normalized transverse emittance  $\epsilon_n$  from the limit of defocusing (blue, eq. (2.14)) and radiation wavelength shift (green, eq. (5.23)).

Comparing the scaling of these requirements with  $a_0$  within one column it can be seen that a large undulator strength reduces the focusing distance and electron bunch quality requirements since large undulator strengths increase the number of scattered photons and therefore facilitate radiation back reaction. But the experimentally achievable value of  $a_0$  is limited by available laser power.

When choosing the electron bunch radius  $\sigma_b$  several limits are encountered as well. While larger radii reduce emittance requirements due to smaller bunch divergence, at the same time they increase the requirements on laser power, laser focal distance and electron energy spread. These increases originate from the smaller electron bunch density, and thus smaller plasma frequency, which weakens the radiation back reaction. This on the one hand increases the saturation length and thus the required horizontal laser width which results in an increased focusing distance and laser power requirement. On the other hand the weaker radiation back reaction requires a narrower radiation bandwidth in order to drive electron microbunching which results in a smaller acceptable electron energy spread. In practice a lower limit on reachable electron bunch

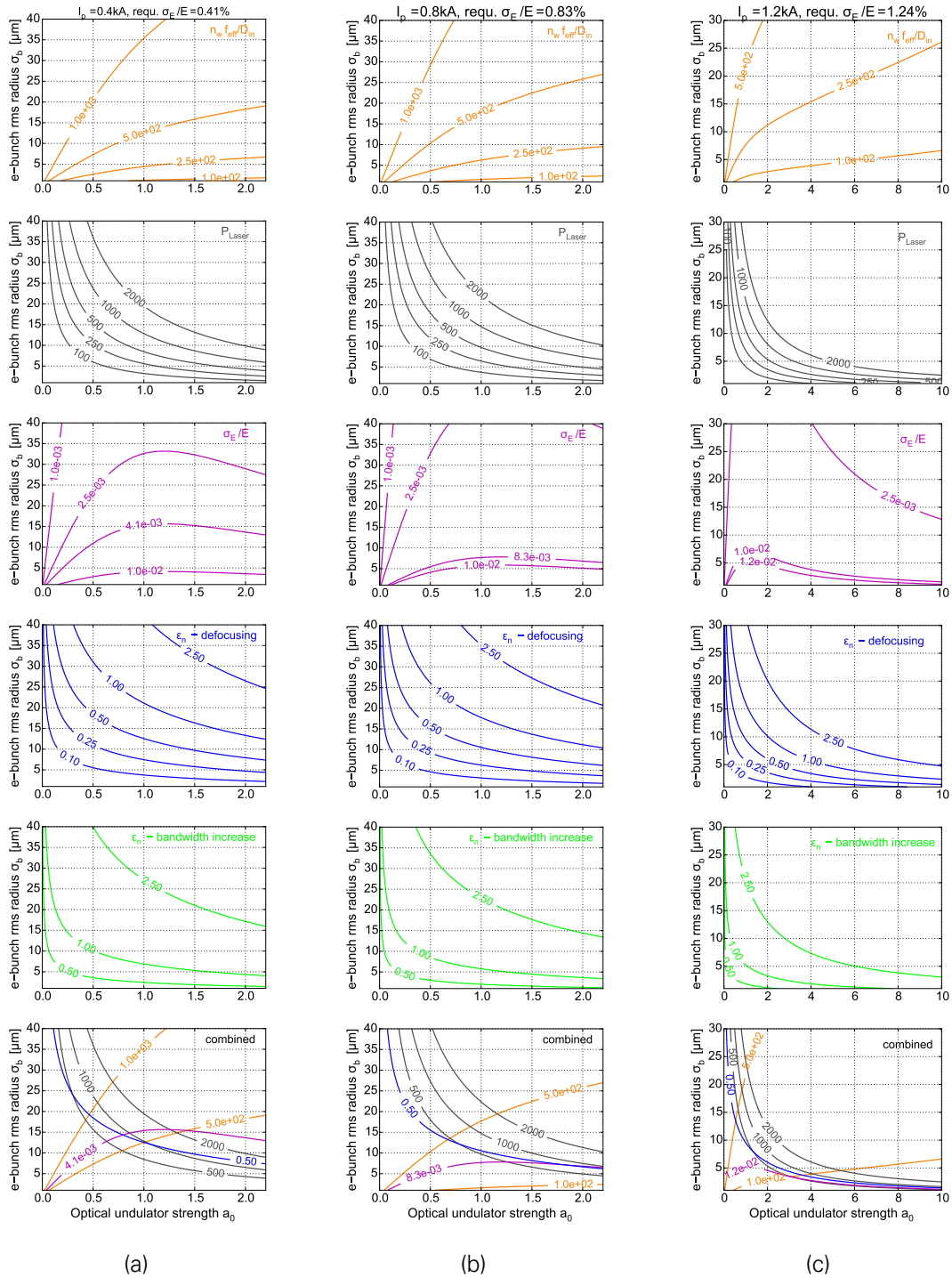


Figure 6.7.: Shows for a TWTS OFEL radiating at 100 nm from top to bottom the scaling of the requirements on focusing distance  $f_{\text{eff}}$  measured in units of input laser width  $D_{\text{in}}$ , laser power  $P_{\text{Laser}}$  in terawatts, electron energy spread acceptance  $\sigma_E/E_b$  and normalized transverse emittance  $\epsilon_n$  in mm mrad from electron bunch defocusing as well as radiation bandwidth increase in dependence of electron bunch rms cross-sectional radius  $\sigma_b$  and optical undulator strength  $a_0$ . Each column shows the scaling for a different electron bunch peak current: (a)  $I_p = 0.4$  kA, (b)  $I_p = 0.8$  kA, (c)  $I_p = 1.2$  kA. The last plot of each column combines the scalings allowing to judge on the effective focal distance in dependence of required energy spread acceptance and provided transv. norm. emittance.

radii exists as well which arises from chromatic aberrations of the final electron beam focusing system.

Values for  $I_p$ ,  $a_0$  and  $\sigma_b$  are determined by comparing the last plots of each column which combine the above scalings. These plots only show the emittance scaling from electron bunch defocusing since it is the tougher of the two emittance scalings and they only show the contour corresponding to the emittance  $\epsilon_n = 0.5 \text{ mm mrad}$  provided by the gun. Furthermore, they only show the electron energy spread acceptance corresponding to the available energy spread which is given by (6.3). From these plots the minimum values of  $(a_0, \sigma_b)$  for a specific peak current are determined by the crossing of available electron bunch energy spread and emittance. By comparing for the different peak currents the position of this crossing point relative to the effective focal distance allows to evaluate the compactness of a setup. The comparison shows that a setup utilizing bunches of 0.8 kA peak current will be compacter than setups utilizing bunches of 0.4 kA while setups utilizing bunches of 1.2 kA can not be realized with this electron source because the required electron bunch quality is higher than the available quality. The smaller laser propagation distance of setups utilizing 0.8 kA bunches comes on the cost of a higher intensity stability requirement due to their higher necessary  $a_0$ .

Finally, a peak current of  $I_p = 0.8 \text{ kA}$ , an electron bunch rms cross-sectional radius of  $\sigma_b = 7 \mu\text{m}$  and an optical undulator strength of  $a_0 = 2$  is chosen. With these parameters the interaction angle needs to be  $\phi = 10.1^\circ$  in order to radiate at the target wavelength.

## 6.2.2. DETERMINING OPTICAL SETUP PARAMETERS

The scalings 6.7 show that not all of the available laser energy is required to provide the interaction distance. Using the full energy of the pulse allows to increase its width at the interaction point at constant optical undulator strength which results in a shorter focusing distance according to eq. (4.33). Increasing the laser width at the interaction point by a factor  $n_w = 1.12$  results in an effective focal distance of  $f_{\text{eff}} = 32.43 \text{ m}$ . Note, using the out-of-focus setup reduces the focusing distance tremendously, an in-focus interaction geometry would require a focal distance of 168 m. The interaction point in the out-of-focus setup is  $\Delta f = -0.65 \text{ m}$  before the focus resulting in a propagation distance  $z_{\text{prop}} = 31.78 \text{ m}$  of the laser from the off-axis cylindrical mirror to the interaction point.

This assumes an input pulse with a rectangular transverse pulse shape of width  $D_{\text{in}} = 17.5 \text{ cm}$ . This width ensures an areal energy density below  $0.4 \text{ J/cm}^2$  on the gratings for normal incidence in order to avoid damage from too high fluences [128, 177].

The second cylindrical mirror, focusing the pulse in the vertical direction for optimum overlap of laser pulse and electron bunch, has a focal distance of  $f_x = 2.97 \text{ m}$  and follows the off-axis cylindrical mirror a distance  $L_{\text{cylinder}} = f_{\text{eff}} + \Delta f - f_x / \sin \phi = 14.86 \text{ m}$  downstream the laser propagation path. Although the laser pulse width in the interaction plane at the cylindrical mirror is already significantly smaller than  $D_{\text{in}}$ , the fluence is still below the damage threshold due to the large incidence angle  $\pi - \phi \approx 80^\circ$ . The width of the cylindrical mirror in the interaction plane needs to be 52 cm.

With the parameters of the focusing mirrors known, the remaining parameters of the optical setup to be determined are those of the gratings:  $\psi_{\text{in},1}$ ,  $n_1$ ,  $\epsilon$ ,  $n_2$  and  $L_{\text{grating}}$ . These are determined by the procedure described in subsection 4.5.2 which is showcased in the following.

First, practical values are assumed for the effective grating separation distance (regarding spatial dispersion)  $L_{\text{grating,eff}} = 2.5 \text{ m}$ , the distance between second grating and off-axis cylindrical mirror  $L_{\text{mirror}} = 2 \text{ m}$  and the deflection angle of the pulse at the off-axis cylindrical mirror of  $\psi_{\text{defl}} = 15^\circ$ .

Second, second grating line density  $n_2$  is chosen with the help of eq. (4.42), which ensures correct pulse-front tilt after the second grating provided pulse-front tilt after the first grating

matches the target value. This equation is used to determine a second grating line density of 1030 l/mm allowing for a second grating incidence angle of  $18.79^\circ$  close to the gratings Littrow angle of  $32.21^\circ$  while at the same time ensuring correct pulse-front tilt of  $0.101^\circ$ , according to eq. (4.40), after the second grating.

Third, a first impression on required first grating line density  $n_1$  is obtained from first grating diffraction angle of  $-23.276^\circ$  and incidence angle  $39.653^\circ$  which are determined using eqs. (4.43) and (4.44), respectively, as well as above  $n_2 = 1030$  l/mm and  $\psi_{in,2} = 18.79^\circ$ .

Fourth, the obtained  $n_1$  of 998.35 l/mm is rounded to a practical value of  $n_1 = 1000$  l/mm. Therefore  $\psi_{in,1}$  and  $\psi_{in,2}$  need to be determined again using relations (4.36) in order to ensure a correct pulse-front tilt and plane of optimum compression orientation of  $\alpha_{tilt} = \phi/2$  and  $\alpha_{poc} = \phi - \pi/2$  at the interaction point, see fig. 4.3b. This can be done graphically as it has been done for the hard X-ray enhanced Thomson source, see fig. 6.5c. Thereby, values of  $\psi_{in,1}$  and  $\psi_{in,2}$  determined in the first iteration are good starting values for the second iteration. With it, the grating pair parameters are finally determined and the true grating separation distance  $L_{grating} = L_{grating,eff} \cos \psi_{in,2} / \cos \psi_{out,2} = 3.60$  m is calculated.

This particular example of a parameter determination procedure yielded practical values for the grating incidence angles which are close but not too close to the Littrow angles of the gratings. If a first iteration yielded an unpractical value for the first grating incidence angle, a different value for second grating line density or any other starting parameter can be chosen which will result in a modified grating setup.

As mentioned in subsection 4.5.2 the input pulse in the out-focus-setup needs to be stretched by a frequency chirp in order to ensure vanishing group-delay dispersion at the interaction point. The required absolute value of incident group-delay dispersion of the input pulse  $GDD_0 = 8.758$  ps<sup>2</sup>, which is obtained by eq. (4.45), can be routinely produced with standard stretchers as they are used in chirped pulse amplification for the generation of high-power laser pulses. For example the stretcher of the PEnELOPE system at HZDR generates  $GDD > 200$  ps<sup>2</sup> while elongating the 60 fs long pulse from the oscillator to 3 ns.

### 6.2.3. OPTICAL COMPONENTS ALIGNMENT TOLERANCES

Misalignment of the gratings or the electron and laser propagation axis lead to non-optimum overlap due to a mismatch between interaction angle and pulse-front tilt as well as plane of optimum compression.

The misalignment tolerances are evaluated by the procedure explained in subsection 4.5.3, i. e. using the analytical relations for pulse-front tilt and plane of optimum compression orientation (4.36) to calculate their deviation if one of the parameters  $\psi_{in,1}$ ,  $\epsilon$ ,  $L_{grating}$ ,  $L_{mirror}$ ,  $\phi$  or  $f_{eff}$  is different from its optimum value. The impact of these deviations is evaluated by inserting them into the analytic relations for irradiance and undulator frequency variation, eqs. (4.27) and (4.28). The variation of a single parameter is defined to be acceptable if the resulting variation in irradiance or optical undulator frequency does not exceed its limit which is given by (4.3). The obtained misalignment tolerances are listed in tab. 6.5.

All of the tolerance limits are set by the limit on intensity variation from non-optimum overlap. The optical undulator frequency variation is always well below its limit for the limits set by intensity variation. All of the acceptable alignment tolerances are achievable today. With  $\mu$ rad alignment precision for optical components available today, the alignment of gratings and mirrors should not impose an obstacle in the realization of this setup. The distance between second grating and off-axis cylindrical mirror is the most insensitive part regarding misalignment since angular dispersion of the pulse is very small after diffraction at the second grating and neither a much longer nor shorter propagation distance significantly changes spatial dispersion of the pulse. Misalignment of the cylindrical mirrors results in a wrong propagation direction of the

laser pulse. Thus their misalignment tolerance is the same as for the interaction angle. However, for large misalignments there is a spatial offset between the electron-laser intersection point and the target interaction point which can result in a difference in laser pulse properties between intersection and interaction point due to laser pulse dispersion.

In conclusion, everything necessary for the realization of this TWTS OFEL exists. Available electron accelerators providing sufficient electron bunch quality exist which is demonstrated by utilizing parameters of the FERMI accelerator. Several short pulse, petawatt peak-power laser systems operate today [178]. The optical components are available from commercial manufacturers today such as PGL which produces suitable multilayer coated dielectric gratings. Even the acceptable misalignment tolerances of the optical components were evaluated and found to be well within current technological capabilities. This VUV TWTS OFEL can be built today.

### 6.3. SCALING TOWARDS SHORTER WAVELENGTHS AND COMPACTER SETUPS

The preceding example shows that TWTS OFELs can be realized today with existing technology for electron accelerators and laser systems. Yet its vacuum ultraviolet radiation wavelength is long compared to modern large scale extreme ultraviolet and soft X-ray FEL facilities. As it has been shown at these large scale facilities, short, intense and spatially coherent pulses at extreme ultraviolet to Ångström wavelengths have many applications in fields of research ranging from structure and dynamics of functional biological units [11] over earth and planetary science [179], novel states of matter [180], nanotechnology [76] to possibly quantum information processing [181]. These applications use the penetration power, spatial coherence and extraordinary high brilliance of X-ray FEL pulses allowing to analyze the bulk behavior of matter, determining the structure of small samples with atomic resolution and imaging the evolution of transient processes on a femtosecond time scale. TWTS OFELs can become a complementary source to these large scale FEL facilities by providing the same kind of short, intense and coherent radiation pulses of extreme ultraviolet (EUV) and Ångström wavelengths yet at a much smaller laboratory size as well as reduced power due to the orders of magnitude smaller electron energies. The following examples outline paths that can be taken to operate TWTS OFELs in the extreme ultraviolet (EUV) and X-ray range.

The preceding example further shows that TWTS OFEL setups are not necessarily “table-top” although the interaction distances are in the centimeter range. The distance required to focus a petawatt laser pulse to a millimeter-scale horizontal width, which is necessary to provide centimeter-scale interaction distances, can be many ten meters due to the large Rayleigh length attending these millimeter-scale pulse widths. In principle the focusing distance could be folded into a small area since it is only propagation distance within a vacuum tube without any pulse shaping. But folding requires mirrors of higher damage threshold than the gratings used to shape laser pulses for TWTS OFELs. Thus the TWTS OFEL scaling laws are analyzed in the following to show means of reducing the propagation distance  $z_{prop}$  from the off-axis cylindrical mirror to the interaction point. This becomes especially relevant when aiming for EUV and soft X-ray TWTS OFELs where gain lengths and interaction distances are larger than for the above example.

At even shorter wavelengths in the Ångström range, however, interaction distances can be large enough to remove the need for focusing since required laser widths  $w_0 = L_{int} \sin \phi$  are already on the order of laser width during pulse transport. These are on the 10 cm scale for petawatt class lasers in order to keep the energy fluence on optical components below their damage threshold. Although hard X-ray TWTS OFEL setups remove the need for 100 m scale propagation distances, they come on the expense of higher necessary electron bunch quality than a setup employing focusing since they operate at smaller undulator strength.

### 6.3.1. EMPLOYING HIGHER POWER LASER PULSES

The presented example of a VUV TWTS OFEL utilized a laser system delivering pulses of one petawatt power. With higher power laser systems being available today, the VUV TWTS OFEL requirements on lab space as well as electron bunch and laser quality can be reduced or the radiation wavelength shortened.

A reduction of required lab space is achieved by allowing for a larger laser pulse oversize at the interaction point compared to the above example, i.e. increasing  $n_w$  from 1.12 to 2.24 if for example 2 PW laser pulses are available. Such an increase of a factor of two in available laser power translates to a reduction of effective focal distance by a factor of  $\sqrt{2}$  due to the increase in input laser diameter becoming necessary to keep the areal energy density of the pulse constant.

This reduction in effective focal distance can be exploited to use setups at lower electron bunch peak current which have lower requirements on laser pulse quality. Comparing the combined TWTS OFEL scalings for electron bunch peak currents of 0.4 kA and 0.8 kA in fig. 6.7, the optimum optical undulator strength is lower at lower peak current, where the optimum value was given by the intersection point of the required relative electron energy acceptance contour and the required norm. transverse emittance acceptance contour. A lower optical undulator strength of  $a_0 = 0.8$  on the one hand allows for a larger variation of laser irradiance since these variations result in a smaller variation of radiation wavelength. On the other hand the effective focal distance is larger compared to the above VUV TWTS OFEL which can be offset by a larger laser oversize.

Using higher power laser pulses in combination with lower peak currents can be also exploited to reduce the electron bunch quality requirements. For the chosen VUV TWTS OFEL parameters of  $I_p = 0.8$  kA,  $a_0 = 2$  and  $\sigma_b = 7$   $\mu$ m the acceptable relative electron energy spread for TWTS OFEL operation is 0.83 %, which is given by the Pierce parameter (eq.(2.12)), just coincides with the energy spread after electron bunch compression, which is determined by the conservation of longitudinal emittance (eq. (6.3)). For equal  $a_0$  and  $\sigma_b$  but at lower peak current of  $I_p = 0.4$  kA, however, the required electron bunch quality is lower because the relative electron energy spread after compression is 0.41 % while the acceptable energy spread is 0.67 % which can be seen again from the combined scalings in fig. 6.7.

More laser power could be also utilized to reduce the radiation wavelength. If one electron source is used to produce radiation at different wavelengths, for example by tuning the interaction angle, the production of shorter wavelengths will require longer interaction distances and more laser power to achieve saturation. But the combination of longer interaction distances and larger laser pulse widths ultimately increases the lab space requirement due to the necessity of longer effective focal distances for sufficiently large pulse widths at the interaction point. For example, the laser propagation distance from the off-axis cylindrical mirror to the interaction point increases to about 54 m when decreasing the radiation wavelength of the VUV TWTS OFEL to 40 nm by utilizing a 2 PW laser system which provides pulses of equal wavelength and duration as the one used for the VUV TWTS OFEL. Furthermore, usage of the same electron source is assumed, and electron bunches are compressed to the same peak current of  $I_p = 0.8$  kA and focused to the same rms radius of  $\sigma_b = 7$   $\mu$ m but accelerated to an energy of 24 MeV. The optical undulator of this example has a strength of  $a_0 = 1.9$  and the laser pulse has an oversize of  $n_w = 1.52$  at the interaction point resulting in a power requirement of  $P_{\text{Laser}} = 2$  PW and a laser pulse diameter of 25 cm before focusing.

Laser system providing pulses of two petawatt peak power and more have been demonstrated at SIOM Qiangguang [182] and CAEP-PW [183] Several multipetawatt laser systems are under construction or planned such as ELI [184], Appolon [185] or SIOM OPCA Qiangguang 10 PW [186]. All of these laser systems generate short pulses at around 1  $\mu$ m central wavelength and 30 fs duration. These may be shorter than the electron bunch duration provided by conventional

accelerators resulting in partial overlap of electrons and laser pulse. This reduces the effective charge of the electron bunch interacting with the optical undulator but does not inhibit OFEL realization. Just the total scattering output is reduced.

For these laser systems as well as for the laser systems providing pulses of higher energy and longer duration, as they are assumed for the above examples, the main challenge, and at the same time a major branch of research on high-power laser development, is the production of large aperture laser media allowing for large pulse diameters in order to keep energy fluences below the elements damage threshold [187].

### 6.3.2. REDUCING ELECTRON ENERGY SPREAD

As seen in the preceding subsection, increasing the laser pulse power has only limited applicability for scaling the VUV TWTS OFEL radiation wavelength into the EUV or soft X-ray range since the lab space requirement increases noticeably.

Compactness of a TWTS OFEL depends on the control over electron energy spread. Saturation lengths of TWTS OFELS become smaller for smaller energy spreads since the ponderomotive potential strength required to initiate microbunching becomes smaller. This results in a compact setup and reduces the laser power requirement which allows to reduce the TWTS OFEL radiation wavelength without spoiling compactness.

Reducing the energy spread of electron bunches becomes possible, for example, by inserting corrugated structures into their beam path. The back reaction of the longitudinal wakefield generated by an electron bunch in the structure allows to precisely manipulate its longitudinal phase space and thus reducing the energy spread. A factor of two reduction of energy spread has been demonstrated for 1 MeV-level as well as 100 MeV-level electron bunches [188, 189]. The technique is going to be implemented at major X-ray FEL facilities around the world [190, 191].

Assuming a factor of two in energy spread reduction could be achieved for the electrons of the VUV TWTS OFEL as well, its radiation wavelength can be reduced to 36 nm at an interaction angle of  $12.7^\circ$  and same electron energy of 15 MeV. A further reduction of radiation wavelength is limited by the accompanying decrease in acceptable optical undulator irradiance variation which was tried to be kept approximately constant. The irradiance stability requirement becomes more demanding with decreasing radiation wavelength because the gain bandwidth of the TWTS OFEL, given by its Pierce parameter, becomes smaller with decreasing radiation wavelength and eventually becomes smaller than the radiation bandwidth induced by irradiance variation. Compared to the VUV TWTS OFEL the reduction of acceptable irradiance variation is mitigated by choosing a smaller optical undulator strength which reduces the impact of irradiance variation on the TWTS OFEL bandwidth. A further reduction of optical undulator strength to achieve lasing at a smaller radiation wavelength only works if the energy spread of the electron bunch is reduced at the same time. The energy spread reduction then makes up for the weaker radiation back-reaction at the smaller radiation wavelength.

The complete set of electron bunch and optical undulator parameters is listed in tab. 6.6.

Assuming the electron energy spread can be reduced by a factor of four after compression and acceleration, the VUV TWTS OFEL radiation wavelength can be reduced to the application-technological relevant wavelength of  $\lambda_{\text{FEL}} = 13.5 \text{ nm}$ . The parameters of this EUV TWTS OFEL are listed in tab. 6.6, too. The electron-laser interaction is optimized by accelerating the bunch of the VUV TWTS OFEL example to a higher energy of 22 MeV and compressing it to a higher peak current of 1.6 kA which essentially allows for larger laser irradiance variation during interaction.

The target radiation wavelength of this EUV TWTS OFEL is widely used in experiments since high reflectivity molybdenum-silicon multilayer mirrors are available reaching  $> 60\%$  reflectivity [77, 192] at almost normal incidence which can be used to guide and focus the EUV radiation.

Table 6.6.: Parameters and requirements on electrons and optical undulator of TWTS OFELs radiating at 36 nm or at the technological relevant wavelength of 13.5 nm. Both TWTS OFELs use the same electron source as the VUV TWTS OFEL but employ energy spread reduction after compression by a factor of two (EUV TWTS OFEL I) or four (EUV TWTS OFEL II).

Electron and optical undulator parameters	EUV TWTS OFEL I	EUV TWTS OFEL II
Resonant wavelength [nm]	36	13.5
Interaction angle [°]	12.7	12.84
Undulator wavelength [ $\mu\text{m}$ ]	41	41
Electron energy [MeV]	15	22
Bunch charge [pC]	350	350
Peak current [kA]	0.8	1.6
Bunch duration (rms) [fs]	175	87
Bunch cross-sectional radius (rms) [ $\mu\text{m}$ ]	8.0	8.0
Norm. transv. emitt. [mm mrad]	0.52	0.52
Rel. energy spread	0.41%	0.28%
Undulator parameter $a_0$	1.1	0.74
Transv. intensity profile stability	2.2%	2.6%
Laser wavelength $\lambda_{\text{Laser}}$ [ $\mu\text{m}$ ]	1.035	1.035
Laser pulse duration as FWHM of irradiance [fs]	120	120
Laser power $P_{\text{Laser}}$ [TW]	1010	1002
Laser oversize at interaction point $n_w$	2.0	3.0
Laser input diameter $D_{\text{in}}$ [cm]	17.5	17.5
Propagation distance $z_{\text{prop}}$ [m]	28.070	25.327
Gain length [ $\mu\text{m}$ ]	463	670
Interaction distance [mm]	7.40	10.71
Peak EUV power [MW]	51	101
Number of photons	$4.05 \times 10^{12}$	$1.5 \times 10^{12}$
Peak spectral brightness [photons/(s mm <sup>2</sup> mrad <sup>2</sup> 0.1% bandwidth)]	$9 \times 10^{26}$	$7 \times 10^{27}$

EUV radiation at 13.5 nm is used for example to image nanoparticle growth [76], ultrafast molecular dynamics [193] and ultrafast many-particle dynamics in highly excited plasma states [194] or for extreme ultraviolet lithography [195].

### 6.3.3. EMPLOYING LONGER WAVELENGTHS LASER SYSTEMS

In order to study biological samples with TWTS OFELs these need to provide radiation in the soft X-ray range around 4.3 nm. This wavelength is close to the carbon K-edge and in the water window of the electromagnetic spectrum. It provides good image contrast when irradiating carbon-containing biological samples [77, 196] due to the high absorption of carbon and the relative transparency of water at this wavelength.

Soft X-ray TWTS OFELs can be realized by longer wavelengths laser systems without further increasing the electron bunch quality requirements compared to the EUV TWTS OFEL example of the last subsection. Due to the longer available undulator periods from longer wavelengths laser systems electron bunches of higher energy can be used which reduces the requirements on the electron source, as has been discussed already in chapter 3.3.

Currently high-power CO<sub>2</sub> laser systems with a wavelength of 10  $\mu\text{m}$  are developed at Brookhaven

Table 6.7.: Parameters and requirements on electrons and optical undulators for TWTS OFELs using a 100 TW CO<sub>2</sub> laser system with 10 μm wavelength.

Electron and optical undulator parameters	EUV CO <sub>2</sub> TWTS OFEL	Soft X-ray CO <sub>2</sub> TWTS OFEL
Resonant wavelength [nm]	13.5	4.3
Interaction angle [°]	7.78	6.62
Undulator wavelength [μm]	1085	1500
Electron energy [MeV]	125	215
Bunch charge [pC]	350	350
Peak current [kA]	4.9	2
Bunch duration (rms) [fs]	28	70
Bunch radius (rms) [μm]	12	34
Norm. transv. emitt. [mm mrad]	0.52	0.5
Rel. energy spread	0.59%	0.06%
Undulator parameter $a_0$	1	0.2
Transv. intensity profile stab.	3.5%	5.8%
Laser wavelength $\lambda_{\text{Laser}}$ [μm]	10.0	10.0
Laser pulse duration as FWHM of irradiance [ps]	5	5
Laser power $P_{\text{Laser}}$ [TW]	102	103
Laser oversize at interaction point $n_w$	1.35	1.0
Laser input diameter $D_{\text{in}}$ [cm]	22.0	22.0
Cyl. mirror focusing dist. $f_{\text{vert}}$ [m]	0.66	1.875
Propagation distance $z_{\text{prop}}$ [m]	41.7	16.3
Gain length [mm]	8.4	119.7
Interaction distance [mm]	134.6	1915
Peak power [MW]	3644	248
Number of photons	$18 \times 10^{12}$	$0.9 \times 10^{12}$
Peak spectral brightness [photons/(s mm <sup>2</sup> mrad <sup>2</sup> 0.1% bandwidth)]	$1 \times 10^{29}$	$3 \times 10^{29}$

National Laboratory with the aim of reaching 100 TW peak power [197, 198]. The pulse duration of such a CO<sub>2</sub> laser is a few picoseconds [197, 199] requiring a few 100 J pulse energy to reach the target power. This is sufficient for TWTS OFEL operation in the EUV and soft X-ray range. Table 6.7 lists parameters of two TWTS OFELs, one radiating at 13.5 nm and the other at 4.3 nm.

The electron source of both EUV and soft X-ray CO<sub>2</sub> TWTS OFEL is again the same as for the VUV TWTS OFEL. For the EUV CO<sub>2</sub> TWTS OFEL electron acceleration is extended to higher energy and compression is increased but no energy spread reduction is assumed which is in contrast to the first EUV TWTS OFEL presented in the preceding subsection. For the soft X-ray CO<sub>2</sub> TWTS OFEL an energy spread reduction about a factor of two is assumed.

The energy spread requirement of the soft X-ray CO<sub>2</sub> TWTS OFEL is set by the chosen setup geometry. A setup without focusing, as depicted in fig. 4.4, is chosen in order to keep the setup size compact and because the scaling offers the possibility to chose OFEL parameters such that the laser pulse transverse size required to provide the interaction distance can be matched to the pulse width during transport. Determining parameters for a setup without focusing is shown in the next section which presents an experiment making use of an Ångström TWTS OFEL to image plasma dynamics during laser driven acceleration of ions from solid foils.

For both EUV and soft X-ray CO<sub>2</sub> TWTS OFEL setups the laser pulse is assumed to have roughly 5 ps duration, 500 J energy and 22 cm transverse size with a rectangular profile which

results in an areal energy density of  $1 \text{ J/cm}^2$ . Since the soft X-ray example does not require focusing in the interaction plane its propagation distance  $z_{\text{prop}}$  reduces to the distance required to cover the focal distance of the cylindrical mirror focusing the laser onto the electron bunch. This distance still spans more than ten meters but may be reduced if two additional mirrors are introduced into the laser pulse path after deflection at the cylindrical mirror. This mirror pair forms a chicane into the laser pulse path where the first of these mirrors redirects the pulse to let it propagate parallel to the cylindrical mirrors axis and thus directly towards its focal line. Then the pulse can quickly cover much of the cylindrical mirrors focal distance. The second mirror redirects the pulse again into its original propagation direction which encloses the interaction angle together with the electron bunch propagation direction.

Applicability of this technique is of course limited by the damage threshold of the inserted mirror pair. In general, damage thresholds of materials vary with e.g. pulse energy, pulse duration, pulse repetition rate and wavelength [128] and cannot be simply carried-over from different laser systems. Unfortunately, data for damage thresholds of picosecond mid-infrared laser pulses is hardly available. The study in ref. [200] shows variation in damage threshold over more than one order of magnitude between  $0.2 \text{ J/cm}^2$  and  $7 \text{ J/cm}^2$ , depending on material.

#### 6.3.4. EMPLOYING LASER WAKEFIELD ACCELERATORS

Reducing the radiation wavelengths of TWTS OFELs to the Ångström scale enables the generation of coherent X-ray pulses containing on the order of  $10^{10}$  photons within a ten femtosecond scale duration similar to the radiation pulses provided by existing X-ray FEL facilities.

Their applications are manifold starting for example in condensed matter physics. One experiment, for example, which is set in the context of high temperature superconductivity research, measured the charge-stripe order during the onset of light-induced superconductivity in a high-temperature superconducting stripe-ordered cuprate system by making use of the subpicosecond X-ray pulses [201]. Another topic of interest which can be studied with an Å TWTS OFEL is future storage device technology and electronics research which aims at exploiting the electron spin in addition to its charge for data processing. Experiments conducted so far, for example, recorded real-space images of ferromagnetic domains in a low-dimensional solid [202] in a single-shot by making use of the femtosecond X-ray pulse duration, X-ray wavelength and spatial coherence of an X-ray FEL which together enable femtosecond temporal and nanometer spatial resolution. The techniques employed in this experiment allowed to study the nanoscale charge and spin dynamics in materials. Many more experiments in areas ranging from Atomic, Molecular and Optical Physics as well as Biology, Chemistry and Soft Matter to Matter in Extreme Conditions utilize the high-intensity or short pulse duration or both of X-ray FELs and are reviewed in ref. [203].

The next section discusses in detail an experiment utilizing an Å TWTS OFEL to image the plasma dynamics in a solid irradiated by a high peak-power laser pulse. Obtaining inside into these dynamics is important for the development of compact and brilliant energetic proton sources from the interaction of a laser pulse with matter at relativistic intensities as it is done at HZDR. Proton radiation oncology maybe one potential application of these sources.

In a practical realization of an X-ray TWTS OFEL providing an Ångström scale radiation wavelength the requirements on electron bunch quality achieved by an electron source are more demanding than for the longer wavelengths TWTS OFELs discussed before. In fact, the requirement on electron bunch emittance from spectral bandwidth broadening due to electron beam divergence, eq. (5.23), may become too demanding to be satisfied by conventional electron sources providing  $0.5 \text{ mm mrad}$  or larger normalized transverse emittance. The smaller acceptable radiation bandwidth of an Å TWTS OFEL requires to use electron sources with ultra-low emittance on the order of  $0.1 \text{ mm mrad}$ .

Possible sources providing such ultra-low emittance bunches include compact laser plasma accelerators [110–112] as well as conventional accelerators using ‘photocathodes’ from laser-cooled atoms [204, 205] or metal needle tips [206, 207] which also might be combined with laser pumped dielectric accelerating structures [208–210] for compactness.

While the latter alternatives to conventional photoinjectors have not yet demonstrated acceleration to relativistic energies as required for TWTS OFELs, electron bunches produced by laser wakefield acceleration (LWFA) have been accelerated to gigaelectronvolt energies [58–60]. Moreover, laser wakefield accelerators demonstrated the production of electron bunches with subpercent level energy spreads [211], several hundred picocoulomb charge [61, 62] and kiloampere peak currents [212] resulting from their few femtosecond durations [213–215]. Yet the *stable* production of electron bunches combining ultra-low emittance, (sub-)percent level energy spreads and kiloampere currents is an ongoing effort and has not been realized today. Current research focuses on the development of techniques allowing stable bunch production [52, 216–221] as well as controlling and constraining the phase space from which electrons are accelerated. These techniques include the use of a second laser pulse [222–225], ionization thresholds [226–228], plasma density gradients to limit injection in time and space [229–233] or staged acceleration [234–238].

Despite these challenges stable production of high quality electron bunches, femtosecond-level synchronization of electron bunches and laser pulses is inherent to the combination of TWTS and LWFA which eases the experimental realization of a TWTS OFEL when using this scheme. When combining TWTS and LWFA a single laser pulse can be split in two parts where a lower energetic part is used to drive the electron acceleration and a higher energetic part provides the optical undulator field. This inherent synchronization of electrons and laser eliminates the experimental challenge of synchronizing a femtosecond laser to radiofrequency accelerating structures, which determine the electron bunch arrival time [161].

In addition, with the laser system being the only machine driving the TWTS OFEL, optimization of its parameters with respect to pulse quality pay off twice. Advances in laser pulse contrast, pointing stability and intensity profile control do not only improve electron bunch quality [217, 239] but improve optical undulator quality, too, which will have a positive effect on the obtained power output and shorten the real gain length of a TWTS OFEL reached in an experiment. However, the most appealing aspect of TWTS OFELs employing LWFA is their compactness. Electron acceleration takes place on a centimeter distance, optical undulator preparation on a few meters and OFEL interaction within a meter. Thus the largest component of this setup is the laser system itself.

Table 6.8 gives parameters of two TWTS OFELs operating at EUV and Ångström wavelengths, 13.5 nm and 1.5 Å respectively. Both utilize laser wakefield accelerated electrons of 5 kA peak current and 50 pC bunch charge. Their normalized transverse emittance requirement is 0.3 mm mrad and 0.2 mm mrad, respectively.

The laser system is again assumed to be of the PEnELOPE type with 1.035 μm central wavelength and a rectangular pulse profile. For the EUV LWFA TWTS OFEL the laser pulse needs to be focused and thus the setup including the off-axis cylindrical mirror, fig. 4.8, will be used in an experimental realization. Unlike the EUV TWTS OFEL the Å TWTS OFEL requires a laser pulse width matching its width during transport in order to provide the necessary interaction length. Thus focusing the laser pulse is not necessary and the setup without focusing will be used, fig. 4.4. The details of this setup are explained in greater detail in the next section which discusses an experiment making use of the Å TWTS OFEL to image plasma dynamics during laser driven acceleration of ions from solid foils.

The EUV LWFA TWTS OFEL setup is a striking example for the advantages of a TWTS geometry over head-on geometries. Its variability with respect to the choice of interaction angle is used to tweak the electron bunch quality requirements towards qualities achievable with ultra-

Table 6.8.: Parameters and requirements on electrons and optical undulators for TWTS OFELs operating at wavelengths of 13.5 Å and 1.5 Å. Both utilize laser wakefield accelerated electrons of ultra-low transverse emittance.

Electron and optical undulator parameters	EUV LWFA	Å LWFA
	TWTS OFEL w/ focusing	TWTS OFEL w/o focusing
Resonant wavelength [nm]	13.5	0.15
Interaction angle [°]	6	7
Undulator wavelength [μm]	188	139
Electron energy [MeV]	61.5	349.6
Bunch charge [pC]	50	50
Peak current [kA]	5	5
Bunch duration (rms) [fs]	4	4
Bunch radius (rms) [μm]	4	10
Norm. transv. emitt. [mm mrad]	0.28	0.2
Rel. energy spread	1%	0.02%
Undulator parameter $a_0$	1.5	0.17
Transv. intensity profile stab.	3.6%	2.8%
Laser wavelength $\lambda_{\text{Laser}}$ [μm]	1.035	1.035
Laser pulse duration as FWHM of irradiance [fs]	120	120
Laser power $P_{\text{Laser}}$ [TW]	851	575
Laser oversize at interaction point $n_w$	2.0	1.0
Laser input diameter $D_{\text{in}}$ [cm]	16.	12.0
Cyl. mirror focusing dist. $f_{\text{vert}}$ [m]	1.55	2.91
Propagation distance $z_{\text{prop}}$ [m]	23.27	23.8
Gain length [mm]	0.88	32
Interaction distance [mm]	14	510
Peak X-ray power [MW]	3030	350
Number of photons	$2 \times 10^{12}$	$2.7 \times 10^9$
Peak spectral brightness [photons/(s mm <sup>2</sup> mrad <sup>2</sup> 0.1% bandwidth)]	$6 \times 10^{28}$	$3 \times 10^{31}$

-compact laser-wakefield accelerators today. The key electron parameters for EUV LWFA TWTS OFEL operation have been demonstrated individually already. Electron bunches of several ten megaelectronvolt energy with several ten picocoulomb charge are routinely produced and ultra-low emittance as well as percent level energy spreads have been demonstrated, see references above.

Therefore the EUV LWFA TWTS OFEL promises a substantially decreased facility size, despite the relatively large laser propagation distance of 25 m, compared to conventional EUV FELs. The whole system is an order of magnitude smaller than the accelerator and undulator system of the conventional EUV FEL FLASH.

Note, setup sizes of EUV and Å TWTS OFEL will not increase by electron bunch refocusing between acceleration and radiation generation if focusing is accomplished in a compact manner by utilizing a capillary discharge cell or a gas jet as a laser-plasma lens [240–242].

A major challenge in the realization of this Å TWTS OFEL clearly is the generation of electron bunches with the required low energy spread. But the setup demonstrates how compact hard X-ray FELs can become once these are available either from conventional radiofrequency or laser wakefield accelerators. The overall setup size will be only a couple of ten meters, even

Table 6.9.: Selected parameters of accelerator, electron bunch, magnet undulator and radiation properties at the Linac Coherent Light Source (LCLS).

Electron bunch and radiation parameters	LCLS
Resonant wavelength [Å]	1.5
Electron energy [GeV]	13.6
Electron accelerator length [m]	860
Bunch charge [pC]	250
Peak current [kA]	3
Bunch duration (rms) [fs]	170
Norm. transv. emitt. [mm mrad]	~1
Rel. energy spread	0.1%
Gain length [m]	3.5
Undulator length [m]	132
Peak X-ray power [GW]	40
Number of photons	$2.3 \times 10^{12}$
Peak spectral brightness [photons/(s mm <sup>2</sup> mrad <sup>2</sup> 0.1% bandwidth)]	$\sim 2 \times 10^{33}$

if a conventional accelerator is used [91, Suppl. Inform.]. Comparing this Å TWTS OFEL to the conventional hard X-ray FELs LCLS and SACLA, its reduction in final electron energy by more than an order of magnitude implies a tremendous decrease in facility size. Today these facilities span several hundred meters [21, 74]. For comparison tab. 6.9 lists the electron and radiation pulse parameters as well as the accelerator and undulator system lengths of LCLS radiating at a wavelength of 1.5 Å, too [74, 243].

This compact Å TWTS OFEL can be realized in principle at HZDR where it can be used to link beam properties of laser accelerated ions to plasma dynamics in targets, as it was introduced at the beginning of this chapter. The techniques behind such an experiment as well as its design and expected performance are detailed in the following section.

## 6.4. Å TWTS OFEL TO OBSERVE PLASMA DYNAMICS DURING LASER DRIVEN ION ACCELERATION FROM SOLID FOILS AT HZDR

### 6.4.1. IMAGING ELECTRON AND ION DISTRIBUTIONS WITH FEMTOSECOND AND NANOMETER SCALE RESOLUTION

A key topic of the laser particle acceleration division at HZDR is the acceleration of ions to relativistic energies by irradiating solid foils with high-power infrared laser pulses. On a long-term basis emphasize is put on the development of a pulsed proton source of sufficient energy and charge to be applied to cancer therapy [244–247]. The development includes activities to explore and test as well as model and simulate acceleration mechanisms [106, 248] and novel target designs. e.g. cone targets [141] and reduced mass targets [249].

Every development in these areas is accompanied by comprehensive simulation studies to design experiments as well as to predict and later interpret their results. Yet modeling and simulating the dynamical processes in these laser driven plasmas as well as predicting measurement results of experimentally accessible observables is a complex task relying on assumptions and approximations whose validity is not always verifiable. The ability to directly compare electron and ion spatial distributions between simulations and experiments with ionization state sensi-

bility as well as femtosecond and nanometer scale resolution during the acceleration process would on the one hand reduce guesswork on initial conditions when interpreting experiments with the help of simulations and on the other hand allow for benchmarking of e.g. ionization models with experiments.

For example, a recent experiment showed net-like fine-scale modulations in the transverse spatial distribution of accelerated protons [250] whose origin is not clear but the existence of these modulations is a severe obstacle with regard to the application of these proton beams to cancer therapy as they result in a spatially inhomogeneous dose distribution within the tumor which may hamper therapy success. Several possible origins of these modulations were named in the study but no definite answer could be given due to a lack of knowledge on the real electron and ion distributions and their driving processes during acceleration.

Methods to experimentally measure electron distributions or ion distributions with elemental and charge state sensitivity as well as nanometer and femtosecond scale resolution are proposed in refs. [141, 251]. They make use of available hard X-ray FEL pulses with femtosecond duration and few electronvolt energy spread. Thereby a high-intensity infrared laser pulse irradiates the target on the front surface to drive the ion acceleration and additionally the FEL pulse illuminates the foil from the side with a short time-delay after the infrared laser pulse. The density distribution of free electrons is then reconstructed from the obtained small-angle X-ray scattering image, provided that differences in electron density in the target are steep enough to yield a distinct scattering signal.

In order to spatially image the ionization dynamics the photon energy of the FEL will correspond to a resonance energy of a bound-bound electron transition for an ion species in a specific charge state of interest. Tuning the FEL wavelength to a resonance also ensures a large scattering cross-section such that the ionic scattering signal stands out against the free electron signal. If the spatial distribution of an ion species forms large scale structures within the foil during infrared laser irradiation, these will be imprinted on the X-ray scattering signal and can be observed by small angle X-ray scattering (SAXS), too [251]. The femtosecond scale duration of the FEL pulse thereby ensures that the ion distribution in the foil is quasi-static during X-ray scattering.

By varying the time delay between infrared pump and X-ray probe pulse a series of scattering images is obtained from which the temporal evolution of the electron or ion density distribution can be observed.

## 6.4.2. DETERMINING PARAMETERS OF THE Å TWTS OFEL

### ELECTRON BUNCH AND OPTICAL UNDULATOR PARAMETERS

Providing Ångström scale radiation wavelengths requires to provide electron bunches of very high quality as indicated by the scaling of the Pierce parameter with radiation wavelength and normalized electron energy  $\rho \propto \gamma_0^{1/3} \lambda_{\text{FEL}}^{2/3}$ . The scaling essentially reflects that the strength of radiation back reaction on the electron bunch drops rapidly for X-ray FELs when the plasma frequency of the electron bunch becomes small compared to the radiation wavelength and the bunch becomes transparent.

Compared to the VUV TWTS OFEL the target radiation wavelengths is almost a factor of one thousand smaller while the electron energy should not increase by the same factor in order to keep the setup compact and the interaction angle at a feasible value. Especially the propagation distance required to cover the focal distance of the vertically focusing cylindrical mirror  $\propto f_x / \sin \phi$  becomes huge for very shallow interaction angles. As a result, the Pierce parameter will become smaller for shorter radiation wavelength if feasible setup parameters are chosen. Therefore, requirements on electron energy spread and transverse emittance, which are proportional to the Pierce parameter, will become more demanding, too.

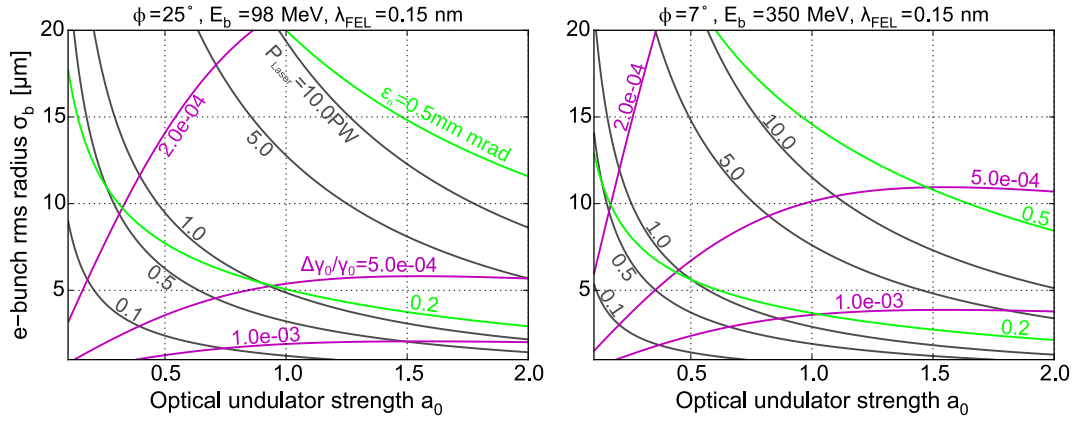


Figure 6.8.: Scaling of the requirements on laser power (grey), electron energy spread (magenta) and normalized transverse emittance (green) for the Å TWTS OFEL at two possible interaction angles, 25° (left) and 7° (right). The requirement on normalized transverse emittance is due to spectral broadening, eq. (5.23). Depicted are contours along which a requirement stays constant for variations in optical undulator strength  $a_0$  and electron bunch rms cross-sectional radius  $\sigma_b$ . Setups operating with feasible radii at the interaction point on the order of 10  $\mu\text{m}$  can be realized only at  $a_0 \sim 0.1$  due to the large laser power requirement for  $a_0 \sim 1$ . Small interaction angles are preferred for the Å TWTS OFEL realization due to the reduced requirements on electron bunch quality and laser power, which can be seen when comparing these for some pair  $(a_0, \sigma_b)$ .

The radiation back reaction becomes stronger again for tight electron bunch focusing and strong compression in order to increase the electron bunch density and thereby plasma frequency. Even for conventional X-ray FELs utilizing electron bunches of several gigaelectronvolt energies these are compressed to several kiloampere currents. Within this range the assumed peak current of the Å TWTS OFEL of  $I_p = 5 \text{ kA}$  is situated, too. Furthermore, a low normalized transverse emittance of 0.2 mm mrad is assumed. As it has been discussed before, laser plasma accelerators can potentially provide these high peak-current, low emittance bunches.

With the radiation back-reaction becoming weaker at smaller radiation wavelengths, interaction lengths can increase into the meter range until saturation is reached. Correspondingly, laser widths increase into the centimeter range. This can be exploited for the Å TWTS OFELs to remove the need for horizontal focusing by making use of the low transverse electron bunch emittance. It allows to choose a small optical undulator strength  $a_0 \ll 1$  where the interaction distance, and laser width with it, becomes even larger. Setups where  $a_0 \sim 0.1$  eventually result in required laser widths matching the laser width during transport which allows to omit focusing.

In view of the scalings depicted in 6.8 the decision to use small optical undulator strengths also appears reasonable when considering the laser power requirement. For large  $a_0 \sim 1$  it is on the order of ten petawatt for setups with reasonable electron bunch radius, assumed to be on the order of 10  $\mu\text{m}$  at the interaction point for feasible focusing. The only advantage offered by optical undulator strength  $a_0 \sim 1$  is the slightly higher acceptable electron energy spread.

After the decision to use small optical undulator strengths, and thus compact setups without horizontal focusing, the next step is to choose an interaction angle, and thereby the electron energy. Figure 6.9 plots for two interaction angles, 25° and 7° respectively, two contours of laser width requirements to drive the interaction until saturation in dependence of optical undulator

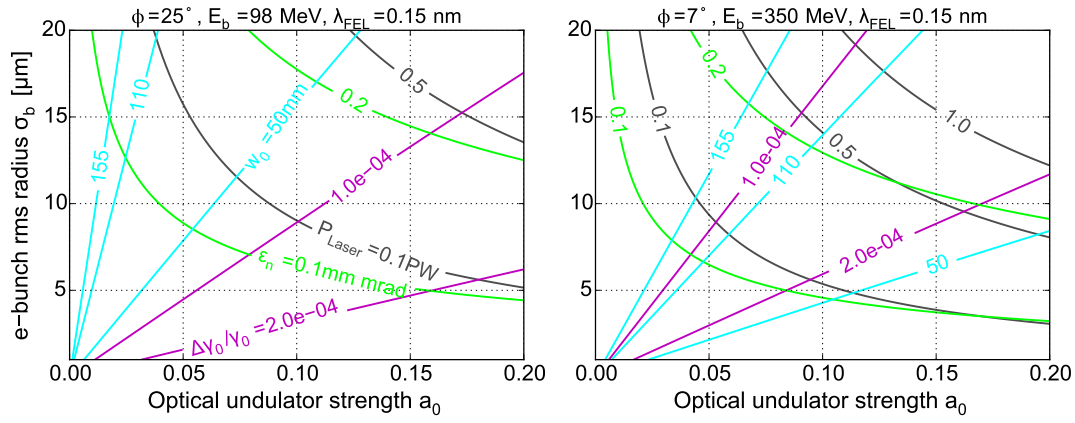


Figure 6.9.: Choosing parameters for the Å TWTS OFEL in the setup without laser pulse focusing in the interaction plane. Depicted are contours of requirements for TWTS OFEL operation on electron bunch quality and laser power along which these are constant. The requirements are: Laser power (grey), electron energy spread (magenta), normalized transverse emittance (green) and laser pulse width to maintain interaction until saturation (aqua). The values chosen for the requirement on laser pulse width of 50 mm, 110 mm and 155 mm correspond to pulse diameters resulting in an areal energy density of  $0.5 \text{ J cm}^{-2}$  for pulses of power 0.1 PW, 0.5 PW and 1.0 PW, respectively. Thus these pulse diameters may be used for pulse transport. Small interaction angles are preferred for a compact realization of the Å TWTS OFEL since electron bunch quality requirements are less demanding while larger laser pulses are required to maintain interaction until saturation. This allows for compact laser pulse preparation setups without focusing in the interaction plane.

strength  $a_0$  and rms electron bunch cross-sectional radius  $\sigma_b$ . The two chosen laser widths contours thereby correspond to the minimum laser pulse widths required to ensure an areal energy density below  $0.5 \text{ J cm}^{-2}$ . Contours of requirements on electron energy spread and normalized transverse emittance as well as laser power are printed for comparison, too.

Comparing the scalings for the different interaction angles a setup at  $7^\circ$  can be identified as the more practical case for the Å TWTS OFEL. At this interaction angle the requirements on laser width and energy spread are closer to each other. Therefore, a setup aiming at a large laser pulse width also has a higher electron energy spread acceptance if a smaller interaction angle is chosen for the realization.

An interaction angle of  $\phi = 7^\circ$  is chosen for the Å TWTS OFEL since smaller interaction angles result in larger focal distances. The laser propagation distance required to cover the focal length  $f_x$  of the vertically focusing cylindrical mirror scales as  $f_x / \sin \phi$ . One design goal was to keep this distance below 25 m.

From the  $7^\circ$ -scaling a setup with an energy spread acceptance of  $\Delta\gamma_0/\gamma_0 = 2.0 \times 10^{-4}$ , a norm. transverse emittance limit of  $\epsilon_n = 0.2 \text{ mm mrad}$  and an electron bunch radius of  $\sigma_b = 10 \mu\text{m}$  at the interaction point becomes feasible at an optical undulator strength of  $a_0 = 0.17$ . Note, this choice of parameters requires a laser width of about 62 mm to maintain interaction until saturation. This is about a factor of two smaller than the width of 12 mm which is required to keep the laser areal energy density below  $0.5 \text{ J cm}^{-2}$  at the required laser power of about 576 PW. The necessary reduction in pulse width can be realized by making use of the pulse size reduction during diffraction at the gratings which align pulse-front tilt and plane of optimum

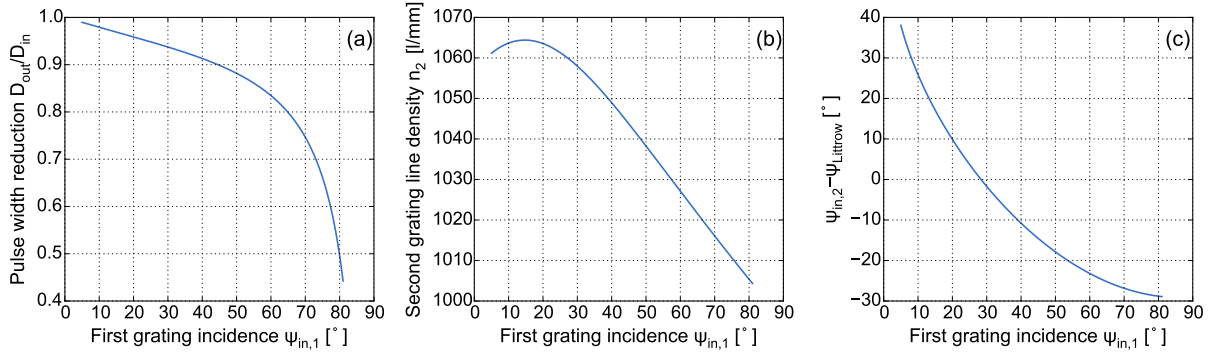


Figure 6.10.: Scaling of (a) laser pulse width reduction, (b) second grating line density and (c) second grating incidence angle deviation from its Littrow angle with first grating incidence angle to ensure correct orientation of plane of optimum compression and pulse-front tilt for an Å TWTS OFEL setup where the first grating line density is 1000 l/mm. For the required pulse width reduction of about 50 % the first and second grating incidence angles are far from their Littrow angles. Thus a different first grating line density of  $n_1 = 1500$  l/mm is chosen for the setup.

compression according to the requirements of the interaction geometry.

The following subsection shows how to determine the parameters of the gratings in order to achieve the three aims of aligning pulse-front tilt and plane optimum compression correctly as well as providing the necessary pulse size reduction.

## OPTICAL SETUP PARAMETERS AND ALIGNMENT TOLERANCES

The laser system of the setup is again assumed to be of PEnELOPE type, i.e.  $\lambda_{Laser} = 1.035 \mu\text{m}$  as well as about a petawatt of maximum available power, and its pulses have a rectangular transverse profile with a flat-top irradiance distribution.

The procedure to determine the grating line densities and incidence angles is in principle identical to the procedure for the incoherent hard X-ray source by TWTS, subsection 6.1.1, which uses the same setup type without focusing in the interaction plane.

In a nutshell, by searching for roots of the implicit function (6.1) within a range of first grating line densities  $n_1$  and incidence angles  $\psi_{in,1}$  a subset of these parameters ensuring correct orientation of plane of optimum compression  $\alpha_{poc} = -83^\circ$  and pulse-front tilt  $\alpha_{tilt} = 7^\circ$  can be determined first.

Second, out of this subset the combinations providing sufficient pulse width reduction from  $D_{in} = 120.00$  mm to  $w_0 = 62.23$  mm, which is about 52 % of the original size, are determined. The reduction of laser pulse width from the original value  $D_{in}$  to  $D_{out}$  after passing a grating pair is given by

$$D_{out} = \frac{\cos \psi_{out,2} \cos \psi_{out,1}}{\cos \psi_{in,2} \cos \psi_{in,1}} D_{in},$$

assuming the width increase due to spatial dispersion is small or compensated beforehand or afterwards. The range of usable first grating line densities extends roughly from 1000 l/mm to 1500 l/mm and the incidence angle on the first grating ensuring enough pulse width reduction is always around  $80^\circ$ . Figure 6.10 depicts the scaling of pulse width reduction with first grating incidence angle for a first grating line density of 1000 l/mm. Scalings of required second grating line density and incidence angle ensuring correct orientation of pulse-front tilt and plane of optimum compression are printed too. The combination of this low first grating line density and

Table 6.10.: Parameters of optical components and their alignment tolerances for the 1.5 Å TWTS OFEL in the setup without focusing in the interaction plane visualized in fig. 4.4.

Optical setup parameters and alignment tolerances	Å TWTS OFEL w/o focusing
1st grating line density $n_1$ [l/mm]	1500
1st grating incidence angle $\psi_{in,1}$ [°]	82.663
1st grating incidence angle variation $\Delta\psi_{in,1}$ [μrad]	60
Distance between gratings $L_{grating}$ [mm]	11075
2nd grating incidence angle $\psi_{in,2}$ [°]	34.028
2nd grating rotation angle $\epsilon$ [°]	-0.076
2nd grating rotation angle variation $\Delta\epsilon$ [μrad]	29
2nd grating line density $n_2$ [l/mm]	1505
2nd grating diffraction angle $\psi_{out,2}$ [°]	-86.452
Distance between 2nd grating and mirror 1 [mm]	1500
Mirror 1 deflection angle [°]	82
Cylindrical mirror focusing dist. $f_{vert}$ [mm]	2906
Propagation distance from cyl. mirror to interaction point [m]	23.8
Interaction angle variation $\Delta\phi$ [μrad]	245

the large required incidence angle around 80° has some drawbacks: the first grating incidence angle is far from the first gratings Littrow angle and the second grating incidence angle is far from the second gratings Littrow angle, as shown in fig. 6.10c. Both of these drawbacks can be remedied by choosing a higher first grating line density. This has furthermore the advantage that the pulse-front tilt during propagation between first and second grating is larger. With a larger pulse-front tilt the spatial dispersion precompensation for spatial dispersion generated during propagation between second grating and interaction point can be generated on a shorter distance. Thus the final choice for first grating line density is  $n_1 = 1500$  l/mm.

Third, a good estimate for the second grating line is obtained by a scaling graph similar to fig. 6.10b but for a first grating line density of 1500 l/mm. A second grating line density of 1505 l/mm yields a suitable pulse reduction of 48.4 % at grating incidence angles  $\psi_{in,1} = 82.663^\circ$  and  $\psi_{in,2} = 34.028^\circ$ , at first and second grating respectively, providing correct orientation of plane of optimum compression and pulse-front tilt. These angles are obtained by a scaling similar to fig. 6.5c.

Note, here the assumption of 100% diffraction efficiency at the gratings is made as well as the energy taken away from the pulse for electron acceleration is assumed to be negligible. In a real setup both assumptions will not hold but make an initially higher laser energy necessary which goes along with larger transverse pulse size to keep the areal energy density constant. However, the principle of the method outlined here for optical undulator preparation is still applicable when refining the setup to take the above factors into account.

Tabular 6.10 gives an overview on the parameters of the optical components and their alignment tolerances.

These are again obtained by varying one of the parameters, while leaving the others at their optimum value, and observing the resulting variation in laser irradiance and optical undulator frequency, calculated with eqs. (4.27) and (4.28), which have limits according to eqs. (4.3).

The limits obtained are solely determined by the loss of overlap between electron bunch and laser pulse from alignment errors in the course of interaction. Optical undulator frequency variation due to misalignment is negligible within these limits.

Compared to the VUV TWTS OFEL example, the required alignment precision of this Å TWTS

OFEL is higher due to the longer interaction distance. It causes a larger offset between electron bunch and laser pulse from the same angular divergence at the end of the interaction.

The setup presented is very compact compared to standard X-ray FELs such as LCLS or SACLA, both realizing radiation generation on a kilometer scale. Nevertheless, the in-vacuum propagation distances of about 11 m between the gratings and about 25 m from the second grating to the interaction point are challenging due to the one meter scale beam diameter in the horizontal direction around the second grating. Therefore aperture sizes of the laser beam transport system are on the square meter scale.

The reason for this large pulse width is spatial dispersion. During propagation of the pulse from the cylindrical mirror focusing on the electron trajectory a large spatial dispersion develops due to the large distance the pulse needs propagate until it covers the focal distance, where the pulse propagation direction encloses the interaction angle with the mirror surface. In this setup the spatial dispersion precompensation is generated within the grating pair where the pulse-front tilt orientation is opposite compared to propagation after the grating pair. Therefore the grating separation distance is large as well.

These large propagation distances can be reduced if the electron bunch quality allows to use larger interaction angles or optics of higher damage threshold are available allowing for smaller laser cross-sections.

### 6.4.3. APPLYING THE Å TWTS OFEL TO PLASMA DYNAMICS STUDIES

#### EXPERIMENTAL SETUP

A sketch of the setup and the experimental area is presented in fig. 6.11. The experiment uses both petawatt-class laser systems, DRACO and PEnELOPE, that are (or will be) available at HZDR. Compared to PEnELOPE laser pulses, which were already utilized in the preceding examples, DRACO pulses have a wavelength of  $\lambda_{\text{Laser}} = 800 \text{ nm}$  and a pulse duration of  $\tau_{\text{FWHM},I} = 30 \text{ fs}$ , where  $\tau_{\text{FWHM},I}$  is measured as full-width at half-maximum of the intensity profile.

The petawatt branch of the DRACO system is used to accelerate protons from a solid density target. The pulse is focused to a few micron full-width at half maximum resulting in a relativistic irradiance exceeding  $1.0 \times 10^{21} \text{ W cm}^{-2}$ . Protons are accelerated from the rear side of the target and their distribution in space and energy can be measured with a radiochromic film stack. Furthermore, processes such as e.g. electron transport, ultrafast ionization as well as hole-boring and shock propagation or the development of instabilities and filamentation occur in the plasma and can be recorded in space and time utilizing the intense and few femtosecond long pulses from the Å TWTS OFEL, which contain more than  $1.0 \times 10^9$  photons.

These pulses are generated utilizing pulses of the PEnELOPE laser system as optical undulators for the Å TWTS OFEL. In order to ensure proper synchronization of infrared pump and X-ray probe pulse at the target the PEnELOPE and DRACO oscillators are synchronized. The time delay between pump and probe is controlled with a delay stage in the DRACO petawatt branch since the propagation distance of the DRACO pump pulse is much shorter than that of the PEnELOPE pulse. A pulse from the PEnELOPE system passes the grating pair and the cylindrical mirror, both of which have been described in detail in the last subsection, to prepare it as an optical undulator of sufficient field strength and with proper orientation of pulse-front tilt and plane of optimum compression.

Relativistic electron bunches producing  $1.5 \text{ Å}$  radiation are generated by laser wakefield acceleration which is driven by the 150 TW branch of DRACO. These DRACO pulses pass a delay stage after they left the DRACO compressor in order to ensure optimum synchronization between optical undulator pulse and accelerated electrons at the interaction point. After the delay stage the lower energetic pulse is focused into a gas jet in order to drive laser wakefield acceleration

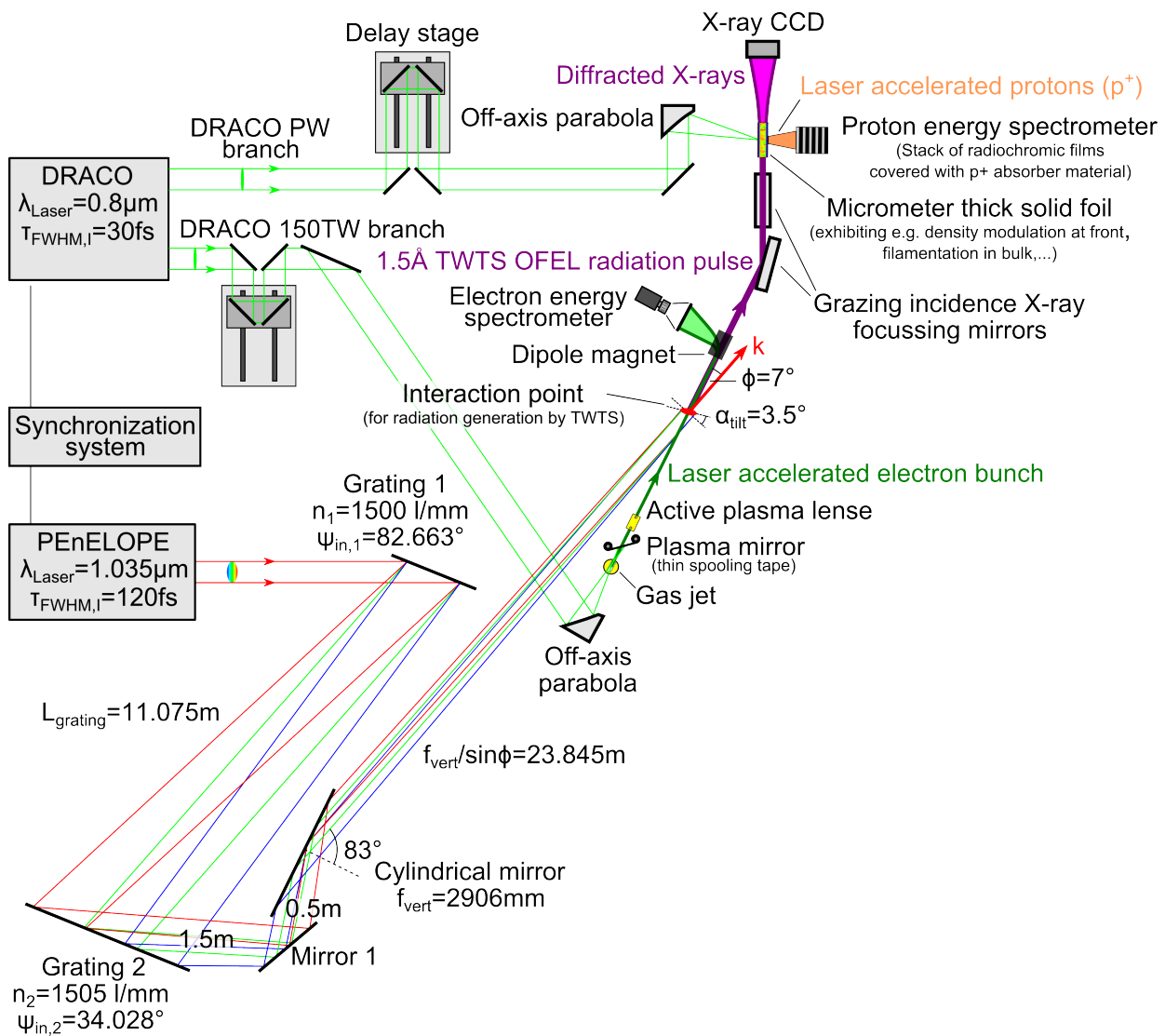


Figure 6.11.: Experimental setup for nanoscale femtosecond imaging of a hot plasma by small-angle X-ray scattering or resonant coherent X-ray diffraction [141, 251]. The plasma is created during laser ion acceleration from solid density targets. Both laser systems available at HZDR are used. DRACO to accelerate protons from the target and electrons from a gas jet. PEnELOPE to provide the optical undulator for the Å TWTS OFEL. (not to scale)

of electrons. The required energy of about 350 MeV can be reached within a few centimeter distance. After acceleration the driver laser pulse is reflected out of the electron bunch path by a foil, e.g. an aluminum foil or VHS tape [252]. Then the rapidly defocusing electron beam is refocused which can be realized in a compact manner by either an active plasma lens [240–242] or by a miniature permanent magnet quadrupole triplet [100, 253].

The focused electron bunch then interacts with the optical undulator pulse at an interaction angle of  $7^\circ$  to produce radiation at the desired wavelength of  $1.5 \text{ \AA}$ . A dipole magnet separates the radiation from the electron bunch, which can be analyzed by directing the electrons onto a phosphor screen where the spatial distribution of electrons corresponds to their energy distribution. The diverging radiation is collimated again by two grazing incidence cylindrical mirrors allowing for large reflection efficiency due to total external reflection [77]. If required, a high-

-power grating monochromator for the X-rays pulses can be inserted at this position as well [82]. Then the focused X-ray pulse arrives at the target and is diffracted for instance at large scale plasma structures allowing to obtain information on the target properties by analyzing e. g. the small angle X-ray scattering (SAXS) signal.

## ALIGNMENT TOLERANCES OF OPTICAL COMPONENTS

The alignment stability required in this example is technically feasible today. The compressor gratings of existing high-power laser systems are aligned with  $\mu\text{rad}$  accuracy [124, 254] and conventional accelerators feature  $\mu\text{rad}$  pointing stability [75, 255]. Though the typically achieved pointing stability in the mrad range [218, 220] of laser wakefield accelerated electrons is not sufficient, yet better than  $400 \mu\text{rad}$  pointing stability has been reported for low energy electrons [217] where the measurement was actually limited by the resolution of the imaging system and  $600 \mu\text{rad}$  have been reported for 2.7 GeV electrons [216]. Beyond these encouraging results, electron beam pointing stability is addressed by a number of projects targeting at the operation of a free-electron laser using laser wakefield accelerated electrons [256–261].

## LIGHT SOURCE PERFORMANCE

The  $\text{\AA}$  TWTS OFEL provides  $3 \times 10^9$  photons per pulse at a rate of ten pulses per second. Its repetition rate is defined by the 10 Hz repetition rate of the PEnELOPE laser system providing the optical undulator pulses.

The incident photon number of the  $\text{\AA}$  TWTS OFEL is reduced from the  $10 \times 10^{12}$  photons typically provided by a traditional X-ray FEL for two reasons. First, its electron bunch charge is smaller with 50 pC in contrast to 180 pC at LCLS. Second, its electron energy is lower resulting in less X-ray photon production as expressed by the scaling of radiated peak power  $P \approx \rho \gamma_0 m c^2 I_p / e$ .

Furthermore, the emitted radiation of the  $\text{\AA}$  TWTS OFEL is not fully transversely coherent due to non-optimum matching of radiation and electron bunch divergence which requires spatial filtering of the radiation pulse. The coefficient  $\hat{\epsilon}$  indicating the degree of spatial coherence, which is optimally around unity for full spatial coherence according to refs. [87, 88] (cf. eq. (2.17)), yields a value of 8.7. But the requirement of  $\hat{\epsilon} \approx 1$  should not be taken too strictly, for example the hard X-ray FEL SACLA yields a transverse coherence parameter of 3.7 for 1.24  $\text{\AA}$  X-rays but reaches full transverse coherence [75].

Despite the lower photon number of this  $\text{\AA}$  TWTS OFEL, its radiation pulses can be used to image the plasma dynamics in the laser driven target by non-resonant X-ray scattering. The recent LN04 experiment conducted at the Matter under Extreme Conditions Instrument at LCLS in October 2016, which was lead by Thomas Kluge and aimed at establishing the SAXS method to probe laser-driven plasmas on femtosecond timescales, did diffraction experiments at crystallographically sharp step targets as well as targets with a grating structure and targets composed of copper and silicon with a grating structure at the interface. During these experiments the incident X-ray pulses contained  $10^{12}$  photons. Although they were attenuated by two orders of magnitude, the X-ray CCD camera used for measuring the scattered X-ray signal almost saturated during the experiments at the step and grating targets due to the large scattering signal [262]. Therefore even another order of magnitude reduction in incident photon number should yield a measurable scattering signal. Thus, the  $\text{\AA}$  TWTS OFEL can be a useful source for these kind of experiments aiming at imaging steep electron density gradients or testing instruments and diagnostic tools by scattering from artificial structures where the recorded signal is theoretically known beforehand.

The applicability of this  $\text{\AA}$  TWTS OFEL to image femtosecond and nanometer scale plasma dynamics is further substantiated in a simulation study where the electron density distribution

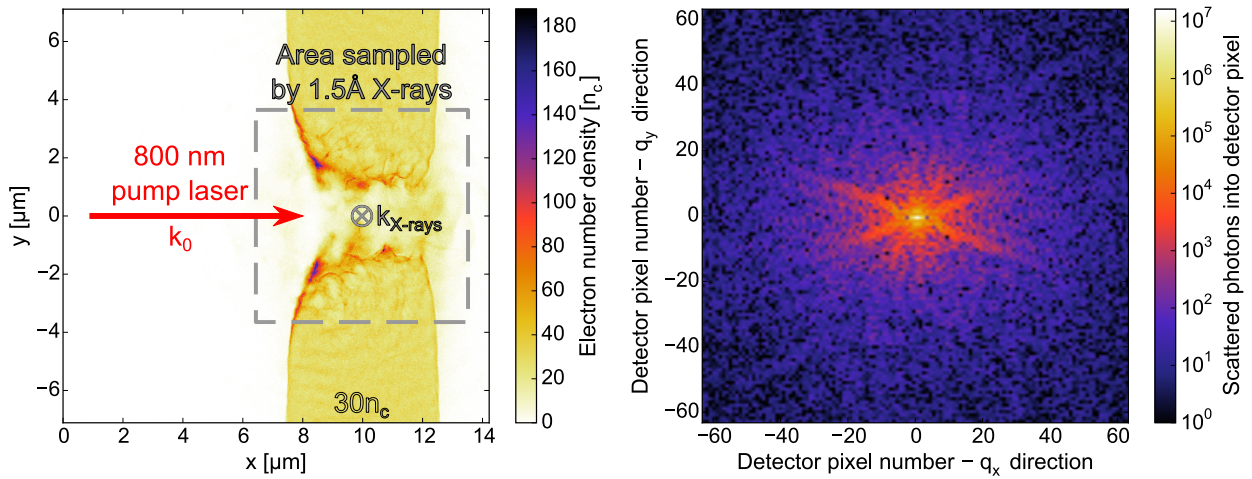


Figure 6.12.: Small-angle X-ray scattering (SAXS) signal from a laser driven cryogenic hydrogen strand. The left image shows the electron number density distribution 134 fs after a 30 fs, 105 TW infrared driver laser pulse has hit the 5  $\mu\text{m}$  thick solid hydrogen strand. The laser is incident from the left and focused to a spot size of 3  $\mu\text{m}$  full-width at half maximum of the intensity profile which yields a scaled intensity of  $a_0 = 22$ . The initial hydrogen number density is thirty critical densities  $n_c = k_0^2 \epsilon_0 m c^2 / q^2$  for the laser wavelength of  $\lambda_{\text{Laser}} = 800 \text{ nm}$ . During laser irradiation electrons are pushed by the laser ponderomotive force leading to hole boring and an increase in density near the laser propagation axis. The electron density distribution can be imaged by small-angle X-ray scattering with an X-ray pulse of femtosecond scale duration. X-ray pulse and pump laser direction of propagation are perpendicular such that the 1.5  $\text{\AA}$  wavelength X-ray pulse illuminates the target from the side on a 7  $\mu\text{m} \times 7 \mu\text{m}$  area. The right image shows the corresponding synthetic scattering signal on an X-ray camera 62 cm behind the target. The incident X-ray pulse parameters match those in tab. 6.8. With photon counts in the range of 100–1000 per 13  $\mu\text{m} \times 13 \mu\text{m}$  detector pixel the scattering signal is well-measurable. Thus, the  $\text{\AA}$  TWTS OFEL is well suited to probe the femtosecond and nanometer scale plasma dynamics of laser driven solid density materials. (Electron density data obtained from PICLS simulations carried out by João Branco. See appendix B)

in a thin laser driven solid density material is recorded by small-angle X-ray scattering (SAXS). Figure 6.12 shows a synthetic SAXS scattering image from a cryogenic hydrogen strand irradiated by a 105 TW infrared laser pulse. The scattering of 1.5  $\text{\AA}$  pulses, obtained from this  $\text{\AA}$  TWTS OFEL, produces on a detector 62 cm behind the strand a photon count of more than 100 per detector pixel within the pronounced cross-shaped region. Even with a quantum efficiency of the detector around 10 % the signal is strong enough for state-of-the-art X-ray detectors capable of single-photon counting [263].

Imaging dynamics in higher density materials such as titanium, copper or gold is also possible with this  $\text{\AA}$  TWTS OFEL. For 1.5  $\text{\AA}$  radiation the critical plasma density, which marks the largest penetrable electron density, is orders of magnitude larger than the density of these materials. Furthermore, structures in electron density which develop on a scale larger than the plasma Debye length [264] are still resolvable, too. The Debye length, scaling with electron temperature and density as well as ionic charge, for 20+ copper at a temperature of 400 eV is 2.6 nm while in principle structures with a scale length of the X-ray wavelength of 1.5  $\text{\AA}$  are resolvable.

The photon yield of the  $\text{\AA}$  TWTS OFEL can be increased by tweaking the laser wakefield

acceleration to yield higher bunch charges, as it has recently been done in an experimental campaign with the DRACO laser at HZDR [61]. This may result in lower quality electron bunches but the increased photon yield could make up for this.

All in all, scattering experiments from laser driven plasmas with nanometer and femtosecond resolution, and possibly elemental and charge state sensitivity when taking advantage of resonant scattering, seems to be feasible with the Å TWTS OFEL at HZDR once the required electron bunch and laser quality is available. A project of this kind clearly is to be seen as an ambitious long-term goal which would demonstrate the full power of all-optical free-electron lasers. These compact high-brightness radiation sources, realized by the combination of laser wakefield acceleration and Traveling-Wave Thomson-Scattering, can be built on a much smaller footprint than existing X-ray free-electron lasers. Combining all the available resources of the ELBE Center for High-Power Radiation Sources at HZDR, the petawatt laser systems DRACO and PEnELOPE as well as the facilities for laser wakefield or radio frequency electron acceleration, an Å TWTS OFEL is realizable at HZDR.

On a mid-term time scale pump-probe experiments using an all-optical, high-flux, incoherent TWTS X-ray source, such as the 30 keV source presented at the beginning of this chapter, can be imagined. These ultrafast and tunable TWTS X-ray sources could be used for example to image transient processes on the one hundred femtosecond scale by phase-contrast imaging [265]. Again, these experiments would make use of the unique research infrastructure at HZDR by combining the two petawatt-class laser-systems and possibly the conventional electron accelerator ELBE. The reduced electron bunch and laser pulse quality requirements of a yield-enhanced Thomson source by TWTS remove the highest realization hurdle encountered in an Å TWTS OFEL realization, at the cost of a reduced photon output. Thus, an enhanced Thomson source can represent an intermediate stage towards TWTS OFEL realization.

# 7. CONCLUSION & OUTLOOK

## CONCLUSION

Traveling-Wave Thomson-Scattering (TWTS) optical free-electron lasers (OFELs) can be realized today. This final result of the thesis can be drawn from its work on the theory as well as the implementation of TWTS.

The theoretical possibility of operating a TWTS OFEL is proven by a 1.5D analytical model of the interaction between electrons, laser pulse and radiation field showing microbunching of the electron bunch and subsequent coherent radiation amplification in TWTS. Furthermore, it is shown that TWTS OFELs can become fully transverse coherent, do not suffer from the photon emission recoil even at hard X-ray wavelengths and that they have lower requirements on electron bunch quality than head-on Thomson scattering OFEL schemes. Implementing TWTS OFELs becomes possible with the presented optical setups for the generation of pulse-front tilted laser pulses featuring local second-order dispersion compensation.

These setups form the basis of the optical design of the presented examples of TWTS OFELs. Combining the findings gained from these examples leads to the conclusion that TWTS OFELs are realizable today. The specific example of a VUV TWTS OFEL demonstrates that existing electron accelerators deliver bunches of sufficient quality for TWTS OFEL operation. Furthermore, by inserting corrugated structures into the electron beam path the electron bunch energy spread can be reduced after acceleration, which has been demonstrated experimentally already, allowing for the realization of EUV TWTS OFELs today. All examples demonstrate that laser systems delivering pulses of sufficient peak power for TWTS OFEL realization are available today. In addition, the necessary optical components for the generation of pulse-front tilted laser pulses featuring local second-order dispersion compensation are available today and technology exists to achieve the necessary alignment precision.

The presented TWTS OFEL examples also demonstrate that their lab space requirement is at least an order of magnitude smaller than those of conventional FELs radiating at the same wavelength. The compactness of TWTS OFELs mainly arises from their lower required electron energy compared to conventional FELs. At least an order of magnitude lower electron energy is required for TWTS OFELs which becomes possible by the two or more orders of magnitude smaller period of optical undulators compared to typical magnetic undulators employed at existing FELs. TWTS OFELs become exceedingly compact if electrons are laser wakefield accelerated. Then the same laser system can be used to accelerate electrons and provide the optical undulator if laser pulses are split in two part and used accordingly. This offers inherent synchronization of electrons and optical undulator, and reduces the complexity of the entire TWTS OFEL by reducing the number of complex devices to the one laser system. Thus, improvements in

laser pulse quality, e. g. pulse contrast, transverse profile uniformity or pointing stability, are of twofold benefit to a TWTS OFEL realization since they do not only improve the quality of electron bunches but also of optical undulators.

The reduced lab space requirement of TWTS OFELs has a significant impact on the construction cost of an FEL. Especially at X-ray wavelengths, where conventional free-electron lasers employ 100 m long magnetic undulators and kilometer scale electron accelerators, TWTS OFELs require less than a tenth of the area a conventional free-electron laser facility occupies which decreases their construction cost tremendously. For example, during the European XFEL construction about a third of the total construction cost was spent on civil engineering which amounts to EUR 430 million in total and EUR 23 million per hectare. The presented Ångström TWTS OFEL is realizable on an area less than one hectare, being less than a tenth of the area spanned by the European XFEL, giving rise to a significant reduction of construction cost.

Today all of the existing high peak-brilliance FEL light sources are large-scale devices requiring large-scale infrastructure, for example, in civil and electrical engineering, data communication, power supply and personnel. Compact TWTS OFELs also require less infrastructure reducing their daily operation cost in addition to their lower construction cost, but at the expense of lower peak-brilliance being reduced by about two orders of magnitude due to the smaller photon yield as seen from the examples. Yet not all of the experiments conducted at existing free-electron lasers make use of their full photon flux and thus TWTS OFELs can become a valuable addition to the existing landscape of high peak-brilliance light sources by offering beam time to these experiments at reduced cost. Possible experiments conducted at TWTS OFELs primarily make use of their femtosecond scale pulse durations and transverse coherence but study objects containing sufficient scatterers, for example solid density materials, to obtain a measurable scattering signal. The combination of short pulse durations and transverse coherence enables recording of scattering signals from samples before the radiation damage significantly alters their structural or chemical properties, which is known as the *diffract-before-destroy* principle [266–268]. If the photon yield of a TWTS OFEL is large enough, the full spectroscopic or structural information of a small and irreproducible sample can be obtained within a single shot. Examples of such samples are single nano objects [76, 269] or biological specimen which can not be grown in crystals large enough for synchrotron sources [270–272]. The ability to rely on single shot analysis even removes the need to keep biological samples at cryogenic temperatures allowing to study these in a fully functional state and with nanometer resolution [11].

## OUTLOOK

While this thesis focused on the possibility, requirements and necessary techniques to operate a TWTS OFEL, a TWTS light source does not need to operate as an optical FEL with high requirements on the quality of electron bunches and laser pulses. The realization of a compact incoherent TWTS source is a less elaborate task and can precede the realization of a TWTS OFEL. Compared to a head-on Thomson scattering source, an incoherent TWTS source can produce radiation with orders of magnitude higher peak spectral-brightness due to the available longer interaction distances in the TWTS geometry and can thus be seen as a *yield-enhanced Thomson* source. Its radiation pulses have higher intensity and smaller bandwidth than those of a comparable head-on source, since the scattered photon number scales linearly to the number of undulator periods and the bandwidth scales inversely proportional to it. Optical undulators provided by petawatt laser pulses being focused only vertically are long but not too strong. Their non-relativistic strengths allow to produce radiation well within the linear regime of Thomson scattering [45, 273]. Yield-enhanced Thomson sources will be especially relevant if they are operated at large interaction angles where the Doppler shift is large and megaelectronvolt photon energies are achievable. They have the potential to become the brightest controllable light

source in the megaelectronvolt photon energy range. Yield-enhanced Thomson sources with unprecedented peak brightness at a hundred kiloelectronvolt to several megaelectronvolt photon energies can become a tool, for example, to nondestructively analyze the isotopic composition of materials, such as spent nuclear fuel, via nuclear resonance fluorescence [142, 274–277]. The production of positron beams copropagating with the radiation that produced them is an example which models astrophysical scenarios in laboratory experiments [278, 279]. Other possible applications include transmuting nuclear waste [143], testing nondestructively [280], studying dense-liquid-jet flow dynamics [281] or the structure of nuclei [282, 283]. Even more applications are investigated at ELI-NP [284]. Furthermore, the possibility to adjust the bandwidth of a yield-enhanced Thomson source by the laser pulse width could be exploited to fulfill the needs of a range of applications requiring percent-level bandwidths X-ray pulses (*pink beams*) [37, 285–287]. Control over the optical undulator lengths, which controls the bandwidth, is simply achieved in TWTS by blocking outer parts of the laser pulse with an aperture allowing for experiment specific tuning of undulator length and thus bandwidth. A couple of challenges remain for their realization such as the development of diagnostic tools to measure the correct orientation of pulse-front tilt and plane of optimum compression as well as the 100 fs-scale synchronization of electron bunches and laser pulses.

Once the necessary diagnostics exist, the realization of a TWTS OFEL is in reach. Radiation wavelengths in the vacuum or extreme ultraviolet range suggest itself as target wavelengths of the first TWTS OFELs since the required quality of electrons and laser pulses are lower at these longer wavelengths. From today's perspective the major task encountered when building TWTS OFELs is the development of techniques granting control over the laser pulse transverse irradiance variation on the 1 % level whereas electron bunches of sufficient quality can be already provided by existing accelerators. Fields of research targeted by a VUV TWTS OFEL are, for example, ionization dynamics in many-particle systems [140] as well as temporal observation of reaction kinetics at surfaces [163–165] and ablation from material surfaces [139, 166]. While the former is relevant to engineer catalysts for the chemical or pharmaceutical industry, the latter is of relevance to micromachining and -structuring.

The continuous advance of electron and laser quality as well as laser power enables the reduction of TWTS OFEL radiation wavelengths. Advancing to hard X-ray wavelengths in the Ångström range is especially attractive since these can penetrate deep into samples and allow to image the structure of matter at atomic length scales. Experiments making use of this and the femtosecond scale X-ray pulse duration study, for example, the ultrafast dynamics of non-crystalline materials at nanometer length scales [15, 180, 251], such as the probing of the laser-driven solid hydrogen strand discussed in the last chapter, observe real-time changes in electronic structure at material surfaces [288] and X-ray irradiance induced damage of materials [289], obtain three-dimensional information of small biological structures such as proteins [16, 290], chromosomes [291], bacteria [11] and viruses [10], or identify particular atomic elements in (living) organic material [292] on a subcellular scale. Experiments in the field condensed matter physics study different types of order in high temperature superconductors, such as spin and charge density waves or magnetic excitations, that either compete or compel with superconductivity at its onset [203, 293, 294], or visualize the dynamics of magnetic fluctuations and magnetization relaxation processes in low-dimensional matter [202, 203, 295] which is a topic relevant to research on future storage device technology and electronics utilizing the electrons spin.

TWTS even allows to produce attosecond radiation pulses to probe subfemtosecond electron dynamics. Evolved schemes exist for classical FELs to produce such pulses [296, 297], but TWTS makes their generation possible with electron pulses of femtosecond and longer pulse duration. In interaction scenarios where the laser pulse is shorter than the electron bunch the part of the electron bunch interacting with the laser pulse is the same over the whole interaction duration which simply follows from the choice and condition of pulse front tilt angle. Thus, with

attosecond laser pulses [298] as optical undulators only an attosecond part of the electron bunch produces radiation which defines the radiation pulse duration. Furthermore, monocycle radiation pulses may be generated by the method presented in ref. [299]. It was originally developed for conventional FELs, but can be realized by TWTS with multiple chirped laser pulses.

The development of TWTS OFELs needs to be accompanied by comprehensive simulation studies taking realistic experimental conditions into account [KSc2]. The TWTS OFEL performance is expected to depend on the real laser profile, electron bunch energy spread and normalized transverse emittance, as well as radiation diffraction and walk-off. Their impact on radiation amplification needs to be quantified and weighed up against each other in order to design optimized setups which well suit to a particular combination of electron accelerator and laser system. However, an analysis of the widely used FEL codes PUFFIN [300] and GENESIS [301] revealed that none of these is able to model the fundamental interaction between a laser field, a radiation field and an electron bunch in TWTS OFELs correctly. Both codes intrinsically assume the existence of a magnetic undulator by integrating the FEL pendulum equations. In order to model and calculate the fundamental interaction correctly, thereby taking all realistic experimental conditions into account, a particle in cell code, such as PICONGPU [302, 303], can be used. Being able to simulate the fundamental interaction comes at the cost of a very high computational power requirement. In order to resolve the electron and radiation field dynamics on the simulation grid and self-consistently calculate their interaction, the entire FEL amplification needs to be simulated with temporal and spatial resolution better than the radiation period and wavelength, respectively, over a volume enclosing the electron bunch and over an interaction duration until saturation is reached after nanoseconds. PICONGPU is fast enough to make this possible on a timescale of weeks, contrary to legacy codes where this is simply not feasible. At the same time the radiation emitted by all electrons during the interaction can be calculated in-situ and time-resolved allowing to analyze the complete spectrum of emitted radiation which also provides a diagnostic tool to analyze electron dynamics [KSc3–KSc5].

Beyond the application of TWTS as a light source, it can find use in other applications, too. These applications can make use of the optical designs for the generation of dispersion-controlled laser pulses being presented in this thesis. Implementations of TWTS can serve as a laboratory to study fundamental quantum effects in the interaction of electron bunches with high intensity lasers [304] where it can be applied to investigate e. g. quantum mechanical approaches to cancel the ponderomotive line broadening by an optimized laser pulse frequency chirp [137] or the FEL startup from shotnoise [305–308] which may be described by the quantum free-electron laser interaction [113, 309, 310]. TWTS laser pulses can also be used to cool electron bunches in electron storage rings [311] or to accelerate electrons beyond the dephasing and depletion limit in laser-wakefield accelerators (*Traveling-Wave Electron-Acceleration: TWEAC*) [KSc6].

To conclude, the numerous described applications of TWTS strongly motivate its realization and this thesis prepares the ground for it. With possible realizations as a driver for fundamental quantum physics, compact high-energy electron accelerators or compact high-brilliance light sources it can be foreseen that bringing TWTS from theory to life will significantly contribute to the advance of fundamental and applied science.

# A. MACRO TO EVALUATE LASER PULSE DISPERSIONS IN ZEMAX

In order to determine plane of optimum compression orientation and pulse-front tilt in the optical design software ZEMAX, during the thesis work a macro was written in the ZEMAX Programming Language ZPL which is callable within the program.

Section 6.1 already introduced the principle of determining pulse-front tilt and plane of optimum compression orientation by sampling time-delay  $TD$  and group-delay dispersion  $GDD$  in planes coinciding with expected pulse-front and plane of optimum compression, respectively. When using the presented method to calculate  $TD$  and  $GDD$  as derivatives of the optical phase from optical path length differences between different wavelengths, the optical path length as it is given by the function `OPTH()` in ZEMAX for a particular wavelength needs to be corrected if the wavelength is not the central laser wavelength.

For a correct calculation of  $TD$  and  $GDD$  optical phase differences between different wavelengths need to be calculated, where the phases for all wavelengths are evaluated at the same spatial position along the laser path. But there is no build-in function in ZEMAX returning the path length of a ray until it reaches a certain position within the path. Such a complex function would either need to interpolate the correct starting position of a ray in the entrance plane by following many rays or it would need to reverse raytrace a ray through the setup where its starting parameters could be approximated from a forward raytrace.

The compensation calculation chosen in the following macro is simpler by estimating true path lengths from path lengths obtained in ZEMAX for rays originating from the same point. Figure A.1 gives a geometric overview on the compensation calculation. From every starting position of a central wavelength ray in the entrance plane two accompanying rays of different wavelengths, where  $\lambda_2 < \lambda_1 = \lambda_{\text{Laser}} < \lambda_3$ , start as well. The central wavelength ray serves as a *reference ray* for the other two rays. Three wavelengths are raytraced for every position where dispersion is evaluated in order to calculate the numerical derivatives (6.2). The position where the reference ray reaches the target plane, assumed to be the pulse front in the picture, defines an intersection point between the target plane and planes normal to the propagation direction of each of the other two rays. The latter two planes serve as *reference planes* until which the path length of a ray is measured in order to obtain a better estimate on the path length of a ray until the position where dispersion is evaluated for the calculation of  $TD$  and  $GDD$ . This yields a better estimate for the path length of ray by subtracting the additional distance covered by a ray until it reaches the target plane where ZEMAX stops measuring the path length. An even better estimate could be obtained by also subtracting the path length difference that two parallel rays of equal wavelength

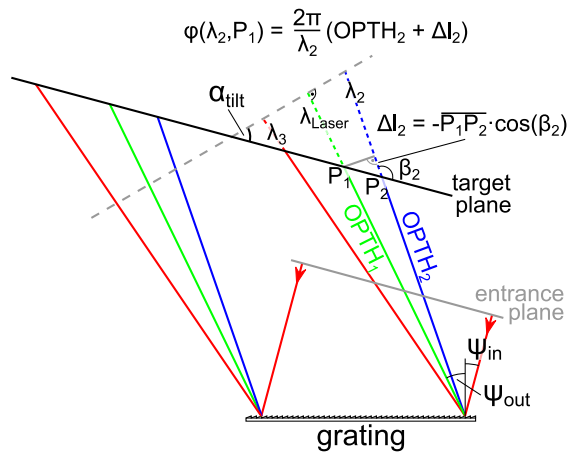


Figure A.1.: Approximating path length compensation for wavelength  $\lambda_3$  to calculate dispersion at point  $P$  in the reference plane by eqs. (6.2). To approximate the path of a ray of wavelength  $\lambda_3$  until it reaches  $P$  the path length of a ray with equal wavelength and starting at the same position as a reference ray of central laser wavelength is measured by ZEMAX until it reaches the target plane. The target is plane is chosen to be the pulse front in this example. From this path length the correction  $\Delta l$  is subtracted. (Originally in [KS4])

can have due to pulse-front tilt.

In this macro the path length of a ray of different wavelength than the central laser wavelength is estimated by subtracting the length  $\Delta l$  from the path length returned by ZEMAX. For this compensation calculation the distance  $a$  between a rays point of incidence on the target plane and the central wavelengths point of incidence can be obtained via the built-in function RAYY() returning the incidence position of a single ray on the target plane. Furthermore the angle  $\beta$  enclosed by the target plane and a rays propagation direction can be obtained by the build in function RAYM(). Then the correction  $\Delta l$  to the path length can be approximated by

$$\Delta l = a \cos \beta .$$

Whether the correction  $\Delta l$  needs to be subtracted or added to the ZEMAX value of a path length also depends on the propagation direction (+ or -z) of the pulse at the target plane. Thus the final propagation direction is an input parameter of the macro. The general layout of the macro follows the macro given in ref. [312].

```
!*****
! Zemax macro to compute the angular dispersion and
! group delay dispersion of a laser pulse.
!
!
! Klaus Steiniger, 2016
! Last review 28 Jun 2017
!
!*****
! Constants and input parameter
!
pi = 4*ATAN(1)
```

```

cspeed = 0.299792458      # [cspeed] = 1E9 * m / s = mm / ps

INPUT "Central Wavelength of laser in micrometer", lambda0
PRINT "Central Laser wavelength [mum] = ", lambda0          #[lambda] = 1E-6 m

bandw = 0.001*lambda0
nlambda = 3 #odd number!
dlambda = bandw/(nlambda-1)

INPUT "Surface at which to calculate dispersion", NSURF
PRINT "NSUR = ", NSURF

INPUT "Propagation direction at plane of measurement? (z = 1, -z = -1)", coord_sys

PRINT ""

SETSYSTEMPROPERTY 201, nlambda

!*****
! Set wavelengths for dispersion calculation
!
SETSYSTEMPROPERTY 202, 1, lambda0
VEC1(1) = lambda0          # Vector of the wavelengths which are
                          # propagated through the setup
                          # [VEC1] = 1E-6 m

K=-INTE(.5*nlambda)

! Set wavelength smaller than central
!
FOR J, 2, INTE(.5*nlambda) + 1, 1
    lambda = lambda0 + K*dlambda
    SETSYSTEMPROPERTY 202, J, lambda
    VEC1(J) = lambda
    K = K+1
NEXT

K = K+1 # leave out center frequency in frequency calculation

! Set wavelength larger than central
!
FOR J, INTE(.5*nlambda) + 2, nlambda, 1
    lambda = lambda0 + K*dlambda
    SETSYSTEMPROPERTY 202, J, lambda
    VEC1(J) = lambda
    K = K+1
NEXT

!*****
! Calculate Dispersions

```

```

!
PRINT ""

PRINT "Entrance pupil coordinate py, y-coordinate at plane[mm], TD[ps], GDD[fs^2]"

transv_samples = 3 # Refactor to an input value if necessary

!*** Produce container ***
DECLARE PHASES, DOUBLE, 1, 1000 # container for optical phase
DECLARE TD, DOUBLE, 1, 1000 # container for time delay
DECLARE GDD, DOUBLE, 1, 1000 # container for group delay dispersion

!*** Sample over multiple ray starting positions across the entrance pupil ***
!***
For L, 1, transv_samples, 1
  !*** Equally distribute the starting positions ***
  py = -1 + (L-1)*2/(transv_samples - 1)

  FOR J, 1, nlambda, 1
    RAYTRACE 0, 0, 0, py, J
    !-----
    ! Calculate compensation of optical path length for rays of different
    ! frequency than the central frequency.
    !
    ! For the calculation of dispersion, the optical path length
    ! of a ray must be measured until its phase-front overlaps with the
    ! point of dispersion measurement.
    ! That is, at the position where the central frequency ray hits the
    ! measurement plane in Zemax.
    ! Since Zemax calculates optical path lengths of rays until they hit
    ! the measurement plane, the optical path length of
    ! non-central-frequency rays needs to be corrected.
    ! Which is done in the following.
    !
    ! Assumes that propagation is in vacuum (n=1)
    ! Sign of compensation depends on the propagation direction with
    ! respect to coord.-system in the measurement plane.
    !
    ypos = RAYY(NSURF)
    IF (J==1) THEN plane_intercept_c = ypos
    plane_intercept_difference = ypos - plane_intercept_c
    opth_compensation = plane_intercept_difference * RAYM(NSURF)
    path_length = OPTH(NSURF) - coord_sys*opth_compensation
    # OPTH returns the path in millimeter
    # [path_length] = 1E-3 m
    PHASES(J) = 2*PI*path_length/VEC1(J)
    # Phase from optical path along the ray
    # VEC1 is wavelength in microns
    # [PHASES] = 1E3
  NEXT

```

```

dlambda = -lambda0*lambda0/(2*pi*c*speed)      # [dlambda] = 1E-21 m s
ddlambda = -lambda0 * dlambda / (pi*c*speed)    # [ddlambda] = 1E-36 m s**2

FOR J, 2, INTE(.5*nlambda) + 1, 1
  h = VEC1(1)-VEC1(J)                            # [h] = 1E-6 m
  !-----
  ! optical phase derivatives with respect to frequency (TD and GDD)
  !
  dphase = (PHASES(nlambda+2-J)-PHASES(J))/2/h    # [dphase] = 1E9 / m
  ddphase = (PHASES(nlambda+2-J)-2*PHASES(1)+PHASES(J))/h/h
                                                    # [ddphase] = 1E15 / m**2
  TD(J) = dphase*dlambda                          # [TD] = 1E-12 s = ps
  GDD(J) = ddphase*dlambda*dlambda + dphase*ddlambda
                                                    # [GDD] = 1E-27 s**2
  PRINT py, ", ", plane_intercept_c, ", ", TD(J), ", ", GDD(J)*1E3
NEXT
NEXT
NEXT

```



## B. CALCULATING SCATTERING IMAGES FROM 2D ELECTRON NUMBER DENSITY DATA

Section 6.4 presented an x-ray diffraction image, fig. 6.12, from a laser pumped solid hydrogen target as it can be obtained by small angle X-ray scattering. This appendix explains the details behind the calculation of this scattering image.

The electron number density distribution was obtained by a two dimensional particle-in-cell simulation within a window of  $32 \mu\text{m} \times 32 \mu\text{m}$ . For write-out the electron density was sampled on an equidistant grid of  $1152 \times 1152$  nodes corresponding to a sample spacing of  $d = 1/36 \mu\text{m}$ . The simulation was carried out by João Branco with the PICLS code [313].

For the simulation the cryogenic hydrogen target is assumed to be fully ionized already before the main laser pulse interaction.

Thus all the electrons in the target can be considered free and the scattering signal on the detector is simply the superposition of radiation emitted by all electrons individually as a response to the X-ray probe field.

The electric field radiated by a single electron and measured at a position  $\mathbf{r}$  at time  $t$  can be approximated from the fields obtained from the Liénard-Wiechert potentials by [77, 314]

$$E(\mathbf{r}, t) = \frac{q}{4\pi\epsilon_0} \frac{[\mathbf{p} \times (\mathbf{p} \times \ddot{\mathbf{w}})]}{c^2 p^3}, \quad (\text{B.1})$$

with  $\epsilon_0$ ,  $m$ ,  $q$ ,  $c$  being the vacuum permittivity, electron mass and charge as well as vacuum speed of light, respectively. As illustrated in fig. B.1, in this formula  $\mathbf{w}(t)$  is the vector pointing from the origin of ordinates to the particle position at time  $t$ ,  $\ddot{\mathbf{w}}$  its second derivative with respect to time,  $\mathbf{p}(t) = \mathbf{r} - \mathbf{w}$  is the vector pointing from the particles position to the point where the field is evaluated,  $p$  its scalar value. This approximation assumes that the incident field does not accelerate the electron to relativistic energies as well as the angle enclosed by the polarization direction of the incident radiation field  $\mathbf{E}_{\text{in},0}$  and the observation direction  $\mathbf{p}$  is close to ninety degree. That is, radiation is observed in a narrow cone around the forward propagation direction of the incident radiation. Under these conditions the vector  $\mathbf{u} = c\mathbf{p}/p - \dot{\mathbf{w}}$  and the scalar product  $\mathbf{p}\mathbf{u}$ , which appear in the exact field calculation obtained from the Liénard-Wiechert potentials of a moving point charge, can be approximated by  $\mathbf{u} = c\mathbf{p}/p$  and  $\mathbf{p}\mathbf{u} = cp$ , respectively, which leads to the above formula.

In the right hand side of this formula the electron position and acceleration have to be evaluated at the retarded time  $t_{\text{ret}}$  taking into account that the field produced by the charge  $q$  at time  $t_{\text{ret}} < t$



The electric field observed at the position  $\mathbf{r}$  is a superposition of the fields radiated by all  $N_e$  electrons within the target

$$E(\mathbf{r}, t) = \sum_{j=1}^{N_e} E_j(\mathbf{r}, t) = \frac{r_e}{r} E_{in,0} e^{ik(ct-r)} \sum_{j=1}^{N_e} e^{i\mathbf{Q}\mathbf{w}_j},$$

where  $r_e = q^2/4\pi\epsilon_0 mc^2$  is the classical electron radius,  $\mathbf{Q} = \mathbf{k}' - \mathbf{k}$  is the scattering vector and its scalar value is given by the angle  $\theta$  which is one half of the angle enclosed by the wave vectors of incident and observed radiation

$$|Q| = 2k \sin \theta.$$

For small-angle X-ray scattering considered here, where  $\theta \ll 1$ , the angle  $\vartheta$  is almost ninety degree for all points of observation which was exploited in the derivation of the above formula by approximating  $\sin \vartheta \approx 1$ .

The calculation of the scattering signal from the electric field at the observation point can be simplified by rewriting the sum over all electrons into an integral over the target volume. To do so, the sum over all electrons is replaced by a sum over volume elements  $d^3w$  within which all electrons are assumed to equally contribute to the scattering signal, i. e.  $\mathbf{w}_j = \text{const}$  for all electrons within the volume element  $d^3w$ . The number of equally contributing electrons  $N_v$  within a volume element is obtained from the continuous electron number density  $n(\mathbf{w}, t)$  by evaluating it at the position of the volume element and multiplying by the volume of the element  $N_v(\mathbf{w}_j, t) = n(\mathbf{w}_j, t)d^3w$ . In total the sum is rewritten as

$$\sum_{j=1}^{N_e} e^{i\mathbf{Q}\mathbf{w}_j} \rightarrow \sum_j n(\mathbf{w}_j, t) e^{i\mathbf{Q}\mathbf{w}_j} d^3w.$$

In the limit  $d^3w \rightarrow 0$  the summation becomes an integration which has the form of a Fourier transform of the electron number density. Thus the observed scattered field can be calculated by

$$E(\mathbf{r}, t) = \frac{r_e}{r} E_{in,0} e^{ik(ct-r)} f(\mathbf{Q}),$$

where the scattering factor  $f(\mathbf{Q})$  is defined by

$$f(\mathbf{Q}) = \int d^3w n(\mathbf{w}, t) e^{i\mathbf{Q}\mathbf{w}}.$$

In a scattering experiment the signal is recorded on a detector at a distance  $L$  behind the target. The detector measures the number of radiated photons per detector pixel. This signal can be approximated from the above formula for the scattered field by first calculating the irradiance  $I(\mathbf{r}) = \frac{1}{2} c\epsilon_0 |E(\mathbf{r}, t)|^2$  on the detector from it. Second rewriting the scattered irradiance as a scattered photon flux  $n_{\text{phot}}$  by dividing the irradiance by the incident photon energy  $E_{\text{phot}}$ , thereby assuming elastic scattering,

$$n_{\text{phot}}(\mathbf{r}) = \frac{P_i}{E_{\text{phot}} A_i} \frac{r_e^2}{L^2} |f(\mathbf{Q})|^2,$$

where the incident X-ray pulse irradiance is expressed in terms of the power  $P_i$  and area  $A_i$  of the pulse and where  $r = L/\cos(2\theta) \approx L$  is approximated for the considered small-angle scattering. Third, to obtain the number of photons  $N_D$  scattered into a detector pixel at position  $\mathbf{r}_D$  the scattered photon density is evaluated at a detector pixel center and multiplied by the detector

pixel area  $A_D$  as well as X-ray pulse duration, which is approximately the electron pulse duration  $\tau_{el}$ ,

$$N_D(\mathbf{r}_D) = \frac{P_i \tau_{el} A_D}{E_{phot} A_i} \frac{r_e^2}{L^2} |f(\mathbf{Q}_D)|^2 ,$$

where  $\mathbf{Q}_D$  is a scattering vector pointing to a detector pixel center. Using the simple multiplication to convert from the scattered photon flux density to scattered photons per detector pixel assumes that the photon flux density is approximately constant in time and space over a detector pixel area.

To facilitate the calculation of the complex scattering factor  $f(\mathbf{Q}_D)$  from a sampled two dimensional electron number density  $n(\mathbf{w})$ , which is obtained by a two dimensional particle-in-cell simulation in the case of the example presented in section 6.4, it is assumed that the electron distribution along the (not simulated) third dimension is a constant continuation of the simulated 2D slice. This can be a good assumption if the target depth is smaller or on the size of the pump-laser diameter as it is the case for the simulated solid hydrogen. Under this assumption, the three-dimensional volume integral over the three-dimensional electron number density reduces to a two-dimensional area integral over the two-dimensional electron number density times the target depth

$$f(\mathbf{Q}) = (\text{target depth}) \cdot \int d^2 w n(\mathbf{w}) e^{i\mathbf{Q}\mathbf{w}} ,$$

where  $\mathbf{w}$  is now a two dimensional vector within a cross-sectional area of the target.

The two dimensional Fourier transform of the sampled two dimensional electron number density is performed by a fast Fourier transform (FFT). For the FFT the two dimensional electron number density is sampled on an equidistant grid with two dimensional vectors  $\mathbf{w}$  pointing to its nodes. These vectors can be written as  $\mathbf{w} = \mathbf{w}_{j,k} = (j \cdot d, k \cdot d)$  with  $j, k \in [0, 1, \dots, N-1]$  where  $N$  is the number of sampling points along one of the two orthogonal directions spanning the cross-sectional area. Further,  $d = |w_{j+1,k} - w_{j,k}|$  is the sample spacing which together with the number of samples defines the sample window width  $D = N \cdot d = |w_{N-1,k} - w_{0,k}|$ . The number of samples  $N$  should be a value of the kind  $2^n$ , where  $n = 1, 2, 3, \dots$ , in order to avoid unphysical structures in calculated scattering images which originate from zero-padding by the FFT algorithm. The window width  $D$  determines the frequency spacing  $\Delta Q = 2\pi/D$  in  $Q$ -space. The  $Q$ -space frequencies, for which a contribution to the scattering signal is calculated, are  $Q_{l,m} = (l \cdot \Delta Q, m \cdot \Delta Q)$  with  $l, m \in [0, 1, \dots, (N/2) - 1, -N/2, \dots, -1]$  (for the `scipy.fftpack.fft()` routine from SciPy which is used in this thesis).

The electron number density obtained from the PIC simulation is given relative to the critical density. Thus, in order to ensure correctness of the scattering factor calculated by the FFT, the matrix of the fast Fourier transformed electron number density is rescaled to yield at  $\mathbf{Q} = (0, 0) = Q_{00}$  the number  $N_e$  of electrons contributing to the scattering signal as it is demanded by the above relation for  $f(\mathbf{Q})$ .

The wave vector differences  $\mathbf{Q}$  for which scattering signals are calculated by the FFT are related to coordinates  $\mathbf{r}_D$  in the detector plane by the distance  $L$  between target and detector. A relation can be derived by analyzing

$$\mathbf{r} = r \frac{\mathbf{k}'}{k}$$

$$\Leftrightarrow L \mathbf{e}_z + r_{Dx} \mathbf{e}_x + r_{Dy} \mathbf{e}_y = \frac{L}{k \cos(2\theta)} (\mathbf{k} + Q_z \mathbf{e}_z + Q_x \mathbf{e}_x + Q_y \mathbf{e}_y) .$$

Using  $Q_z = -k [1 - \cos(2\theta)]$  the following relation between coordinates in the detector plane

$(r_{Dx}, r_{Dy})$  and transverse components of the scattering vector  $(Q_x, Q_y)$  can be given

$$r_{Dx} = \frac{L}{k \cos(2\theta)} Q_x \approx \frac{L}{k} Q_x \quad r_{Dy} = \frac{L}{k \cos(2\theta)} Q_y \approx \frac{L}{k} Q_y,$$

where the approximation is again valid for the considered case of small-angle scattering. In the calculation of the scattering signal in section 6.4 the distance  $L$  between target and detector is chosen to let the  $Q$ -space spacing  $\Delta Q$  correspond to a spacing on the detector plane equal to a detector pixel size, which is assumed to be  $13 \mu\text{m}$ . This eliminates the need to interpolate and average the scattered photon flux density in the detector plane over a pixel size.



# PUBLICATIONS BY THE AUTHOR

## Important parts of this thesis are treated in

- [KS1] K Steiniger, A Debus, A Irman, A Jochmann, R Pausch, U Schramm, and M Bussmann. „Brilliant and Efficient Optical Free-Electron Lasers with Traveling-Wave Thomson-Scattering“. In: *AIP Conference Proceedings* 1777.1, 080016 (2016). DOI: 10.1063/1.4965673 (cit. on pp. 8, 30, 32, 33).
- [KS2] K Steiniger, M Bussmann, R Pausch, T Cowan, A Irman, A Jochmann, R Sauerbrey, U Schramm, and A Debus. „Optical free-electron lasers with Traveling-Wave Thomson-Scattering“. In: *J. Phys. B: At. Mol. Opt. Phys.* 47.23 (2014), p. 234011. DOI: 10.1088/0953-4075/47/23/234011 (cit. on pp. 8, 9, 29, 31, 39, 70, 88).
- [KS3] K Steiniger, A Debus, A Irman, A Jochmann, R Pausch, U Schramm, T Cowan, and M Bussmann. „All-optical free-electron lasers using Traveling-Wave Thomson-Scattering“. In: *IPAC2014 - Proceedings*. 2014. ISBN: 978-3-95450-132-8 (cit. on p. 8).
- [KS4] K Steiniger, D Albach, A Debus, M Loeser, R Pausch, F Roeser, U Schramm, M Siebold, and M Bussmann. „Building an Optical Free-Electron Laser in the Traveling-Wave Thomson-Scattering Geometry“. in internal review (cit. on pp. 10, 28, 39, 45, 48, 49, 51, 56, 57, 90, 91, 124).
- [KS5] K Steiniger, R Widera, R Pausch, A Debus, M Bussmann, and U Schramm. „Wave optical description of the Traveling-Wave Thomson-Scattering optical undulator field and its application to the TWTS-FEL “. In: *Nucl. Instr. Meth. Phys. Res. A* 740 (2014). Proceedings of the first European Advanced Accelerator Concepts Workshop 2013, pp. 147–152. ISSN: 0168-9002. DOI: 10.1016/j.nima.2013.10.091 (cit. on p. 39).

## Furthermore, the author contributed to

- [KSc1] U Schramm et al. „First Results with the Novel Peta-Watt Laser Acceleration Facility in Dresden“. In: *Proc. of International Particle Accelerator Conference (IPAC'17), Copenhagen, Denmark, 14-19 May, 2017*. (Copenhagen, Denmark). International Particle Accelerator Conference 8. Geneva, Switzerland: JACoW, 2017, pp. 48–52. ISBN: 978-3-95450-182-3. DOI: 10.18429/JACoW-IPAC2017-MOZB1 (cit. on p. 83).
- [KSc2] C Fortmann-Grote et al. „Simulations of ultrafast x-ray laser experiments“. In: *Proc. SPIE* 10237 (2017). DOI: 10.1117/12.2270552 (cit. on p. 122).

- [KSc3] R Pausch, A Debus, R Widera, K Steiniger, A Huebl, H Burau, M Bussmann, and U Schramm. „How to test and verify radiation diagnostics simulations within particle-in-cell frameworks “. In: *Nucl. Instr. Meth. Phys. Res. A* 740 (2014). Proceedings of the first European Advanced Accelerator Concepts Workshop 2013, pp. 250–256. ISSN: 0168-9002. DOI: 10.1016/j.nima.2013.10.073 (cit. on p. 122).
- [KSc4] R Pausch, H Burau, M Bussmann, JP Couperus, T Cowan, A Debus, A Huebl, A Irman, A Köhler, U Schramm, K Steiniger, and R Widera. „Computing Angularly-resolved Far Field Emission Spectra in Particle-in-cell Codes using GPUs“. In: *IPAC2014 - Proceedings*. 2014. ISBN: 978-3-95450-132-8 (cit. on p. 122).
- [KSc5] R Pausch, M Bussmann, A Huebl, K Steiniger, R Widera, and A Debus. „Identifying the linear phase of the relativistic Kelvin-Helmholtz instability and measuring its growth rate via radiation“. In: *Phys. Rev. E* (2017). in press (cit. on p. 122).
- [KSc6] A Debus, R Pausch, A Huebl, K Steiniger, R Widera, T Cowan, U Schramm, and M Bussmann. „Breaking the dephasing and depletion limits of laser-wakefield acceleration“. In: *Nature communications* (2017). submitted (cit. on p. 122).
- [KSc7] U Schramm, M Bussmann, J Couperus, T Cowan, A Debus, A Irman, A Jochmann, R Pausch, R Sauerbrey, and K Steiniger. „Bright X-ray Pulse Generation by Laser Thomson-Backscattering and Traveling Wave Optical Undulators“. In: *Frontiers in Optics 2014*. Optical Society of America, 2014, FTu4G.2. DOI: 10.1364/FIO.2014.FTu4G.2.

## REFERENCES

- [1] J Schulz, L Jašíková, A Škríba, and J Roithová. „Role of Gold(I)  $\alpha$ -Oxo Carbenes in the Oxidation Reactions of Alkynes Catalyzed by Gold(I) Complexes“. In: *Journal of the American Chemical Society* 136.32 (2014), pp. 11513–11523. DOI: 10.1021/ja505945d (cit. on p. 7).
- [2] A Shayeghi, RL Johnston, DM Rayner, R Schäfer, and A Fielicke. „The Nature of Bonding between Argon and Mixed Gold–Silver Trimers“. In: *Angewandte Chemie International Edition* 54.36 (2015), pp. 10675–10680. ISSN: 1521-3773. DOI: 10.1002/anie.201503845 (cit. on p. 7).
- [3] T Schlathölter, G Reitsma, D Egorov, O Gonzalez-Magaña, S Bari, L Boschman, E Bode-wits, K Schnorr, G Schmid, CD Schröter, R Moshhammer, and R Hoekstra. „Multiple Ionization of Free Ubiquitin Molecular Ions in Extreme Ultraviolet Free-Electron Laser Pulses“. In: *Angewandte Chemie* 128.36 (2016), pp. 10899–10903. ISSN: 1521-3757. DOI: 10.1002/ange.201605335 (cit. on p. 7).
- [4] B Nagler, U Zastra, RR Fäustlin, SM Vinko, T Whitcher, A Nelson, R Sobierajski, J Krzywinski, J Chalupsky, E Abreu, et al. „Turning solid aluminium transparent by intense soft X-ray photoionization“. In: *Nature Physics* 5.9 (2009), pp. 693–696. DOI: 10.1038/nphys1341 (cit. on p. 7).
- [5] Y Huismans et al. „Time-Resolved Holography with Photoelectrons“. In: *Science* 331.6013 (2011), pp. 61–64. ISSN: 0036-8075. DOI: 10.1126/science.1198450 (cit. on p. 7).
- [6] B Erk et al. „Imaging charge transfer in iodomethane upon x-ray photoabsorption“. In: *Science* 345.6194 (2014), pp. 288–291. ISSN: 0036-8075. DOI: 10.1126/science.1253607 (cit. on p. 7).
- [7] B Zaks, R Liu, and M Sherwin. „Experimental observation of electron-hole recollisions“. In: *Nature* 483.7391 (2012), pp. 580–583. DOI: 10.1038/nature10864 (cit. on p. 7).
- [8] A Dienst, E Casandruc, D Fausti, L Zhang, M Eckstein, M Hoffmann, V Khanna, N Dean, M Gensch, S Winnerl, et al. „Optical excitation of Josephson plasma solitons in a cuprate superconductor“. In: *Nature materials* 12.6 (2013), pp. 535–541. DOI: 10.1038/nmat3580 (cit. on p. 7).
- [9] M Beye, S Schreck, F Sorgenfrei, C Trabant, N Pontius, C Schüßler-Langeheine, W Wurth, and A Föhlisch. „Stimulated X-ray emission for materials science“. In: *Nature* 501.7466 (2013), pp. 191–194. DOI: 10.1038/nature12449 (cit. on p. 7).

- [10] MM Seibert, T Ekeberg, FR Maia, M Svenda, J Andreasson, O Jönsson, D Odić, B Iwan, A Rocker, D Westphal, et al. „Single mimivirus particles intercepted and imaged with an X-ray laser“. In: *Nature* 470.7332 (2011), pp. 78–81. DOI: 10.1038/nature09748 (cit. on pp. 7, 121).
- [11] G Van Der Schot, M Svenda, FR Maia, M Hantke, DP DePonte, MM Seibert, A Aquila, J Schulz, R Kirian, M Liang, et al. „Imaging single cells in a beam of live cyanobacteria with an x-ray laser“. In: *Nature communications* 6.5704 (2015). DOI: 10.1038/ncomms6704 (cit. on pp. 7, 100, 120, 121).
- [12] NK Sauter et al. „No observable conformational changes in PSII“. In: *Nature* 533.7603 (2016), E1–E2. DOI: 10.1038/nature17983 (cit. on p. 7).
- [13] G Ramian. *The World Wide Web Virtual Library: Free Electron Laser research and applications*. 2016. URL: [http://sbfel3.ucsb.edu/www/vl\\_fel.html](http://sbfel3.ucsb.edu/www/vl_fel.html) (cit. on p. 7).
- [14] HN Chapman, A Barty, MJ Bogan, S Boutet, M Frank, SP Hau-Riege, S Marchesini, BW Woods, S Bajt, WH Benner, et al. „Femtosecond diffractive imaging with a soft-X-ray free-electron laser“. In: *Nature Physics* 2.12 (2006), pp. 839–843. DOI: 10.1038/nphys461 (cit. on p. 7).
- [15] A Barty, S Boutet, MJ Bogan, S Hau-Riege, S Marchesini, K Sokolowski-Tinten, N Stojanovic, H Ehrke, A Cavalleri, S Düsterer, et al. „Ultrafast single-shot diffraction imaging of nanoscale dynamics“. In: *Nature Photonics* 2.7 (2008), pp. 415–419. DOI: 10.1038/nphoton.2008.128 (cit. on pp. 7, 83, 121).
- [16] HN Chapman, P Fromme, A Barty, TA White, RA Kirian, A Aquila, MS Hunter, J Schulz, DP DePonte, U Weierstall, et al. „Femtosecond X-ray protein nanocrystallography“. In: *Nature* 470.7332 (2011), pp. 73–77. DOI: 10.1038/nature09750 (cit. on pp. 7, 121).
- [17] LF Gomez et al. „Shapes and vorticities of superfluid helium nanodroplets“. In: *Science* 345.6199 (2014), pp. 906–909. ISSN: 0036-8075. DOI: 10.1126/science.1252395 (cit. on p. 7).
- [18] M Dean, Y Cao, X Liu, S Wall, D Zhu, R Mankowsky, V Thampy, X Chen, J Vale, D Casa, et al. „Ultrafast energy-and momentum-resolved dynamics of magnetic correlations in the photo-doped Mott insulator Sr2IrO4“. In: *Nature materials* 15.6 (2016), pp. 601–605. DOI: 10.1038/nmat4641 (cit. on p. 7).
- [19] CA Stan, D Milathianaki, H Laksmono, RG Sierra, TA McQueen, M Messerschmidt, GJ Williams, JE Koglin, TJ Lane, MJ Hayes, et al. „Liquid explosions induced by X-ray laser pulses“. In: *Nature Physics* advance online publication (2016). DOI: 10.1038/nphys3779 (cit. on p. 7).
- [20] Laboratoire de Chimie Physique. *The accelerator of the CLIO Free-Electron Laser*. 2016. URL: [http://clio.lcp.u-psud.fr/clio\\_eng/accel.html](http://clio.lcp.u-psud.fr/clio_eng/accel.html) (cit. on p. 7).
- [21] *SACLA Map*. 2016. URL: <http://xfel.riken.jp/eng/sacla/image/xfelworkinglarge.jpg> (cit. on pp. 7, 108).
- [22] SLAC National Accelerator Laboratory. *LCLS Facility Map*. 2016. URL: <http://lcls.slac.stanford.edu/FacilityMap.aspx> (cit. on p. 7).
- [23] T Plettner and RL Byer. „Proposed dielectric-based microstructure laser-driven undulator“. In: *Phys. Rev. ST Accel. Beams* 11 (3 2008), p. 030704. DOI: 10.1103/PhysRevSTAB.11.030704 (cit. on p. 8).

- [24] G Travish and RB Yoder. „Laser-powered dielectric-structures for the production of high-brightness electron and x-ray beams“. In: *Laser Acceleration of Electrons, Protons, and Ions; and Medical Applications of Laser-Generated Secondary Sources of Radiation and Particles*. Vol. 8079. 2011. DOI: 10.1117/12.890263 (cit. on p. 8).
- [25] S Tantawi, M Shumail, J Neilson, G Bowden, C Chang, E Hemsing, and M Dunning. „Experimental Demonstration of a Tunable Microwave Undulator“. In: *Phys. Rev. Lett.* 112 (16 2014), p. 164802. DOI: 10.1103/PhysRevLett.112.164802 (cit. on p. 8).
- [26] SV Kuzikov, AV Savilov, and AA Vikharev. „Flying radio frequency undulator“. In: *Applied Physics Letters* 105.3, 033504 (2014). DOI: 10.1063/1.4890586 (cit. on p. 8).
- [27] J Gea-Banacloche, G Moore, R Schlicher, M Scully, and H Walther. „Soft x-ray free-electron laser with a laser undulator“. In: *Quantum Electronics, IEEE Journal of* 23.9 (1987), pp. 1558–1570. DOI: 10.1109/JQE.1987.1073559 (cit. on pp. 8, 29).
- [28] JC Gallardo, RC Fernow, R Palmer, and C Pellegrini. „Theory of a free-electron laser with a gaussian optical undulator“. In: *Quantum Electronics, IEEE Journal of* 24.8 (1988), pp. 1557–1566. DOI: 10.1109/3.7085 (cit. on pp. 8, 29).
- [29] PR Ribič and G Margaritondo. „The physics behind free electron lasers (FELs) based on magnetostatic and optical undulators“. In: *physica status solidi (b)* 249.6 (2012), pp. 1210–1217. ISSN: 1521-3951. DOI: 10.1002/pssb.201100513 (cit. on p. 8).
- [30] RW Schoenlein, WP Leemans, AH Chin, P Volfbeyn, TE Glover, P Balling, M Zolotarev, KJ Kim, S Chattopadhyay, and CV Shank. „Femtosecond X-ray Pulses at 0.4 Å Generated by 90° Thomson Scattering: A Tool for Probing the Structural Dynamics of Materials“. In: *Science* 274.5285 (1996), pp. 236–238. ISSN: 0036-8075. DOI: 10.1126/science.274.5285.236 (cit. on p. 8).
- [31] IV Pogorelsky et al. „Demonstration of  $8 \times 10^{18}$  photons/second peaked at 1.8 Å in a relativistic Thomson scattering experiment“. In: *Phys. Rev. ST Accel. Beams* 3 (9 2000), p. 090702. DOI: 10.1103/PhysRevSTAB.3.090702 (cit. on pp. 8, 16).
- [32] N Pietralla et al. „Parity Measurements of Nuclear Levels Using a Free-Electron-Laser Generated  $\gamma$ -Ray Beam“. In: *Phys. Rev. Lett.* 88 (1 2001), p. 012502. DOI: 10.1103/PhysRevLett.88.012502 (cit. on p. 8).
- [33] D Gibson et al. „PLEIADES: A picosecond Compton scattering x-ray source for advanced backlighting and time-resolved material studies“. In: *Phys. of Plasmas* 11.5 (2004), pp. 2857–2864. DOI: 10.1063/1.1646160 (cit. on pp. 8, 16).
- [34] K Chouffani, F Harmon, D Wells, J Jones, and G Lancaster. „Determination of electron beam parameters by means of laser-Compton scattering“. In: *Phys. Rev. ST Accel. Beams* 9 (5 2006), p. 050701. DOI: 10.1103/PhysRevSTAB.9.050701 (cit. on p. 8).
- [35] DJ Gibson et al. „Design and operation of a tunable MeV-level Compton-scattering-based  $\gamma$ -ray source“. In: *Phys. Rev. ST Accel. Beams* 13 (7 2010), p. 070703. DOI: 10.1103/PhysRevSTAB.13.070703 (cit. on p. 8).
- [36] G Priebe et al. „First results from the Daresbury Compton backscattering x-ray source (COBALD)“. In: vol. 7805. 2010, pp. 13–14. DOI: 10.1117/12.859671 (cit. on p. 8).
- [37] A Jochmann et al. „High Resolution Energy-Angle Correlation Measurement of Hard X Rays from Laser-Thomson Backscattering“. In: *Phys. Rev. Lett.* 111 (11 2013), p. 114803. DOI: 10.1103/PhysRevLett.111.114803 (cit. on pp. 8, 16, 121).

- [38] A Jochmann et al. „Operation of a picosecond narrow-bandwidth Laser–Thomson-backscattering X-ray source“. In: *Nucl. Instr. Meth. Phys. Res. B* 309 (2013). The 5th International Conference on Charged & Neutral Particles Channeling Phenomena (Channeling 2012), September 23–28, 2012, Alghero (Sardinia), Italy, pp. 214–217. ISSN: 0168-583X. DOI: 10.1016/j.nimb.2013.01.065 (cit. on p. 8).
- [39] H Weller, M Ahmed, H Gao, W Tornow, Y Wu, M Gai, and R Miskimen. „Research opportunities at the upgraded H $\gamma$ S facility“. In: *Progress in Particle and Nuclear Physics* 62.1 (2009), pp. 257–303. DOI: 10.1016/j.pnpnp.2008.07.001 (cit. on p. 8).
- [40] S Amano, K Horikawa, K Ishihara, S Miyamoto, T Hayakawa, T Shizuma, and T Mochizuki. „Several-MeV  $\gamma$ -ray generation at NewSUBARU by laser Compton backscattering“. In: *Nucl. Instr. Meth. Phys. Res. A* 602.2 (2009), pp. 337–341. ISSN: 0168-9002. DOI: j.nima.2009.01.010 (cit. on p. 8).
- [41] Y Du, L Yan, J Hua, Q Du, Z Zhang, R Li, H Qian, W Huang, H Chen, and C Tang. „Generation of first hard X-ray pulse at Tsinghua Thomson Scattering X-ray Source“. In: *Review of Scientific Instruments* 84.5, 053301 (2013). DOI: 10.1063/1.4803671 (cit. on p. 8).
- [42] E Esarey, SK Ride, and P Sprangle. „Nonlinear Thomson scattering of intense laser pulses from beams and plasmas“. In: *Phys. Rev. E* 48 (4 1993), pp. 3003–3021. DOI: 10.1103/PhysRevE.48.3003 (cit. on pp. 8, 11, 15).
- [43] SK Ride, E Esarey, and M Baine. „Thomson scattering of intense lasers from electron beams at arbitrary interaction angles“. In: *Physical Review E* 52.5 (1995), pp. 5425–5442 (cit. on pp. 8, 26, 73–75).
- [44] M Boca and V Florescu. „Nonlinear Compton scattering with a laser pulse“. In: *Phys. Rev. A* 80 (5 2009), p. 053403. DOI: 10.1103/PhysRevA.80.053403 (cit. on p. 8).
- [45] D Seipt and B Kämpfer. „Nonlinear Compton scattering of ultrashort intense laser pulses“. In: *Phys. Rev. A* 83 (2 2011), p. 022101. DOI: 10.1103/PhysRevA.83.022101 (cit. on pp. 8, 120).
- [46] H Schworer, B Liesfeld, HP Schlenvoigt, KU Amthor, and R Sauerbrey. „Thomson-Backscattered X Rays From Laser-Accelerated Electrons“. In: *Phys. Rev. Lett.* 96 (1 2006), p. 014802. DOI: 10.1103/PhysRevLett.96.014802 (cit. on p. 8).
- [47] K Ta Phuoc, S Corde, C Thaury, V Malka, A Tafzi, JP Goddet, R Shah, S Sebban, and A Rousse. „All-optical Compton gamma-ray source“. In: *Nature Photonics* 6.5 (2012), pp. 308–311. DOI: 10.1038/nphoton.2012.82 (cit. on p. 8).
- [48] Y Mori, H Kuwabara, K Ishii, R Hanayama, T Kawashima, and Y Kitagawa. „Head-On Inverse Compton Scattering X-rays with Energy beyond 10 keV from Laser-Accelerated Quasi-Monoenergetic Electron Bunches“. In: *Applied Physics Express* 5.5 (2012), p. 056401. DOI: 10.1143/APEX.5.056401 (cit. on p. 8).
- [49] S Chen et al. „MeV-Energy X Rays from Inverse Compton Scattering with Laser-Wakefield Accelerated Electrons“. In: *Phys. Rev. Lett.* 110 (15 2013), p. 155003. DOI: 10.1103/PhysRevLett.110.155003 (cit. on pp. 8, 16).
- [50] ND Powers, I Ghebregziabher, G Golovin, C Liu, S Chen, S Banerjee, J Zhang, and DP Umstadter. „Quasi-monoenergetic and tunable X-rays from a laser-driven Compton light source“. In: *Nature Photonics* 8.1 (2014), pp. 28–31. DOI: 10.1038/nphoton.2013.314 (cit. on p. 8).

- [51] G Sarri et al. „Ultra-high Brilliance Multi-MeV  $\gamma$ -Ray Beams from Nonlinear Relativistic Thomson Scattering“. In: *Phys. Rev. Lett.* 113 (22 2014), p. 224801. DOI: 10.1103/PhysRevLett.113.224801 (cit. on p. 8).
- [52] K Khrennikov, J Wenz, A Buck, J Xu, M Heigoldt, L Veisz, and S Karsch. „Tunable All-Optical Quasimonochromatic Thomson X-Ray Source in the Nonlinear Regime“. In: *Phys. Rev. Lett.* 114 (19 2015), p. 195003. DOI: 10.1103/PhysRevLett.114.195003 (cit. on pp. 8, 106).
- [53] A Döpp, E Guillaume, C Thaur, J Gautier, I Andriyash, A Lifschitz, V Malka, A Rousse, and KT Phuoc. „An all-optical Compton source for single-exposure x-ray imaging“. In: *Plasma Physics and Controlled Fusion* 58.3 (2016), p. 034005. DOI: 10.1088/0741-3335/58/3/034005 (cit. on p. 8).
- [54] C Yu, R Qi, W Wang, J Liu, W Li, C Wang, Z Zhang, J Liu, Z Qin, M Fang, et al. „Ultra-high brilliance quasi-monochromatic MeV  $\gamma$ -rays based on self-synchronized all-optical Compton scattering“. In: *Scientific Reports* 6 (2016), p. 29518. DOI: 10.1038/srep29518 (cit. on pp. 8, 16).
- [55] J Faure, Y Glinec, A Pukhov, S Kiselev, S Gordienko, E Lefebvre, JP Rousseau, F Burgy, and V Malka. „A laser-plasma accelerator producing monoenergetic electron beams“. In: *Nature* 431.7008 (2004), pp. 541–544. ISSN: 0028-0836. DOI: 10.1038/nature02963 (cit. on p. 8).
- [56] CGR Geddes, C Toth, J van Tilborg, E Esarey, CB Schroeder, D Bruhwiler, C Nieter, J Cary, and WP Leemans. „High-quality electron beams from a laser wakefield accelerator using plasma-channel guiding“. In: *Nature* 431.7008 (2004), pp. 538–541. ISSN: 0028-0836. DOI: 10.1038/nature02900 (cit. on p. 8).
- [57] SPD Mangles et al. „Monoenergetic beams of relativistic electrons from intense laser-plasma interactions“. In: *Nature* 431.7008 (2004), pp. 535–538. ISSN: 0028-0836. DOI: 10.1038/nature02939 (cit. on p. 8).
- [58] WP Leemans, B Nagler, AJ Gonsalves, C Toth, K Nakamura, CGR Geddes, E Esarey, CB Schroeder, and SM Hooker. „GeV electron beams from a centimetre-scale accelerator“. In: *Nature Physics* 2.10 (2006), pp. 696–699. ISSN: 1745-2473. DOI: 10.1038/nphys418 (cit. on pp. 8, 106).
- [59] X Wang, R Zgadzaj, N Fazel, Z Li, S Yi, X Zhang, W Henderson, YY Chang, R Korzekwa, HE Tsai, et al. „Quasi-monoenergetic laser-plasma acceleration of electrons to 2 GeV“. In: *Nature communications* 4 (2013), p. 1988. DOI: 10.1038/ncomms2988 (cit. on pp. 8, 106).
- [60] WP Leemans et al. „Multi-GeV Electron Beams from Capillary-Discharge-Guided Sub-petawatt Laser Pulses in the Self-Trapping Regime“. In: *Phys. Rev. Lett.* 113 (24 2014), p. 245002. DOI: 10.1103/PhysRevLett.113.245002 (cit. on pp. 8, 106).
- [61] J Couperus et al. „Demonstration of a beam loaded nanocoulomb-class laser wakefield accelerator“. In: (2017). accepted by Nature communications (cit. on pp. 8, 106, 118).
- [62] YF Li et al. „Generation of 20kA electron beam from a laser wakefield accelerator“. In: *Physics of Plasmas* 24.2 (2017), p. 023108. DOI: 10.1063/1.4975613. eprint: <http://dx.doi.org/10.1063/1.4975613> (cit. on pp. 8, 106).
- [63] E Esarey, CB Schroeder, and WP Leemans. „Physics of laser-driven plasma-based electron accelerators“. In: *Rev. Mod. Phys.* 81 (3 2009), pp. 1229–1285. DOI: 10.1103/RevModPhys.81.1229 (cit. on p. 8).

- [64] A Bacci, C Maroli, V Petrillo, A Rossi, L Serafini, and P Tomassini. „Compact X-ray free-electron laser based on an optical undulator“. In: *Nucl. Instr. Meth. Phys. Res. A* 587.2–3 (2008), pp. 388–397. ISSN: 0168-9002. DOI: 10.1016/j.nima.2007.12.041 (cit. on p. 8).
- [65] V Petrillo, L Serafini, and P Tomassini. „Ultrahigh brightness electron beams by plasma-based injectors for driving all-optical free-electron lasers“. In: *Phys. Rev. ST Accel. Beams* 11 (7 2008), p. 070703. DOI: 10.1103/PhysRevSTAB.11.070703 (cit. on pp. 8, 29).
- [66] P Sprangle, B Hafizi, and JR Peñano. „Laser-pumped coherent x-ray free-electron laser“. In: *Phys. Rev. ST Accel. Beams* 12 (5 2009), p. 050702. DOI: 10.1103/PhysRevSTAB.12.050702 (cit. on pp. 8, 29).
- [67] A Debus, S Bock, M Bussmann, TE Cowan, A Jochmann, T Kluge, SD Kraft, R Sauerbrey, K Zeil, and U Schramm. „Linear and Non-Linear Thomson-Scattering X-Ray Sources Driven by Conventionally and Laser Plasma Accelerated Electrons“. In: *Proc. SPIE* 7359 (2009), p. 735908. DOI: 10.1117/12.820741 (cit. on pp. 8, 10, 26, 87).
- [68] A Debus, M Bussmann, M Siebold, A Jochmann, U Schramm, T Cowan, and R Sauerbrey. „Traveling-wave Thomson scattering and optical undulators for high-yield EUV and X-ray sources“. In: *Applied Physics B: Lasers and Optics* 100 (1 2010), pp. 61–76. ISSN: 0946-2171. DOI: 10.1007/s00340-010-3990-1 (cit. on pp. 8, 81).
- [69] I Andriyash, P Balcou, and V Tikhonchuk. „Collective properties of a relativistic electron beam injected into a high intensity optical lattice“. In: *The European Physical Journal D* 65.3 (2011), pp. 533–540. DOI: 10.1140/epjd/e2011-20254-5 (cit. on p. 10).
- [70] IA Andriyash, E d’Humières, VT Tikhonchuk, and P Balcou. „X-Ray Amplification from a Raman Free-Electron Laser“. In: *Phys. Rev. Lett.* 109 (24 2012), p. 244802. DOI: 10.1103/PhysRevLett.109.244802 (cit. on p. 10).
- [71] C Chang, J Liang, D Hei, MF Becker, K Tang, Y Feng, V Yakimenko, C Pellegrini, and J Wu. „High-brightness X-ray free-electron laser with an optical undulator by pulse shaping“. In: *Opt. Express* 21.26 (2013), pp. 32013–32018. DOI: 10.1364/OE.21.032013 (cit. on p. 10).
- [72] JE Lawler, J Bisognano, RA Bosch, TC Chiang, MA Green, K Jacobs, T Miller, R Wehlitz, D Yavuz, and RC York. „Nearly copropagating sheared laser pulse FEL undulator for soft x-rays“. In: *J. Phys. D: Appl. Phys.* 46.32 (2013), p. 325501. DOI: 10.1088/0022-3727/46/32/325501 (cit. on p. 10).
- [73] B Green, S Kovalev, V Asgekar, G Geloni, U Lehnert, T Golz, M Kuntzsch, C Bauer, J Hauser, J Voigtlaender, et al. „High-Field High-Repetition-Rate Sources for the Coherent THz Control of Matter“. In: *Scientific Reports* 6.22256 (2016). DOI: 10.1038/srep22256 (cit. on p. 11).
- [74] P Emma, R Akre, J Arthur, R Bionta, C Bostedt, J Bozek, A Brachmann, P Bucksbaum, R Coffee, FJ Decker, et al. „First lasing and operation of an ångstrom-wavelength free-electron laser“. In: *Nature Photonics* 4.9 (2010), pp. 641–647. DOI: 10.1038/nphoton.2010.176 (cit. on pp. 11, 108).
- [75] T Ishikawa, H Aoyagi, T Asaka, Y Asano, N Azumi, T Bizen, H Ego, K Fukami, T Fukui, Y Furukawa, et al. „A compact X-ray free-electron laser emitting in the sub-ångstrom region“. In: *Nature Photonics* 6.8 (2012), pp. 540–544. DOI: 10.1038/nphoton.2012.141 (cit. on pp. 11, 33, 116).

- [76] I Barke, H Hartmann, D Rupp, L Flückiger, M Sauppe, M Adolph, S Schorb, C Bostedt, R Treusch, C Peltz, et al. „The 3D-architecture of individual free silver nanoparticles captured by X-ray scattering“. In: *Nature communications* 6 (2015). DOI: 10.1038/ncomms7187 (cit. on pp. 13, 83, 100, 103, 120).
- [77] D Attwood. *Soft X-Rays and Extreme Ultraviolet Radiation: Principles and Applications*. 2007. ISBN: 9780521029971 (cit. on pp. 13, 22, 102, 103, 115, 129).
- [78] H Wiedemann. *Particle Accelerator Physics, 4th ed.* Springer, 2015. Chap. 26. ISBN: 978-3-319-18316-9. DOI: 0.1007/978-3-319-18317-6 (cit. on pp. 15, 94).
- [79] JB Murphy and C Pellegrini. „Generation of high-intensity coherent radiation in the soft-x-ray and vacuum-ultraviolet region“. In: *J. Opt. Soc. Am. B* 2.1 (1985), pp. 259–264. DOI: 10.1364/JOSAB.2.000259 (cit. on pp. 15, 19).
- [80] Z Huang and KJ Kim. „Review of x-ray free-electron laser theory“. In: *Phys. Rev. ST Accel. Beams* 10 (3 2007), p. 034801. DOI: 10.1103/PhysRevSTAB.10.034801 (cit. on pp. 15, 18, 19, 33).
- [81] A Siegman. *Lasers*. University Science Books, 1986 (cit. on pp. 15, 32, 39).
- [82] P Schmüser, M Dohlus, J Rossbach, and C Behrens. *Springer Tracts in Modern Physics*. Springer Tracts in Modern Physics 258. Springer International Publishing Switzerland, 2014. ISBN: 978-3-319-04080-6. DOI: 10.1007/978-3-319-04081-3 (cit. on pp. 16, 19, 116).
- [83] K Khrennikov, J Wenz, A Buck, J Xu, M Heigoldt, L Veisz, and S Karsch. „Tunable All-Optical Quasimonochromatic Thomson X-Ray Source in the Nonlinear Regime“. In: *Phys. Rev. Lett.* 114 (19 2015). see Supplement, p. 195003. DOI: 10.1103/PhysRevLett.114.195003 (cit. on p. 16).
- [84] G Priebe et al. „Inverse Compton backscattering source driven by the multi-10 TW laser installed at Daresbury“. In: *Laser and Particle Beams* 26 (04 2008), pp. 649–660. ISSN: 1469-803X. DOI: 10.1017/S0263034608000700 (cit. on p. 16).
- [85] TJ Orzechowski, B Anderson, WM Fawley, D Prosnitz, ET Scharlemann, S Yarema, D Hopkins, AC Paul, AM Sessler, and J Wurtele. „Microwave radiation from a high-gain free-electron laser amplifier“. In: *Phys. Rev. Lett.* 54 (9 1985), pp. 889–892. DOI: 10.1103/PhysRevLett.54.889 (cit. on p. 19).
- [86] S Schreiber. „Soft and Hard X-ray SASE Free Electron Lasers“. In: *Reviews of Accelerator Science and Technology* 03.01 (2010), pp. 93–120. DOI: 10.1142/S1793626810000439 (cit. on p. 20).
- [87] E Saldin, E Schneidmiller, and M Yurkov. „Output power and degree of transverse coherence of X-ray free electron lasers“. In: *Optics Communications* 281.18 (2008), pp. 4727–4734. ISSN: 0030-4018. DOI: 10.1016/j.optcom.2008.05.033 (cit. on pp. 21, 116).
- [88] E Saldin, E Schneidmiller, and M Yurkov. „Coherence properties of the radiation from X-ray free electron laser“. In: *Optics Communications* 281.5 (2008), pp. 1179–1188. ISSN: 0030-4018. DOI: 10.1016/j.optcom.2007.10.044 (cit. on pp. 21, 116).
- [89] W Helml et al. „Measuring the temporal structure of few-femtosecond free-electron laser X-ray pulses directly in the time domain“. In: *Nature Photonics* 8 (12 2014), pp. 950–957. DOI: 10.1038/nphoton.2014.278 (cit. on p. 22).
- [90] R Bonifacio, L De Salvo, P Pierini, N Piovella, and C Pellegrini. „Spectrum, temporal structure, and fluctuations in a high-gain free-electron laser starting from noise“. In: *Phys. Rev. Lett.* 73 (1 1994), pp. 70–73. DOI: 10.1103/PhysRevLett.73.70 (cit. on p. 23).

- [91] T Shintake, H Tanaka, T Hara, T Tanaka, K Togawa, M Yabashi, Y Otake, Y Asano, T Bizen, T Fukui, et al. „A compact free-electron laser for generating coherent radiation in the extreme ultraviolet region“. In: *Nature Photonics* 2.9 (2008), pp. 555–559. DOI: 10.1038/nphoton.2008.134 (cit. on pp. 23, 108).
- [92] LH Yu. „Generation of intense uv radiation by subharmonically seeded single-pass free-electron lasers“. In: *Phys. Rev. A* 44 (8 1991), pp. 5178–5193. DOI: 10.1103/PhysRevA.44.5178 (cit. on p. 23).
- [93] T Hara. „Free-electron lasers: Fully coherent soft X-rays at FERMI“. In: *Nature Photonics* 7 (11 2013), pp. 852–854. DOI: 10.1038/nphoton.2013.279 (cit. on p. 23).
- [94] E Allaria, D Castronovo, P Cinquegrana, P Craievich, M Dal Forno, M Danailov, G D’Auria, A Demidovich, G De Ninno, S Di Mitri, et al. „Two-stage seeded soft-X-ray free-electron laser“. In: *Nature Photonics* 7 (11 2013), pp. 913–918. ISSN: 1749-4885. DOI: 10.1038/nphoton.2013.277 (cit. on p. 23).
- [95] G De Ninno et al. „Single-shot spectro-temporal characterization of XUV pulses from a seeded free-electron laser“. In: *Nature communications* 6 (2015), p. 8075. DOI: 10.1038/ncomms9075 (cit. on p. 23).
- [96] KJ Kim. „Three-Dimensional Analysis of Coherent Amplification and Self-Amplified Spontaneous Emission in Free-Electron Lasers“. In: *Phys. Rev. Lett.* 57 (15 1986), pp. 1871–1874. DOI: 10.1103/PhysRevLett.57.1871 (cit. on p. 23).
- [97] LH Yu and S Krinsky. „Gain reduction due to betatron oscillations in a free electron laser“. In: *Phys. Lett. A* 129.8 (1988), pp. 463–469. ISSN: 0375-9601. DOI: 10.1016/0375-9601(88)90320-9 (cit. on p. 23).
- [98] KJ Kim. „Brightness, coherence and propagation characteristics of synchrotron radiation“. In: *Nucl. Instr. Meth. Phys. Res. A* 246.1 (1986), pp. 71–76. ISSN: 0168-9002. DOI: 10.1016/0168-9002(86)90048-3 (cit. on p. 23).
- [99] P Elleaume, J Chavanne, and B Faatz. „Design considerations for a 1 Å {SASE} undulator“. In: *Nucl. Instr. Meth. Phys. Res. A* 455.3 (2000), pp. 503–523. ISSN: 0168-9002. DOI: 10.1016/S0168-9002(00)00544-1 (cit. on p. 25).
- [100] T Eichner, F Grüner, S Becker, M Fuchs, D Habs, R Weingartner, U Schramm, H Backe, P Kunz, and W Lauth. „Miniature magnetic devices for laser-based, table-top free-electron lasers“. In: *Phys. Rev. ST Accel. Beams* 10 (8 2007), p. 082401. DOI: 10.1103/PhysRevSTAB.10.082401 (cit. on pp. 25, 115).
- [101] D Gordon, P Sprangle, B Hafizi, and C Roberson. „Requirements for a laser pumped FEL operating in the X-ray regime“. In: *Nucl. Instr. Meth. Phys. Res. A* 475.1–3 (2001). FEL2000: Proc. 22nd Int. Free Electron Laser Conference and 7th FEL Users Workshop, pp. 190–194. ISSN: 0168-9002. DOI: 10.1016/S0168-9002(01)01694-1 (cit. on p. 29).
- [102] R Bonifacio, C Pellegrini, and L Narducci. „Collective instabilities and high-gain regime in a free electron laser“. In: *Optics Communications* 50.6 (1984), pp. 373–378. DOI: 10.1016/0030-4018(84)90105-6 (cit. on p. 29).
- [103] KJ Kim. „An analysis of self-amplified spontaneous emission“. In: *Nucl. Instr. Meth. Phys. Res. A* 250.1 (1986), pp. 396–403. ISSN: 0168-9002. DOI: 10.1016/0168-9002(86)90916-2 (cit. on p. 29).
- [104] M. Siebold, F. Roeser, M. Loeser, D. Albach, and U. Schramm. „PEneLOPE - a high peak-power diode-pumped laser system for laser-plasma experiments“. In: *Proc. SPIE* 8780 (2013), p. 878005. DOI: 10.1117/12.2017522 (cit. on pp. 30, 54, 93).

- [105] M Siebold. *Penelope Petawatt Laser Development*. 2016. URL: <https://www.hzdr.de/db/Cms?pNid=2098> (cit. on p. 30).
- [106] K Zeil, S Kraft, S Bock, M Bussmann, T Cowan, T Kluge, J Metzkes, T Richter, R Sauerbrey, and U Schramm. „The scaling of proton energies in ultrashort pulse laser plasma acceleration“. In: *New Journal of Physics* 12.4 (2010), p. 045015. DOI: 10.1088/1367-2630/12/4/045015 (cit. on pp. 30, 108).
- [107] U Schramm, S Bock, U Helbig, and R Gebhardt. *Petawatt Laser Draco*. 2016. URL: <https://www.hzdr.de/db/Cms?pNid=2096> (cit. on p. 30).
- [108] W Ackermann, G Asova, V Ayvazyan, A Azima, N Baboi, J Bähr, V Balandin, B Beutner, A Brandt, A Bolzmann, et al. „Operation of a free-electron laser from the extreme ultraviolet to the water window“. In: *Nature Photonics* 1.6 (2007), pp. 336–342. DOI: 10.1038/nphoton.2007.76 (cit. on p. 31).
- [109] C Gulliford et al. „Demonstration of low emittance in the Cornell energy recovery linac injector prototype“. In: *Phys. Rev. ST Accel. Beams* 16 (7 2013), p. 073401. DOI: 10.1103/PhysRevSTAB.16.073401 (cit. on pp. 33, 93).
- [110] S Kneip et al. „Characterization of transverse beam emittance of electrons from a laser-plasma wakefield accelerator in the bubble regime using betatron x-ray radiation“. In: *Phys. Rev. ST Accel. Beams* 15 (2 2012), p. 021302. DOI: 10.1103/PhysRevSTAB.15.021302 (cit. on pp. 33, 106).
- [111] R Weingartner et al. „Ultralow emittance electron beams from a laser-wakefield accelerator“. In: *Phys. Rev. ST Accel. Beams* 15 (11 2012), p. 111302. DOI: 10.1103/PhysRevSTAB.15.111302 (cit. on pp. 33, 106).
- [112] GR Plateau et al. „Low-Emittance Electron Bunches from a Laser-Plasma Accelerator Measured using Single-Shot X-Ray Spectroscopy“. In: *Phys. Rev. Lett.* 109 (6 2012), p. 064802. DOI: 10.1103/PhysRevLett.109.064802 (cit. on pp. 33, 106).
- [113] R Bonifacio, N Piovella, GRM Robb, and A Schiavi. „Quantum regime of free electron lasers starting from noise“. In: *Phys. Rev. ST Accel. Beams* 9 (9 2006), p. 090701. DOI: 10.1103/PhysRevSTAB.9.090701 (cit. on pp. 33, 122).
- [114] S Akturk, X Gu, E Zeek, and R Trebino. „Pulse-front tilt caused by spatial and temporal chirp“. In: *Opt. Express* 12.19 (2004), pp. 4399–4410. DOI: 10.1364/OPEX.12.004399 (cit. on p. 35).
- [115] OE Martinez. „Pulse Distortions in tilted pulse schemes for ultrashort pulses“. In: *Optics Communications* 59.3 (1986), pp. 229–232. DOI: 10.1016/0030-4018(86)90290-7 (cit. on p. 35).
- [116] J Hebling. „Derivation of the pulse front tilt caused by angular dispersion“. In: *Optical and Quantum Electronics* 28.12 (1996), pp. 1759–1763. ISSN: 1572-817X. DOI: 10.1007/BF00698541 (cit. on p. 35).
- [117] S Akturk, M Kimmel, P O’Shea, and R Trebino. „Measuring pulse-front tilt in ultrashort pulses using GRENOUILLE“. In: *Opt. Express* 11.5 (2003), pp. 491–501. DOI: 10.1364/OE.11.000491 (cit. on p. 35).
- [118] S Akturk, X Gu, P Gabolde, and R Trebino. „The general theory of first-order spatio-temporal distortions of Gaussian pulses and beams“. In: *Opt. Express* 13.21 (2005), pp. 8642–8661. DOI: 10.1364/OPEX.13.008642 (cit. on pp. 35, 36).
- [119] P Gabolde, D Lee, S Akturk, and R Trebino. „Describing first-order spatio-temporal distortions in ultrashort pulses using normalized parameters“. In: *Opt. Express* 15.1 (2007), pp. 242–251. DOI: 10.1364/OE.15.000242 (cit. on p. 35).

- [120] JC Diels and W Rudolph. *Ultrashort laser pulse phenomena*. Academic press, 2006 (cit. on pp. 36, 44).
- [121] AM Weiner. *Ultrafast Optics*. Ed. by G Boreman. John Wiley & Sons, Inc., 2009 (cit. on pp. 36, 40).
- [122] R Paschotta. *Encyclopedia of Laser Physics and Technology. Third-order Dispersion*. 2016. URL: [https://www.rp-photonics.com/third\\_order\\_dispersion.html](https://www.rp-photonics.com/third_order_dispersion.html) (cit. on p. 40).
- [123] M Pessot, P Maine, and G Mourou. „1000 times expansion/compression of optical pulses for chirped pulse amplification“. In: *Optics Communications* 62.6 (1987), pp. 419–421. ISSN: 0030-4018. DOI: 10.1016/0030-4018(87)90011-3 (cit. on p. 44).
- [124] IV Yakovlev. „Stretchers and compressors for ultra-high power laser systems“. In: *Quantum Electronics* 44.5 (2014), p. 393. DOI: 10.1070/QE2014v044n05ABEH015429 (cit. on pp. 44, 116).
- [125] O Martinez. „3000 times grating compressor with positive group velocity dispersion: Application to fiber compensation in 1.3-1.6  $\mu\text{m}$  region“. In: *IEEE Journal of Quantum Electronics* 23.1 (1987), pp. 59–64. ISSN: 0018-9197. DOI: 10.1109/JQE.1987.1073201 (cit. on p. 44).
- [126] E Treacy. „Optical pulse compression with diffraction gratings“. In: *IEEE Journal of Quantum Electronics* 5.9 (1969), pp. 454–458. ISSN: 0018-9197. DOI: 10.1109/JQE.1969.1076303 (cit. on p. 44).
- [127] JC Chanteloup, E Salmon, C Sauteret, A Migus, P Zeitoun, A Klisnick, A Carillon, S Hubert, D Ros, P Nickles, and M Kalachnikov. „Pulse-front control of 15-TW pulses with a tilted compressor, and application to the subpicosecond traveling-wave pumping of a soft-x-ray laser“. In: *J. Opt. Soc. Am. B* 17.1 (2000), pp. 151–157. DOI: 10.1364/JOSAB.17.000151 (cit. on pp. 45, 46).
- [128] Spectrogon AB. *Grating Glossary*. 2016. URL: <http://www.spectrogon.com/product-services/gratings/glossary> (cit. on pp. 47, 98, 105).
- [129] G Mourou, G Korn, W Sandner, and J Collier, eds. *ELI Whitebook*. Science and Technology with Ultra-Intense Lasers. 2011 (cit. on p. 54).
- [130] G Zhu, J van Howe, M Durst, W Zipfel, and C Xu. „Simultaneous spatial and temporal focusing of femtosecond pulses“. In: *Opt. Express* 13.6 (2005), pp. 2153–2159. DOI: 10.1364/OPEX.13.002153 (cit. on p. 55).
- [131] E Block, J Thomas, C Durfee, and J Squier. „Integrated single grating compressor for variable pulse front tilt in simultaneously spatially and temporally focused systems“. In: *Opt. Lett.* 39.24 (2014), pp. 6915–6918. DOI: 10.1364/OL.39.006915 (cit. on p. 55).
- [132] W Colson, C Pellegrini, and A Renieri, eds. *Laser Handbook Vol. 6*. North Holland, 1990 (cit. on pp. 68, 76, 77).
- [133] S Reiche. „FEL simulations: History, status and outlook“. In: *Proceedings of FEL2010, Malmö, Sweden (JACoW, 2010), Vol. MOOC11* (2010), pp. 165–172 (cit. on p. 68).
- [134] BWJ McNeil. „X-ray free-electron lasers“. In: *Nature Photonics* 4 (12 2010), pp. 814–821. DOI: 10.1038/nphoton.2010.239 (cit. on pp. 73, 78).
- [135] R Bonifacio, F Casagrande, G Cerchioni, L de Salvo Souza, P Pierini, and N Piovella. „Physics of the high-gain FEL and superradiance“. In: *La Rivista del Nuovo Cimento (1978-1999)* 13.9 (1990), pp. 1–69. ISSN: 1826-9850. DOI: 10.1007/BF02770850 (cit. on p. 77).

- [136] I Ghebregziabher, BA Shadwick, and D Umstadter. „Spectral bandwidth reduction of Thomson scattered light by pulse chirping“. In: *Phys. Rev. ST Accel. Beams* 16.3 (2013), p. 030705. DOI: 10.1103/PhysRevSTAB.16.030705 (cit. on p. 81).
- [137] D Seipt, SG Rykovanov, A Surzhykov, and S Fritzsche. „Narrowband inverse Compton scattering x-ray sources at high laser intensities“. In: *Phys. Rev. A* 91 (3 2015), p. 033402. DOI: 10.1103/PhysRevA.91.033402 (cit. on pp. 81, 122).
- [138] P Gibbon. *Short Pulse Laser Interactions with Matter: An Introduction*. World Scientific Pub Co, 2005. ISBN: 978-1860941351 (cit. on p. 81).
- [139] J Krzywinski et al. „Conductors, semiconductors, and insulators irradiated with short-wavelength free-electron laser“. In: *Journal of Applied Physics* 101.4 (2007), p. 043107. DOI: 10.1063/1.2434989 (cit. on pp. 83, 93, 121).
- [140] H Wabnitz et al. „Multiple ionization of atom clusters by intense soft X-rays from a free-electron laser“. In: *Nature* 420.6915 (2002), pp. 482–485. DOI: 10.1038/nature01197 (cit. on pp. 83, 93, 121).
- [141] T Kluge, C Gutt, LG Huang, J Metzkes, U Schramm, M Bussmann, and TE Cowan. „Using X-ray free-electron lasers for probing of complex interaction dynamics of ultra-intense lasers with solid matter“. In: *Physics of Plasmas* 21.3 (2014), p. 033110. DOI: 10.1063/1.4869331 (cit. on pp. 83, 108, 109, 115).
- [142] T Hayakawa, N Kikuzawa, R Hajima, T Shizuma, N Nishimori, M Fujiwara, and M Seya. „Nondestructive assay of plutonium and minor actinide in spent fuel using nuclear resonance fluorescence with laser Compton scattering“. In: *Nucl. Instr. Meth. Phys. Res. A* 621.1–3 (2010), pp. 695–700. ISSN: 0168-9002. DOI: 10.1016/j.nima.2010.06.096 (cit. on pp. 83, 87, 121).
- [143] D LI, K IMASAKI, K HORIKAWA, S MIYAMOTO, S AMANO, and T MOCHIZUKI. „Iodine Transmutation through Laser Compton Scattering Gamma Rays“. In: *Journal of Nuclear Science and Technology* 46.8 (2009), pp. 831–835. DOI: 10.1080/18811248.2007.9711592 (cit. on pp. 83, 121).
- [144] T Laarmann, W Laasch, R Röhlberger, and D Unger. *Photon Science 2016. Highlights and Annual Report*. Tech. rep. For the first half of 2017 only half of the requests for FLASH beamtime could be satisfied. Deutsches Elektronen-Synchrotron DESY, 2016 (cit. on p. 83).
- [145] SH Glenzer and R Redmer. „X-ray Thomson scattering in high energy density plasmas“. In: *Rev. Mod. Phys.* 81 (4 2009), pp. 1625–1663. DOI: 10.1103/RevModPhys.81.1625 (cit. on p. 83).
- [146] F Grotelüschen, J Vorberger, and D Gericke. *Warm, dicht, extrem. Forscher nehmen neuen Materiezustand unter die Lupe*. 2011. URL: [http://www.deutschlandfunk.de/warm-dicht-extrem.676.de.html?dram:article\\_id=28330](http://www.deutschlandfunk.de/warm-dicht-extrem.676.de.html?dram:article_id=28330) (cit. on p. 83).
- [147] GJ Ackland. „Bearing down on hydrogen“. In: *Science* 348.6242 (2015), pp. 1429–1430. ISSN: 0036-8075. DOI: 10.1126/science.aac6626 (cit. on p. 83).
- [148] Y Glinec, J Faure, LL Dain, S Darbon, T Hosokai, JJ Santos, E Lefebvre, JP Rousseau, F Burgy, B Mercier, and V Malka. „High-Resolution  $\gamma$ -Ray Radiography Produced by a Laser-Plasma Driven Electron Source“. In: *Phys. Rev. Lett.* 94 (2 2005), p. 025003. DOI: 10.1103/PhysRevLett.94.025003 (cit. on p. 87).
- [149] V Ramanathan et al. „Submillimeter-resolution radiography of shielded structures with laser-accelerated electron beams“. In: *Phys. Rev. ST Accel. Beams* 13 (10 2010), p. 104701. DOI: 10.1103/PhysRevSTAB.13.104701 (cit. on p. 87).

- [150] A Ben-Ismaïl, O Lundh, C Rechatin, JK Lim, J Faure, S Corde, and V Malka. „Compact and high-quality gamma-ray source applied to 10  $\mu\text{m}$ -range resolution radiography“. In: *Applied Physics Letters* 98.26, 264101 (2011). DOI: 10.1063/1.3604013 (cit. on p. 87).
- [151] JM Boone and JA Seibert. „A figure of merit comparison between bremsstrahlung and monoenergetic x-ray sources for angiography“. In: *Journal of X-Ray Science and Technology* 4.4 (1994), pp. 334–345. ISSN: 0895-3996. DOI: 10.1016/S0895-3996(05)80050-3 (cit. on p. 87).
- [152] FE Carroll. „Tunable Monochromatic X Rays: A New Paradigm in Medicine“. In: *American Journal of Roentgenology* 179 (3 2002), pp. 583–590. DOI: 10.2214/ajr.179.3.1790583 (cit. on p. 87).
- [153] K Achterhold, M Bech, S Schleede, G Potdevin, R Ruth, R Loewen, and F Pfeiffer. „Monochromatic computed tomography with a compact laser-driven X-ray source“. In: *Scientific Reports* 3 (2013), p. 1313. DOI: 10.1038/srep01313 (cit. on p. 87).
- [154] D Habs, T Tajima, J Schreiber, CP Barty, M Fujiwara, and PG Thirolf. „Vision of nuclear physics with photo-nuclear reactions by laser-driven  $\gamma$  beams“. In: *The European Physical Journal D* 55.2 (2009), p. 279. ISSN: 1434-6079. DOI: 10.1140/epjd/e2009-00101-2 (cit. on p. 87).
- [155] HA Weidenmüller. „Nuclear Excitation by a Zeptosecond Multi-MeV Laser Pulse“. In: *Phys. Rev. Lett.* 106 (12 2011), p. 122502. DOI: 10.1103/PhysRevLett.106.122502 (cit. on p. 87).
- [156] F Albert and AGR Thomas. „Applications of laser wakefield accelerator-based light sources“. In: *Plasma Physics and Controlled Fusion* 58.10 (2016), p. 103001. DOI: 10.1088/0741-3335/58/10/103001 (cit. on p. 87).
- [157] A Arnold and J Teichert. „Overview on superconducting photoinjectors“. In: *Phys. Rev. ST Accel. Beams* 14 (2 2011), p. 024801. DOI: 10.1103/PhysRevSTAB.14.024801 (cit. on p. 87).
- [158] R Pausch. „Electromagnetic Radiation from Relativistic Electrons as Characteristic Signature of their Dynamics“. Diploma thesis. Technische Universität Dresden, 2012 (cit. on p. 87).
- [159] ZEMAX LLC, ed. *Zemax*. Optical design software. 2016. URL: [www.zemax.com](http://www.zemax.com) (cit. on p. 91).
- [160] Amplitude Technologies. *PULSAR laser system*. Ed. by F Canova. 2016. URL: [http://www.amplitude-technologies.com//?fond=produit&id\\_produit=8&id\\_rubrique=1#](http://www.amplitude-technologies.com//?fond=produit&id_produit=8&id_rubrique=1#) (cit. on p. 93).
- [161] S Schulz, I Grguraš, C Behrens, H Bromberger, J Costello, M Czwalińska, M Felber, M Hoffmann, M Ilchen, H Liu, et al. „Femtosecond all-optical synchronization of an X-ray free-electron laser“. In: *Nature communications* 6 (2015), p. 5938. DOI: 10.1038/ncomms6938 (cit. on pp. 93, 106).
- [162] M Kuntzsch, M Gensch, U Lehnert, F Röser, R Schurig, M Bousonville, M Czwalińska, H Schlarb, S Schulz, and S Vilcins. „Optical Synchronization and Electron Bunch Diagnostic at ELBE“. In: *IPAC2013 - Proceedings, Shanghai, China*. Ed. by Z Dai, C Petit-Jean-Genaz, VR Schaa, and C Zhang. 2013. ISBN: 978-3-95450-122-9 (cit. on p. 93).
- [163] *A VUV Free Electron Laser at the TESLA Test Facility at DESY*. Tech. rep. Deutsches Elektronen-Synchrotron, DESY, 1995 (cit. on pp. 93, 121).

- [164] T Pfeifer, C Spielmann, and G Gerber. „Femtosecond x-ray science“. In: *Reports on Progress in Physics* 69.2 (2006), p. 443. DOI: 10.1088/0034-4885/69/2/R04 (cit. on pp. 93, 121).
- [165] A Pietzsch, A Föhlisch, M Beye, M Deppe, F Hennies, M Nagasono, E Suljoti, W Wurth, C Gahl, K Döbrich, and A Melnikov. „Towards time resolved core level photoelectron spectroscopy with femtosecond x-ray free-electron lasers“. In: *New Journal of Physics* 10.3 (2008), p. 033004. DOI: 10.1088/1367-2630/10/3/033004 (cit. on pp. 93, 121).
- [166] K Sugioka and Y Cheng. „Ultrafast lasers – reliable tools for advanced materials processing“. In: *Light Sci Appl* 3 (2014). DOI: 10.1038/lsa.2014.30 (cit. on pp. 93, 121).
- [167] G Penco et al. „Optimization of a high brightness photoinjector for a seeded FEL facility“. In: *Journal of Instrumentation* 8.05 (2013), P05015. DOI: 10.1088/1748-0221/8/05/P05015 (cit. on pp. 93, 94).
- [168] M Abo-Bakr et al. „Status Report of the Berlin Energy Recovery Linac Project BERLin-Pro“. In: *Proc. of International Particle Accelerator Conference (IPAC'16), Busan, Korea, May 8-13, 2016*. (Busan, Korea). International Particle Accelerator Conference 7. Geneva, Switzerland: JACoW, 2016, pp. 1827–1830. ISBN: 978-3-95450-147-2. DOI: 10.18429/JACoW-IPAC2016-TUPOW034 (cit. on p. 93).
- [169] J Teichert et al. „Free-electron laser operation with a superconducting radio-frequency photoinjector at ELBE“. In: *Nucl. Instr. Meth. Phys. Res. A* 743 (2014), pp. 114–120. ISSN: 0168-9002. DOI: 10.1016/j.nima.2014.01.006 (cit. on p. 93).
- [170] P Lu, A Arnold, J Teichert, H Vennekate, and R Xiang. „Simulation of {ELBE} {SRF} gun {II} for high-bunch-charge applications“. In: *Nucl. Instr. Meth. Phys. Res. A* 830 (2016), pp. 536–544. ISSN: 0168-9002. DOI: 10.1016/j.nima.2016.05.087 (cit. on p. 93).
- [171] M Nasse et al. „Status of the Accelerator Physics Test Facility FLUTE“. In: *Proc. 6th International Particle Accelerator Conference, Richmond, VA, USA*. paper TUPWA042, pp. 1506-1508, 2015. ISBN: 978-3-95450-168-7 (cit. on p. 93).
- [172] Y Ding et al. „Measurements and Simulations of Ultralow Emittance and Ultrashort Electron Beams in the Linac Coherent Light Source“. In: *Phys. Rev. Lett.* 102 (25 2009), p. 254801. DOI: 10.1103/PhysRevLett.102.254801 (cit. on p. 93).
- [173] M Krasilnikov et al. „Experimentally minimized beam emittance from an L-band photoinjector“. In: *Phys. Rev. ST Accel. Beams* 15 (10 2012), p. 100701. DOI: 10.1103/PhysRevSTAB.15.100701 (cit. on p. 93).
- [174] E Prat, M Aiba, S Bettoni, B Beutner, S Reiche, and T Schietinger. „Emittance measurements and minimization at the SwissFEL Injector Test Facility“. In: *Phys. Rev. ST Accel. Beams* 17 (10 2014), p. 104401. DOI: 10.1103/PhysRevSTAB.17.104401 (cit. on p. 93).
- [175] K Togawa, T Shintake, T Inagaki, K Onoe, T Tanaka, H Baba, and H Matsumoto. „CeB<sub>6</sub> electron gun for low-emittance injector“. In: *Phys. Rev. ST Accel. Beams* 10 (2 2007), p. 020703. DOI: 10.1103/PhysRevSTAB.10.020703 (cit. on p. 93).
- [176] P Emma. „BUNCH COMPRESSION“. In: *Handbook of Accelerator Physics and Engineering*. Ed. by AW Chao, KH Mess, M Tigner, and F Zimmermann. 2nd. WORLD SCIENTIFIC, 2013. Chap. 4, pp. 334–337. DOI: 10.1142/9789814415859\_0004 (cit. on p. 94).
- [177] N Bonod and J Neauport. „Diffraction gratings: from principles to applications in high-intensity lasers“. In: *Adv. Opt. Photon.* 8.1 (2016), pp. 156–199. DOI: 10.1364/AOP.8.000156 (cit. on p. 98).

- [178] C Danson, D Hillier, N Hopps, and D Neely. „Petawatt class lasers worldwide“. In: *High Power Laser Science and Engineering* 3 (2015), e3. DOI: 10.1017/hpl.2014.52 (cit. on p. 100).
- [179] LB Fletcher et al. „Ultrabright X-ray laser scattering for dynamic warm dense matter physics“. In: *Nature Photonics* 9.4 (2015), 274–279. ISSN: 1749-4885. DOI: {10.1038/NPHOTON.2015.41} (cit. on p. 100).
- [180] D Kraus, A Ravasio, M Gauthier, D Gericke, J Vorberger, S Frydrych, J Helfrich, L Fletcher, G Schaumann, B Nagler, et al. „Nanosecond formation of diamond and lonsdaleite by shock compression of graphite“. In: *Nature communications* 7 (2016). DOI: 10.1038/ncomms10970 (cit. on pp. 100, 121).
- [181] S Takahashi, LC Brunel, DT Edwards, J van Tol, G Ramian, S Han, and MS Sherwin. „Pulsed electron paramagnetic resonance spectroscopy powered by a free-electron laser“. In: *Nature* 489.7416 (2012), 409–413. ISSN: 0028-0836. DOI: {10.1038/nature11437} (cit. on p. 100).
- [182] Y Chu, X Liang, L Yu, Y Xu, L Xu, L Ma, X Lu, Y Liu, Y Leng, R Li, and Z Xu. „High-contrast 2.0 Petawatt Ti:sapphire laser system“. In: *Opt. Express* 21.24 (2013), pp. 29231–29239. DOI: 10.1364/OE.21.029231 (cit. on p. 101).
- [183] X Zeng et al. „Multi-petawatt laser facility fully based on optical parametric chirped-pulse amplification“. In: *Opt. Lett.* 42.10 (2017), pp. 2014–2017. DOI: 10.1364/OL.42.002014 (cit. on p. 101).
- [184] „Extreme Light“. In: *Nature materials* 15 (2016). Editorial, p. 1. DOI: 10.1038/nmat4533 (cit. on p. 101).
- [185] J Zou, C Le Blanc, D Papadopoulos, G Chériaux, P Georges, G Mennerat, F Druon, L Lecherbourg, A Pellegrina, P Ramirez, et al. „Design and current progress of the Apollon 10 PW project“. In: *High Power Laser Science and Engineering* 3 (2015), e2. DOI: 10.1017/hpl.2014.41 (cit. on p. 101).
- [186] L Xu et al. „High-energy noncollinear optical parametric-chirped pulse amplification in LBO at 800nm“. In: *Opt. Lett.* 38.22 (2013), pp. 4837–4840. DOI: 10.1364/OL.38.004837 (cit. on p. 101).
- [187] F Röser, M Loeser, D Albach, M Siebold, S Grimm, D Brand, A Schwuchow, A Langner, G Schötz, D Schönfeld, and U Schramm. „Broadband, diode pumped Yb-doped fused silica laser“. In: *Opt. Mater. Express* 5.4 (2015), pp. 704–711. DOI: 10.1364/OME.5.000704 (cit. on p. 102).
- [188] H Deng et al. „Experimental Demonstration of Longitudinal Beam Phase-Space Linearizer in a Free-Electron Laser Facility by Corrugated Structures“. In: *Phys. Rev. Lett.* 113 (25 2014), p. 254802. DOI: 10.1103/PhysRevLett.113.254802 (cit. on p. 102).
- [189] F Fu et al. „Demonstration of Nonlinear-Energy-Spread Compensation in Relativistic Electron Bunches with Corrugated Structures“. In: *Phys. Rev. Lett.* 114 (11 2015), p. 114801. DOI: 10.1103/PhysRevLett.114.114801 (cit. on p. 102).
- [190] S Bettoni, P Craievich, M Pedrozzi, and S Reiche. „Simulation of a corrugated beam pipe for the chirp compensation in SWISS-FEL“. In: *Proceedings of the 2013 Free-Electron Laser Conference*. 2013, pp. 214–218. ISBN: 978-3-95450-126-7 (cit. on p. 102).
- [191] Z Zhang, K Bane, Y Ding, Z Huang, R Iverson, T Maxwell, G Stupakov, and L Wang. „Electron beam energy chirp control with a rectangular corrugated structure at the Linac Coherent Light Source“. In: *Phys. Rev. ST Accel. Beams* 18 (1 2015), p. 010702. DOI: 10.1103/PhysRevSTAB.18.010702 (cit. on p. 102).

- [192] S Schröder, T Herffurth, M Trost, and A Duparré. „Angle-resolved scattering and reflectance of extreme-ultraviolet multilayer coatings: measurement and analysis“. In: *Appl. Opt.* 49.9 (2010), pp. 1503–1512. DOI: 10.1364/AO.49.001503 (cit. on p. 102).
- [193] A Rudenko and D Rolles. „Time-resolved studies with FELs“. In: *Journal of Electron Spectroscopy and Related Phenomena* 204, Part B (2015). Gas phase spectroscopic and dynamical studies at Free-Electron Lasers and other short wavelength sources, pp. 228–236. ISSN: 0368-2048. DOI: 10.1016/j.elspec.2015.07.010 (cit. on p. 103).
- [194] L Flückiger et al. „Time-resolved x-ray imaging of a laser-induced nanoplasma and its neutral residuals“. In: *New Journal of Physics* 18.4 (2016), p. 043017 (cit. on p. 103).
- [195] C Wagner and N Harned. „EUV lithography: Lithography gets extreme“. In: *Nature Photonics* 4.1 (2010), pp. 24–26. DOI: 10.1038/nphoton.2009.251 (cit. on p. 103).
- [196] C Spielmann, N Burnett, S Sartania, R Koppitsch, M Schnürer, C Kan, M Lenzner, P Wobrauschek, and F Krausz. „Generation of coherent X-rays in the water window using 5-femtosecond laser pulses“. In: *Science* 278.5338 (1997), pp. 661–664. DOI: 10.1126/science.278.5338.661 (cit. on p. 103).
- [197] MN Polyanskiy, IV Pogorelsky, and V Yakimenko. „Picosecond pulse amplification in isotopic CO<sub>2</sub> active medium“. In: *Opt. Express* 19.8 (2011), pp. 7717–7725. DOI: 10.1364/OE.19.007717 (cit. on p. 104).
- [198] *Sub-PW Ultra-fast CO<sub>2</sub> Laser*. 2016. URL: <https://www.bnl.gov/atf/capabilities/ultrafast-CO2.php> (cit. on p. 104).
- [199] D Haberberger, S Tochitsky, and C Joshi. „Fifteen terawatt picosecond CO<sub>2</sub> laser system“. In: *Opt. Express* 18.17 (2010), pp. 17865–17875. DOI: 10.1364/OE.18.017865 (cit. on p. 104).
- [200] R Agustsson, E Arab, A Murokh, B O’Shea, A Ovodenko, I Pogorelsky, J Rosenzweig, V Solovyov, and R Tilton. „Measuring single-shot, picosecond optical damage threshold in Ge, Si, and sapphire with a 5.1-µm laser“. In: *Opt. Mater. Express* 5.12 (2015), pp. 2835–2842. DOI: 10.1364/OME.5.002835 (cit. on p. 105).
- [201] M Först et al. „Melting of Charge Stripes in Vibrationally Driven La<sub>1.875</sub>Ba<sub>0.125</sub>CuO<sub>4</sub>: Assessing the Respective Roles of Electronic and Lattice Order in Frustrated Superconductors“. In: *Phys. Rev. Lett.* 112 (15 2014), p. 157002. DOI: 10.1103/PhysRevLett.112.157002 (cit. on p. 105).
- [202] T Wang et al. „Femtosecond Single-Shot Imaging of Nanoscale Ferromagnetic Order in Co/Pd Multilayers Using Resonant X-Ray Holography“. In: *Phys. Rev. Lett.* 108 (26 2012), p. 267403. DOI: 10.1103/PhysRevLett.108.267403 (cit. on pp. 105, 121).
- [203] C Bostedt, S Boutet, DM Fritz, Z Huang, HJ Lee, HT Lemke, A Robert, WF Schlotter, JJ Turner, and GJ Williams. „Linac Coherent Light Source: The first five years“. In: *Rev. Mod. Phys.* 88 (1 2016), p. 015007. DOI: 10.1103/RevModPhys.88.015007 (cit. on pp. 105, 121).
- [204] WJ Engelen, MA van der Heijden, DJ Bakker, EJD Vredenburg, and OJ Luiten. „High-coherence electron bunches produced by femtosecond photoionization“. In: *Nat Commun* 4.1693 (2013). DOI: 10.1038/ncomms2700 (cit. on p. 106).
- [205] AJ McCulloch, DV Sheludko, M Junker, and RE Scholten. „High-coherence picosecond electron bunches from cold atoms“. In: *Nat Commun* 4.1692 (2013). DOI: 10.1038/ncomms2699 (cit. on p. 106).

- [206] M Krüger, M Schenk, and P Hommelhoff. „Attosecond control of electrons emitted from a nanoscale metal tip“. In: *Nature* 475 (7354 2011), pp. 78–81. DOI: 10.1038/nature10196 (cit. on p. 106).
- [207] D Ehberger, J Hammer, M Eisele, M Krüger, J Noe, A Högele, and P Hommelhoff. „Highly Coherent Electron Beam from a Laser-Triggered Tungsten Needle Tip“. In: *Phys. Rev. Lett.* 114 (22 2015), p. 227601. DOI: 10.1103/PhysRevLett.114.227601 (cit. on p. 106).
- [208] J Breuer and P Hommelhoff. „Laser-Based Acceleration of Nonrelativistic Electrons at a Dielectric Structure“. In: *Phys. Rev. Lett.* 111 (13 2013), p. 134803. DOI: 10.1103/PhysRevLett.111.134803 (cit. on p. 106).
- [209] EA Peralta et al. „Demonstration of electron acceleration in a laser-driven dielectric microstructure“. In: *Nature* 503 (7474 2013), pp. 91–94. DOI: 10.1038/nature12664 (cit. on p. 106).
- [210] J McNeur, M Kozak, D Ehberger, N Schönenberger, A Tafel, A Li, and P Hommelhoff. „A miniaturized electron source based on dielectric laser accelerator operation at higher spatial harmonics and a nanotip photoemitter“. In: *Journal of Physics B: Atomic, Molecular and Optical Physics* 49.3 (2016), p. 034006 (cit. on p. 106).
- [211] WT Wang et al. „High-Brightness High-Energy Electron Beams from a Laser Wakefield Accelerator via Energy Chirp Control“. In: *Phys. Rev. Lett.* 117 (12 2016), p. 124801. DOI: 10.1103/PhysRevLett.117.124801 (cit. on p. 106).
- [212] O Lundh, J Lim, C Rechatin, L Ammoura, A Ben-Ismaïl, X Davoine, G Gallot, J Goddet, E Lefebvre, V Malka, et al. „Few femtosecond, few kiloampere electron bunch produced by a laser-plasma accelerator“. In: *Nature Physics* 7.3 (2011), pp. 219–222. DOI: 10.1038/nphys1872 (cit. on p. 106).
- [213] J van Tilborg, CB Schroeder, CV Filip, C Tóth, CGR Geddes, G Fubiani, R Huber, RA Kaindl, E Esarey, and WP Leemans. „Temporal Characterization of Femtosecond Laser-Plasma-Accelerated Electron Bunches Using Terahertz Radiation“. In: *Phys. Rev. Lett.* 96 (1 2006), p. 014801. DOI: 10.1103/PhysRevLett.96.014801 (cit. on p. 106).
- [214] AD Debus et al. „Electron Bunch Length Measurements from Laser-Accelerated Electrons Using Single-Shot THz Time-Domain Interferometry“. In: *Phys. Rev. Lett.* 104 (8 2010), p. 084802. DOI: 10.1103/PhysRevLett.104.084802 (cit. on p. 106).
- [215] A Buck, M Nicolai, K Schmid, CMS Sears, A Savert, JM Mikhailova, F Krausz, MC Kaluza, and L Veisz. „Real-time observation of laser-driven electron acceleration“. In: *Nature Physics* 7.7 (2011), pp. 543–548. ISSN: 1745-2473. DOI: 10.1038/nphys1942 (cit. on p. 106).
- [216] AJ Gonsalves et al. „Generation and pointing stabilization of multi-GeV electron beams from a laser plasma accelerator driven in a pre-formed plasma waveguide“. In: *Physics of Plasmas* 22.5, 056703 (2015). DOI: 10.1063/1.4919278 (cit. on pp. 106, 116).
- [217] Z He, B Hou, J Nees, J Easter, J Faure, K Krushelnick, and A Thomas. „High repetition-rate wakefield electron source generated by few-millijoule, 30 fs laser pulses on a density downramp“. In: *New Journal of Physics* 15.5 (2013), p. 053016. DOI: 10.1088/1367-2630/15/5/053016 (cit. on pp. 106, 116).
- [218] S Banerjee et al. „Stable, tunable, quasimonoenergetic electron beams produced in a laser wakefield near the threshold for self-injection“. In: *Phys. Rev. ST Accel. Beams* 16 (3 2013), p. 031302. DOI: 10.1103/PhysRevSTAB.16.031302 (cit. on pp. 106, 116).

- [219] SY Kalmykov, SA Yi, A Beck, AF Lifschitz, X Davoine, E Lefebvre, V Khudik, G Shvets, and MC Downer. „Dark-current-free petawatt laser-driven wakefield accelerator based on electron self-injection into an expanding plasma bubble“. In: *Plasma Physics and Controlled Fusion* 53.1 (2011), p. 014006. DOI: 10.1088/0741-3335/53/1/014006 (cit. on p. 106).
- [220] J Osterhoff et al. „Generation of Stable, Low-Divergence Electron Beams by Laser-Wakefield Acceleration in a Steady-State-Flow Gas Cell“. In: *Phys. Rev. Lett.* 101 (2008), p. 085002. DOI: 10.1103/PhysRevLett.101.085002 (cit. on pp. 106, 116).
- [221] S Karsch et al. „GeV-scale electron acceleration in a gas-filled capillary discharge waveguide“. In: *New Journal of Physics* 9.11 (2007), p. 415. DOI: 10.1088/1367-2630/9/11/415 (cit. on p. 106).
- [222] J Faure, C Rechatin, A Norlin, A Lifschitz, Y Glinec, and V Malka. „Controlled injection and acceleration of electrons in plasma wakefields by colliding laser pulses“. In: *Nature* 444.7120 (2006), pp. 737–739. DOI: 10.1038/nature05393 (cit. on p. 106).
- [223] C Rechatin, J Faure, A Ben-Ismaïl, J Lim, R Fitour, A Specka, H Videau, A Tafzi, F Burgy, and V Malka. „Controlling the Phase-Space Volume of Injected Electrons in a Laser-Plasma Accelerator“. In: *Phys. Rev. Lett.* 102 (16 2009), p. 164801. DOI: 10.1103/PhysRevLett.102.164801 (cit. on p. 106).
- [224] M Chen, E Esarey, CGR Geddes, E Cormier-Michel, CB Schroeder, SS Bulanov, C Benedetti, LL Yu, S Rykovanov, DL Bruhwiler, and WP Leemans. „Electron injection and emittance control by transverse colliding pulses in a laser-plasma accelerator“. In: *Phys. Rev. ST Accel. Beams* 17 (5 2014), p. 051303. DOI: 10.1103/PhysRevSTAB.17.051303 (cit. on p. 106).
- [225] CB Schroeder, C Benedetti, SS Bulanov, M Chen, E Esarey, CGR Geddes, JL Vay, LL Yu, and WP Leemans. „Ultra-low emittance beam generation using two-color ionization injection in laser-plasma accelerators“. In: *Proc. SPIE* 9514 (2015). DOI: 10.1117/12.2178577 (cit. on p. 106).
- [226] CE Clayton et al. „Self-Guided Laser Wakefield Acceleration beyond 1 GeV Using Ionization-Induced Injection“. In: *Phys. Rev. Lett.* 105 (10 2010), p. 105003. DOI: 10.1103/PhysRevLett.105.105003 (cit. on p. 106).
- [227] BB Pollock et al. „Demonstration of a Narrow Energy Spread,  $\sim 0.5$  GeV Electron Beam from a Two-Stage Laser Wakefield Accelerator“. In: *Phys. Rev. Lett.* 107 (4 2011), p. 045001. DOI: 10.1103/PhysRevLett.107.045001 (cit. on p. 106).
- [228] M Mirzaie, S Li, M Zeng, N Hafz, M Chen, G Li, Q Zhu, H Liao, T Sokollik, F Liu, et al. „Demonstration of self-truncated ionization injection for GeV electron beams“. In: *Scientific Reports* 5.14659 (2015). DOI: 10.1038/srep14659 (cit. on p. 106).
- [229] CGR Geddes, K Nakamura, GR Plateau, C Toth, E Cormier-Michel, E Esarey, CB Schroeder, JR Cary, and WP Leemans. „Plasma-Density-Gradient Injection of Low Absolute-Momentum-Spread Electron Bunches“. In: *Phys. Rev. Lett.* 100 (21 2008), p. 215004. DOI: 10.1103/PhysRevLett.100.215004 (cit. on p. 106).
- [230] A Gonsalves, K Nakamura, C Lin, D Panasenkov, S Shiraishi, T Sokollik, C Benedetti, C Schroeder, C Geddes, J Van Tilborg, et al. „Tunable laser plasma accelerator based on longitudinal density tailoring“. In: *Nature Physics* 7.11 (2011), pp. 862–866. DOI: 10.1038/nphys2071 (cit. on p. 106).

- [231] SY Kalmykov. „Dark-current-free laser-plasma acceleration in blowout regime using non-linear plasma lens“. In: *AIP Conference Proceedings* 1507.1 (2012), pp. 921–926. DOI: 10.1063/1.4788989 (cit. on p. 106).
- [232] A Buck, J Wenz, J Xu, K Khrennikov, K Schmid, M Heigoldt, JM Mikhailova, M Geissler, B Shen, F Krausz, S Karsch, and L Veisz. „Shock-Front Injector for High-Quality Laser-Plasma Acceleration“. In: *Phys. Rev. Lett.* 110 (18 2013), p. 185006. DOI: 10.1103/PhysRevLett.110.185006 (cit. on p. 106).
- [233] E Guillaume, A Döpp, C Thaury, K Ta Phuoc, A Lifschitz, G Grittani, JP Goddet, A Tafzi, SW Chou, L Veisz, and V Malka. „Electron Rephasing in a Laser-Wakefield Accelerator“. In: *Phys. Rev. Lett.* 115 (15 2015), p. 155002. DOI: 10.1103/PhysRevLett.115.155002 (cit. on p. 106).
- [234] JS Liu et al. „All-Optical Cascaded Laser Wakefield Accelerator Using Ionization-Induced Injection“. In: *Phys. Rev. Lett.* 107 (3 2011), p. 035001. DOI: 10.1103/PhysRevLett.107.035001 (cit. on p. 106).
- [235] HT Kim, KH Pae, HJ Cha, IJ Kim, TJ Yu, JH Sung, SK Lee, TM Jeong, and J Lee. „Enhancement of Electron Energy to the Multi-GeV Regime by a Dual-Stage Laser-Wakefield Accelerator Pumped by Petawatt Laser Pulses“. In: *Phys. Rev. Lett.* 111 (16 2013), p. 165002. DOI: 10.1103/PhysRevLett.111.165002 (cit. on p. 106).
- [236] M Vargas, W Schumaker, ZH He, Z Zhao, K Behm, V Chvykov, B Hou, K Krushelnick, A Maksimchuk, V Yanovsky, and AGR Thomas. „Improvements to laser wakefield accelerated electron beam stability, divergence, and energy spread using three-dimensional printed two-stage gas cell targets“. In: *Applied Physics Letters* 104.17, 174103 (2014). DOI: 10.1063/1.4874981 (cit. on p. 106).
- [237] G Golovin, S Chen, N Powers, C Liu, S Banerjee, J Zhang, M Zeng, Z Sheng, and D Umstadter. „Tunable monoenergetic electron beams from independently controllable laser-wakefield acceleration and injection“. In: *Phys. Rev. ST Accel. Beams* 18 (1 2015), p. 011301. DOI: 10.1103/PhysRevSTAB.18.011301 (cit. on p. 106).
- [238] S Steinke, J van Tilborg, C Benedetti, CGR Geddes, J Daniels, KK Swanson, AJ Goncalves, K Nakamura, BH Shaw, CB Schroeder, E Esarey, and WP Leemans. „Staging of laser-plasma accelerators“. In: *Physics of Plasmas* 23.5, 056705 (2016). DOI: 10.1063/1.4948280 (cit. on p. 106).
- [239] S Mangles, A Thomas, M Kaluza, O Lundh, F Lindau, A Persson, Z Najmudin, CG Wahlström, C Murphy, C Kamperidis, et al. „Effect of laser contrast ratio on electron beam stability in laser wakefield acceleration experiments“. In: *Plasma physics and controlled fusion* 48.12B (2006), B83. DOI: 10.1088/0741-3335/48/12B/S08 (cit. on p. 106).
- [240] J van Tilborg et al. „Active Plasma Lensing for Relativistic Laser-Plasma-Accelerated Electron Beams“. In: *Phys. Rev. Lett.* 115 (18 2015), p. 184802. DOI: 10.1103/PhysRevLett.115.184802 (cit. on pp. 107, 115).
- [241] C Thaury et al. „Demonstration of relativistic electron beam focusing by a laser-plasma lens“. In: *Nature Communications* 6 (2015), p. 6868. DOI: 10.1038/ncomms7860 (cit. on pp. 107, 115).
- [242] S Kuschel et al. „Demonstration of passive plasma lensing of a laser wakefield accelerated electron bunch“. In: *Phys. Rev. Accel. Beams* 19 (7 2016), p. 071301. DOI: 10.1103/PhysRevAccelBeams.19.071301 (cit. on pp. 107, 115).
- [243] Linac & FEL Division at SLAC Accelerator Directorate. *LCLS Machine Parameters*. 2017. URL: [https://portal.slac.stanford.edu/sites/lclscore\\_public](https://portal.slac.stanford.edu/sites/lclscore_public) (cit. on p. 108).

- [244] U Schramm et al. „Ultrashort Pulse Laser Accelerated Proton Beams for First Radiobiological Applications“. In: *AIP Conference Proceedings* 1299.1 (2010), pp. 731–736. DOI: 10.1063/1.3520421 (cit. on p. 108).
- [245] SD Kraft et al. „Dose-dependent biological damage of tumour cells by laser-accelerated proton beams“. In: *New Journal of Physics* 12.8 (2010), p. 085003. DOI: 10.1088/1367-2630/12/8/085003 (cit. on p. 108).
- [246] J Metzkes, T Cowan, L Karsch, S Kraft, J Pawelke, C Richter, T Richter, K Zeil, and U Schramm. „Preparation of laser-accelerated proton beams for radiobiological applications“. In: *Nucl. Instr. Meth. Phys. Res. A* 653.1 (2011). Superstrong 2010, pp. 172–175. ISSN: 0168-9002. DOI: 10.1016/j.nima.2010.12.065 (cit. on p. 108).
- [247] C Richter, L Karsch, Y Dammene, SD Kraft, J Metzkes, U Schramm, M Schürer, M Sobbiella, A Weber, K Zeil, and J Pawelke. „A dosimetric system for quantitative cell irradiation experiments with laser-accelerated protons“. In: *Physics in Medicine and Biology* 56.6 (2011), p. 1529. DOI: 10.1088/0031-9155/56/6/002 (cit. on p. 108).
- [248] K Zeil, J Metzkes, T Kluge, M Bussmann, T Cowan, S Kraft, R Sauerbrey, and U Schramm. „Direct observation of prompt pre-thermal laser ion sheath acceleration“. In: *Nat Commun* 3 (2012), p. 874. DOI: 10.1038/ncomms1883 (cit. on p. 108).
- [249] K Zeil, J Metzkes, T Kluge, M Bussmann, TE Cowan, SD Kraft, R Sauerbrey, B Schmidt, M Zier, and U Schramm. „Robust energy enhancement of ultrashort pulse laser accelerated protons from reduced mass targets“. In: *Plasma Physics and Controlled Fusion* 56.8 (2014), p. 084004. DOI: 10.1088/0741-3335/56/8/084004 (cit. on p. 108).
- [250] J Metzkes, T Kluge, K Zeil, M Bussmann, SD Kraft, TE Cowan, and U Schramm. „Experimental observation of transverse modulations in laser-driven proton beams“. In: *New Journal of Physics* 16.2 (2014), p. 023008 (cit. on p. 109).
- [251] T Kluge, M Bussmann, HK Chung, C Gutt, LG Huang, M Zacharias, U Schramm, and TE Cowan. „Nanoscale femtosecond imaging of transient hot solid density plasmas with elemental and charge state sensitivity using resonant coherent diffraction“. In: *Physics of Plasmas* 23.3, 033103 (2016). DOI: 10.1063/1.4942786 (cit. on pp. 109, 115, 121).
- [252] BH Shaw, S Steinke, J van Tilborg, and WP Leemans. „Reflectance characterization of tape-based plasma mirrors“. In: *Physics of Plasmas* 23.6 (2016), p. 063118. DOI: 10.1063/1.4954242. eprint: <http://aip.scitation.org/doi/pdf/10.1063/1.4954242> (cit. on p. 115).
- [253] S Becker, M Bussmann, S Raith, M Fuchs, R Weingartner, P Kunz, W Lauth, U Schramm, M El Ghazaly, F Grüner, H Backe, and D Habs. „Characterization and tuning of ultrahigh gradient permanent magnet quadrupoles“. In: *Phys. Rev. ST Accel. Beams* 12 (10 2009), p. 102801. DOI: 10.1103/PhysRevSTAB.12.102801 (cit. on p. 115).
- [254] M Hornung, R Bödefeld, M Siebold, M Schnepf, J Hein, R Sauerbrey, and MC Kaluza. „Alignment of a tiled-grating compressor in a high-power chirped-pulse amplification laser system“. In: *Applied Optics* 46.30 (2007), pp. 7432–7435. DOI: 10.1364/AO.46.007432 (cit. on p. 116).
- [255] R Brinkmann, K Flöttmann, J Roßbach, P Schmüser, N Walker, and H Weise. „TESLA Technical Design Report Part II: The Accelerator“. In: (2001). Section 9.8.3 (cit. on p. 116).
- [256] ME Couprie et al. „The LUNEX5 project in France“. In: *Journal of Physics: Conference Series* 425.7 (2013), p. 072001. DOI: 10.1088/1742-6596/425/7/072001 (cit. on p. 116).
- [257] *Compact Future Light Sources*. 2016. URL: <http://bella.lbl.gov/research/bella-center-research-compact-future-light-sources/> (cit. on p. 116).

- [258] OM Apsimon, G Burt, K Hanahoe, B Hidding, J Smith, and G Xia. „iMPACT, Undulator-Based Multi-Bunch Plasma Accelerator“. In: *Proc. of International Particle Accelerator Conference (IPAC'16), Busan, Korea, May 8-13, 2016*. (Busan, Korea). International Particle Accelerator Conference 7. Geneva, Switzerland: JACoW, 2016, pp. 2609–2612. ISBN: 978-3-95450-147-2. DOI: 10.18429/JACoW-IPAC2016-WEPMY025 (cit. on p. 116).
- [259] Y Xu, J Lu, W Li, F Wu, Y Li, C Wang, Z Li, X Lu, Y Liu, Y Leng, R Li, and Z Xu. „A Stable 200TW / 1Hz Ti:sapphire laser for driving full coherent XFEL“. In: *Optics & Laser Technology* 79 (2016), pp. 141–145. ISSN: 0030-3992. DOI: <http://dx.doi.org/10.1016/j.optlastec.2015.11.023> (cit. on p. 116).
- [260] *Alpha-X – Advanced Laser-Plasma High-Energy Accelerators towards X-rays*. 2016. URL: <http://alpha-x.phys.strath.ac.uk/> (cit. on p. 116).
- [261] *LUX*. 2016. URL: <http://lux.cfel.de/> (cit. on p. 116).
- [262] T Kluge. private communication. 2016 (cit. on p. 116).
- [263] A Jochmann. „Development of a Tunable Ultrafast X-ray Source via Inverse-Compton-Scattering“. PhD thesis. Helmholtz-Zentrum Dresden-Rossendorf, 2014 (cit. on p. 117).
- [264] P Mulser and D Bauer. *High Power Laser-Matter Interaction*. Springer Tracts in Modern Physics 238. Springer-Verlag Berlin Heidelberg, 2010. ISBN: 978-3-540-46065-7. DOI: 10.1007/978-3-540-46065-7 (cit. on p. 117).
- [265] SW Wilkins, TE Gureyev, D Gao, A Pogany, and AW Stevenson. „Phase-contrast imaging using polychromatic hard X-rays“. In: *Nature* 384 (6607 1996), pp. 335–338. DOI: 10.1038/384335a0 (cit. on p. 118).
- [266] R Neutze, R Wouts, D van der Spoel, E Weckert, and J Hajdu. „Potential for biomolecular imaging with femtosecond X-ray pulses“. In: *Nature* 406.6797 (2000), pp. 752–757. DOI: 10.1038/35021099 (cit. on p. 120).
- [267] JC Spence and P Hawkes. „Diffract-and-destroy: Can X-ray lasers “solve” the radiation damage problem?“ In: *Ultramicroscopy* 108.12 (2008), pp. 1502–1503. ISSN: 0304-3991. DOI: 10.1016/j.ultramic.2008.05.003 (cit. on p. 120).
- [268] HN Chapman et al. „Ultrafast coherent X-ray diffractive imaging with the FLASH Free-Electron Laser“. In: *Ultrafast Phenomena XVI: Proceedings of the 16th International Conference, Palazzo dei Congressi Stresa, Italy, June 9–13, 2008*. Ed. by P Corkum, S Silvestri, AK Nelson, E Riedle, and WR Schoenlein. Berlin, Heidelberg: Springer Berlin Heidelberg, 2009, pp. 143–145. ISBN: 978-3-540-95946-5. DOI: 10.1007/978-3-540-95946-5\_47 (cit. on p. 120).
- [269] MJ Bogan et al. „Single Particle X-ray Diffractive Imaging“. In: *Nano Letters* 8.1 (2008), pp. 310–316. DOI: 10.1021/nl072728k (cit. on p. 120).
- [270] K Gaffney and H Chapman. „Imaging atomic structure and dynamics with ultrafast x-ray scattering“. In: *Science* 316.5830 (2007), pp. 1444–1448. DOI: 10.1126/science.1135923 (cit. on p. 120).
- [271] HN Chapman, SP Hau-Riege, MJ Bogan, S Bajt, A Barty, S Boutet, S Marchesini, M Frank, BW Woods, WH Benner, et al. „Femtosecond time-delay X-ray holography“. In: *Nature* 448.7154 (2007), pp. 676–679. DOI: 10.1038/nature06049 (cit. on p. 120).
- [272] A Barty, C Caleman, A Aquila, N Timneanu, L Lomb, TA White, J Andreasson, D Arnlund, S Bajt, TR Barends, et al. „Self-terminating diffraction gates femtosecond X-ray nanocrystallography measurements“. In: *Nature Photonics* 6.1 (2011), pp. 35–40. DOI: 10.1038/nphoton.2011.297 (cit. on p. 120).

- [273] SG Rykovanov, CGR Geddes, JL Vay, CB Schroeder, E Esarey, and WP Leemans. „Quasi-monoenergetic femtosecond photon sources from Thomson Scattering using laser plasma accelerators and plasma channels“. In: *Journal of Physics B: Atomic, Molecular and Optical Physics* 47.23 (2014), p. 234013. DOI: 10.1088/0953-4075/47/23/234013 (cit. on p. 120).
- [274] F Albert et al. „Characterization and applications of a tunable, laser-based, MeV-class Compton-scattering  $\gamma$ -ray source“. In: *Phys. Rev. ST Accel. Beams* 13 (7 2010), p. 070704. DOI: 10.1103/PhysRevSTAB.13.070704 (cit. on p. 121).
- [275] W Bertozzi and RJ Ledoux. „Nuclear resonance fluorescence imaging in non-intrusive cargo inspection“. In: *Nucl. Instr. Meth. Phys. Res. B* 241.1–4 (2005). Proceedings of the Eighteenth International Conference on the Application of Accelerators in Research and Industry (CAARI 2004), pp. 820–825. ISSN: 0168-583X. DOI: 10.1016/j.nimb.2005.07.202 (cit. on p. 121).
- [276] R HAJIMA, T HAYAKAWA, N KIKUZAWA, and E MINEHARA. „Proposal of Nondestructive Radionuclide Assay Using a High-Flux Gamma-Ray Source and Nuclear Resonance Fluorescence“. In: *Journal of Nuclear Science and Technology* 45.5 (2008), pp. 441–451. DOI: 10.1080/18811248.2008.9711453 (cit. on p. 121).
- [277] BJ Quiter, BA Ludewigt, VV Mozin, and SG Prussin. „Nuclear Resonance Fluorescence for Materials Assay“. In: *IEEE Transactions on Nuclear Science* 58.2 (2011), pp. 400–403. ISSN: 0018-9499. DOI: 10.1109/TNS.2011.2112777 (cit. on p. 121).
- [278] G Sarri et al. „Table-Top Laser-Based Source of Femtosecond, Collimated, Ultrarelativistic Positron Beams“. In: *Phys. Rev. Lett.* 110 (25 2013), p. 255002. DOI: 10.1103/PhysRevLett.110.255002 (cit. on p. 121).
- [279] X Ribeyre, E d’Humières, O Jansen, S Jequier, VT Tikhonchuk, and M Lobet. „Pair creation in collision of  $\gamma$ -ray beams produced with high-intensity lasers“. In: *Phys. Rev. E* 93 (1 2016), p. 013201. DOI: 10.1103/PhysRevE.93.013201 (cit. on p. 121).
- [280] SS Singh, JJ Williams, P Hruby, X Xiao, F De Carlo, and N Chawla. „In situ experimental techniques to study the mechanical behavior of materials using X-ray synchrotron tomography“. In: *Integrating Materials and Manufacturing Innovation* 3.1 (2014), pp. 1–14. ISSN: 2193-9772. DOI: 10.1186/2193-9772-3-9 (cit. on p. 121).
- [281] Y Wang, X Liu, KS Im, WK Lee, J Wang, K Fezzaa, DL Hung, and JR Winkelman. „Ultrafast X-ray study of dense-liquid-jet flow dynamics using structure-tracking velocimetry“. In: *Nature Physics* 4 (4 2008), pp. 305–309. DOI: 10.1038/nphys840 (cit. on p. 121).
- [282] V Baran, M Colonna, M Di Toro, A Croitoru, and D Dumitru. „Connecting the pygmy dipole resonance to the neutron skin“. In: *Phys. Rev. C* 88 (4 2013), p. 044610. DOI: 10.1103/PhysRevC.88.044610 (cit. on p. 121).
- [283] BA Brown and A Schwenk. „Constraints on Skyrme equations of state from properties of doubly magic nuclei and *ab initio* calculations of low-density neutron matter“. In: *Phys. Rev. C* 89 (1 2014), p. 011307. DOI: 10.1103/PhysRevC.89.011307 (cit. on p. 121).
- [284] A Cocioceanu and L Serban. *ELI-NP | Extreme Light Infrastructure - Nuclear Physics*. Many more possible applications of high peak brilliance  $\gamma$ -ray beams are investigated in the context of ELI-NP, see the White Book and publications on the ELI-NP website. 2016. URL: <http://www.eli-np.ro/> (cit. on p. 121).

- [285] L Pollack, MW Tate, AC Finnefrock, C Kalidas, S Trotter, NC Darnton, L Lurio, RH Austin, CA Batt, SM Gruner, and SGJ Mochrie. „Time Resolved Collapse of a Folding Protein Observed with Small Angle X-Ray Scattering“. In: *Phys. Rev. Lett.* 86 (21 2001), pp. 4962–4965. DOI: 10.1103/PhysRevLett.86.4962 (cit. on p. 121).
- [286] M Salomé et al. „Fluorescence X-ray micro-spectroscopy activities at ESRF“. In: *Journal of Physics: Conference Series* 186.1 (2009), p. 012014. DOI: 10.1088/1742-6596/186/1/012014 (cit. on p. 121).
- [287] Y Shinohara, A Watanabe, H Kishimoto, and Y Amemiya. „Combined measurement of X-ray photon correlation spectroscopy and diffracted X-ray tracking using pink beam X-rays“. In: *Journal of Synchrotron Radiation* 20.5 (2013), pp. 801–804. DOI: 10.1107/S090904951301844X (cit. on p. 121).
- [288] W Wurth. „Surface Science Studies with Free Electron Lasers: Real-Time Observations of Electronic Structure Changes during Reactions“. In: *Synchrotron Radiation News* 29.3 (2016), pp. 32–35. DOI: 10.1080/08940886.2016.1174045 (cit. on p. 121).
- [289] T Burian et al. „Soft x-ray free-electron laser induced damage to inorganic scintillators“. In: *Opt. Mater. Express* 5.2 (2015), pp. 254–264. DOI: 10.1364/OME.5.000254 (cit. on p. 121).
- [290] P Fromme and JC Spence. „Femtosecond nanocrystallography using X-ray lasers for membrane protein structure determination“. In: *Current Opinion in Structural Biology* 21.4 (2011). Engineering and design / Membranes, pp. 509–516. ISSN: 0959-440X. DOI: 10.1016/j.sbi.2011.06.001 (cit. on p. 121).
- [291] Y Nishino, Y Takahashi, N Imamoto, T Ishikawa, and K Maeshima. „Three-Dimensional Visualization of a Human Chromosome Using Coherent X-Ray Diffraction“. In: *Phys. Rev. Lett.* 102 (1 2009), p. 018101. DOI: 10.1103/PhysRevLett.102.018101 (cit. on p. 121).
- [292] R McRae, P Bagchi, S Sumalekshmy, and CJ Fahrni. „In Situ Imaging of Metals in Cells and Tissues“. In: *Chemical Reviews* 109.10 (2009). PMID: 19772288, pp. 4780–4827. DOI: 10.1021/cr900223a (cit. on p. 121).
- [293] SL Johnson et al. „Femtosecond Dynamics of the Collinear-to-Spiral Antiferromagnetic Phase Transition in CuO“. In: *Phys. Rev. Lett.* 108 (3 2012), p. 037203. DOI: 10.1103/PhysRevLett.108.037203 (cit. on p. 121).
- [294] J Chang et al. „Direct observation of competition between superconductivity and charge density wave order in YBa<sub>2</sub>Cu<sub>3</sub>O<sub>6.67</sub>“. In: *Nature Physics* 8 (12 2012), pp. 871–876. DOI: 10.1038/nphys2456 (cit. on p. 121).
- [295] CE Graves et al. „Nanoscale spin reversal by non-local angular momentum transfer following ultrafast laser excitation in ferrimagnetic GdFeCo“. In: *Nat Mater* 12 (4 2013), pp. 293–298. DOI: 10.1038/nmat3597 (cit. on p. 121).
- [296] NR Thompson and BWJ McNeil. „Mode Locking in a Free-Electron Laser Amplifier“. In: *Phys. Rev. Lett.* 100 (20 2008), p. 203901. DOI: 10.1103/PhysRevLett.100.203901 (cit. on p. 121).
- [297] G Stupakov. „Using the Beam-Echo Effect for Generation of Short-Wavelength Radiation“. In: *Phys. Rev. Lett.* 102 (7 2009), p. 074801. DOI: 10.1103/PhysRevLett.102.074801 (cit. on p. 121).
- [298] GA Mourou. „Compression of High Energy Pulses to the Sub-attosecond Regime: Route to Exawatt Laser Subatomic Physics“. In: *High-Brightness Sources and Light-Driven Interactions*. Optical Society of America, 2016, JS1A.2. DOI: 10.1364/EUVXRAY.2016.JS1A.2 (cit. on p. 122).

- [299] T Tanaka. „Proposal to Generate an Isolated Monocycle X-Ray Pulse by Counteracting the Slippage Effect in Free-Electron Lasers“. In: *Phys. Rev. Lett.* 114 (4 2015), p. 044801. DOI: 10.1103/PhysRevLett.114.044801 (cit. on p. 122).
- [300] LT Campbell and BWJ McNeil. „Puffin: A three dimensional, unaveraged free electron laser simulation code“. In: *Physics of Plasmas* 19.9 (2012), p. 093119. DOI: 10.1063/1.4752743 (cit. on p. 122).
- [301] S Reiche, P Musumeci, and K Goldammer. „Recent upgrade to the free-electron laser code GENESIS 1.3“. In: *2007 IEEE Particle Accelerator Conference (PAC)*. 2007, pp. 1269–1271. DOI: 10.1109/PAC.2007.4441052 (cit. on p. 122).
- [302] H Burau, R Widera, W Honig, G Juckeland, A Debus, T Kluge, U Schramm, TE Cowan, R Sauerbrey, and M Bussmann. „PIConGPU: A Fully Relativistic Particle-in-Cell Code for a GPU Cluster“. In: *IEEE Transactions on Plasma Science* 38.10 (2010), pp. 2831–2839. ISSN: 0093-3813. DOI: 10.1109/TPS.2010.2064310 (cit. on p. 122).
- [303] M Bussmann et al. „Radiative signature of the relativistic Kelvin-Helmholtz Instability“. In: *2013 SC - International Conference for High Performance Computing, Networking, Storage and Analysis (SC)*. 2013, pp. 1–12. DOI: 10.1145/2503210.2504564 (cit. on p. 122).
- [304] A Di Piazza, C Müller, KZ Hatsagortsyan, and CH Keitel. „Extremely high-intensity laser interactions with fundamental quantum systems“. In: *Rev. Mod. Phys.* 84 (3 2012), pp. 1177–1228. DOI: 10.1103/RevModPhys.84.1177 (cit. on p. 122).
- [305] R Bonifacio, N Piovella, and G Robb. „Quantum theory of SASE FEL“. In: *Nucl. Instr. Meth. Phys. Res. A* 543.2–3 (2005), pp. 645–652. ISSN: 0168-9002. DOI: 10.1016/j.nima.2005.01.324 (cit. on p. 122).
- [306] CB Schroeder, C Pellegrini, and P Chen. „Quantum effects in high-gain free-electron lasers“. In: *Phys. Rev. E* 64 (5 2001), p. 056502. DOI: 10.1103/PhysRevE.64.056502 (cit. on p. 122).
- [307] HK Avetissian and GF Mkrtchian. „Quantum self-amplified spontaneous emission regime of the x-ray Compton laser“. In: *Phys. Rev. ST Accel. Beams* 10 (3 2007), p. 030703. DOI: 10.1103/PhysRevSTAB.10.030703 (cit. on p. 122).
- [308] GRM Robb and R Bonifacio. „Competition between coherent emission and broadband spontaneous emission in the quantum free electron laser“. In: *Physics of Plasmas* 20.3, 033106 (2013). DOI: 10.1063/1.4794731 (cit. on p. 122).
- [309] R Bonifacio, N Piovella, M Cola, L Volpe, A Schiavi, and G Robb. „The quantum free-electron laser“. In: *Nucl. Instr. Meth. Phys. Res. A* 593.1–2 (2008). Proceedings of the International Workshop on Frontiers in FEL Physics and Related Topics, pp. 69–74. ISSN: 0168-9002. DOI: 10.1016/j.nima.2008.04.028 (cit. on p. 122).
- [310] P Kling, E Giese, R Endrich, P Preiss, R Sauerbrey, and WP Schleich. „What defines the quantum regime of the free-electron laser?“ In: *New Journal of Physics* 17.12 (2015), p. 123019. DOI: 10.1088/1367-2630/17/12/123019 (cit. on p. 122).
- [311] A Debus. „Brilliant radiation sources by laser-plasma accelerators and optical undulators“. PhD thesis. Technische Universität Dresden & Helmholtz-Zentrum Dresden-Rossendorf, 2012 (cit. on p. 122).
- [312] DC O’Shea. „Group velocity dispersion using commercial optical design programs“. In: *Appl. Opt.* 45.19 (2006), pp. 4740–4746. DOI: 10.1364/AO.45.004740 (cit. on p. 124).

## References

- [313] R Mishra, P Leblanc, Y Sentoku, MS Wei, and FN Beg. „Collisional particle-in-cell modeling for energy transport accompanied by atomic processes in dense plasmas“. In: *Physics of Plasmas* 20.7 (2013), p. 072704. DOI: 10.1063/1.4812701 (cit. on p. 129).
- [314] DJ Griffiths. *Introduction to Electrodynamics*. 3rd ed. Pearson Prentice Hall, 1999 (cit. on p. 129).
- [315] A Kranz. *Fruchtwein selbstgemacht - Der Fruchtweinkeller*. 2018. URL: <http://www.fruchtweinkeller.de> (cit. on p. 162).
- [316] JJ Palmer. *How To Brew: Everything You Need to Know to Brew Great Beer Every Time*. Fourth edition. Brewers Publications, 2017. ISBN: 1938469356 (cit. on p. 162).
- [317] J Zainasheff and JJ Palmer. *Brewing Classic Styles: 80 Winning Recipes Anyone Can Brew*. Brewers Publications, 2007. ISBN: 0937381926 (cit. on p. 162).

# EIN HERZLICHES DANKESCHÖN

an alle, die mir die Promotion ermöglichten sowie währenddessen mit Unterstützung und Hilfe zur Seite standen!

Zuallererst danke ich Uli und Michael für die Möglichkeit über TWTS eine Doktorarbeit in der Theoriegruppe der Abteilung Laser-Teilchenbeschleunigung anfertigen zu dürfen. Insbesondere einen großen Dank an Uli für die zahlreichen Möglichkeiten TWTS auf spannenden und erlebnisreichen Konferenzen zu präsentieren sowie jederzeit mit einem kurzen Rat oder Hinweis zu helfen wenn es nötig war.

Außerdem danke ich Atoosa und Tom für die Anfertigung der Gutachten sowie Prof. Geck, Prof. Kämpfer und Frau Prof. Pospiech für die Mitwirkung in der Promotionskommission.

Ein besonderes Dankeschön nun noch einmal an Michael, für Deinen unermesslich hohen Einsatz stets die bestmögliche Qualität zu erreichen, sowohl in der geleisteten Arbeit als auch in deren Darstellung, sowie auf dem Weg dorthin nie aufzugeben und nicht den Glauben in meine Fähigkeiten zu verlieren, sondern mich zu bestärken und mit Rat zur Seite zu stehen. Auch wenn Letzterer in seiner Form manchmal schwer verdaulich war, würde ich nie auf ihn verzichten, denn er war immer wertvoll und führte immer zu einem signifikanten Qualitätsanstieg.

Alex, an Dich geht ein ebenso großes Dankeschön für Dein anhaltendes Engagement zu jeder Zeit jede Frage mit Dir im Detail besprechen zu können. Dabei zu erleben, wie man auf scheinbar jedes Problem eine Antwort findet und auch Rückschläge in Fortschritt dreht, halfen mir unglaublich beim Voranschreiten im Thema und Hochhalten der Motivation.

Richard, Du warst genauso zu jeder Zeit eine große Hilfe wenn ich Diskussionsbedarf über Ansätze, Rechnungen, Methoden oder ähnliches hatte oder uneingeschränkten Zugriff auf Dein Pythonwissen genießen durfte. Vielen Dank dafür!

Tom, your fascination for physics is viral and solving the (Fermi) question "How many water molecules in this bottle of water ran through Jesus' bladder" with your help was memorable, edifying and inspiring. Thank you!

Karl, vielen Dank auch an Dich für die interessanten Einblicke in die Experimente und vor allem für die tolle Prüfungsvorbereitung!

Für die viele Zeit für Diskussionen zum TWTS-Aufbau und Einblicke in Laserbau danke ich auch ganz besonders dem PENELOPE Team: Fabian, Mathias, Daniel und Markus.

Weil ich die Arbeit allein im stillen Kämmerchen nie durchgehalten hätte, ergeht zusätzlich ein großer Dank für interessante Hallway-Meetings und Busfahrten, Mitfahrgelegenheiten, Kuchen, lustige Abende auf Dienstreisen sowie Joy and Happiness während der Arbeitszeit (powered by Candy League) als auch für Fußball danach ans gesamte Team: Axel Hübl, Erik, Thomas Kluge, Jan, Heiko, Ilja, Jakob, João, Marco, Anton, Leon, Shuan, Lingen, Weiqiang, Alexander Grund, Melanie, Katja, Maximilian Böhme, Malte, Anja, Wolfgang, Lotti, Martin, Omid, Alexan-

der Köhler, Tim, Jakob, Jurjen, Arie, Thomas Kurz, Axel Jochmann, HP, Flo Brack, Stephan Kraft, Josefine, Stefan Bock, Uwe, Constantin, Gunther, Harald und Thomas Püschel. Insbesondere danke ich den Organisatoren unserer Fußballgruppe: Simon, René Gebhardt und Christoph. Unsere Fußballspiele außerhalb der Arbeit sorgen für Spaß und Entspannung aber vor allem auch für einen lockeren Umgang miteinander sowie den Kollegen aus anderen Arbeitsgruppen. Für die Organisation des beliebten Weihnachtsfußballturniers gebührt euch ein besonderer Dank.

Fußball zur körperlichen Betätigung in der Freizeit genoss ich im Laufe der Jahre auch im Kreise der Carl Stahl Soccer-Connection (Robin, Marko, Jan, Ronald, Heiko, Stefan R, Stefan G, Sven, Martin, Raphael, Henryk) und als Teil der Schiedsrichter Gruppe des TSV Rotation Dresden (Ocki, Jens, David, Wolfgang, Dirk, Martin, Julius, Bastian, Micha, Janis, Esse). Vielen Dank auch an Euch für die stets unterhaltsamen Treffen!

Einiges an Zeit Abseits der Arbeit verbrachte ich auch mit René Widera. Vielen Dank für die zahllosen Heimfahrten, die dazugehörigen Gespräche, Gartentreffen und die dabei geernteten Früchte. Deren Genuss und Vergärung bereiteten mir viel Freude.

Doch nicht nur die Herstellung von Wein, sondern auch das Brauen von Bier erfüllte mich mit Freude aufgrund der Abwechslung und des Kontrasts zur Arbeit. Für die tollen Einführungen und Anleitungen zum Keltern und Brauen danke ich Dr. Andreas Kranz, John Palmer und Jamil Zainasheff [315–317].

Am liebsten genoss ich das gute Homebrew während der gemeinsamen freudbetonten und immer spaßigen Feiern mit meinen Studienkollegen und deren Partnern. Ein Hoch auf uns!

Unvergessen bleiben dabei die legendären Ausflüge mit dem BHP, zum Beispiel nach Leipzig, zur MotoGP, ins Legoland, in die sächs. Schweiz oder andere abgelegene Wälder und zugige Anhöhen, welche wir während der Jagd nach Dr. Muggel, dem Heiligen Gral und anderen Schätzen erkundeten. Und sei es nur das Bier beim unregelmäßigen Stammtisch, unsere Zusammenkünfte und Gespräche gaben mir Zuversicht in schwierigen Zeiten und sicherten mein geistiges Wohlergehen. Thomas, Roland, Mo und Flo, unsere Gemeinschaft liegt mir am Herzen und war unfassbar wichtig für das Gelingen der Arbeit. Ohne Euch hätte ich es nie geschafft. Danke!

Die Doktorarbeit überhaupt beginnen zu können erforderte vor allem von meinen Eltern viel Vertrauen und Unterstützung. Beides brachten sie mir bedingungslos und umfassend entgegen. Darüber hinaus waren sie jederzeit verfügbar und flexibel zur Bewältigung aller möglichen organisatorischen und familiären Herausforderungen. Ihr wart immer ein verlässlicher und starker Rückhalt, vielen Dank dafür!

Vertrauen, Rückhalt und Unterstützung erfuhr ich ebenfalls zu jederzeit im größeren Familienkreis, bei meinen Schwiegereltern und Verwandten, vor allem aber bei Gesine. Dir gebührt zusätzlich ein großes Dankeschön für Dein Verständnis und Deine Einsatzbereitschaft, wenn es darum ging, für die Kinder zu sorgen während ich wiedereinander auf Dienstreise, länger auf Arbeit oder bis in die Nacht in der Bibliothek zum Lernen war.

**DANKESCHÖN!**

## Erklärungen

Hiermit versichere ich, dass ich die vorliegende Arbeit ohne unzulässige Hilfe Dritter und ohne Benutzung anderer als der angegebenen Hilfsmittel angefertigt habe; die aus fremden Quellen direkt oder indirekt übernommenen Gedanken sind als solche kenntlich gemacht. Die Arbeit wurde bisher weder im Inland noch im Ausland in gleicher oder ähnlicher Form einer anderen Prüfungsbehörde vorgelegt.

Die Dissertation wurde unter der wissenschaftlichen Betreuung von Prof. Dr. Ulrich Schramm, Dr. Michael Bussmann und Dr. Alexander Debus am Helmholtz-Zentrum Dresden – Rossendorf angefertigt.

Die Promotionsordnung der Fakultät Mathematik und Naturwissenschaften an der Technischen Universität Dresden vom 23. Februar 2011 mit letzten Änderungen vom 18. Juni 2014 erkenne ich an.

Dresden, 25. Juli 2017

Klaus Steiniger







Bautzner Landstr. 400  
01328 Dresden, Germany  
Tel. +49 351 260-3639  
Fax +49 351 260-13639  
k.steiniger@hzdr.de  
<http://www.hzdr.de>